



**HAL**  
open science

# Experimental and numerical modeling of the dissolution of delta ferrite in the Fe-Cr-Ni system: application to the austenitic stainless steels

Mahmoud Saied

► **To cite this version:**

Mahmoud Saied. Experimental and numerical modeling of the dissolution of delta ferrite in the Fe-Cr-Ni system: application to the austenitic stainless steels. Materials. Université Grenoble Alpes, 2016. English. NNT: 2016GREAI016 . tel-01337983

**HAL Id: tel-01337983**

**<https://theses.hal.science/tel-01337983>**

Submitted on 27 Jun 2016

**HAL** is a multi-disciplinary open access archive for the deposit and dissemination of scientific research documents, whether they are published or not. The documents may come from teaching and research institutions in France or abroad, or from public or private research centers.

L'archive ouverte pluridisciplinaire **HAL**, est destinée au dépôt et à la diffusion de documents scientifiques de niveau recherche, publiés ou non, émanant des établissements d'enseignement et de recherche français ou étrangers, des laboratoires publics ou privés.

## THÈSE

Pour obtenir le grade de

### **DOCTEUR DE LA COMMUNAUTÉ UNIVERSITÉ GRENOBLE ALPES**

Spécialité : **Matériaux, Mécanique, Génie civil, Electrochimie**

Arrêté ministériel : 7 août 2006

Présentée par

**Mahmoud SAIED**

Thèse dirigée par **Muriel VERON** et  
codirigée par **Catherine TASSIN**

préparée au sein du **Laboratoire SIMaP**  
dans **l'École Doctorale I-MEP2**

### **Experimental and numerical modeling of the dissolution of $\delta$ -ferrite in the Fe-Cr-Ni system: Application to austenitic stainless steels**

Thèse soutenue publiquement le **24 mai 2016**,  
devant le jury composé de :

**M. Jean-Hubert SCHMITT**

Professeur, Ecole Centrale Paris, Président

**M. Michel PEREZ**

Professeur, INSA Lyon, Examineur

**M. Mohamed GOUNE**

Professeur, Université de Bordeaux, Rapporteur

**M. Dehmas MOUKRANE**

Maître de conférences, Université de Lorraine, Rapporteur

**M. Hatem ZUROB**

Professeur associé, McMaster University, Examineur

**M<sup>me</sup> Muriel VERON**

Professeur, Grenoble INP, Directeur de thèse

**M<sup>me</sup> Catherine TASSIN**

Maître de conférences, Grenoble INP, Co-directeur de thèse

**M. Jean-Denis MITHIEUX**

Ingénieur de recherche, APERAM Isbergues, Examineur

**M<sup>me</sup> Jessica DELACROIX**

Ingénieur de recherche, APERAM Isbergues, Invité

**M. Yves DU TERRAIL COUVAT**

Ingénieur de recherche, Grenoble INP, Invité





## Remerciements

Cette thèse n'aurait pas pu aboutir sans le concours et le soutien d'un grand nombre de personnes auxquelles je souhaite exprimer ma reconnaissance. Je tiens en premier lieu à remercier les membres du Jury qui ont accepté de prendre part à ma soutenance et qui ont contribué à enrichir la discussion autour de ce sujet de thèse. Merci à Dehmas Moukrane et à Mohamed Gouné pour le soin apporté à la relecture du manuscrit ainsi que vos remarques et suggestions ouvrant de nouvelles perspectives.

J'adresse un merci tout particulier à mes directrices de thèse Muriel Véron et Catherine Tassin qui m'ont fait confiance tout au long de cette thèse et qui ont fait preuve de patience vis-à-vis de errements intellectuels. Muriel, merci d'avoir choisi de m'encadrer, de tes multiples conseils et des heures consacrées à diriger cette recherche. Catherine, j'apprécie tout particulièrement ton accompagnement au jour le jour et ta disponibilité. Au delà de l'expertise métallurgique et thermodynamique dont tu m'as fait part, tu m'as implicitement transmis tes qualités de persévérance et d'optimisme face aux moments difficiles.

Cette thèse a été financée par APERAM Stainless. J'exprime ma gratitude à tous ceux qui ont contribué de près ou de loin au lancement et à l'aboutissement de ce projet de recherche. Je tiens à remercier Jean-Michel Damas pour m'avoir donné confiance et accepté au sein de l'équipe de métallurgie du centre de recherche d'Isbergues. Mes remerciements vont également à Jean-Denis Mithieux et Jessica Delacroix qui ont été à l'origine de ce sujet et l'intérêt qu'il ont porté à mon travail tout au long de nos nombreuses discussions. Jean-Denis, je ne saurai oublier le sens de l'humour dont tu as fait preuve et qui a agrémenté à bien des égards nos réunions. J'adresse un merci tout particulier à Virginie Beck qui m'a accompagné tout au long de ma thèse notamment sur les aspects expérimentaux et qui n'a eu de cesse de répondre positivement à toutes mes demandes et interrogations.

Plusieurs collaborations ont contribué à la réussite de ces travaux de thèse. Je tiens à remercier à ce titre:

- Yves du Terrail (SIMaP, groupe EPM) pour sa contribution continue au développement du code de transformation de phase ainsi que l'expertise numérique qu'il a su me transmettre au cours de nos réunions.
- Emmanuel Rigal pour la fabrication des microstructures modèles par Compression Isostatique à Chaud au(CEA Grenoble).
- Sophie Cazottes (INSA Lyon) pour les cartographies EBSD ainsi que pour son invitation à animer une session du séminaire scientifique du laboratoire MATEIS et

les discussions portant sur les aspects numériques que j'ai eu avec Michel Perez, Carole Dessolin ainsi que Patrice Chantrenne.

La contribution des membres du laboratoire SIMaP est aussi déterminante quant à l'aboutissement de ces travaux de recherche. Je remercie en premier lieu Florence Robaut et Rachel Martin pour les dizaines de profils à la microsonde ainsi que les cartographies EBSD qu'elles ont eu la gentillesse de réaliser. Merci aussi à Frédéric Charlot pour m'avoir accompagné sur le MEB et avoir été à ma disposition en cas de besoin d'aide technique. Mes remerciements s'adressent aussi à Alain Domène pour les multiples découpes réalisés avec brio et en temps voulu ainsi qu'à Gilles Renou pour les observations au MET et Laurent Artaud pour ce qui concerne la thermique.

Au SIMaP on ne fait pas que de la métallurgie, mais s'intéresse aussi à d'autres sujets. J'ai particulièrement apprécié les longues discussions que j'ai eu avec Bruno Gilles et portant souvent sur l'histoire et l'actualité politiques. Bruno, j'ai beaucoup appris de tes réflexions et de ta lecture des évènements. Côté technologie, je ne saurais oublier de remercier Bruno Mallery pour le savoir-faire dont il m'a fait part à chaque fois que je le sollicitais.

Au cours de ces trois ans, j'ai eu l'opportunité d'encadrer deux stagiaires: José et Augusto. Ils ont largement contribué à l'avancement de ces travaux de recherche et m'ont beaucoup appris sur le plan humain. Ils étaient en deuxième année cycle ingénieur Phelma. Je leur adresse mes remerciements et leur souhaite bon vent.

Par là même je souhaite saluer l'ensemble des membres du groupe PM et en particulier mes amis thésards avec qui j'ai partagé ces trois années: Olivier, Hasan, Fanny, Nicolas, Rosen ainsi que d'autres. Aussi, merci à Hugo Van Landeghem qui nous a rejoint récemment et avec qui j'ai beaucoup échangé tant sur des problématiques numériques que sur des aspects métallurgiques et qui a notamment apporté un regard extérieur sur mes travaux de recherche. Je te souhaite une bonne réussite dans ton parcours.

Enfin, mes remerciements vont aussi à tous ceux qui ont contribué à faire de ces trois années passées à Grenoble un moment de vie agréable. Merci à mes copains grenoblois pour les moments de convivialité partagés ensemble aux cafés de Saint-Bruno et notamment les festins hebdomadaires organisés ensemble. Merci à mon père et à ma mère qui, de longue date, ont investi de leur temps et de leur argent et ont tout misé pour ma réussite professionnelle. J'estime que leurs efforts ont porté leurs fruits. Et finalement merci à celle qui sera ma future épouse: Donia.

# Contents

<b>Remerciements .....</b>	<b>2</b>
<b>Contents .....</b>	<b>4</b>
<b>Introduction Industrial and scientific motivations.....</b>	<b>7</b>
I. The fabrication of flat austenitic stainless steels .....	7
II. Industrial and scientific motivations .....	9
III. Outline of the thesis.....	10
<b>Chapter I Literature review .....</b>	<b>12</b>
I. Austenitic stainless steels.....	12
II. Solidification modes of stainless steels.....	12
III. Residual ferrite in 304L austenitic stainless steels .....	15
III.1. Morphologies of residual ferrite.....	16
III.2. Distribution of residual Ferrite in continuously cast austenitic stainless steels.....	17
IV. Ferrite dissolution in austenitic stainless steels .....	18
IV.1. Experimental observations .....	18
IV.2. Modeling of the $\alpha \rightarrow \gamma$ diffusion-controlled phase transformations.....	22
IV.3. Modeling the $\alpha \rightarrow \gamma$ transformation in the Fe-Cr-Ni system.....	25
V. Summary and conclusion.....	31
<b>Chapter II Experimental techniques .....</b>	<b>33</b>
I. Metallographic preparations.....	33
II. Quantitative image analysis .....	34
II.1. Measurement of ferrite fraction in the ternary cast alloy .....	35
II.2. Morphological evolution of ferrite particles.....	36
II.3. Morphological separation of vermicular ferrite in the as-cast microstructure.....	36
II.4. Equivalent size of ferrite particles .....	38
II.5. In the multilayered microstructure .....	39
III. Orientation relationship .....	40
IV. Dissolution heat treatments .....	40
V. Chemical analysis and composition measurement .....	42
<b>Chapter III Experimental study of <math>\delta</math>-ferrite dissolution in ternary Fe-Cr-Ni alloys : as-cast and multilayered microstructures.....</b>	<b>44</b>
I. Ferrite dissolution in an ingot cast alloy .....	44
I.1. Composition and thermodynamic calculations.....	44
I.2. Characterization of the as-cast state .....	46
I.3. Kinetics of ferrite dissolution .....	51
II. Ferrite dissolution in the multilayered microstructures .....	60
II.1. Elaboration of the multilayered microstructures .....	61
II.2. Microstructures in the as-received states.....	64
II.3. Dissolution of ferrite bands at 1240°C: results and discussion .....	70
III. Summary and conclusion .....	82

<b>Chapter IV Modeling the ferrite to austenite transformation in the Fe-Cr-Ni system.....</b>	<b>84</b>
I. Problem description .....	84
II. Thermodynamical description and diffusion coefficients .....	85
II.1. Coupling with phase diagram .....	85
II.2. Interdiffusion coefficients .....	87
III. Model hypotheses.....	88
IV. Constitutive equations .....	88
V. Numerical techniques .....	90
V.1. Variable grid spacing .....	90
V.2. Numerical schemes .....	91
V.3. Grid points distribution .....	93
V.4. Calculation algorithm.....	95
V.5. Stability treatments.....	100
VI. Model validation .....	102
VI.1. Comparison with Vitek's numerical results .....	102
VI.2. Comparison to the experiments of Kajihara .....	105
VII. Conclusions and perspectives .....	108
<b>Chapter V Application of the model to analyze ferrite dissolution in the Fe-Cr-Ni cast and multilayered microstructures .....</b>	<b>110</b>
I. Review of the Kajihara experiments .....	110
II. Ferrite dissolution in the multilayered microstructure at 1240°C.....	113
II.1. Design of the simulations .....	113
II.2. Application to ferrite dissolution.....	115
II.3. Discussion .....	126
III. Ternary cast alloy: dissolution of vermicular ferrite .....	132
III.1. Design of the simulation .....	132
III.2. Preliminary results.....	134
III.3. Application of the model to the dissolution of vermicular ferrite .....	148
III.4. Discussion .....	154
IV. Conclusion .....	162
<b>Chapter VI Conclusions and perspectives .....</b>	<b>165</b>
I. Overview of the work and scientific contribution .....	165
II. Recommendations for easy prediction of ferrite dissolution .....	166
III. Perspectives .....	167
<b>Bibliography .....</b>	<b>170</b>
<b>Appendix A Morphological evolutions of vermicular ferrite during its dissolution .....</b>	<b>175</b>
<b>Appendix B The multilayered microstructure at different states .....</b>	<b>181</b>
I. In the first hot rolling state (HR1).....	181
I.1. Microstructures .....	181
I.2. Composition profiles .....	182
II. In the first cold rolling state (CR1) .....	183
II.1. Microstructures .....	183
II.2. Composition profiles .....	183
III. In the second hot rolling state (HR2).....	184
III.1. Microstructures .....	184
III.2. Composition profiles .....	185

---

IV. In the second cold rolling state (CR2).....	186
<b>Appendix C Thermodynamic descriptions .....</b>	<b>188</b>
I. The Ptimec-Miettinen module.....	188
II. The TCFE6 thermodynamic database.....	190
<b>Appendix D Interdiffusion coefficients in ferrite and austenite.....</b>	<b>192</b>
I. Main vs. coupled interdiffusion coefficients .....	192
II. Sensitivity of interdiffusion coefficients to composition .....	193
<b>Appendix E Discretization schemes .....</b>	<b>196</b>
<b>Appendix F Comparison of several meshings: sensitivity of the calculation results to the number of grid points .....</b>	<b>199</b>
I. Uniform meshing .....	199
I.1. Effect of the meshing size in the austenitic phase region .....	199
I.2. Effect of the meshing size in the ferritic phase region .....	200
I.3. Discussion .....	200
II. Geometrical meshing: accuracy and mass loss .....	201
III. Double-uniform meshing.....	203
IV. Conclusion .....	203
<b>Appendix G Stability analysis for the of the diffusion-transport equation.....</b>	<b>205</b>
<b>Appendix H where does numerical diffusion come from?.....</b>	<b>206</b>
I. Why do centered schemes underestimate diffusion ?.....	206
II. Why do upwind schemes overestimate diffusion ?.....	207

# Introduction

## Industrial and scientific motivations

Austenitic stainless steels are the most common and familiar types of stainless steel. They present numerous advantages from a metallurgical point of view and represent more than 70% of the market with a predominance of flat products (more than half of the total trade market in 2013 [1]). A typical composition of austenitic stainless steels is that of the 304L grade which contains approximately 18%Cr, 8%Ni, 0.02%C and other alloying elements at small amounts.

Nevertheless, defects linked to the presence of residual  $\delta$ -ferrite in the solidification microstructure, appear during the hot working process. This leads to material waste and an increase in the manufacturing costs.

In this introduction the fabrication process of flat austenitic stainless steels is described. The industrial and scientific motivations of this PhD work are detailed. Finally the outline of the thesis is presented.

### I. The fabrication of flat austenitic stainless steels

The fabrication process of flat austenitic stainless steels implies several steps, starting from the continuous casting to thickness reduction by hot and cold rollings and ending by surface finishing. In the framework of this research work, attention will be focused on the continuous casting and the hot rolling steps (Figure 1):

- a. The molten steel is first solidified and cooled during the continuous casting. At the end of this step, the solid steel is cut into slabs weighting up to 30 tons, up to 12m long, 2m wide and 200mm thick.
- b. Slabs are then introduced into a reheating furnace to be prepared for hot rolling. The increase in temperature inside the furnace is made in order to reduce segregations and reach thermal homogeneity of slabs prior to hot rolling. The reheating temperature (between 1200°C and 1300°C) depends on the grade and the duration of this stage is about 3h.
- c. A first reduction thickness from 200 to 40mm is achieved through several passes on the roughing mill.
- d. A final thickness, generally between 3 to 12mm, is obtained after the finishing mills composed of several rolling strands.
- e. After coiling and cooling, "black coils" (due their oxidized surface) are formed and then transferred to the cold rolling mills for the processing steps.

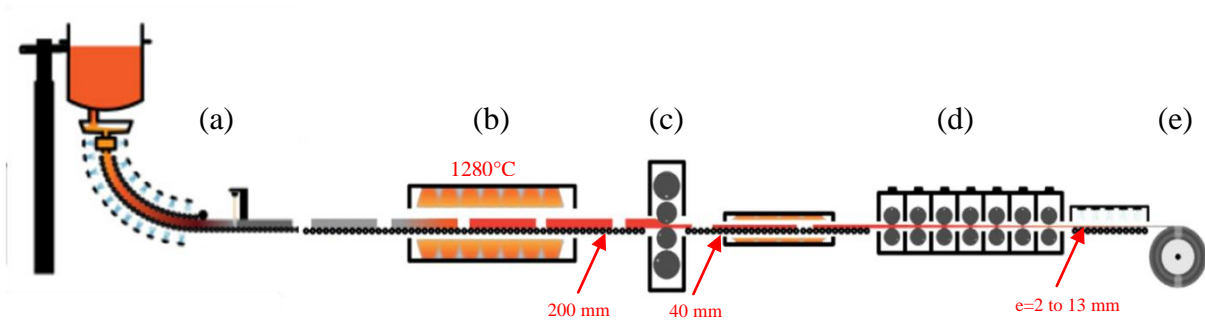


Figure 1: Schematic illustration of (a) the continuous casting, (b) the reheating furnace, (c) the roughing mill, (d) the finishing mills and (e) the black coil [2].

Although expected to be fully austenitic at room temperature, the as-cast microstructure of austenitic stainless steels generally contains a small amount of residual  $\delta$ -ferrite, as shown in the microstructure of a 304L stainless steel in Figure 2.a. The presence of ferrite is highly desirable at the beginning of the solidification ( $\sim 1470^\circ\text{C}$ ), since it reduces hot cracking susceptibility of austenitic stainless steels that is mainly due to the presence of an excess of phosphorous and sulfur contents [3]. Upon cooling, ferrite is supposed to dissolve in austenite as predicted by the phase diagram of Figure 2.b. However due to the cooling rate of slabs, this transformation is incomplete since it is limited by the slow process of solutes redistribution in ferrite and austenite. Residual ferrite is even still present after the slab reheating prior to the hot rolling for the same kinetic reasons.

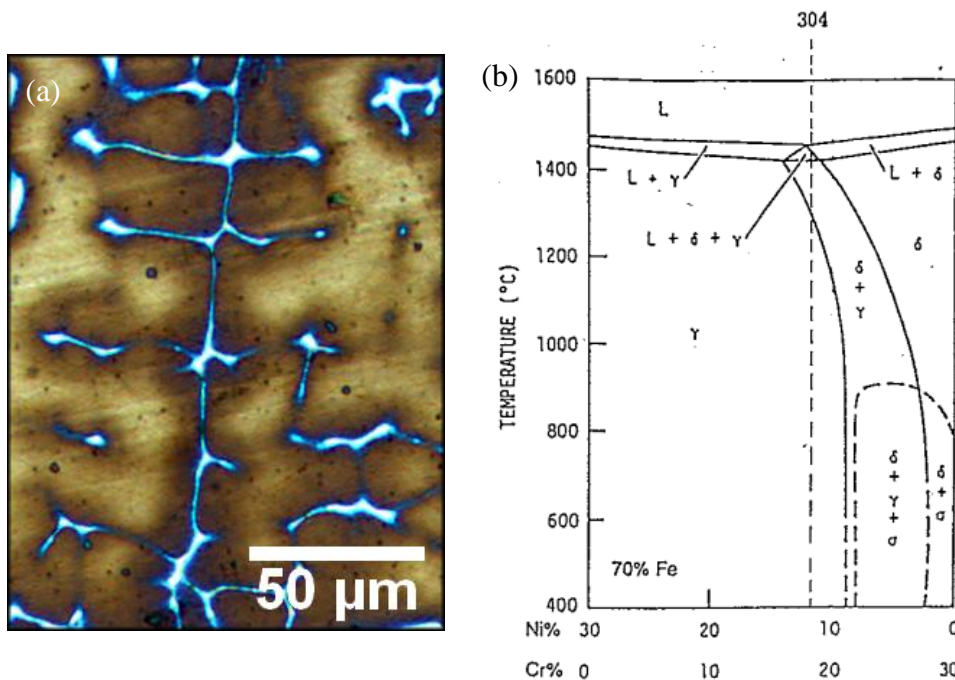
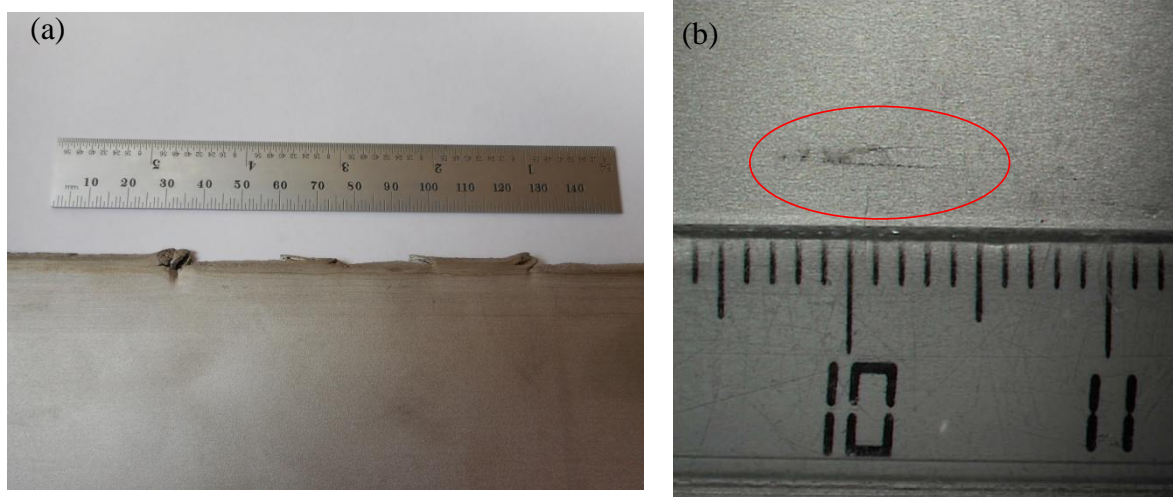


Figure 2: (a) As-cast microstructure of continuously cast austenitic 304L stainless steel showing the presence of residual  $\delta$ -ferrite in white and austenite in yellow and brown [4] (b) Isolethal section at 70% wt.%Fe of the Fe-Cr-Ni phase diagram [5].

The presence of  $\delta$ -ferrite is detrimental to the hot ductility of austenitic stainless steels and can lead to cracks appearing either at the edge of the hot-rolled slab as "open cracks" or at the

finished surface as sliver defects containing oxides (Figure 3). These cracks originate from rheological differences between hard austenite and soft ferrite that give raise to damage at the  $\delta/\gamma$  interface where mechanical constraints are the highest [4][5]. Their presence impairs the quality of steel products, such as the deterioration the resistance to pitting corrosion as well as the surface finishing quality caused by sliver defects.

Therefore, additional operations like grinding and sheet slitting are often required to eliminate these defects. These operations lead to material waste and increase the manufacturing costs.



**Figure 3: Illustration of the poor hot-workability of austenitic stainless steels: (a) edge cracks at in the sheets after hot rolling and (b) sliver defect at the surface after cold rolling and surface finishing (Images from APERAM).**

Consequently, the challenging issue of improving products quality and cost reduction is to eliminate the  $\delta$ -ferrite phase during the fabrication cycle of austenitic stainless steels.

## II. Industrial and scientific motivations

The solution, that is the object of the present PhD work, is to completely dissolve ferrite by appropriate heat treatment prior the hot rolling. Hence, there is a need to understand the mechanisms underlying ferrite dissolution in austenitic stainless steels and the impact of thermal, microstructural, physical and chemical parameters on its kinetics.

This PhD work was intended to provide scientific responses for these needs. The fixed objectives are twofold:

- Understand the general characteristics of the ferrite to austenite transformation in 304L austenitic stainless steels. To properly accomplish this task, ferrite dissolution will be studied in two simplified configurations: a ternary Fe-Cr-Ni cast alloy with a simplified composition close to the one encountered in industrial stainless steels and a model multilayered microstructure alternating austenite and ferrite of the Fe-Cr-Ni system separated by planar interfaces.

- Develop a one-dimensional finite difference model in order to predict dissolution kinetics of ferrite in complex microstructures (representative of industrial slabs) and under anisothermal treatments.

As a validation step, the model will first be applied to the prediction of the kinetics of ferrite dissolution in the multilayered microstructure and then in the cast alloy in order to bring more insight into the mechanisms of this transformation. On the basis of the scientific results that will be raised in this study, industrial recommendations will be formulated.

### III. Outline of the thesis

This thesis is subdivided into five chapters. After the introduction:

- **Chapter I** starts with a bibliographic review of the main mechanisms of ferrite formation in cast austenitic stainless steels and the impact of physical parameters like solidification conditions and chemical composition on its features (amount, morphology, etc.). Works dedicated to the high temperature ferrite dissolution are then presented and main characteristics of the transformation are outlined and qualitatively discussed on the basis of simple analytical models. Finally, available modeling works for the  $\delta \rightarrow \gamma$  transformation are presented in terms of equations, assumptions and numerical techniques. Their application to the analysis of the  $\delta \rightarrow \gamma$  transformation is then presented and discussed.
- In **Chapter II**, the experimental techniques and quantification procedures used for the characterization of the microstructures and the study of the dissolution kinetics are presented.
- **Chapter III** is divided into two main parts. In the first one, the ternary Fe-Cr-Ni alloy will first be characterized in the as-cast state and then kinetics of  $\delta$ -ferrite dissolution will be established at several temperatures and described in terms of ferrite's fraction and morphology as well as solutes distribution. In the second part, the elaborated of the multilayered microstructure is first presented. After characterization in the as-received states, the dissolution of ferrite in the multilayered microstructure is experimentally studied and main features outlined.
- The subject of **Chapter IV** is to develop a numerical phase transformation model in order to analyze the experimental results relative to ferrite dissolution in both multilayered and cast microstructures. After presenting the governing equations and deriving them under the formulated hypotheses, numerical techniques used for the approximation of the equations and stability treatments are presented. Finally the model is validated on experimental results from literature.
- **Chapter V** is dedicated to the analysis of the experimental data using the developed model. The goal of this chapter is twofold. First, understand the mechanisms of ferrite dissolution in the Fe-Cr-Ni cast alloy. Second develop a modeling methodology for the prediction of ferrite dissolution in cast alloys. To accomplish this, the numerical model is preliminarily applied to the dissolution of ferrite in the multilayered microstructure. This microstructure presents a simple study case in which the impact

of model assumptions as well as several metallurgical and physical parameters on the prediction is assessed.

The last chapter is dedicated to a general conclusion followed by scientific perspectives and industrial recommendations based on the present work. Finally the appendices will be found at the end of this thesis.

# Chapter I

## Literature review

This chapter aims at introducing the context of this study through a general literature review. In the first part, the aspects related to the formation of  $\delta$ -ferrite during solidification austenitic stainless steels will be presented and the effect of various metallurgical parameters on the amount and the shape of ferrite discussed. In the second part, a review of existent works on ferrite dissolution in austenite will be shown, and main features of the transformation will be outlined. In the final part, the focus will be on the modeling approaches used so far in the numerical prediction of  $\delta \rightarrow \gamma$  transformation.

### I. Austenitic stainless steels

Stainless steels are iron-based alloys that contain at least 10.5%Cr<sup>1</sup> enabling them to be resistant to wet corrosion. This stainless property is achieved by forming a very thin passive layer of Cr<sub>2</sub>O<sub>3</sub> at the surface. The addition of alloying elements as Ni, Mo, Mn and other minor ones gives to these steels more functional and mechanical properties in order to match their environmental and economical criteria. On the basis of their crystalline structure at room temperature, stainless steels can be divided into four families:

- Austenitic stainless steels
- Martensitic stainless steels
- Ferritic stainless steels
- Duplex stainless steels

Austenitic stainless steels are the most used ones and represent more than 70% of the stainless steel market. The commonly used austenitic grade is 304L, which typically contains 18%Cr-8 to 10%Ni and 0.02%C in addition to other alloying elements [8].

### II. Solidification modes of stainless steels

The solidification sequence of stainless steels is usually predicted using Fe-Cr-Ni phase diagram. The projection of the liquidus, ferrite ( $\alpha$ ) solidus and austenite ( $\gamma$ ) solidus lines in the Fe-Cr-Ni ternary diagram (Figure I. 1) shows a peritectic reaction Liquid +  $\alpha \rightarrow \gamma$  at the iron-rich corner of the phase diagram. The peritectic behavior still occurs until the liquidus

<sup>1</sup> According to the European standard EN-10088-1[2]

line crosses the austenite solidus line, after which the reaction becomes eutectic: Liquid  $\rightarrow \alpha + \gamma$ . The chemical composition relative to this intersection point has been situated at: 8 wt.%Cr and 5.5 wt.%Ni according to Speich *et al.* (1973 [9]), 14.6 wt.%Cr and 9.6 wt. %Ni according to Shurmann *et al.* (1977, [10]) and 17.2 wt.%Cr and 11.9 wt. %Ni according to Fredriksson (1979, [11]). This latter composition lies near the composition range of 304 stainless steels, which causes, for certain grades, an ambiguity as to peritectic or eutectic nature of the transformation in the three phase region. This ambiguity is even higher in real solidification conditions where solutes segregation can affect the nature of the transformation.

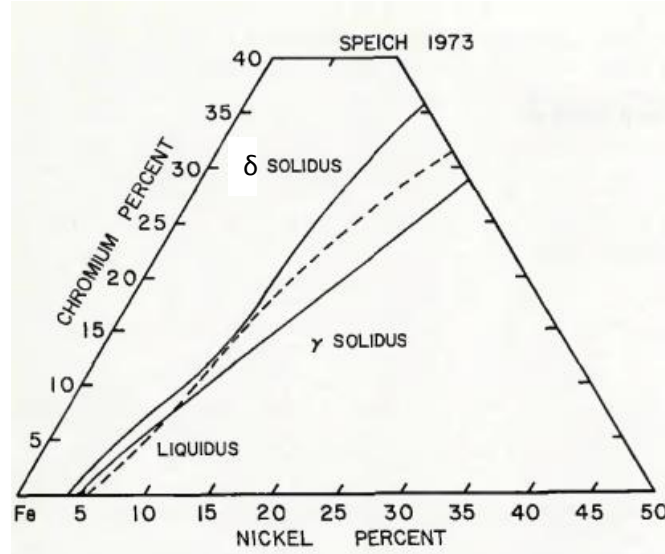


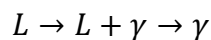
**Figure I. 1: The liquidus, ferrite solidus and austenite solidus projection lines plotted on the Fe-Cr-Ni phase diagram [5].**

In order to predict the solidification sequence, complex compositions are reduced to the Fe-Cr-Ni ternary system using chromium and nickel equivalents. Several equivalents formulae exist in literature [12][13]. In the case of conventionally-cast stainless steels, the Hammar and Svensson formulae are usually considered [14]<sup>2</sup>:

$$\begin{cases} (Cr)_{eq} = \%Cr + \%Mo + 1.5\%Si + 2\%Nb + 3\%Ti \\ (Ni)_{eq} = \%Ni + 0.31\%Mn + 22\%C^* + 14.2\%N^* + \%Cu \end{cases}$$

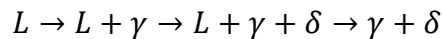
Most commercial stainless steels contain less than 80 wt.% Fe and their solidification are often discussed on the basis of constant Fe isoplethal sections like the one shown in Figure I. 2.a which exhibits a eutectic behavior. Depending on the value of the equivalence ratio  $k = Cr_{eq}/Ni_{eq}$ , solidification sequence can occur according to one of the following four modes. The correspondent microstructures at room temperature are shown in Figure I. 2.b:

- **Mode A** : primary austenite solidification without appearance of ferrite

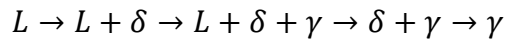


<sup>2</sup> \* N\* and C\* represent interstitial carbon and nitrogen.

- **Mode AF:** primary austenite solidification followed by nucleation and growth of ferrite by eutectic reaction in the remaining inter-dendritic Cr-enriched liquid.



- **Mode FA:** primary ferrite precipitation followed, on further cooling, by austenite formation in the three phase region. The reaction in the three phase region of this pseudo-binary phase diagram is eutectic. Below the solidus line, ferrite transforms to austenite at the solid-state until its complete dissolution.



- **Mode F:** primary ferrite solidification with austenite forming a Widmanstätten structure along the ferrite boundaries upon cooling in the solid state. At very high equivalence ratios, the end product microstructure can however be fully ferritic.

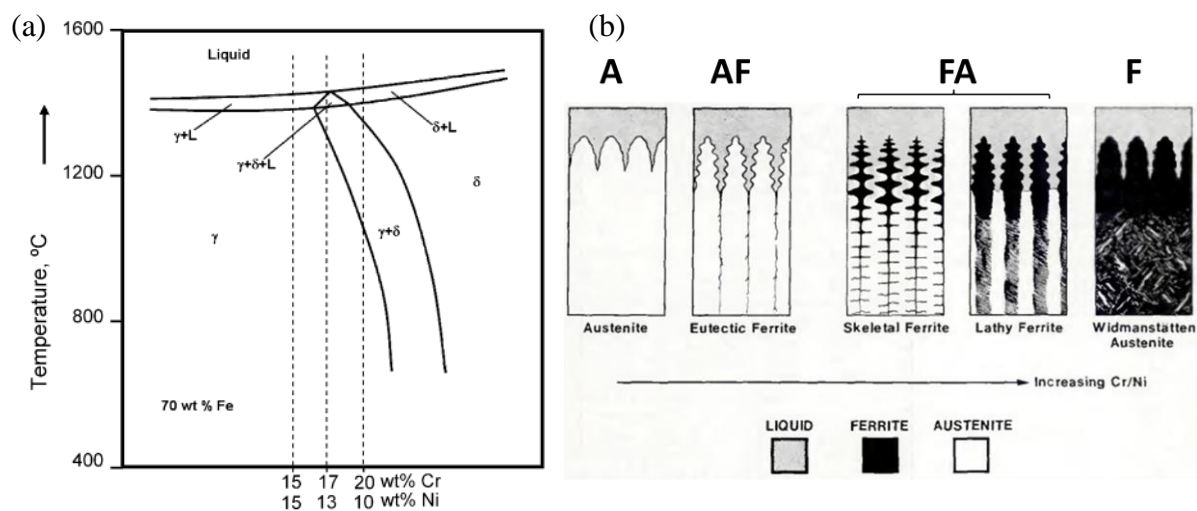
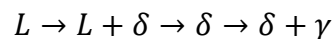
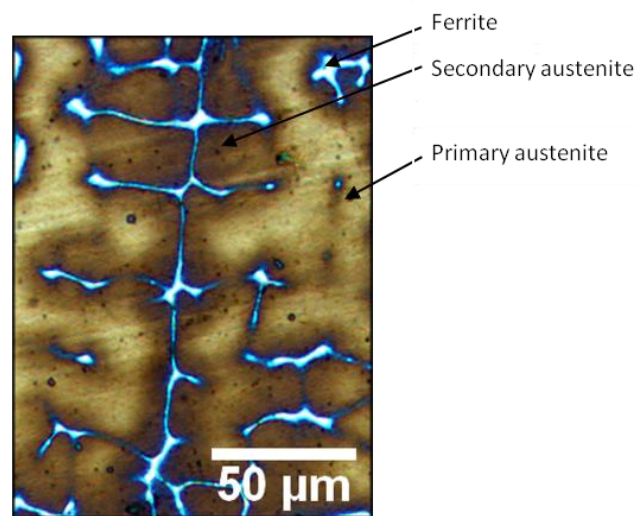


Figure I. 2: (a) Vertical 70 wt.%Fe section of Fe-Cr-Ni ternary diagram [15]. (b) Typical structures at room temperature [16].

The use of phase diagram depicts the influence of the global composition on the solidification sequence under equilibrium conditions. However in real cases the solidification sequence depends also the solidification rate which influences the possible growth competition between stable and metastable solid phases through the kinetic undercooling required for their growth. In austenitic 304L steels, the first solid crystal in equilibrium with the liquid is ferrite. However, transition from primary ferrite to metastable austenite mode has been observed by many authors [15][16] in conventional casting processes when the velocity of the solid-liquid interface exceeds a critical value. At even higher solidification rates solidification can even occur in the F mode as it has been reported by Elmer *et al.* [19]. Variations in the solidification rate also impacts the amount of ferrite and causes its increase or decrease depending on the solidification sequence under the considered solidification rate. Furthermore, what also renders the use of phase diagrams sometimes misleading is the fact that the solidification path does not necessarily lie in a constant Fe section [20]. Accordingly, these pseudo diagrams provide only a very approximate basis for the discussion of the solidification path.

Regarding 304L austenitic stainless steels, their solidification is known to occur in the FA mode, as their equivalent Cr and Ni compositions generally lie on the ferritic side of the monovariant line of Figure I. 2.a. Experimental results have shown that, contrarily to the eutectic behavior predicted by the phase diagram of Figure I. 2.a, the transformation in the three phase region is peritectic [6][19]–[21]: ferrite growth in liquid is interrupted by precipitation of primary austenite from the liquid that envelops the ferritic dendrite and then solidification ends within a narrow temperature range. On further cooling, a large amount of ferrite is consumed by austenite (secondary austenite) by a diffusion-controlled solid-state transformation. The stability of the remaining ferrite is enhanced by Cr rejection into ferrite and Ni partitioning in austenite during the transformation [21]. A representative microstructure of an as-cast microstructure of a 304L stainless steel is given in Figure I. 3.



**Figure I. 3:** As-cast microstructure of a continuously cast 304L stainless steel presenting vermicular residual ferrite. Residual ferrite appears in white, primary austenite in yellow and secondary austenite in brown (Lichtenegger and Bloesch etching) [4].

### III. Residual ferrite in 304L austenitic stainless steels

Although 304L stainless steels are predominantly austenitic, they contain a small amount of residual  $\delta$ -ferrite formed during solidification (FA mode) and whose transformation to austenite upon cooling is incomplete. The presence of ferrite as the first appearing solid crystal is highly desirable at the beginning of solidification, since it reduces the segregation of harmful impurities like phosphorous and sulfur [24], [25]. In the case of primary austenitic solidification, such elements are rejected into the inter-dendritic spacing and form low melting point inclusions that lead further to hot cracking during the solidification[8] [23] [24]. The conventional guideline to prevent this hot-cracking susceptibility is that the material should contain a sufficient amount of ferrite, which should be at least 3 vol.% according to Brooks *et al.* [27].

In this section we will present some characteristic features of the residual  $\delta$ -ferrite in the as-cast microstructures of austenitic stainless steel.

### III.1. Morphologies of residual ferrite

In cast products two types of ferrite morphology are frequently observed: skeletal and lathy (Figure I. 4). Skeletal ferrite is the most commonly observed in austenitic stainless steels. It occupies the very core of dendrite primary and secondary arms. The lathy morphology is characterized by interlaced ferrite networks located in primary ferrite dendrites and surrounded by austenite. Both morphologies are the result of the high temperature solid-state decomposition of ferrite driven by Cr and Ni diffusion [19][26][27] and not the product of massive transformation as has been initially suggested by Lippold *et al.* [24]. Those conclusions are substantiated by the shape of Cr and Ni microsegregation in both ferrite and austenite and in particular the Cr and Ni partitions near the phase boundaries which are consistent with a diffusive solid-state transformation [28].

Conditions affecting the morphology of residual ferrite have been investigated in stainless steel welds. Takalo *et al.* [30] reported that a direct correlation exists between the amount of ferrite and its morphology in the as-welded microstructure. For ferrite contents increasing up to 20%, skeletal ferrite is gradually replaced by lathy one. Suutala *et al.*[29] studied the variation of the amount of lathy ferrite in AISI 300 series welds of different compositions under conditions of shielded metal arc weldings. They found that the content of lathy ferrite increases with the  $Cr_{\acute{e}q}/Ni_{\acute{e}q}$  equivalence ratio.

Despite those numerous studies the mechanisms of the formation of these morphologies are still unclear. Brooks *et al.*[20] reported that the lathy morphology may be the result of morphological instability during the motion of the  $\delta/\gamma$  interface, in an analogous way to the instability theory of Mullins and Sekerka [31] in solidification. In contrast, the movement of the interface in the vermicular-type ferrite maintains its planar or nearly planar shape.

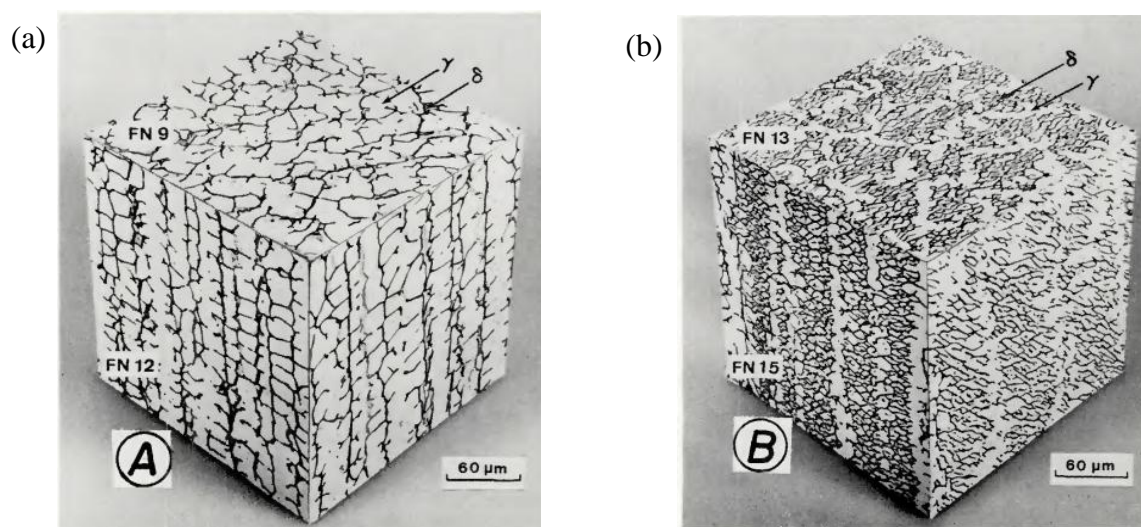
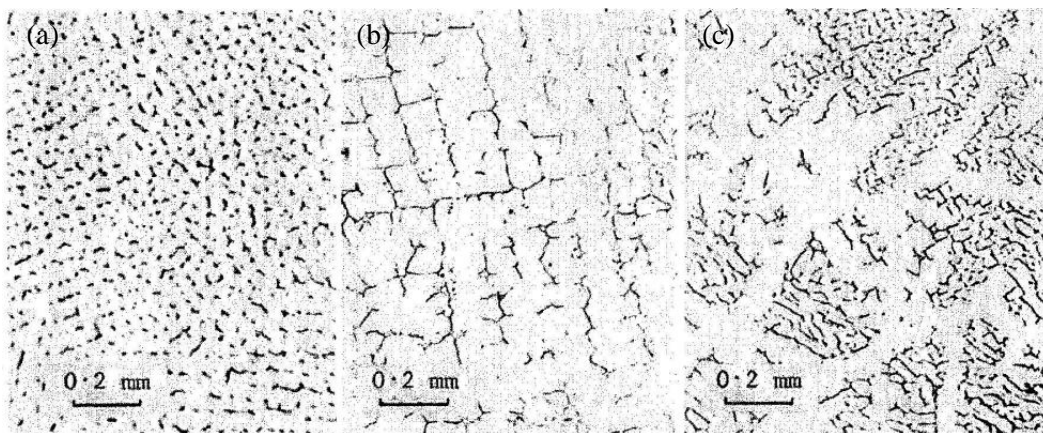


Figure I. 4: Ferrite morphologies in ferritic-austenitic solidification welds: (a) skeletal, (b) lathy [32].

### III.2. Distribution of residual Ferrite in continuously cast austenitic stainless steels

In cast products various morphologies of  $\delta$ -ferrite may be encountered across an ingot section. Pereira *et al.* [33] studied the evolution of ferrite morphologies in an austenitic stainless steel solidifying under the FA mode in a metallic mould under an cooling rate of  $3.2^\circ\text{C/s}$ . Figure I. 5 structures typical of the outside, intermediate and centre position of the ingot. Close to the chill (Figure I. 5.a) the fine ferrite particles correspond to very fine dendrites owing to the initially high cooling rate that become rounded by further cooling. At the intermediate position (Figure I. 5.b), ferrite adopts a vermicular (skeletal) morphology and at the center (Figure I. 5.c) it becomes lathy and much finer. Other morphologies have been reported, but corresponding to stainless steels solidifying under other sequences.



**Figure I. 5: Mapping of the evolution of the morphology of delta ferrite from the edge to the center of a continuously cast austenitic stainless steel slab [4].**

The distribution of residual ferrite content and size across the width of cast products is usually M-shaped as shown in Figure I. 6.a. The amount of ferrite increases with the distance from the edge of the slab and undergoes a decrease at the center [32][33]. The secondary dendrite arm spacing  $\lambda_2$  increases with the distance from the edge of the slab (Figure I. 6.b) as a result of an increase in the local solidification time: several empirical correlations have been evidenced which take the form of the following equation [16][33][34]:

$$\lambda_2 = Ct^n \quad (\text{I.1})$$

Here C is a constant that depends on the material. Empirically the exponent  $n$  ranges from 0.25 to 0.4, which is the signature of the coalescence and ripening of dendrites during solidification (the theoretical value of  $n$  is  $\frac{1}{3}$ ). This means that the longer the material is held at high temperature (near the center of the slab) the more numerous are dendrite arms that disappear by ripening. As a consequence the larger is the SDAS.

In addition to the secondary dendrite arm spacing which sets the diffusion distances of solutes, another factor that determines the variation in ferrite content throughout the slab is the cooling rate in the solid state. This parameter determines the diffusion time and thus the extent of  $\delta \rightarrow \gamma$  transformation [5].

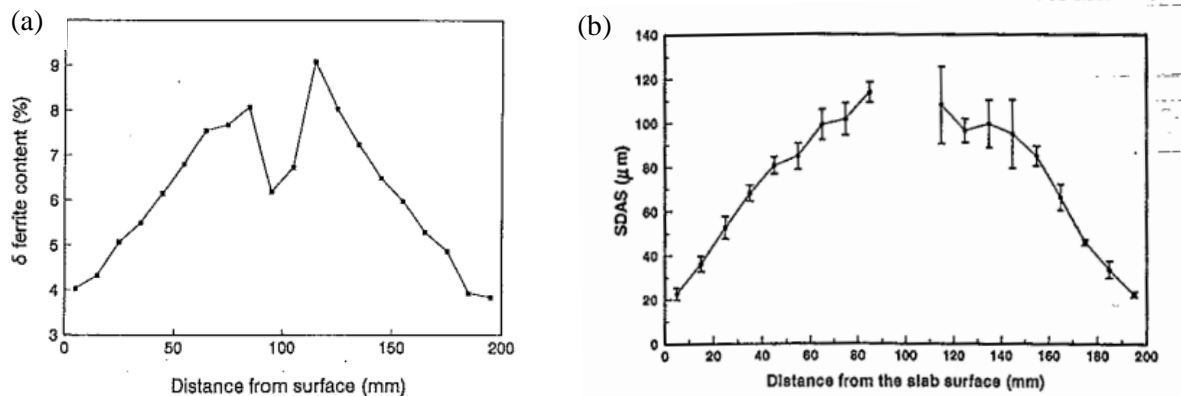


Figure I. 6: : (a) Delta ferrite content and (b) secondary dendrite arm spacing (SDAS) with depth from surface of continuously cast type 304 stainless steel slabs [5].

#### IV. Ferrite dissolution in austenitic stainless steels

Austenitic stainless steels exhibit in the as-cast state a two phase microstructure comprising austenite and residual ferrite. The formation of delta ferrite has been the object of extensive studies, either in cast or weld microstructures. However very few studies have paid attention to its dissolution by subsequent heat treatments.

In fact, experimental investigations are rather focused on simple Fe-Cr-Ni-based systems (diffusion couples) or conducted on materials (phase composition and thickness, etc.) and in experimental conditions (temperature) far from those encountered in industrial contexts.

We will present in this section the experimental works conducted on ferrite dissolution in austenitic stainless steels and equivalent Fe-Cr-Ni-based alloys. In the following sections the symbol  $\alpha$  will designate ferrite that is not formed at high temperature (versus the high-temperature  $\delta$  ferrite formed during a casting process).

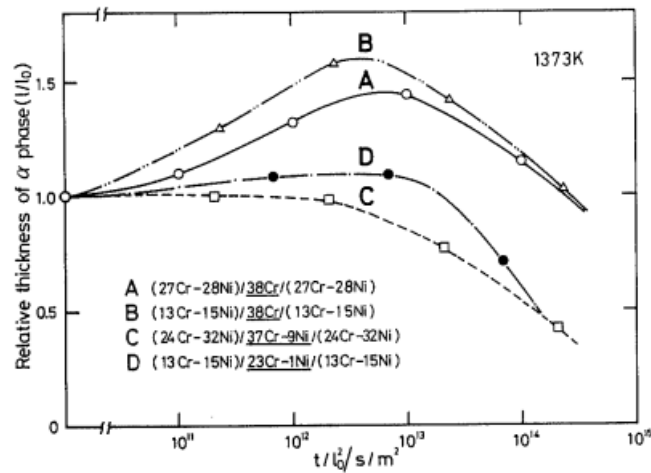
##### IV.1. Experimental observations

The  $\alpha \rightarrow \gamma$  transformation was studied in the ternary Fe-Cr-Ni system at 1100°C by Kajihara *et al.* [36] using four  $\gamma/\alpha/\gamma$  diffusion couples. Ferrite ( $\alpha$ ) and austenite ( $\gamma$ ) compositions and initial thicknesses are listed in Table I. 1.

Experiments show that ferrite dissolution can occur according to two possible ways (Figure I. 7): in the first one, ferrite undergoes a transient thickening at the beginning of the transformation followed by the dissolution stage until complete disappearance (couples A, B and D). In the second one, the dissolution is straightforward and no initial growth stage occurred (couple C). This apparently unusual behavior of the interface migration is a direct consequence of the respective amplitudes of the diffusional fluxes in ferrite  $J^\alpha$  and austenite  $J^\gamma$  in the course of the transformation. We will show in §IV.3.a *Analytical approach* in which conditions the initial growth occurs.

**Table I. 1: Composition and initial thickness of ferrite and austenite phases in the diffusion couples studied by Kajihara [36].**

Diffusion couple	Composition (wt. %)		Thickness ( $\mu\text{m}$ )	
	Ferrite	Austenite	Ferrite	Austenite
A	38 Cr	27 Cr, 28 Ni	188	2000
B	38 Cr	13 Cr, 15 Ni	124	2000
C	37 Cr, 9 Ni	24 Cr, 32 Ni	130.6	2000
D	23 Cr, 1 Ni	13 Cr, 15 Ni	71.6	2000

**Figure I. 7: Relative thickness of ferrite as function of the aging time at 1100°C in the four diffusion couples studied by Kajihara *et al.* [36].**

In industrial grades, the situation is more complex since other alloying elements influence both the thermodynamics (changing phase equilibria) and the kinetics of the ferrite to austenite transformation (through their diffusion in both phases). The dissolution of residual vermicular-type  $\delta$ -ferrite in an industrial strip-cast 304 stainless steel was conducted by Kim *et al.*[37] at temperatures ranging from 1050°C to 1200°C (Figure I. 8). The material containing 0.06%C was initially coiled at 600°C. The dissolution of ferrite comprises two stages, as in the previous case, but shows other characteristics. Instead of a transient increase, the first stage corresponds to the dissolution of 50% of ferrite within 60s, *i.e.* before the specimen reaches its target temperature. This rapid dissolution results from the very low chromium content in ferrite resulting from the precipitation of  $M_{23}C_6$  carbides at the  $\delta/\gamma$  interfaces during coiling. This Cr depletion (13.3%Cr in ferrite against 18.2%Cr in nominal composition) increases thermodynamic instability of ferrite and enhances its dissolution. After carbides dissolve when reaching the annealing temperature, the kinetics of ferrite dissolution becomes controlled by volume diffusion of Cr and Ni in austenite with an activation energy of 251.4 kJ.mol<sup>-1</sup>.

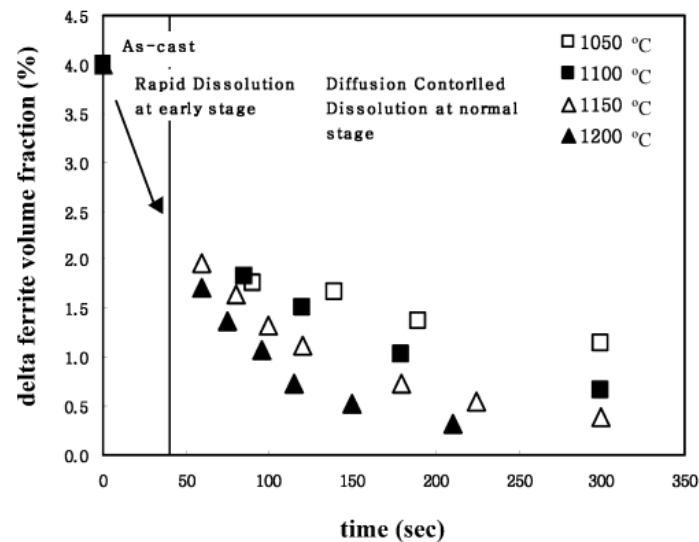


Figure I. 8: Variation in  $\delta$ -ferrite's fraction with dissolution temperature and time [37].

Simultaneously, with further annealing, ferrite's morphology was seen to evolve from a 3 dimensional honeycomb dendritic morphology to spheroidized particles. This process is widely known to be driven by the excess of surface energy at the  $\delta/\gamma$  interface. The work of Raghunathan *et al.*[38] paid more attention to the change of morphology and reported that the dissolution of a skeletal-type ferrite during post-weld heat treatment of 316 welds between 900 and 1100°C is accompanied by the same morphological evolution (see Figure I. 9). The authors proposed the following equation for the kinetics of ferrite spheroidization [39]:

$$R^n = \alpha Gt \quad (\text{I.2})$$

where R is an appropriate linear dimension, *i.e.* the radius of the rod,  $\alpha$  is a geometric factor and G is a parameter characteristic of the appropriate transport mechanism. The exponent n can take the values 1, 2, 3 and 4 depending on the rate controlling process of spheroidization: plastic flow, interface reaction, volume diffusion and interface diffusion respectively. If the dendrite could be approximated by a rod of cylindrical geometry, the microstructural parameter G can be approximated by the ratio between the average diameter D and the length of ferrite particles L. From the slopes of plots in Figure I. 10.b the spheroidization of ferrite appears to be interface-controlled ( $n=4$ ). Such results are substantiated by the kinetics of the dissolution process which reveals that the activation energy is 132  $\text{kJ}\cdot\text{mol}^{-1}$  versus 251.4  $\text{kJ}\cdot\text{mol}^{-1}$  for volume diffusion of Cr as calculated by Kim *et al.*[37].

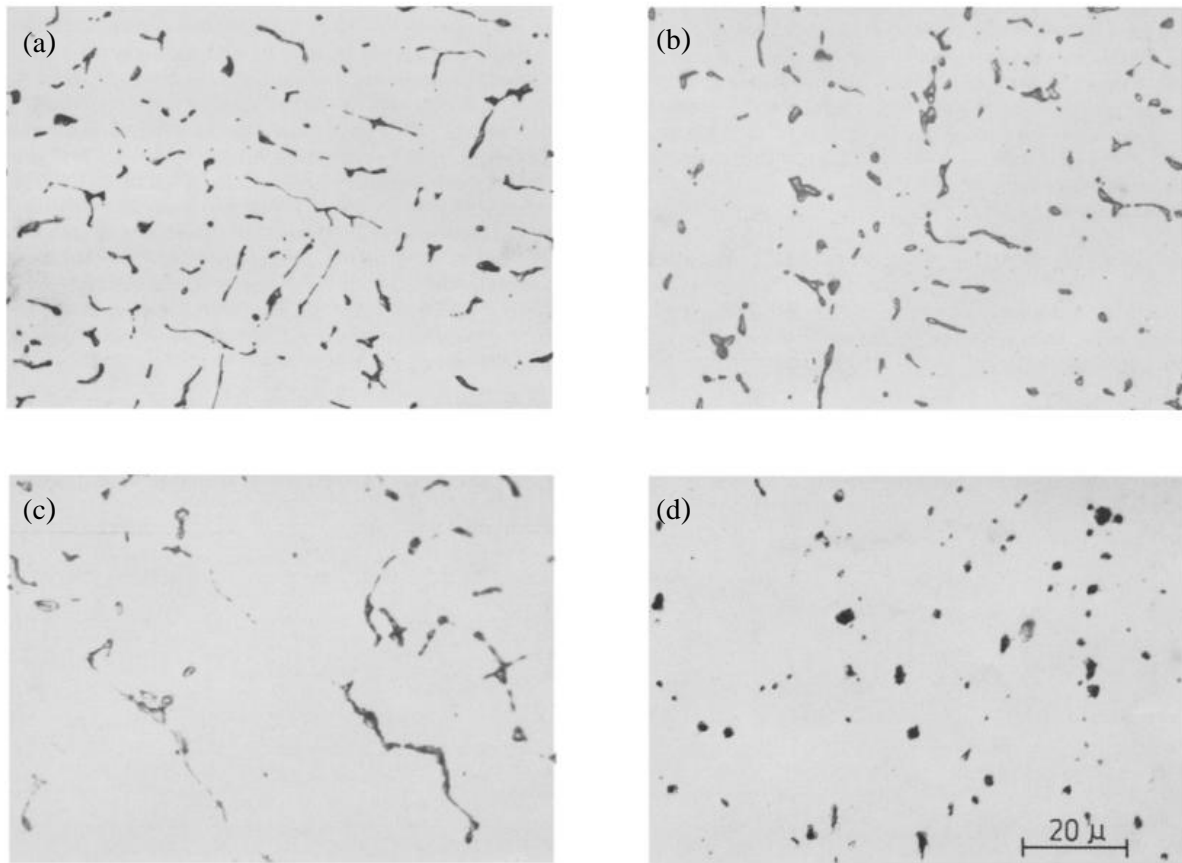


Figure I. 9: Sequence of optical micrographs of a 316 stainless steel weld obtained after heat treatment at 950°C: (a) 1hr, (b) 5hrs, (c) 10hrs and (d) 40hrs. The micrographs shows the progressive breakup of the ferrite networks and their subsequent spheroidization driven by solute diffusion at the  $\delta/\gamma$  interfaces [38].

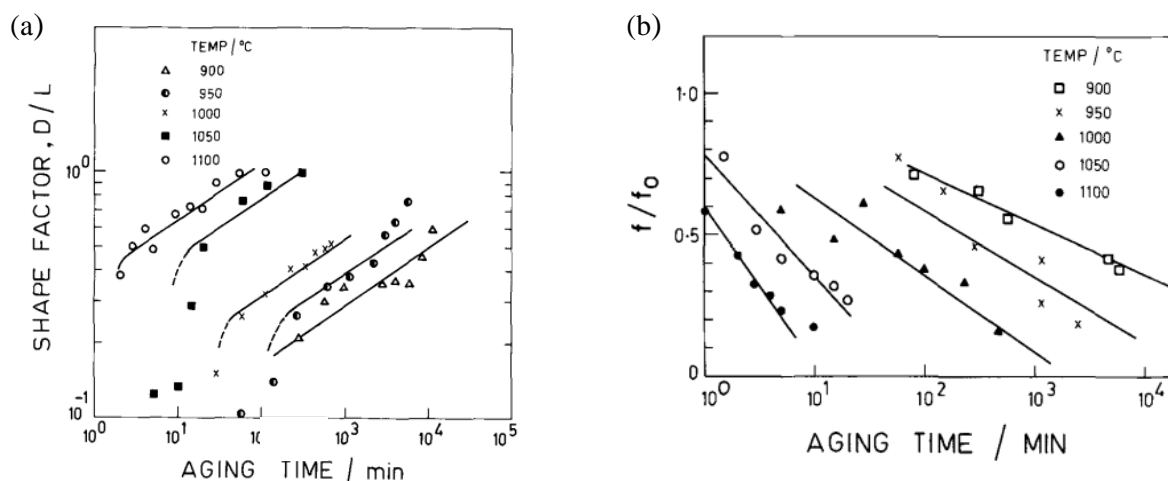


Figure I. 10: Evolution with aging time of (a) the shape factor  $D/L$  and (b) the fraction of ferrite in a 316 stainless steel welds [38].

The change in the kinetics of the dissolution process, from a volume activated one at 1050°C-1200°C [37] to an boundary-diffusion controlled one between 900-1100°C[38] can be explained by the fact that volume diffusion is only activated above 1050-1100°C.

## IV.2. Modeling of the $\alpha \rightarrow \gamma$ diffusion-controlled phase transformations

Diffusion controlled phase transformations in metallic alloys have been first treated analytically in binary and ternary alloys only under strong restrictions such those concerning the geometry, the extent of the phases and the nature of coupling between solutes [39][40]. Moreover analytical solutions are only valid for isothermal annealings. Nowadays, with the advent of improved computer resources, numerical treatment of such transformations in industrial alloys becomes compulsory with regard to the complexity of the involved microstructures, the increasing number of chemical elements, the geometry of the phases as well as increasingly sophisticated heat treatments.

In this section an overview of the mathematical formalism describing Fickian diffusion in metallic alloys will first be presented followed by a brief review of the available tools providing thermodynamic and kinetic descriptions. The  $\alpha \rightarrow \gamma$  transformation in Fe-Cr-Ni systems is generally treated with the moving boundary model. A brief presentation will be given afterwards.

### IV.2.a. Diffusion theory in multicomponent alloys

Diffusion in multicomponent alloys is generally treated on the basis of Fick's law, *i.e.* the movement of atoms in a concentration gradient. In the case of one phase binary alloy under isothermal and isobaric conditions, Fick's first law describing the diffusion of a specie k in one direction z is expressed by:

$$J_k = -D_{kk} \frac{\partial c_k}{\partial z} \quad (\text{I.3})$$

where  $J_k$  is the interdiffusional flux,  $D_{kk}$  is the interdiffusion coefficient of specie k and  $c_k$  is its concentration. It is to be noticed that in the case where k is an interstitial specie,  $J_k$  is related to solute gradient by the intrinsic diffusivity  $D_k$ .

In multicomponent systems the situation is more complex as chemical interactions between solutes can occur. The solute flux  $J_k$  of any specie k does not solely depend on its concentration gradient but also on the concentration gradients of the other species.

The real driving force for diffusion of any specie k is the gradient of its chemical potential  $\mu_k = \mu(c_1, c_2, \dots, c_n)$ , as demonstrated by Darken [42] in his uphill diffusion experiments where solutes can diffuse against their concentration gradients. For a multicomponent alloy and for a small deviation from equilibrium, the solute flux can then be expressed using Onsager's equation [42] [43]:

$$J_k = - \sum_{j=1}^n L'_{kj} \frac{\partial \mu_j}{\partial z} \quad (\text{I.4})$$

Where  $L'_{kj}$  is a proportionality factor that depends on the mobility M of individual species. Using the chain rule of derivation, fluxes can be viewed as

$$J_k = - \sum_{j=1}^n L'_{kj} \sum_{i=1}^n \frac{\partial \mu_j}{\partial c_i} \frac{\partial c_i}{\partial z} = - \sum_{i=1}^n D_{ki} \frac{\partial c_i}{\partial z} \quad (\text{I.5})$$

Here diffusivities are introduced as:

$$D_{ki} = \sum_{j=1}^n L'_{kj} \frac{\partial \mu_j}{\partial c_i} \quad (\text{I.6})$$

For more details the reader is encouraged to consult references [45] [46]. Combining Eq.(I.5) with the continuity equation which expresses solute conservation:

$$\frac{\partial c_k}{\partial t} + \frac{\partial J_k}{\partial z} = 0 \quad (\text{I.7})$$

we obtain the fundamental differential equation of diffusion, or the Fick's second law for multicomponent systems:

$$\frac{\partial c_k}{\partial t} = \sum_{i=1}^n \frac{\partial}{\partial z} (D_{ki}^{\varphi} \frac{\partial c_i^{\varphi}}{\partial z}) \quad (\text{I.8})$$

Finally diffusion in multicomponent alloys can be modeled by a system of coupled partial differential equations:

$$\begin{cases} J_k = - \sum_{i=1}^n D_{ki} \frac{\partial c_i}{\partial z} \\ \frac{\partial c_k^{\varphi}}{\partial t} = \sum_{i=1}^n \frac{\partial}{\partial z} (D_{ki}^{\varphi} \frac{\partial c_i^{\varphi}}{\partial z}) \end{cases} \quad (\text{I.9})$$

#### IV.2.b. Thermodynamic and kinetic databases

In order to compute diffusion processes, appropriate thermodynamic and kinetic descriptions are required. The accuracy of the calculations will depend on the quality of these data. One of the most powerful methods to produce thermodynamic data is the CALPHAD (Calculation of Phase Diagrams) method [46][47]. This approach is based on the modeling of the Gibbs energy of individual phases as a function of temperature, pressure and composition. These information being known, equilibria are determined by minimizing the total Gibbs energy of the system. This method stems its powerfulness from the fact that thermodynamic calculations for multicomponent systems can be extrapolated from data assessed on binary, ternary and quaternary sub-systems using appropriate interpolation polynomials.

Kinetic data are derived using the same approach. Since in n-component systems diffusion coefficients are numerous, interrelated and functions of compositions, kinetic data are rather expressed in terms of atomic mobilities M. Such a perspective permits to substantially reduce the number of stored data from  $(n - 1)^2$  interdiffusion coefficients to  $n$  mobilities and to lift their interdependency. Interdiffusion coefficients are hence constructed from mobilities through equations involving thermodynamic parameters.

#### IV.2.c. Moving boundary models

In case of ferrite to austenite phase transformation, moving boundary models are used. In such models two adjacent matrix phases  $\alpha$  and  $\gamma$  are separated by a sharp moving interface

that should move as a consequence of solute diffusion across it. In order to conserve solutes in the system, the movement of the interface should obey the following mass balance equation:

$$v_k [c_k^{\alpha/\gamma} - c_k^{\gamma/\alpha}] = J_k^\alpha - J_k^\gamma, \quad \text{for specie } k = 1, 2, \dots, n-1 \quad (\text{I.10})$$

where  $c_k^{\alpha/\gamma}$  and  $c_k^{\gamma/\alpha}$  are the molar fractions of the component  $k$  in  $\alpha$  and  $\gamma$  at the interface,  $v_k$  is the interface migration rate relative to component  $k$  and  $J_k^\alpha$  and  $J_k^\gamma$  are the diffusional fluxes on each side of the interface : their expression is derived from Eq.(I.3). The molar fractions on both sides of the interface  $c_k^{\alpha/\gamma}$  and  $c_k^{\gamma/\alpha}$  are fixed by thermodynamical constraints. If the interfacial reaction is fast compared to the diffusion rates then local equilibrium is assumed to hold at the interface (Figure I. 11). The rate of the transformation is thus controlled only by diffusion of species to and from the interface. Local equilibrium implies that the chemical potential of various species is continuous at the interface and that interface concentrations  $c_k^{\alpha/\gamma}$  and  $c_k^{\gamma/\alpha}$  are to be read from phase diagrams. At a given temperature, interface concentrations  $c_k^{\alpha/\gamma}$  and  $c_k^{\gamma/\alpha}$  are uniquely determined in binary systems and they do not change with time. In higher order systems, the situation is more complex. Since there are additional degrees of freedom, there is an infinity of possible couples of equilibrium concentrations  $c_k^{\alpha/\gamma}$  and  $c_k^{\gamma/\alpha}$  that verify the local equilibrium. Therefore there is a need for an additional criterion to fix the operating tie-line at the interface: the interface velocities obtained from the mass balance equations of all diffusion species should be equal. This condition must be verified at each time, so that the operating tie-line is continuously moving until the system reaches its final equilibrium.

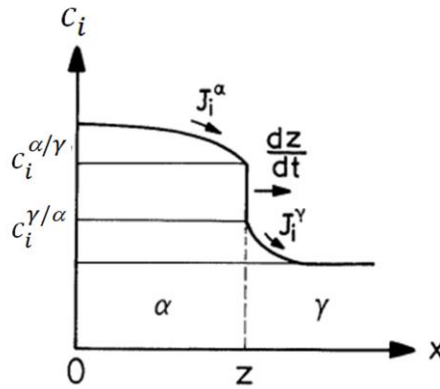


Figure I. 11: Schematic concentration profile across the moving  $\alpha/\gamma$  interface [49].

Once the interface concentrations and position are determined, diffusion in each phase region can be solved separately using Fick's second law. In multicomponent systems this generates a set of non-linear equations that has to be solved by iterative procedure:

$$\begin{cases} v_k [c_k^{\alpha/\gamma} - c_k^{\gamma/\alpha}] = J_k^\alpha - J_k^\gamma & k = 1, \dots, n \\ \frac{\partial c_k^\varphi}{\partial t} = \sum_{i=1}^n \frac{\partial}{\partial z} (D_{ki}^\varphi \frac{\partial c_i^\varphi}{\partial z}) & \varphi = \alpha, \gamma \end{cases} \quad (\text{I.11})$$

### IV.3. Modeling the $\alpha \rightarrow \gamma$ transformation in the Fe-Cr-Ni system

#### IV.3.a. Analytical approach (Kajihara *et al.* [36])

Kajihara discussed the transient growth of ferrite (Figure I. 7) with approximate solutions of the diffusion equations for the semi-infinite  $\gamma/\alpha/\gamma$  diffusion couple in the Fe-Cr-Ni system. The motion of the interface is governed by the mass balance equation (Eq.I.10). Since cross-diffusion coefficients  $D_{kj}^\varphi$  are less than 1/6 of main ones  $D_{kk}^\varphi$ , solute fluxes are expressed only with  $D_{kk}^\varphi$ . Assuming that both phases have the same molar volume, Eq. (I.10) becomes

$$(c_k^{\alpha/\gamma} - c_k^{\gamma/\alpha}) \frac{dz}{dt} = D_{kk}^\gamma \left. \frac{\partial c}{\partial x} \right|^\gamma - D_{kk}^\alpha \left. \frac{\partial c}{\partial x} \right|^\alpha \quad (\text{I.12})$$

where  $c_k^\varphi$  is the molar fraction of solute  $k = Cr, Ni$  in phase  $\varphi = \alpha, \gamma$ . At the beginning of the transformation solute fields do not overlap (Figure I. 12.a). Hence each phase can be regarded as semi-infinite. In this situation solute gradients at the interface can be expressed with the following linear approximations:

$$\frac{\partial c^\gamma}{\partial x} = \frac{\Delta c_k^\gamma}{\Delta x_k^\gamma} = \frac{c_{k,0}^\gamma - c_k^{\gamma/\alpha}}{\Delta x_k^\gamma} \quad (\text{I.13.a})$$

$$\frac{\partial c^\alpha}{\partial x} = \frac{\Delta c_k^\alpha}{\Delta x_k^\alpha} = \frac{c_k^{\alpha/\gamma} - c_{k,0}^\alpha}{\Delta x_k^\alpha} \quad (\text{I.13.b})$$

where  $c_{k,0}^\alpha$  and  $c_{k,0}^\gamma$  are the initial solute molar fractions in the core of ferrite and austenite respectively and  $\Delta x_k^\varphi$  is the diffusion length inside each phase. Assuming that the interface motion is small compared with the volume diffusion,  $\Delta x_k^\varphi$  may be correlated to the annealing time by:

$$\Delta x_k^\varphi \approx 2 \sqrt{D_{kk}^\varphi t} \quad (\text{I.14})$$

Inserting Eqs.(I.13) and Eq.(I.14) into Eq.(I.12), the interface mass balance equation can be rewritten as:

$$(c_k^{\alpha/\gamma} - c_k^{\gamma/\alpha}) \frac{dz}{dt} = D_{kk}^\gamma \frac{c_k^{\gamma/\alpha} - c_{k,0}^\gamma}{2 \sqrt{D_{kk}^\gamma t}} - D_{kk}^\alpha \frac{c_k^{\alpha/\gamma} - c_{k,0}^\alpha}{2 \sqrt{D_{kk}^\alpha t}} \quad (\text{I.15})$$

This equation correlates the movement of the interface with initial compositions in each phase. It can be simplified as follows:

$$(c_k^{\alpha/\gamma} - c_k^{\gamma/\alpha}) \frac{dz}{dt} = \frac{2 \sqrt{D_{kk}^\alpha}}{2 \sqrt{t}} \left[ -\Delta c_k^\delta + \sqrt{\frac{D_{kk}^\gamma}{D_{kk}^\alpha}} \Delta c_k^\gamma \right] \quad (\text{I.16})$$

In the case of Cr,  $c_{Cr}^{\alpha/\gamma} - c_{Cr}^{\gamma/\alpha}$  is always positive. Thus the sign of the interface velocity is the same as  $-\Delta c_{Cr}^\alpha + \sqrt{\frac{D_{CrCr}^\gamma}{D_{CrCr}^\alpha}} \Delta c_{Cr}^\gamma$ . The initial growth of ferrite ( $\frac{dz}{dt} > 0$ ) is obtained if the relation

$$\frac{\Delta c_{Cr}^\alpha}{\Delta c_{Cr}^\gamma} > \sqrt{\frac{D_{CrCr}^\gamma}{D_{CrCr}^\alpha}} \quad (\text{I.17})$$

is satisfied. At  $1100^{\circ}\text{C}$ , the ratio  $D_{CrCr}^{\gamma}/D_{CrCr}^{\alpha} \approx 1/30$ , the growth of ferrite is observed if  $\Delta c_{Cr}^{\alpha}/\Delta c_{Cr}^{\gamma} > 0.17$ . This condition is satisfied for diffusion couples A, B and D where growth is actually observed (Figure I. 7), but it is not matched in diffusion couple C, which explains the absence of ferrite growth.

The growth of ferrite lasts as long as condition (I.17) is satisfied, *i.e.* if solute gradients in ferrite remain sufficiently high (Figure I. 12.a and b). Given the high solute diffusivities in this phase, solute profiles flatten rapidly (Figure I. 12.c and d) and leads to the inversion of the interface movement and the beginning of ferrite shrink.

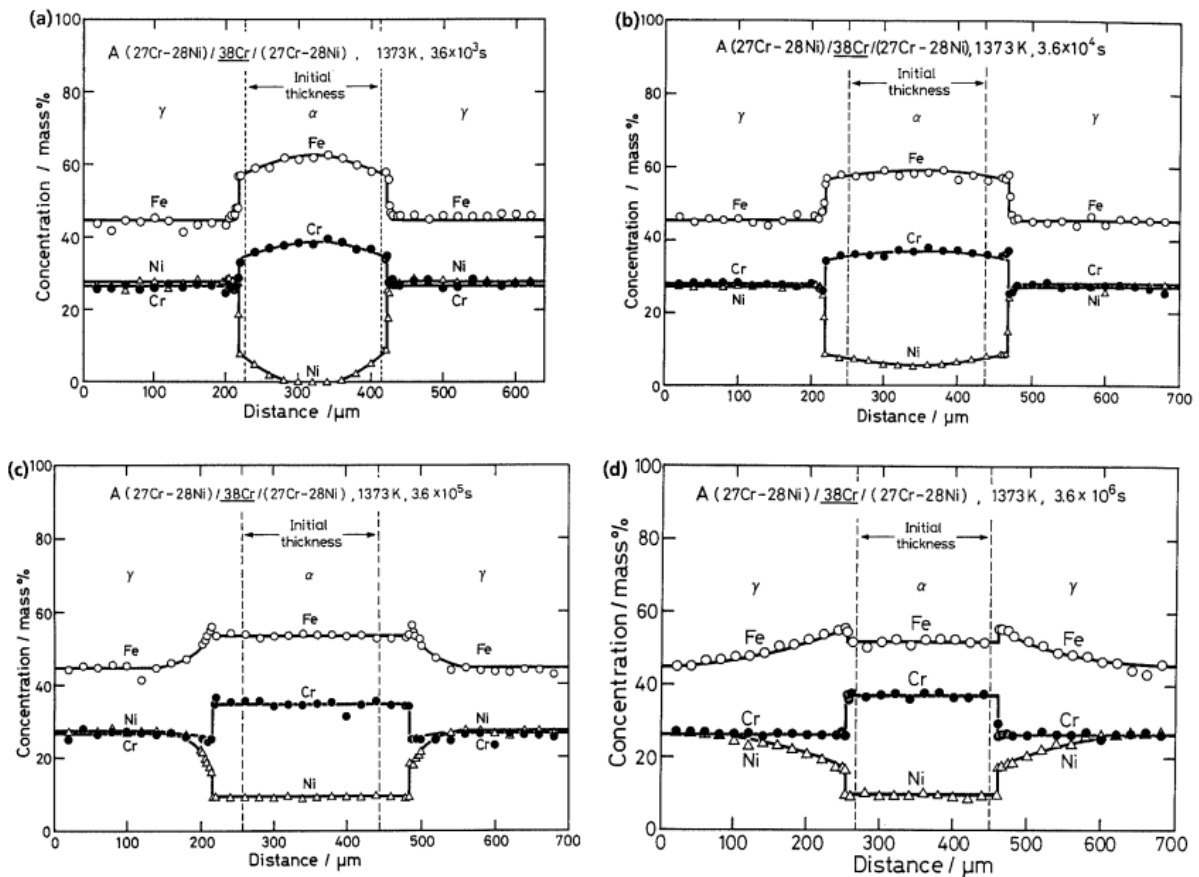


**Figure I. 12:** Composition profiles normal to the  $\alpha/\gamma$  interface in diffusion couple A annealed at  $1100^{\circ}\text{C}$  for (a) 1hr, (b) 10hrs, (c) 100hrs and (d) 1000hrs [36]. At the beginning of the transformation (1hr) chromium and nickel gradients are sufficiently high to ensure ferrite growth. At this stage ferrite can be considered as semi-infinite to apply analytical solution of the diffusion equation. After 10hrs, chromium and nickel profiles rapidly overlap in ferrite and begin to flatten, signaling the end of the growth stage. At 100 and 1000hrs, chromium and nickel profiles are already flat in ferrite and the latter is already in dissolution.

The extent of the early growth of ferrite depends on the location of the initial ferrite composition with respect to the  $\alpha/(\alpha+\gamma)$  phase boundary in the phase diagram: if initial compositions are located far from the phase boundary (Figure I. 13.a), solute gradients are important and Cr and Ni fluxes are high according to Fick's first law and thus the extent of ferrite thickening is high (in diffusion couples A and B). On the contrary, when initial

compositions lie close to the phase boundary, solute gradients are much less important so that the thickening of ferrite is small or even not observed (Figure I. 13.b).

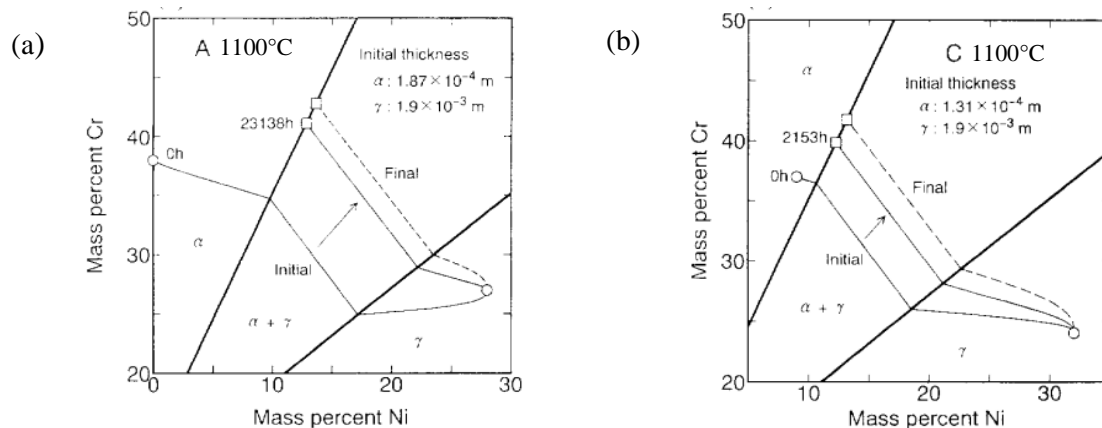


**Figure I. 13:** Location of initial phase compositions with respect to the phase boundaries on the 1100°C isothermal section of the Fe-Cr-Ni phase diagram: (a) diffusion couple A, (b) diffusion couple C. Note that initial ferrite composition in diffusion couple A is remote from ferritic phase boundary which satisfies the condition of ferrite growth. In diffusion couple C, ferrite initial composition is very close to the ferritic phase boundary so that no growth is not observed [49].

#### IV.3.b. Numerical approach

The analytical approach permits to qualitatively describe and predict the kinetics of ferrite dissolution. It is however mandatory to yield quantitative predictions using appropriate numerical tools.

For the  $\alpha \rightarrow \gamma$  phase transformation numerical calculations are carried using moving interface models. They have first been numerically implemented in the pioneering works of Heckel *et al.* [50], and Tanzilli *et al.* [51] in binary systems. They were then extended to ternary systems by Randich *et al.* [52] under non isothermal conditions and successfully applied to phosphide growth in ferrite in the ternary Fe-Ni-P system.

In the Fe-Cr-Ni system Kajihara *et al.* [49] were the first to use numerical analysis in order to study the general characteristics of the ferrite dissolution in austenitic stainless steels and discuss their experimental results on diffusion couples presented in Figure I. 7 and Figure I. 12 : they developed a one-dimension model using the finite difference method and a flexible space grid proposed by Murray *et al.* [53] in order to obtain the exact position of the interface. A trapezoidal scheme has been used to solve the finite difference equations [51]. Mathematical formulations are based on the simplifying hypothesis mentioned above: (a) coupled interdiffusion coefficients between Cr and Ni are assumed to be negligible with regard to main ones. (b) diffusion coefficients do not depend on composition, (c) local equilibrium holds at the interface and (d) molar volumes of ferrite and austenite are assumed to be the same. Thermodynamic descriptions are extracted from the work of Hasebe *et al.* [54]. The procedure to obtain equilibrium tie-lines in the 1100°C isothermal section of the Fe-Cr-Ni system is simplified by approximating phase boundaries by straight lines (Figure I. 14 .a). Diffusion coefficients of chromium and nickel were adjusted by fitting the

calculations to the experimental results and compared to those experimentally obtained by Duh. *et al.* [55].

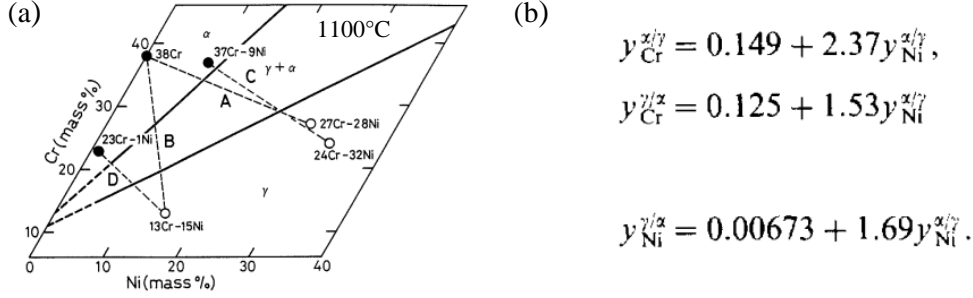


**Figure I. 14: (a) Linearized isothermal section at 1100°C of the Fe-Cr-Ni phase diagram. (b) correspondent interpolation equations extracted from [36].**

In order to avoid numerical instability at the very beginning of the simulation due to the very steep concentration gradients near the interface, analytical solutions of the diffusion equations for semi-infinite two phase ternary system [41] have been used at the early stages of the transformation. According to these equations concentration of each solute,  $k = Cr, Ni$  at a distance  $x$  from the interface is given by

$$c_k^\alpha = c_{k,0}^\alpha + \frac{c_k^{\alpha/\gamma} - c_{k,0}^\alpha}{1 + \operatorname{erf}(K_k^\alpha)} \left[ 1 + \operatorname{erf}\left(\frac{x - z_0}{2\sqrt{D_{kk}^\alpha t}}\right) \right] \quad (\text{I.18})$$

for  $x < z$ , whereas

$$c_k^\gamma = c_{k,0}^\gamma + \frac{c_k^{\gamma/\alpha} - c_{k,0}^\gamma}{1 - \operatorname{erf}(K_k^\gamma)} \left[ 1 - \operatorname{erf}\left(\frac{x - z_0}{2\sqrt{D_{kk}^\gamma t}}\right) \right] \quad (\text{I.19})$$

for  $x > z$ . Here  $z_0$  stands for the initial interface position at  $t = 0$ ,  $z$  is the interface position at  $t > 0$ ,  $c_{k,0}^\alpha$  and  $c_{k,0}^\gamma$  are initial concentration of solute  $k$  at the core of the  $\alpha$  and  $\gamma$  phases respectively,  $c_k^{\alpha/\gamma}$  and  $c_k^{\gamma/\alpha}$  are interface concentration of solute  $k$  at the  $\alpha$  and  $\gamma$  sides respectively. The dimensionless kinetic parameters  $K_k^\varphi$  are related to the interface position  $z = z(t)$  by:

$$z(t) = 2K_k^\varphi \sqrt{D_{kk}^\varphi t}, \quad k = Cr, Ni; \quad \varphi = \alpha, \gamma \quad (\text{I.20})$$

Only one of these four parameters is independent. They are used to calculate the interface concentration using the following equations :

$$c_k^{\gamma/\alpha} - c_k^{\alpha/\gamma} = \frac{(c_{k,0}^\alpha - c_k^{\alpha/\gamma}) \exp(-K_k^{\alpha 2})}{K_k^\alpha \sqrt{\pi} (1 + \operatorname{erf}(K_k^\alpha))} + \frac{(c_{k,0}^\gamma - c_k^{\gamma/\alpha}) \exp(-K_k^{\gamma 2})}{K_k^\gamma \sqrt{\pi} (1 - \operatorname{erf}(K_k^\gamma))} \quad (\text{I.21})$$

The thickness of ferrite in the annealed diffusion couples was numerically calculated as a function of annealing time and the results are plotted in Figure I. 15.a. Experimental data are reported as well. Broken curves correspond to analytical solutions. The experimental results are quantitatively reproduced by the numerical model. In particular by choosing the proper values of the kinetic parameters  $K_k^\varphi$  the analytical model is able to quantitatively predict the

growth of ferrite in the initial stage of the transformation. It should be reminded that the analytical solutions are only valid for semi-infinite media. At the early stage of the transformation this hypothesis holds since diffusion fields in ferrite did not overlap, experimentally. The diffusion path for each diffusion couple are compared with experimental results as well (Figure I. 15.b for diffusion couple A). Satisfactory agreement between calculations and experiment has been reached at each annealing time. Further numerical calculations revealed that interface compositions starts to change when the diffusion fields of the fastest element in either the matrix or the second phase start to overlap. It has also been revealed that even in case where the interface compositions are the same at the initial and final stages, the interface compositions can change in the course of the transformation.

The success of this model in understanding the general characteristics of the ferrite to austenite transformation in the Fe-Cr-Ni ternary system permitted to validate the hypothesis under which the numerical model has been build, namely: (a) the transformation is diffusion-controlled, (b) diffusion coefficients are independent of the composition, (c) coupled diffusion between Cr and Ni is negligible, and (d) the molar volumes of ferrite and austenite are the same. These hypotheses will therefore be used in the numerical model to be build in the framework of this thesis.

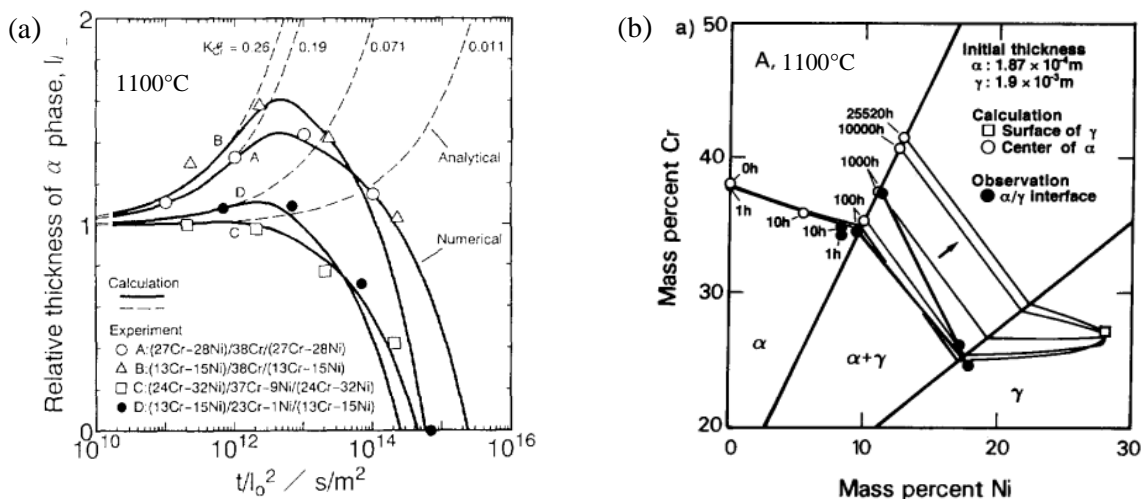


**Figure I. 15:** (a) Thickness of ferrite as function of the annealing time: numerical calculation (bold lines) are compared to experimental results (symbols). Analytical solutions are represented by dashed lines. (b) Experimental and computed diffusion path in diffusion couple A [56].

It should be noted that numerical calculations are highly dependent on the kinetic and thermodynamical properties injected into the model. Andersson *et al.* [57] carried the same calculations using the DICTRA® software [58] and the thermodynamic description by Hillert *et al.* [59] and kinetic parameters derived from diffusion coefficients reported by Friedberg *et al.* [60]. Their numerical results have been less accurate than those obtained by Kajihara [49]. In fact general dissolution trends have been well predicted though absolute values are slightly different in Figure I. 16.a. Growth of ferrite is too low while dissolution is too fast. Some example of calculated and experimental composition profiles in diffusion couple B after 100hrs annealing is shown in Figure I. 16.b. Calculated compositions in ferrite

show a slight discrepancy with respect to the experiment, which is attributed to the thermodynamic description used.

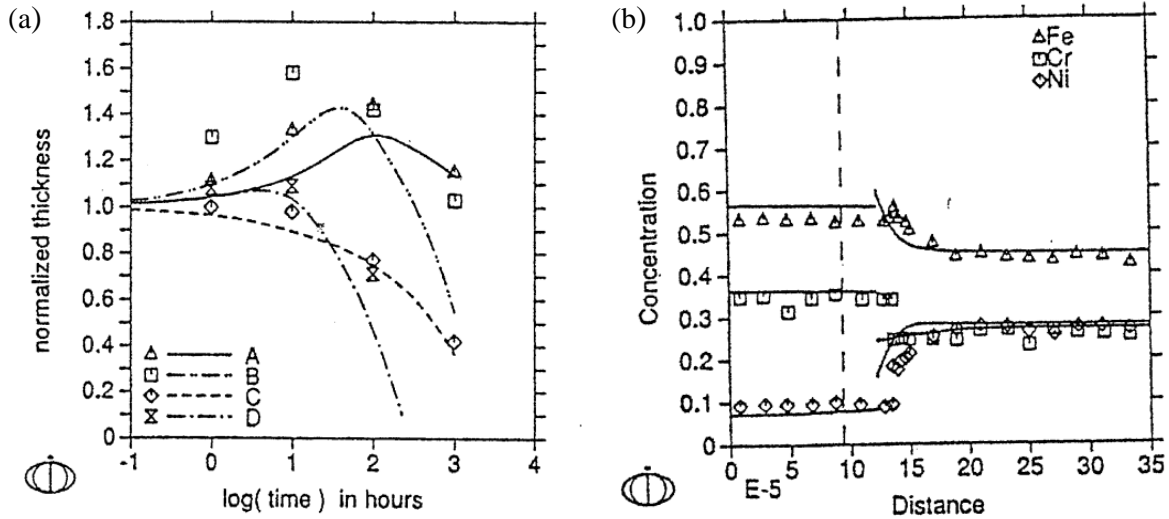


**Figure I. 16:** (a) Comparison between experimental and calculated time-evolution of ferrite thickness at 1100°C. (b) Experimental and calculated concentration profiles for diffusion couple B after 100hrs annealing with ferrite phase on the left side. Experimental data are extracted from the work of Kajihara *et al.* [36] and calculations are performed using the DICTRA package [57], the thermodynamic description of Hillert *et al.* [59] and diffusion coefficients of Friedberg *et al.* [60].

The approach initiated by Tanzilli *et al.* [51] and successfully applied by Kajihara [49] on ferrite dissolution in Fe-Cr-Ni system was also adopted by Vitek *et al.*[61] in order to model the ferrite to austenite transformation behavior at temperatures ranging from 700°C to 1300°C in stainless steel welds during multipass weldings or high temperature service. Model assumptions and numerical schemes are those used previously. Some calculation results will be shown in chapter IV as a comparison basis with the phase transformation model that will be developed in this PhD work. But in this chapter we will only focus on the numerical issues encountered in Vitek's modeling.

First a full detail of the interpolation procedure of the ferrite and austenite phase boundaries of isothermal sections of the Fe-Cr-Ni phase diagram has been presented. It includes second order interpolation instead of linear one used by Kajihara *et al.*[36] in order to reach better accuracy and wider range of interface compositions. The use of the TCFE thermodynamic database used in the ThermoCalc® software permitted to generate several isothermal sections, so that it was possible to constitute a non isothermal interpolation of the phase diagram from 700°C to 1300°C. Second, since calculations are performed over a ternary system, the research loop of interface concentrations and velocity at each time step by solving the mass balance equation was explained, in particular a second order approximation of interface fluxes has been used in order to improve accuracy. Faster research algorithm using the Newton-Raphson algorithm was proposed by Liu *et al.*[62]. The major issue addressed in this study concerns the accuracy and the conservation of mass during calculation.

Two main sources of mass loss have been addressed: the first is due to the use of inappropriate approximation of the concentration gradient near the interface during the first

time steps when solute gradients are very sharp. This leads to a non monotonic composition profile that can be avoided either by using analytical calculations or using correct approximation scheme. This relative error could be reduced to less than 0.01% relative if a proper number of grid points is chosen. The second, which is the largest source of mass loss, is that the set of nonlinear equations describing the problem is not solved iteratively. This implies that, in setting up the mass balance at the interface, values of bulk compositions from previous time step and interface compositions at present time step are used to define solute fluxes. Such a routine can lead to a loss of accuracy especially that may reach 5% relative when values of compositions vary significantly from one step to another and when large time steps are employed. In a later paper the authors proposed an iterative scheme to solve the non-linear system of equations [63]: according to them, this new routine considerably reduced the inaccuracy so that mass conservation was "nearly perfect".

Nevertheless it should be emphasized that the case considered by Vitek *et al.* [63] is not severe in that initial ferrite and austenite compositions lie close to the ferritic and austenitic phase boundaries. In such case, the authors have shown that the numerical solution is in excellent agreement with analytical one. In more severe cases, where supersaturation is important, *i.e.* phase compositions lie far from phases boundaries, a deviation from the analytical solution was observed as it had been demonstrated by Crusius *et al.*[64]. According to the authors this discrepancy introduced cumulative errors on global mass balance that tends to increase with increasing discrepancy (for low supersaturation values the relative mass error is lower than 1% and at a supersaturation of 0.95 it is 30%). It was revealed that those errors come from the Murray Landis approximation where the moving grid leads to a poor-accuracy interpolation of the concentration values at grid nodes after displacement. The authors suggested a new method based on the Murray-Landis grid transformation and including a modification of the flux at the phase interface as well as the correction of the concentration on the moving grid points under the constraint of mass conservation using Lagrange multipliers. Their method, though successful in the case they studied, is time and effort consuming. Lee *et al* [65]–[67] suggested a new method based on fixed grid points and newly derived approximation of the interface mass balance equation using trapezoidal integration technique. Their simulation was applied to several diffusion-controlled transformations in binary and multicomponent systems and showed excellent performances in terms of mass conservation and prediction capabilities.

## V. Summary and conclusion

Austenitic stainless steels in the as-cast state contain a variety of complex austenite-ferrite microstructures. These microstructures are the result of phase transformations at the solidification stage and the subsequent solid-state. Their distribution in the continuously-cast slabs are intimately linked to the cooling conditions. Ternary Fe-Cr-Ni phase diagrams generally furnish a basis to discuss the solidification sequence of austenitic stainless steels. However, they can lead to confusion when it comes to study non equilibrium transformations such those encountered during casting. So far, though the scientific literature is rich in studies of the solidification of Fe-Cr-Ni alloys, the formation mechanism of residual ferrite is not clearly understood, especially in the three phase region of the phase diagram.

Few studies have paid attention to the ferrite to austenite solid-state transformation. A review of the existent literature has been presented in this chapter. The investigations are generally conducted on materials and under experimental conditions that are far from those encountered for continuously-cast austenitic stainless steels. Nevertheless they permitted to bring to light the general characteristics of the  $\alpha \rightarrow \gamma$  transformation: the transient growth of ferrite and its correlation to the evolution of solute profiles, the spheroidization of ferrite particles during their dissolution, etc.

It should be noted, however, that a detailed characterization of ferrite dissolution in continuously-cast austenitic stainless steels still lacks in literature. The first experimental axis of this PhD work will provide responses to fill the gap (Chapters III and V).

Existent numerical models have proved capable in predicting the dissolution kinetics of ferrite in simple cases, such as the diffusion couples experiments. Their efficiency depends heavily on the thermodynamic and kinetics data injected in the model and on the numerical techniques employed in modeling. A description of the numerical model was supplied in this chapter and a brief review of the encountered numerical issues has been addressed. These elements will be used in Chapter IV for the development of a numerical model to be used for the analysis of the future experimental results of ferrite dissolution.

So far, numerical models have only been applied to 1D diffusion problems (diffusion couples). In continuously-cast austenitic stainless steels, the morphology of the  $\delta/\gamma$  is far more complex (3D). No description of such a microstructure that is compatible with the 1D model has been suggested in literature. It is thus necessary in this PhD work to focus the modeling effort on this issue and to suggest a methodology of describing the complex microstructure of residual ferrite with a 1D numerical model.



# Chapter II

## Experimental techniques

The goal of this chapter is to present the experimental techniques and procedures used for the characterization of the microstructures in the as-received state and during the dissolution of ferrite.

### I. Metallographic preparations

For optical observations, surfaces were prepared using grinding with SiC papers of P-600, P-800 and P-1200 for 2min each and then with diamond polishing of 6 $\mu$ m for 5min, 3 $\mu$ m for 3min and 1 $\mu$ m for 2min.

Several etchings were used to reveal the microstructure of the studied microstructures. Lichtenegger and Bloesch chemical solution (100mL H<sub>2</sub>O, 20g NH<sub>4</sub>HF<sub>2</sub>, 0.5g K<sub>2</sub>S<sub>2</sub>O<sub>5</sub>, 30s at 30°C) was used for its ability to color the austenitic phase with respect to the level of microsegregation of Ni: in cast microstructures, "primary" austenite (grown from the liquid) can be distinguished from the "secondary" austenite formed at the solid-state by coloring: yellow for the first one and brown for the second one (Figure II. 1.a).

In order to measure ferrite fraction by image analysis, the optimal procedure is to electrolytically etch the samples using 40% aqueous NaOH, with a current density of 0.15mA/cm<sup>2</sup> during 30s at room temperature. This etching colors only ferrite, which provides high contrast with austenite, rendering image gray levels thresholding easier [68] (Figure II. 1.b).

Electrolytic etching in nitric acid (40mL. H<sub>2</sub>O, 60mL. HNO<sub>3</sub>, 2V, 200mA/cm<sup>2</sup>) was used to reveal grains inside austenite and ferrite bands in the multilayered microstructure. This etching also reveals the martensite that forms at the  $\delta/\gamma$  interface as can be shown in Figure II. 1.c. In the ternary alloy, the Beraha etching is preferred for the revealing of martensite (Figure II. 1.d).

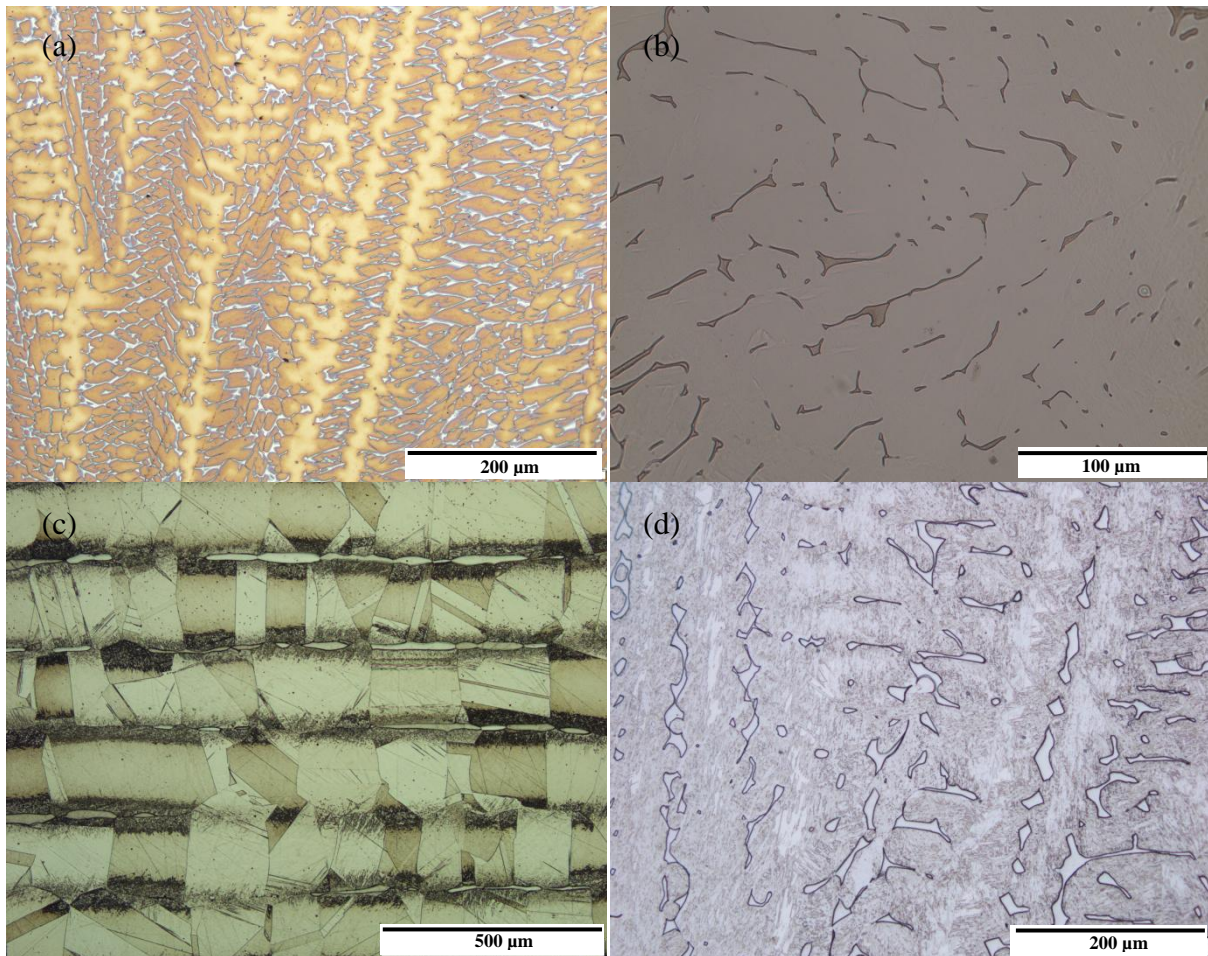


**Figure II. 1:** Micrographs showing a typical outcome of the etchings used in revealing the microstructures and quantifying the amount of ferrite: (a) Ternary Fe-17.3%Cr-9.4%Ni alloy etched with Lichtenegger and Bloesch showing primary (yellow) and secondary (brown) austenites in addition to ferrite (white). (b) Microstructure of the same alloy revealed by NaOH etching and showing the net contrast between ferrite and austenite. This etching is the most appropriate for ferrite quantification. (c) Electrolytic etching in nitric acid of the multilayered microstructures showing grains of ferrite and austenite bands as well as martensite (black) at the  $\alpha/\gamma$  interfaces. (d) Beraha etching of the microstructure of the Fe-17.3%Cr-9.4%Ni alloy showing the transformation of secondary austenite to strain-induced martensite after cutting and polishing. Note that primary austenite (white areas) remains stable due to its higher Ni content.

## II. Quantitative image analysis

In literature, several techniques are commonly used for the quantification of the amount of ferrite in austenitic stainless steels. The magnetic methods (Fischer Ferritescope<sup>®</sup>, Sigma-meter) are the most widely used and have the advantage of being rapid. They are based on the measurement of the amount of ferromagnetic phases, *i.e.* ferrite and martensite.

In the present study, the investigated alloys are not exempt of martensite. In fact, strain-induced martensite has been shown to form from unstable austenite in the as-cast and multilayered microstructures as a consequence of sample cutting and polishing (Figure II. 1.c and d). Therefore, the measurement of ferrite fraction was not possible with the magnetic methods, but was instead carried out by image analysis. Optical images were

acquired with an Olympus BX60M microscope equipped with a CCD camera. Fields were afterwards analyzed with the ImageJ software.

### II.1. Measurement of ferrite fraction in the ternary cast alloy

The quantification of the **amount of ferrite** by image analysis was performed with care, since the fraction of ferrite is very small (few percents). For each analyzed region, the quantification procedure is performed as follows:

- Acquisition of adjacent fields in order to reduce bias that can result from a non-purely random human field selection. Fields are acquired at a magnification of 500 (field size  $270\mu\text{m} \times 210\mu\text{m}$ ), which is the best compromise between image resolution and processing time.
- Sufficient number of fields is acquired to ensure that the cumulative average value of ferrite fraction converges to a robust one. Cumulative average value is calculated using the first  $n$  values of ferrite fraction. It permits to evaluate the effect of the  $n^{\text{th}}$  value of ferrite fraction on the average one calculated with the first  $n - 1$  fields ( Figure II. 2). In practice this procedure implies to acquire about 30 to 40 fields per analyzed region. For simplification, each set of fields is acquired at the same brightness to ensure a collective treatment of fields.

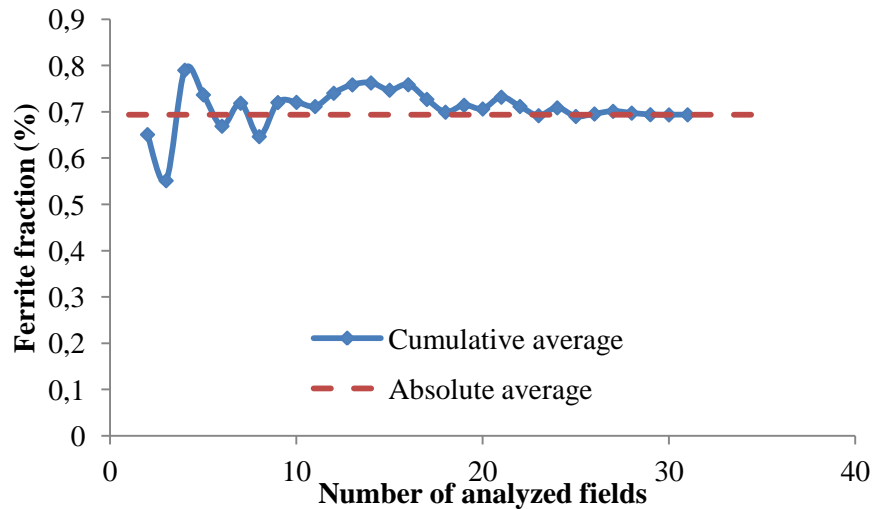


Figure II. 2: Convergence of the cumulative average of ferrite fraction to the robust average value.

- Image segmentation is performed by thresholding stacks of grayscale images. Ferrite fraction is measured by calculating the surface fraction of ferrite particles. Upper and lower thresholds are chosen for each stack and the median one is chosen as a representative of ferrite fraction. The error committed at this operation is of 0.1% absolute. Particle size filter is then applied in order to remove very tiny particles (surface  $< 100\text{pixels}^2$ ) that results from background noise as well as polishing and etching residues. The loss of ferrite fraction corresponding to this operation is very low (0.1% absolute). In addition, statistical uncertainties are calculated at  $2\sigma$  dispersion (95% confidence). All these errors are afterwards summed to calculate global uncertainties.

Given the random distribution of ferrite particles into the ingot, it is assumed that, any metallographic section is representative of the volume fraction of ferrite (surface fraction=volume fraction).

## II.2. Morphological evolution of ferrite particles

The **morphology** of ferrite particles during their dissolution was described using the *circularity* shape descriptor which is defined, for a given particle, as:

$$circularity = \frac{4\pi [Area]}{[Perimeter]^2} \quad (II.1)$$

Circularity ranges from 0 for an infinitely long particle to 1 for a perfect circle. This shape descriptor permits to qualitatively assess the evolution of ferrite's morphology during its dissolution.

## II.3. Morphological separation of vermicular ferrite in the as-cast microstructure

For the modeling of ferrite dissolution, there is a need to describe the morphology of ferrite particles in the as-cast state with simple geometries (planar, cylindrical and spherical). To derive quantitative parameters that match this requirement, ferrite particles are separated into several groups according to their shape, and appropriate quantitative descriptors are derived for each group. For vermicular ferrite (Figure II. 3), two shape-based groups can be distinguished: (i) elongated particles corresponding to primary and secondary dendrite arms and (ii) coarse particles corresponding to the intersection between secondary and primary arms and the tips of secondary arms.

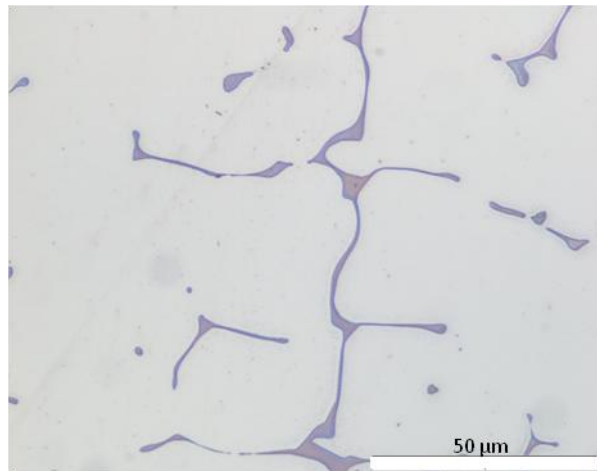


**Figure II. 3:** Typical vermicular morphology of residual ferrite in the as-cast microstructure of the Fe-17.3%Cr-9.4%Ni alloy.

The separation of the elongated particles from the coarse ones is performed with the following procedure (Figure II. 4) applied on a stack of 54 images of the vermicular zone:

**1. Extraction of coarse particles.** In order to obtain the coarse particles (intersection between dendrite arms) from the initial fields of the as-cast microstructure, the elongated thin parts (dendrite arms) were eliminated through the application of 5 successive image openings (Figure II. 4.b) corresponding to 5 erosions followed by 5 dilations of 1pixel each.

**2. Reconstruction of elongated particles** by subtracting the coarse-particle fields from the as-cast ones, as shown in Figure II. 4.c. After the subtraction, very tiny particles (few pixels size, called artifacts) can be seen around the former location of the dendrite arms intersections. These artifacts result from the openings performed in step 1: after openings, coarse particles do not exactly recover their initial spatial extent since some pixels can be removed or added. Therefore the artifacts will be found in the elongated-particle fields as a result of the subsequent subtraction of the coarse-particle fields from the as-cast ones.

**3. Artifacts removal.** In order not to consider the artifacts as independent ferrite particles, they are removed from the elongated particles fields and then transferred to the coarse particles fields and merged with the correspondent coarse particles. The transferring and merging of these artifacts are performed by simple field subtraction and addition.

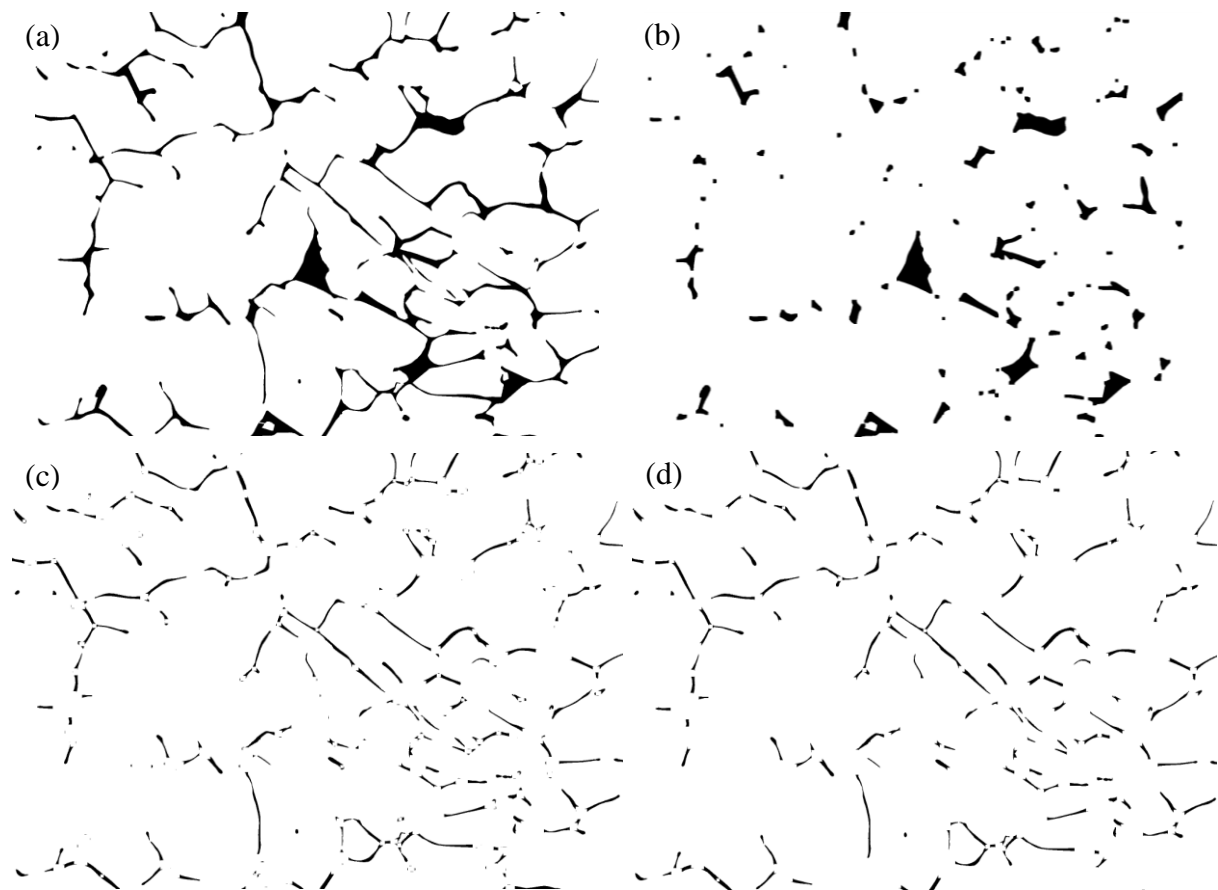


**Figure II. 4:** Sketch of the separation procedure of a vermicular microstructure. (a) Microstructure in the as-cast state after grey levels segmentation. (b) Population of coarse particles after the opening operations. (c) Elongated particles after subtraction of the coarse-particles from the initial images and before removal of artifacts. (d) Elongated particles after artifacts removal.

## II.4. Equivalent size of ferrite particles

After step 3, two particle populations are obtained: coarse and elongated. The chosen quantitative descriptor of the size of a coarse particle is the radius  $R_{eq}$  of the disc possessing the equivalent area. For an elongated particle, the relevant size descriptor is the average half thickness, which can be measured with three different quantifiers:

- half the minor axis of the equivalent ellipse.
- half the thickness of the equivalent rectangle whose length is the F eret diameter.
- half the thickness of the equivalent rectangle whose length is the geodesic diameter.

The equivalent ellipse and rectangle are those whose areas are equivalent to that of the considered particle. The minor axis of the equivalent ellipse yields accurate estimation of the thickness of a particle when the latter has a rather straight shape (Figure II. 5.a). However, for highly curved particles, it overestimates the average thickness (Figure II. 5.b). In such a case, the use of the equivalent rectangles is more appropriate, as it will be shown in the next paragraph. The F eret diameter is the maximum length of the particle (also known as the maximum caliper). The geodesic diameter is the length of the longest path within the particle that connects two points in the particle. This parameter is a good descriptor for branched particles and serves to measure the length of a particle as if it were unfolded.

Figure II. 6 shows the radii distribution of the elongated particles in the as-cast stack of images, measured using the three approaches. F eret-equivalent and geodesic-equivalent rectangles yield the same radii distribution with an average radius of 0.4 and 0.39  $\mu\text{m}$  respectively, while the equivalent ellipse approach overestimates the average radius: 0.56  $\mu\text{m}$ . The reason behind this overestimation stems from the fact that for curved and arched elongated particles, the equivalent ellipse approach overestimates their radius. For this reason, and given that it is much simpler to implement with ImageJ on a stack of images, the F eret equivalent rectangle will be used in the quantification of dendrite arms thickness.

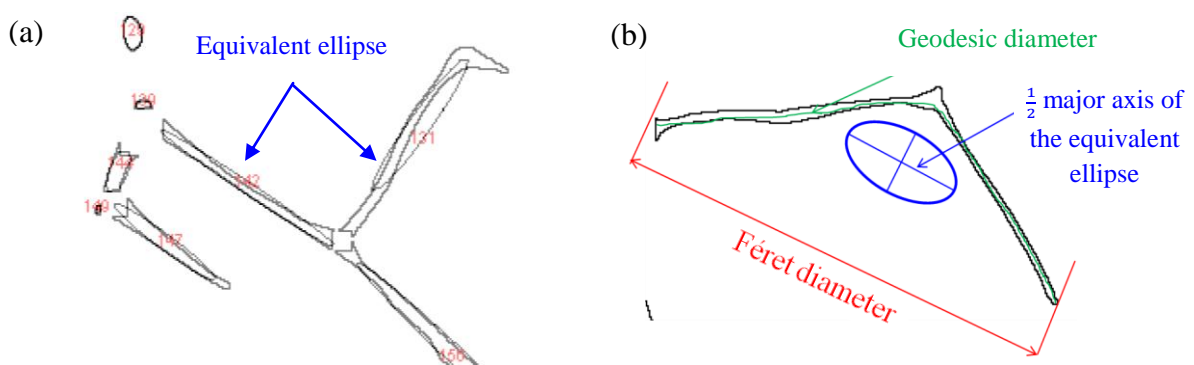


**Figure II. 5 :** (a) The equivalent ellipse of elongated particles of straight form. (b) Schematics of the equivalent ellipse, the geodesic diameter and the F eret diameter of a curved particle. The minor axis of the equivalent ellipse largely overestimate the thickness of the particle.

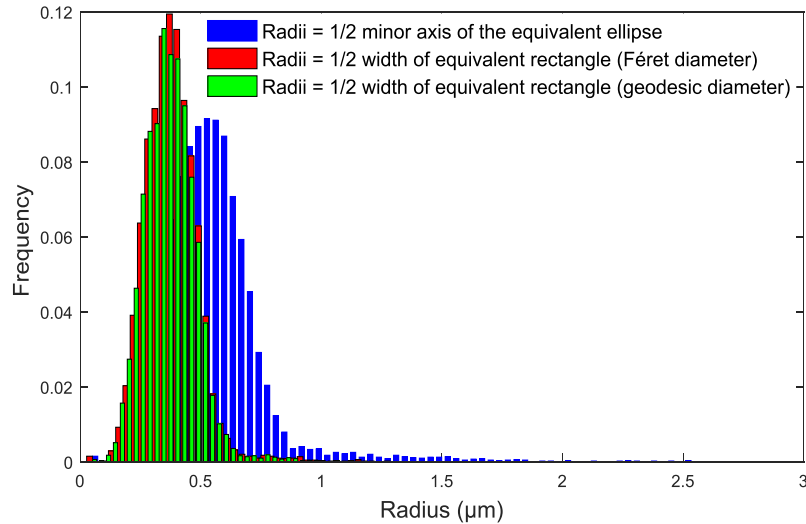


**Figure II. 6:** Distributions of the radii of the elongated particles using half the minor axis of the equivalent ellipse (blue), half the thickness of the equivalent rectangle with F eret diameter as length (red) and, half the thickness of the equivalent rectangle with geodesic diameter as length (green).

### II.5. In the multilayered microstructure

In the multilayered microstructure, given that ferrite represents 20% of the initial total surface area, there is no need to analyze as much images as in the case of the ternary alloy. Analysis was only performed on 10 aligned fields at a 500 magnification. The total investigated length of each ferrite band is thus  $10 \times 250 = 2500\mu\text{m}$ . In order to establish the kinetics of ferrite dissolution, the amount of ferrite was quantified by the equivalent thickness  $\ell$  of ferrite bands. This parameter corresponds to the thickness of a virtual rectangle with the same area as the ferrite band and whose length is that of the image field (Figure II. 7.a). By construction,  $\ell$  is proportional to the surface fraction of ferrite bands ( $\ell = \text{surface fraction} \times \text{width of image}$ ) but is easier to measure. This approach was applied either to continuous or broken ferrite bands as shown in Figure II. 7.c.

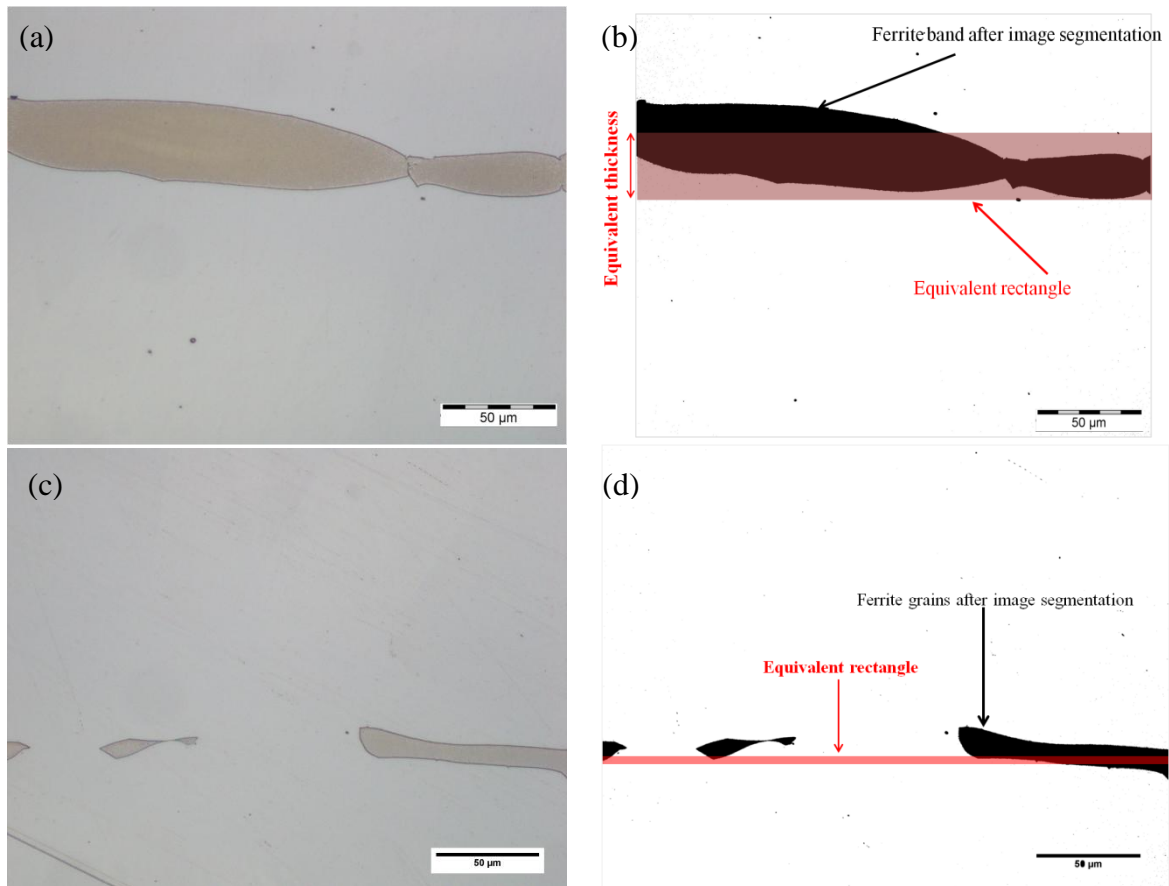


**Figure II. 7: Measurement of the average thickness of a ferrite band in the multilayered microstructure: (a) optical image before segmentation (NaOH etching), (b) segmented image and measurement of the thickness of the equivalent rectangle of the ferrite band. (c, d) The case of broken ferrite bands is treated with the same approach.**

### III. Orientation relationship

Electron back-scattered diffraction (EBSD) analysis was used to study the evolution of orientation relationships between ferrite and austenite during ferrite dissolution. Samples were prepared with classical grinding and polishing techniques followed by a polishing with colloidal silica suspension in order to achieve the necessary surface quality for phase indexation. The EBSD maps were acquired with a ZEISS Supra 55 VP SEM equipped with an OXFORD detector and AZTEC software under acceleration voltage of 20kV, a specimen tilt of 70° and a scan step of 0.15 μm.

### IV. Dissolution heat treatments

Dissolution heat treatments were performed at temperatures ranging from 1140°C to 1350°C using the set up of Figure II. 8 which is constituted of a tubular furnace (1) equipped with a gas control panel (2) allowing the regulation of gas flows and mixtures, an upstream oxygen removal column (5) and a quartz tube (4) in which samples were put under a 100 sccm flow of pure Argon. At the end of dissolution heat treatments, samples were water quenched (6).

The furnace temperature was measured by a type-S thermocouple attached to the furnace and placed in the central zone where the temperature is homogeneous. A DIGITRON T2029 temperature reader is used to control the target temperature of heat treatments. According to the reader manufacturer, the associated reading uncertainty is of 0.3%, to which is added 0.1% extra measurement uncertainty linked to the thermocouple. Hence the total uncertainty is of  $\pm 6^{\circ}\text{C}$ .

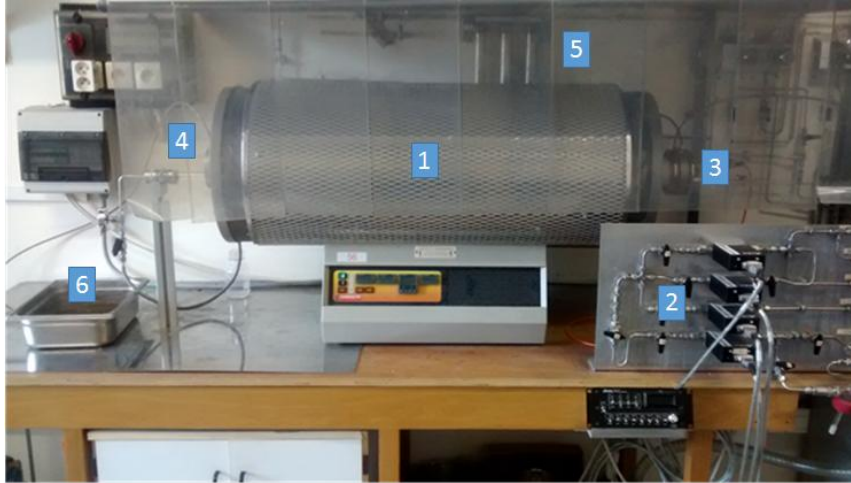


**Figure II. 8:** Experimental set-up for dissolution heat treatments: (1) Tubular furnace, (2) flow regulation device, (3) gas entrance, (4) quartz tube, (5) oxygen removal column and (6) water pool.

In order to evaluate the time needed by the samples to reach the target temperature, preliminary trials have been performed on a test sample having the same dimensions, with a type-S thermocouple welded on its surface and connected to a temperature recorder. Figure II. 9 shows an example of a heating cycle at  $1260^{\circ}\text{C}$ . The heating ramp lasts approximately 90s. Therefore all heat treatments include henceforth, in addition to the isothermal duration, an extra 2 minutes in order to take into account the temperature stabilization in the sample.

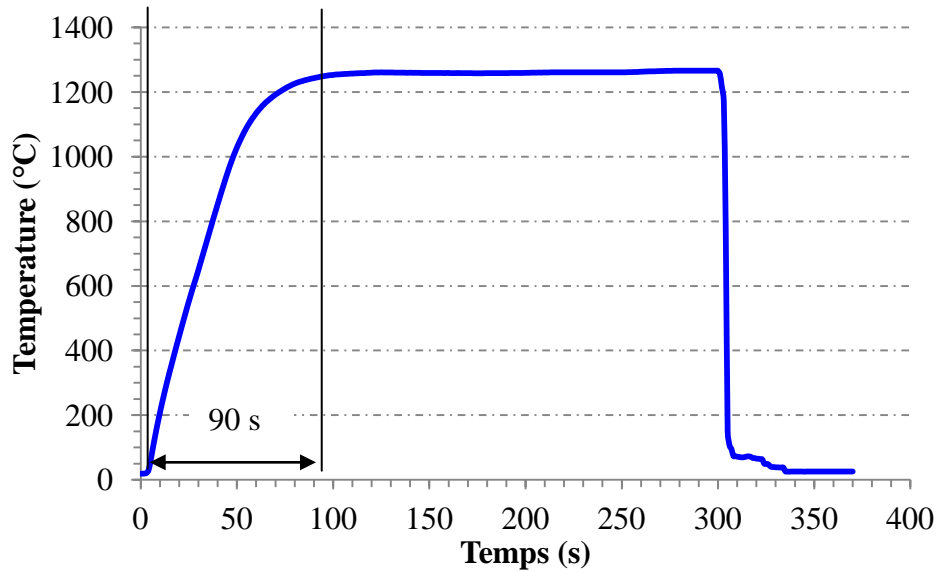


**Figure II. 9:** Example of a measured heating cycle at 1260°C. Temperature reaches its targeted value after approximately 90s.

It is to be noted that the use of a pure argon atmosphere in heat treatments aims at avoiding nitrogen contamination from the ambient air. In fact, with preliminary heat treatments on the ternary alloy performed under air, the amount of nitrogen increased from 44ppm (as-cast state) to 155ppm after 2h at 1200°C.

## V. Chemical analysis and composition measurement

Chemical analysis of cast ingots were performed in APERAM Research Center using X-ray fluorescence (XRF) technique for substitutional elements and combustion and infrared absorption technique (LECO) for C, N, S and O. Each analysis is replicated three times in order to obtain statistically reliable results.

Composition profiles of Cr, Ni and Fe in ferrite and austenite were measured by Electron Probe Micro Analysis (EPMA). This technique is based on the emission of the characteristic X-ray photons of the material under the electron beam. The EPMA measurements were performed in an Electron Probe Micro-Analyzer CAMECA SX50 equipped with the SamX software, with an accelerating voltage of 20kV, a probe intensity of 200nA and a spatial step of 2 $\mu$ m. The use of standard samples provides quantitative measurements with a maximum an error of 0.3% absolute.

In order to measure the composition of Cr and Ni at the  $\delta/\gamma$  interface with enhanced spatial resolution, Energy Dispersive X-ray spectroscopy analysis (EDX) was performed with a JEM-2100 Field Emission Transmission Electron Microscopy (TEM) equipped with a JEOL Centurio detector (1 sr. solid angle) and a spatial step of 30nm. Without the use of standards, this semi-quantitative technique leads to measurement errors estimated at 1% absolute.

Thin foils for Transmission electron Microscopy observations were prepared from 3-mm disc specimens with a thickness of 80-100 $\mu$ m and then electropolished at 5°C and under 25V in 700 mL ethanol, 200mL C<sub>2</sub>H<sub>14</sub>O<sub>4</sub> and 100mL perchloric acid.



# Chapter III

## Experimental study of $\delta$ -ferrite dissolution in ternary Fe-Cr-Ni alloys : as-cast and multilayered microstructures

In this chapter, ferrite dissolution is experimentally studied in the as-cast and the multilayered microstructures of the Fe-Cr-Ni system. The chapter is divided in two parts: in the first part, the Fe-17.3%Cr-9.4%Ni alloy is characterized in the as-cast state and then the dissolution of residual ferrite is studied at several temperatures.

In the second part, the elaboration of multilayered microstructure is first presented. Resulting microstructures are then fully characterized in the as-received state. Finally the dissolution of ferrite bands is studied experimentally.

### I. Ferrite dissolution in an ingot cast alloy

#### I.1. Composition and thermodynamic calculations

The ternary Fe-Cr-Ni alloy was cast in a 2kg-ingot in APERAM Isbergues Research Center. Its chemical composition is reported in Table III. 1.

**Table III. 1: Composition of the ingot cast ternary Fe-Cr-Ni alloy (weight %).**

Element	C	Cr	Cu	Mn	Mo	Ni	Si	Ti	V	N	P	O
wt. %	0.0018	17.3	<0.001	0.016	0.001	9.39	0.055	<0.001	0.044	0.004	0.005	0.016

Phase equilibria of the alloy are computed using two calculation tools: ThermoCalc<sup>®</sup> software [58] together with the TCFE6 database [69] and the CEQCSI software with the Ptimec-module and Miettinen database [70].

Calculation results, in terms of volume fraction of phases as a function of temperature, are presented in Figure III. 1 and characteristic temperatures are listed in Table III. 2. Both databases predict approximately the same characteristic temperatures at the solidification stage (liquidus temperature  $T_L$ , solidus temperature  $T_S$ , eutectic temperature  $T_E$ ). The solidification mode of the alloy is FA as ferrite is the first solid crystal to appear in liquid, followed by austenite. The appearance of austenite in the three phase-region occurs by a eutectic mechanism. Austenite fraction at the end of the solidification is 23% according to TCFE6 versus 32% by Ptimec-Miettinen.

At the solid state, a significant difference between the two predictions is noticed for the A4 temperatures under which the alloy becomes fully austenitic: 1270°C according to TCFE6 versus 1341°C by Ptimec-Miettinen.

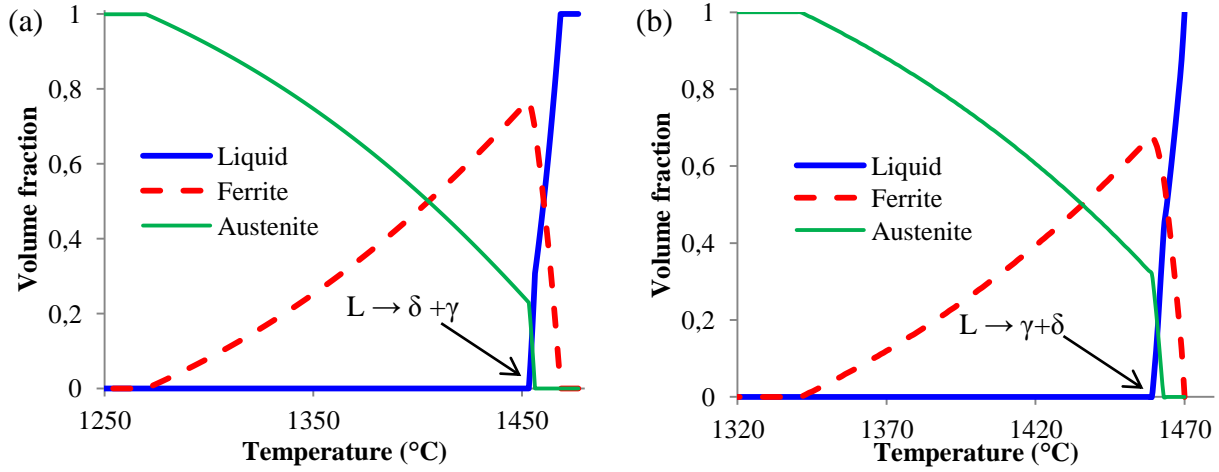


Figure III. 1: Stability phase equilibria in the Fe-17.3%Cr-9.4%Ni alloy computed by (a) ThermoCalc<sup>®</sup> with TCFE6 database and (b) CEQCSI<sup>®</sup> with Ptimec-Miettinen module. All species are used in the calculation and only liquid, ferrite and austenite phases are considered.

Table III. 2: Characteristic features of the Fe-17.3%Cr-9.49%Ni alloy calculated using the TCFE6 and Ptimec-Miettinen databases.

	TCFE6						Ptimec-Miettinen					
	Equilibrium			Scheil			Equilibrium			Scheil		
	T(°C)	% δ	% γ	T(°C)	% δ	% γ	T(°C)	% δ	% γ	T(°C)	% δ	% γ
Liquidus T <sub>L</sub>	1468	3	--	1468	6	--	1469	12	--	1469	12	--
Eutectic T <sub>E</sub>	1456	70	2	1454	54	0.4	1461	64	17.4	1461	68	9.5
Solidus T <sub>S</sub>	1453	77	<b>23</b>	1378	68	<b>30</b>	1459	64	<b>32</b>	1449	68	<b>30</b>
A4	<b>1270</b>	0	100	--	--	--	<b>1341</b>	0	100	--	--	--

Solidification of cast ingots does not occur under equilibrium conditions. In order to take into account solutes distribution during solidification, calculations are carried out using a modified Scheil-Gulliver model and results are compared to equilibrium calculations in Table III. 2 (a solidification path of the alloy computed with a modified Scheil is shown in Figure III. 2). Similar results than with equilibrium calculations are obtained, except the solidus temperature that is largely lowered with ThermoCalc and ferrite fraction that reaches 30%, in accordance with CEQCSI calculations.

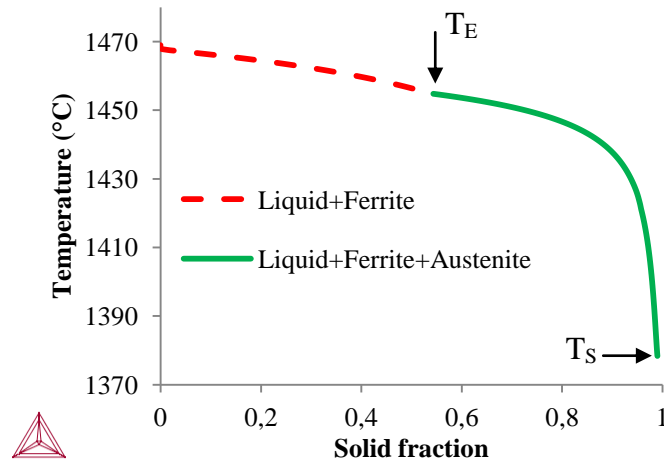


Figure III. 2: Solidification path of the ternary Fe-17.3%Cr-9.4%Ni using a modified Scheil-Gulliver model. All the alloying elements are considered in the calculation.

## I.2. Characterization of the as-cast state

Figure III. 3 shows a transversal section of the ingot. The etching (Lichtenegger and Bloesch) shows mainly columnar solidification grains. However at higher magnifications, equiaxed grains are observed at the skin zone and in the central part of the ingot.

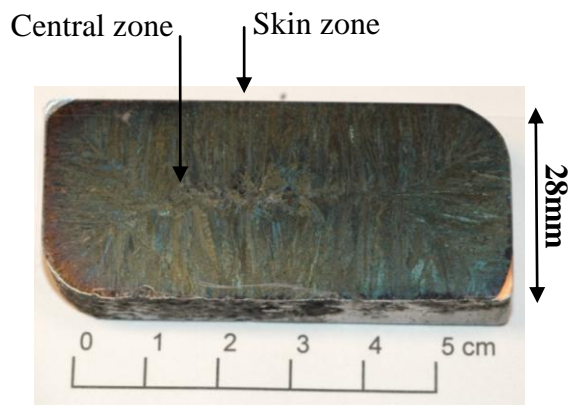


Figure III. 3: Transversal section of the ternary ingot showing the solidification grains (Lichtenegger and Bloesch etching).

The evolution of the morphology of ferrite from the skin of the ingot to its center was carefully investigated in this part. Three ferrite morphologies are evidenced. They are shown in Figure III. 4, 6 and 8. In contrast with the previous equilibrium calculations, this microstructure comprises, in addition to austenite, residual  $\delta$ -ferrite resulting from an incomplete high temperature  $\delta \rightarrow \gamma$  transformation that is due to the cooling conditions of the ingot. The three morphologies are:

- **Lathy ferrite at the skin zone** (Figure III. 4). This ferrite is located inside equiaxed solidification grains that were in contact with the mould. Depending on the orientation of the grain with respect to the cutting plane, ferrite appears either as long thin equally spaced lamellae or constituting honeycomb-like patterns. This microstructure was also observed by

Pereira *et al.* [33] in cast ingots of stainless steels solidifying in the F mode ( $Cr_{eq}/Ni_{eq} = 1.9$ ). In the present case ( $Cr_{eq}/Ni_{eq} = 1.83$ ) solidification is expected to occur in the FA mode. However, according to the microstructure of Figure III. 4, the distribution of ferrite inside each grain suggests that, prior to its solid state transformation to austenite, ferrite apparently occupied the whole grain. This suggests a solidification in the F mode like in [33]. The shift from FA mode to F mode may be the result of:

- either of a difference in composition leading to higher  $Cr_{eq}/Ni_{eq}$  ratio at the skin of the ingot, but EDS measurements over wide areas of this zone contradicted this hypothesis.
- or of kinetic effects modifying the solidification path towards a more ferritic one with increasing cooling rate, as reported by Elmer *et al.* [17] for stainless steels containing 59% Fe with a  $Cr_{eq}/Ni_{eq}$  ratio equal to 1.84 (similar to the present case) and Bobadilla [71] in the case of AISI304 (18.3%Cr - 8.7%Ni) with again a  $Cr_{eq}/Ni_{eq}$  ratio equal to 1.84.

The composition profiles of Cr and Ni across ferrite laths are presented in Figure III. 5. In austenite, profiles are relatively constant showing that only one type of austenite is present in this microstructure. The amounts of Cr and Ni (17% and 10% respectively) are typical of secondary (or regression) austenite as it will be shown in the case of vermicular ferrite (see profiles of Figure III. 7). This is consistent with a solidification in the F mode. Nevertheless further evidence should be supplied in order to clarify the formation of the lathy microstructure in the skin zone.

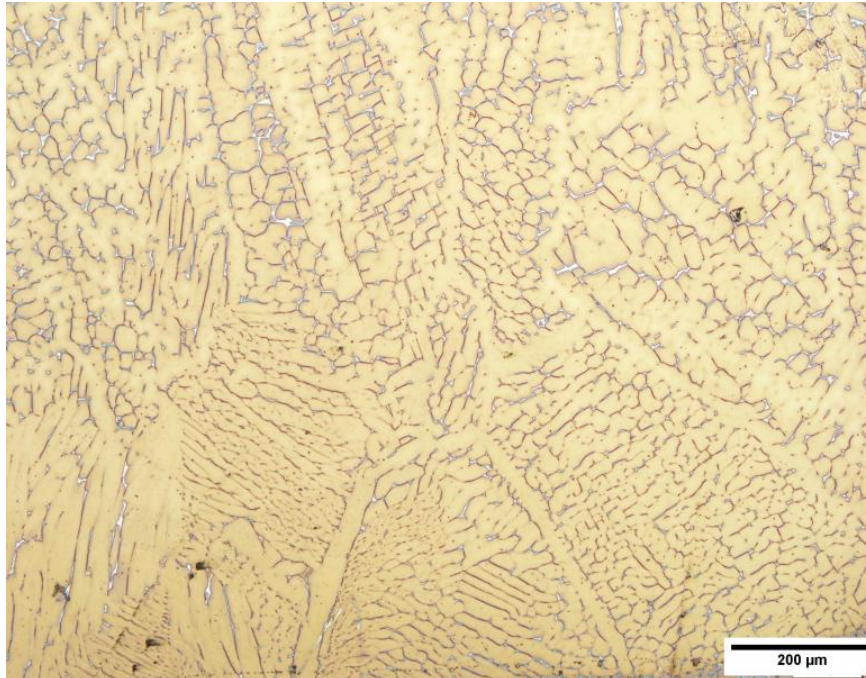


**Figure III. 4:** As-cast Microstructure of the 17.3%Cr-9.4%Ni at the skin of the ingot showing lathy ferrite inside solidification grains. Ferrite appears in white and austenite in yellow (Lichtenegger and Bloesch etching).

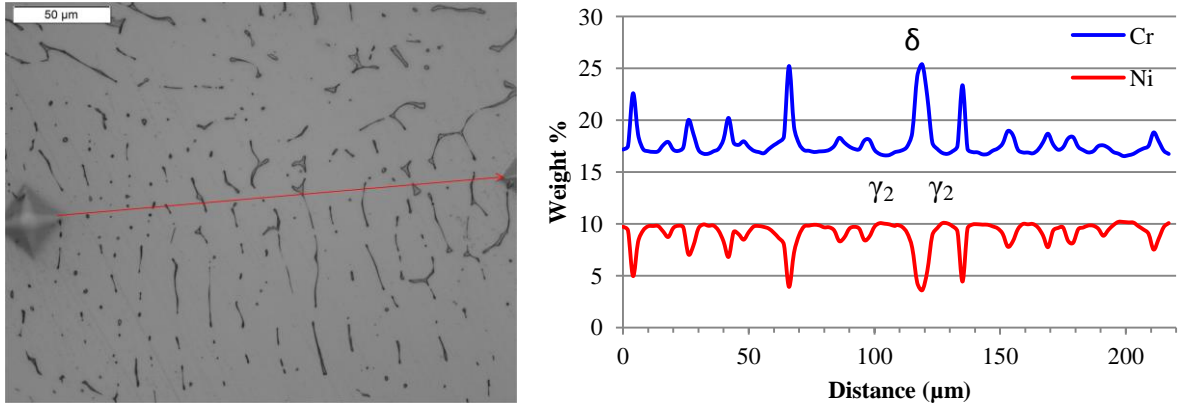


Figure III. 5: Chromium and nickel profiles measured by EPMA in the lathy ferrite zone at the ingot skin (NaOH etching).

• **Vermicular ferrite** (Figure III. 6) is observed from 3 to 5 mm from the edge of the ingot. Ferrite occupies the core of the dendrites and is surrounded by secondary and primary austenites. EPMA measurements (Figure III. 7) that austenite contains two distinct concentration levels corresponding to primary austenite (high Ni content) and secondary austenite resulting from the regression of ferrite at the solid-state. These Cr and Ni microsegregations profiles are rather consistent with a peritectic mechanism during a FA solidification mode:

- Liquid  $\rightarrow$  Liquid +  $\delta$ : formation of primary ferrite.
- Liquid  $\rightarrow$   $\delta$  +  $\gamma_1$ : formation of primary austenite at the  $\delta/L$  interface by a peritectic transformation.
- Liquid  $\rightarrow$   $\gamma_1$ : the remaining liquid transforms to austenite.
- $\delta \rightarrow \gamma_2$ : regression of ferrite and formation of secondary austenite at the solid-state.

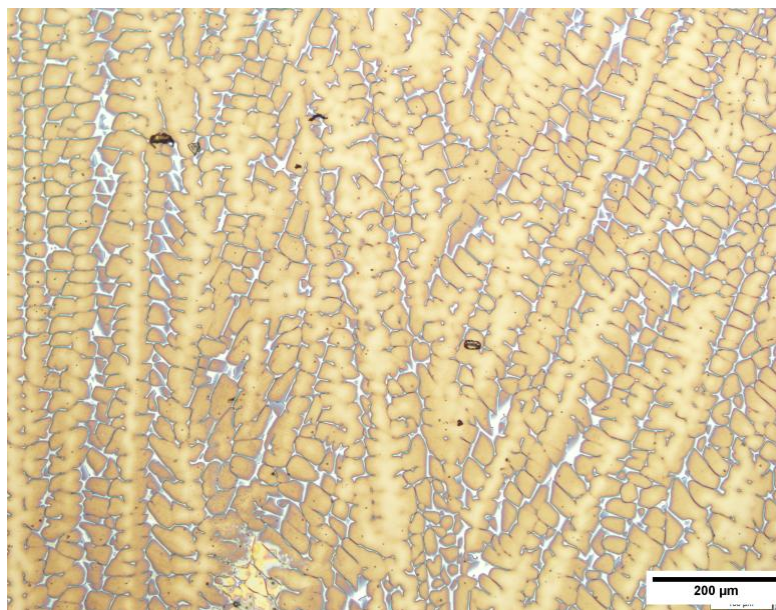


Figure III. 6: As-cast microstructure of the 17.3%Cr-9.4%Ni showing vermicular ferrite at fourth the thickness of the ingot. Primary austenite is colored in yellow, secondary austenite in brown and ferrite in white (Lichtenegger and Bloesch etching).

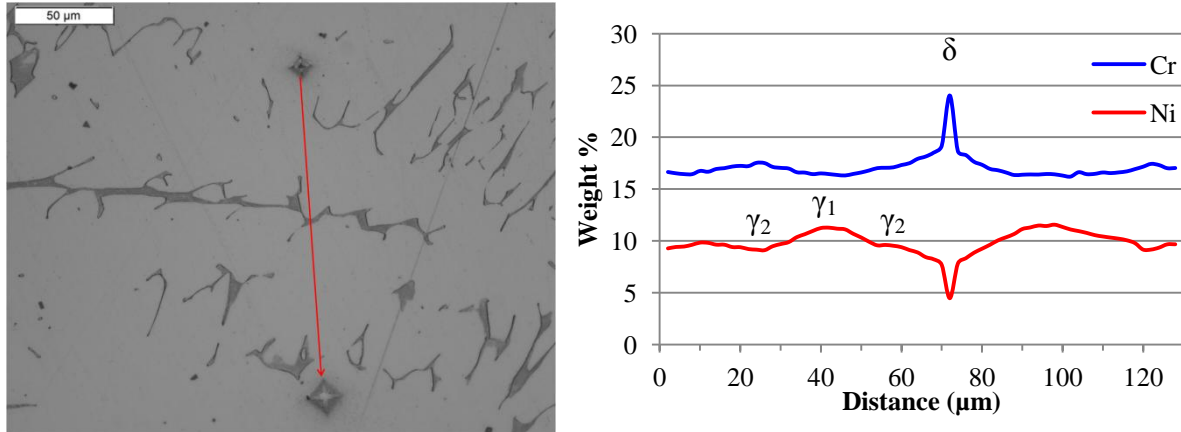


Figure III. 7: : Chromium and nickel profiles measured by EPMA in the vermicular ferrite zone at fourth the thickness of the ingot (NaOH etching).

- **Lathy ferrite in the center** of the ingot (Figure III. 8) is observed from 9 to 14 mm from the edge of the ingot. Ferrite does not occupy the core of dendrites as in the vermicular zone, but forms an interlaced network inside the former ferrite dendrite. This microstructure results from the growth of austenite laths inside ferrite dendrites at the solid state by a Widmanstätten mechanism. In contrast with vermicular ferrite, lathy ferrite is generally observed as the size of former ferritic dendrites increases.

From EPMA measurements in Figure III. 9, ferrite laths keep the same level of Cr enrichment and Ni depletion than in the previous cases. Given that measurements are performed along a ferrite dendritic arm, only secondary austenite appears as surrounding ferrite laths.

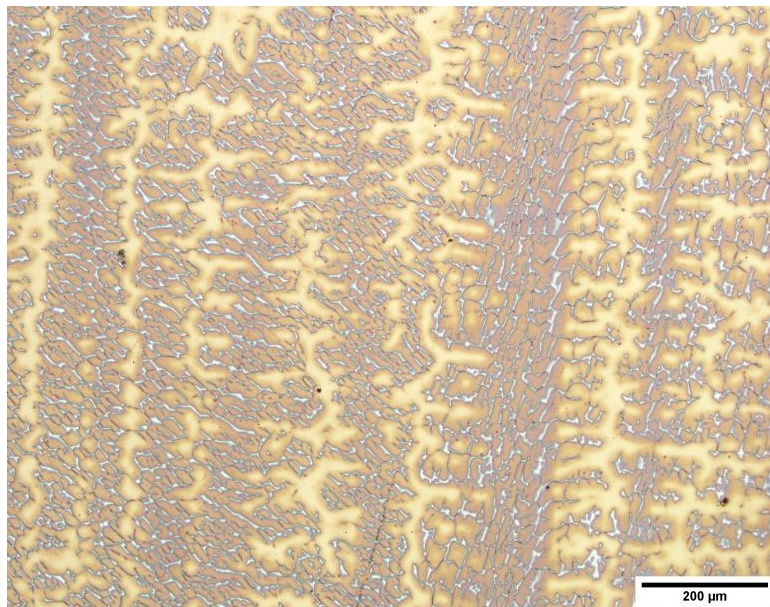


Figure III. 8: As-cast Microstructure of the 17.3%Cr-9.4%Ni at the central part of the ingot showing lathy ferrite (white), secondary austenite occupying the former dendrites of ferrite (brown) and primary austenite (yellow) formed from the liquid (Lichtenegger and Bloesch etching).

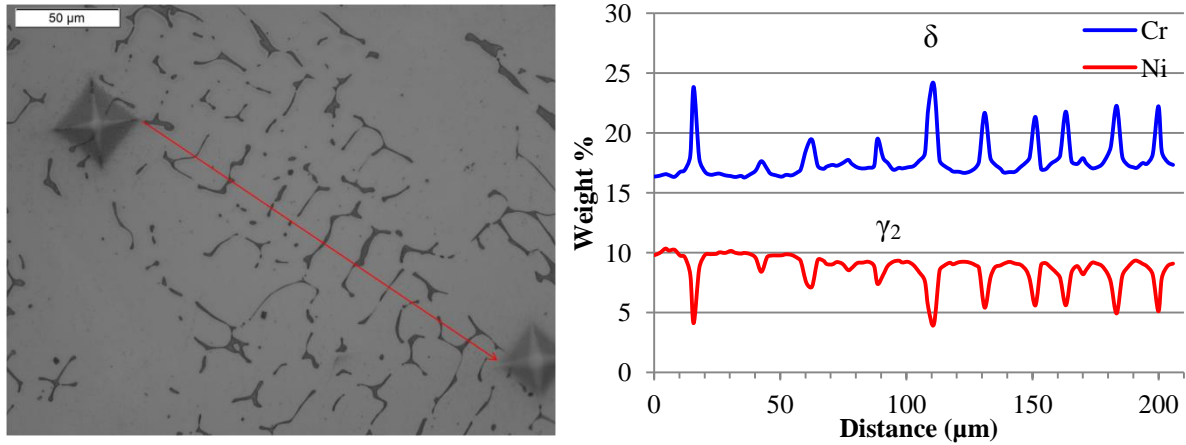


Figure III. 9: Chromium and nickel profiles measured by EPMA in the lathy ferrite zone in the center of the ingot (NaOH etching).

The sketch of Figure III. 10 shows the location of the previously defined morphologies inside the ingot. In addition to these three zones where ferrite has a unique morphology, the ingot contains transition zones where more than one morphology is found.

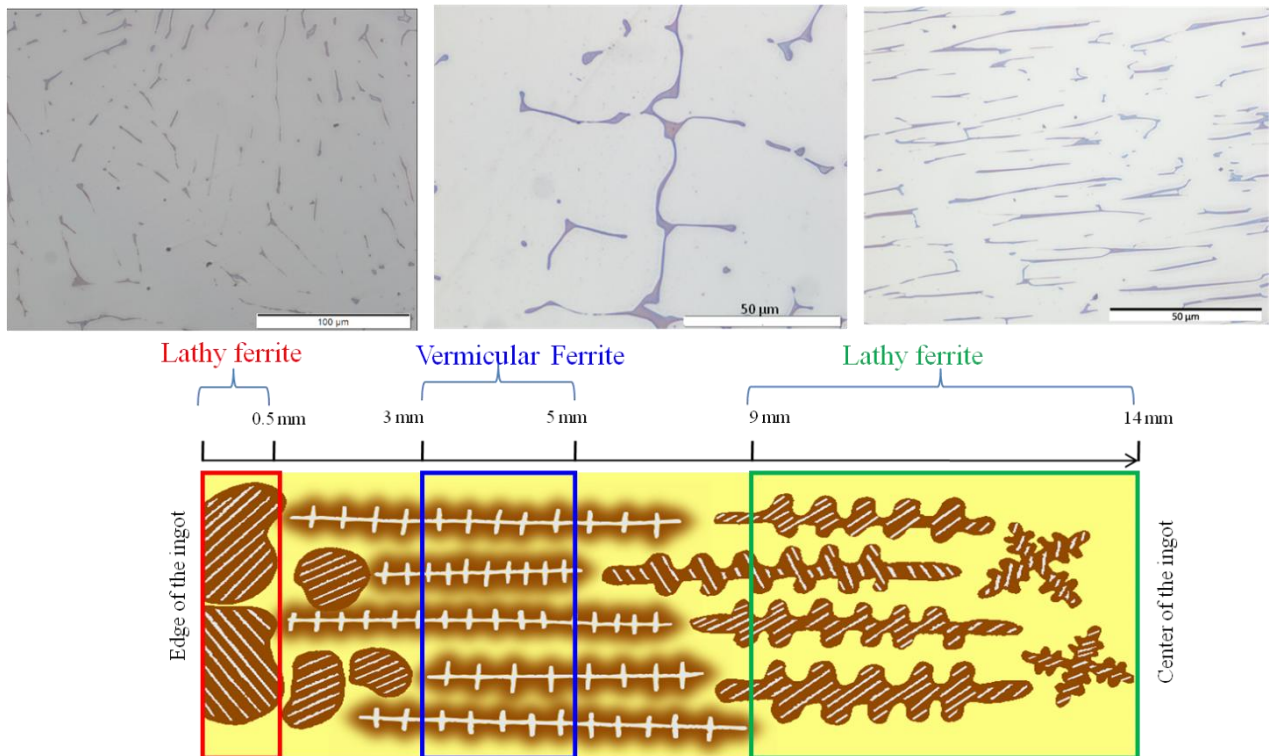


Figure III. 10: Sketch of the evolution of ferrite's morphology from the edge to the center of the ingot. A typical microstructure of each zone is added (NaOH etching).

The fraction of ferrite ( $f_{\delta}$ ) as well as the characteristic lengths ( $\lambda_2$ ,  $\lambda_1$ ,  $d$ ) in each zone are summarized in Table III. 3. Their evolution with distance in the ingot is M-shaped as the one shown in [5]. For each zone only the average values are considered. Ferrite fraction is roughly the same in vermicular and central zones but is twice as high as at the ingot skin. In the

vermicular zone, the amount of solidification austenite is estimated at 35% (by the intercept count method) which is consistent with Scheil calculations (30 vol.%).

The secondary dendrite arm spacing increases with depth from 27 to 60  $\mu\text{m}$  as a result of a decrease in the solidification rate. Inter-lath spacing, keep the same average value in the whole width of the ingot (13  $\mu\text{m}$ ).

**Table III. 3: Ferrite fraction ( $f_\delta$ ), primary dendrite spacing ( $\lambda_1$ ), secondary dendrite arm spacing ( $\lambda_2$ ) and inter-lath spacing (d) in the skin, the vermicular and the central lathy zones.**

Microstructure	$f_\delta$ (%)	$\lambda_1$ ( $\mu\text{m}$ )	$\lambda_2$ ( $\mu\text{m}$ )	d ( $\mu\text{m}$ )
Lathy at the skin	2.7	--	--	13
Vermicular	5.5	80	27	--
Lathy at the center	5.2	140	60	13

From the EPMA analysis shown previously (Figure III. 5, 7 and 9), a certain variability in Cr and Ni contents in ferrite can be noticed. This is partly due to the fine thickness of ferrite particles, which makes the interaction volume of EPMA measurements ( $\sim 1\mu\text{m}^3$ ) take into account the neighboring austenite. In addition, it comes also as a result of the local extent of the solid state  $\delta \rightarrow \gamma_2$  transformation which results both in a more or less Cr rejection/Ni depletion in ferrite and in a variation in ferrite thickness.

Typical Cr and Ni concentrations in ferrite and austenite are reported in Table III. 4. These values will be used as basis for the choice of the ferritic and austenitic alloys to be used in the multilayered microstructure (second part of this chapter). In view of the error committed by the low resolution of EPMA (2 $\mu\text{m}$ ), ferrite composition is selected by choosing the maximum Cr and the minimum Ni measured values, as they are expected to be more representative of the bulk of ferrite.

**Table III. 4: Typical chromium and nickel concentrations in ferrite and austenite in the as-cast state of the Fe-17.%Cr-9.4%Ni alloy.**

	Cr (wt. %)	Ni (wt. %)
Ferrite	25	3.5
Primary austenite	16.5	11.3
Secondary austenite	17.5	9.5

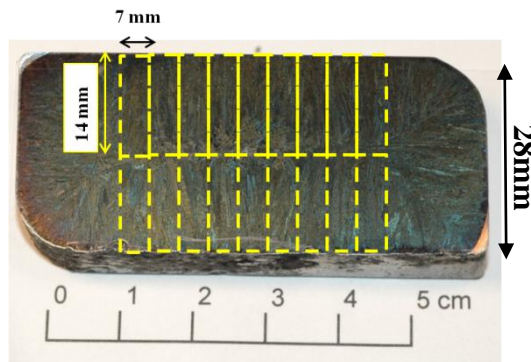
### I.3. Kinetics of ferrite dissolution

The dissolution of ferrite was studied in the three zones previously defined at the temperatures listed in Table III. 5. The considered temperature range (1140°C to 1346°C) is typical of the hot rolling process of austenitic stainless steels and is also selected on the basis of the thermodynamic calculations of the A4 temperature (1270°C with TCFE6 and 1341°C with Ptimec-Miettinen), in order to determine it experimentally.

**Table III. 5: Temperatures selected for the investigation of ferrite dissolution in the Fe-17.3%Cr-9.4%Ni alloy. Heating cycles contain extra 2min in order to reach the targeted temperature.**

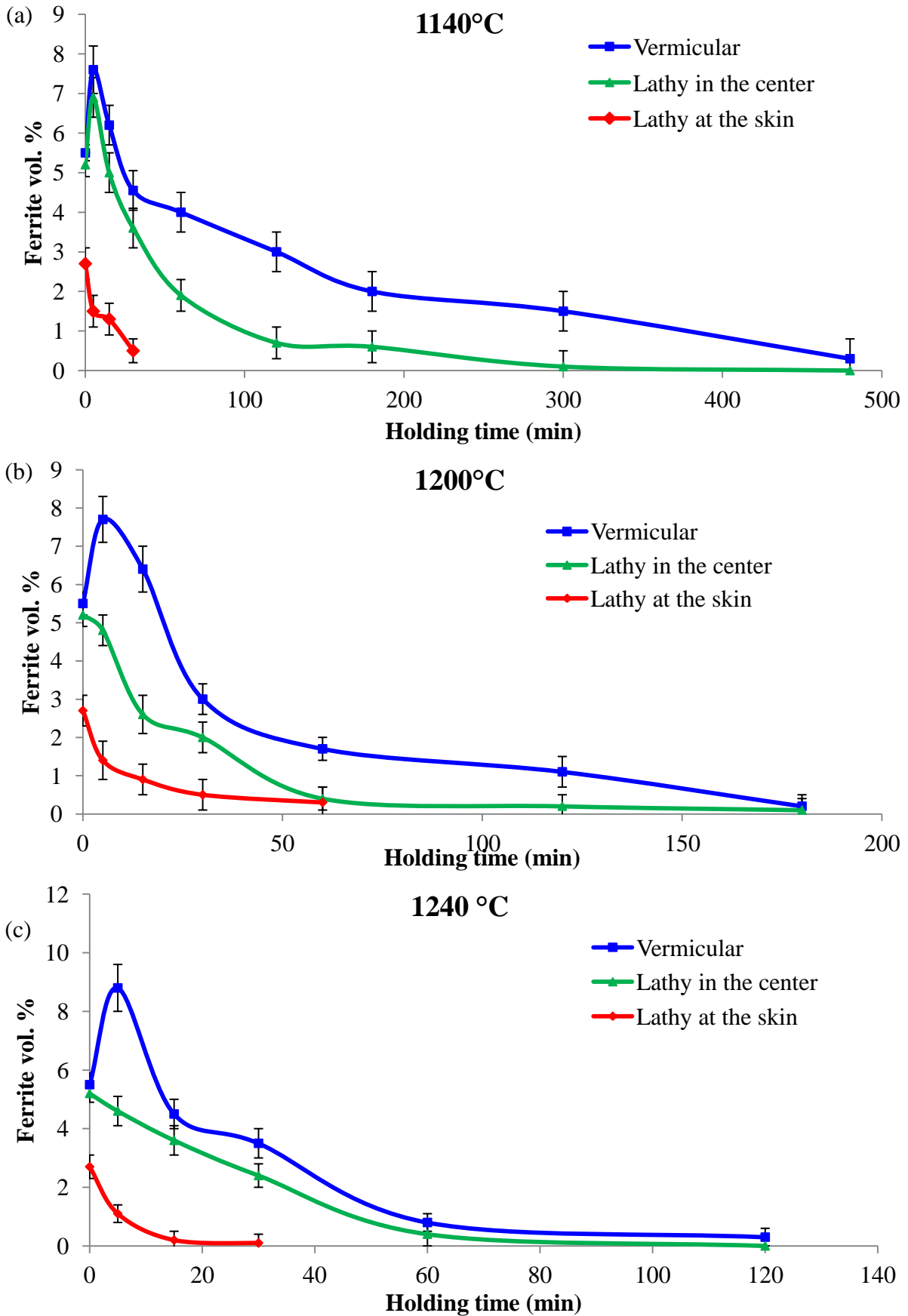
Temperature (°C)	Holding time								
	5min	15min	0.5hr	1hr	2hrs	3hrs	4hrs	5hrs	8hrs
1140	✓	✓	✓	✓	✓	✓		✓	✓
1200	✓	✓	✓	✓	✓	✓			
1240	✓	✓	✓	✓	✓	✓			
1260	✓	✓	✓	✓	✓		✓		
1280	✓	✓	✓	✓	✓	✓			
1300	✓	✓	✓	✓	✓	✓			
1346	✓	✓	✓	✓	✓		✓		

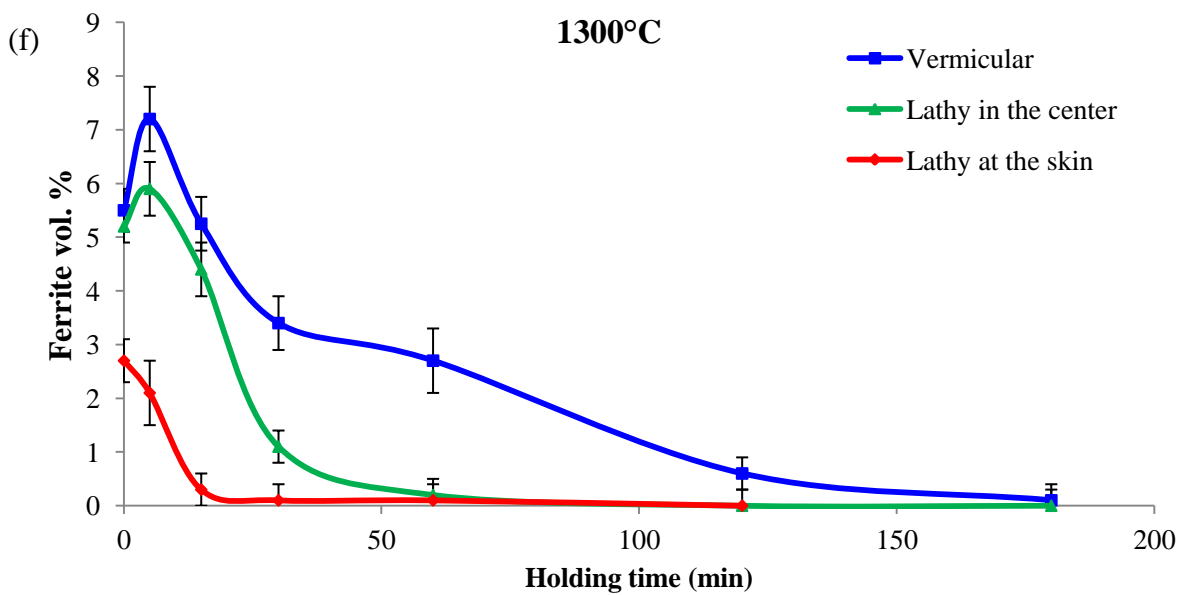
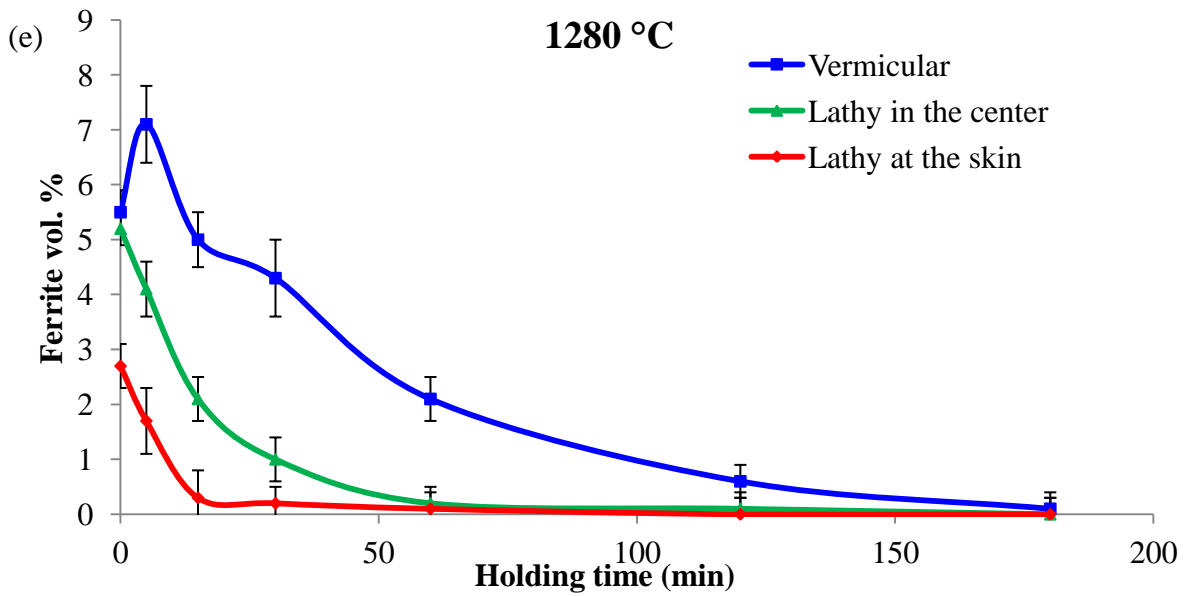
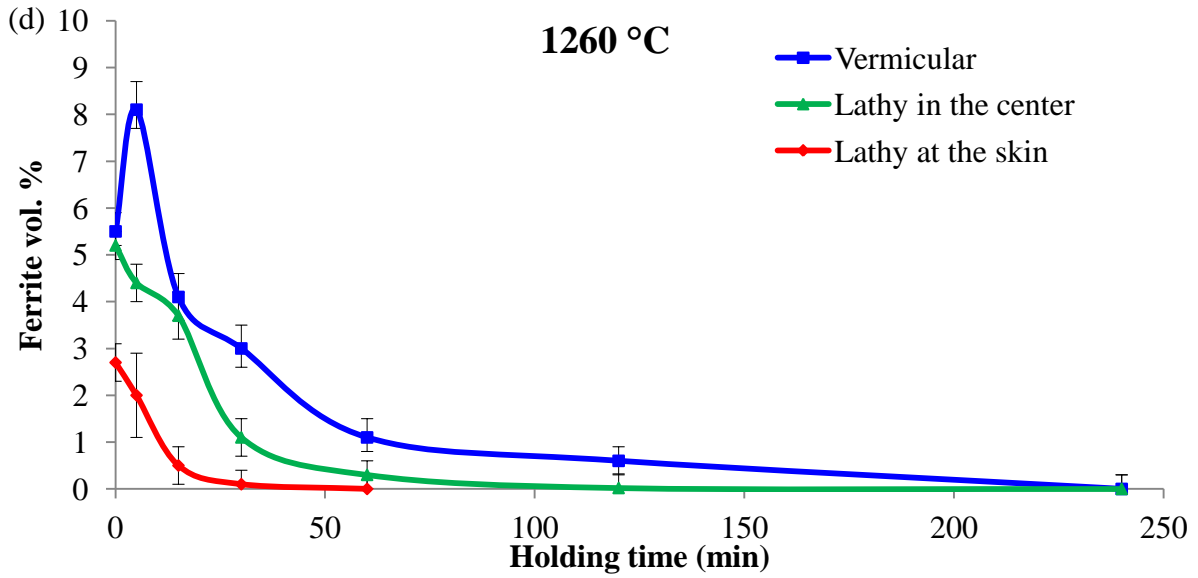
The extraction of samples from the ingot is performed according to the sketch of Figure III. 11. The piece of material shown in the figure is cross-sectioned from the ingot. The length of samples (yellow rectangles, 14mm) is chosen in order to capture all microstructural evolution from the skin to the center of the ingot. Metallographic observations are performed on the transverse plane of the ingot.



**Figure III. 11: Schematic of samples extraction from a transversal section of the cast ingot (Lichtenegger and Bloesch etching).**

The evolution of ferrite fraction with the holding time in each zone is shown in Figure III. 12. For temperatures up to 1300°C ferrite completely dissolves, while at 1346°C its amount stabilizes at about 2% after 4hrs annealing. This suggests that at this temperature the alloy composition lies in the  $\delta+\gamma$  region in the phase diagram. Hence the correspondent A4 temperature, under which the alloy is purely austenitic lies between 1300°C and 1346°C, in good agreement with the prediction from the Ptimec-Miettinen module (1341°C).





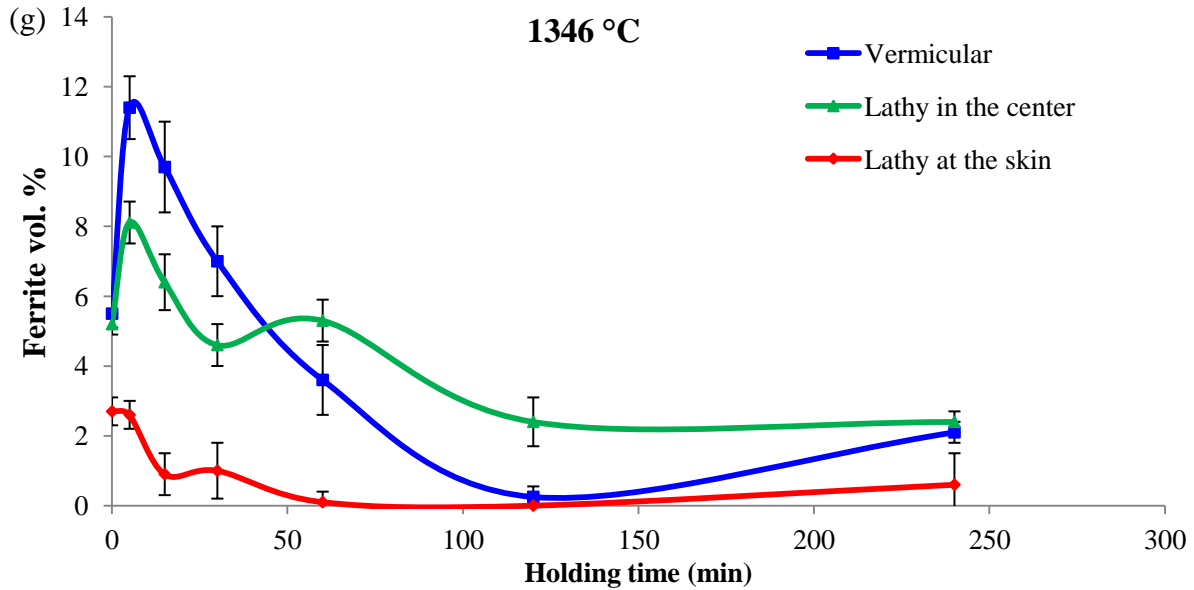


Figure III. 12: Time evolution of ferrite fraction in the lathy at the skin, vermicular and central-lathy zones at (a) 1140°C, (b) 1200°C, (c) 1240°C, (d) 1260°C, (e) 1280°C, (f) 1300°C and (g) 1346°C.

The transition from the fully austenitic to the austenitic-ferritic domain is also perceptible on the morphology of the  $\delta/\gamma$  interface as shown in Figure III. 13. In the microstructure after quenching from 1300°C, and at lower temperatures, the shape of the  $\delta/\gamma$  interface is smooth, while it is lace-like in microstructures quenched from 1346°C. This latter morphology is the result of a partial austenite growth inside the ferrite during quenching from the  $\delta+\gamma$  domain. With this in view, ferrite fraction before quenching from 1346°C should be slightly higher than the measured one at room temperature.

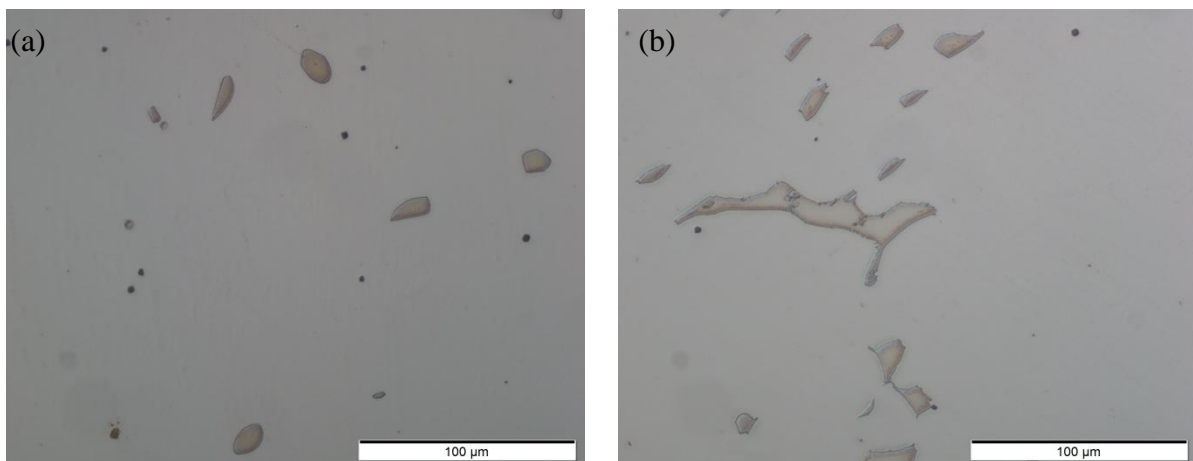


Figure III. 13: Residual ferrite after 2hrs annealing followed by water quench from (a) 1300°C and (b) 1346°C. Note the smooth morphology of the  $\delta/\gamma$  interface at 1300°C and its lace-like morphology at 1346°C.

### I.3.a. Dissolution of the lathy ferrite at the edge

Among the three zones, lathy ferrite at the edge of the ingot is the most rapid to dissolve (< 60 min at all temperatures), as it has the lowest fraction in the as-cast state (2.7%).

### I.3.b. Dissolution kinetics and microstructural change of vermicular ferrite

For vermicular ferrite, the dissolution curves at all temperatures exhibit the same features. By considering the dissolution at 1240°C as a representative case (Figure III. 14), the evolution of ferrite fraction with holding time exhibit three stages:

1. An early ferrite growth stage, which occurs during the first 5min of the transformation.
2. A rapid dissolution stage, which takes place from the end of ferrite growth until 15min.
3. A slow dissolution stage which starts after 15min until complete dissolution.

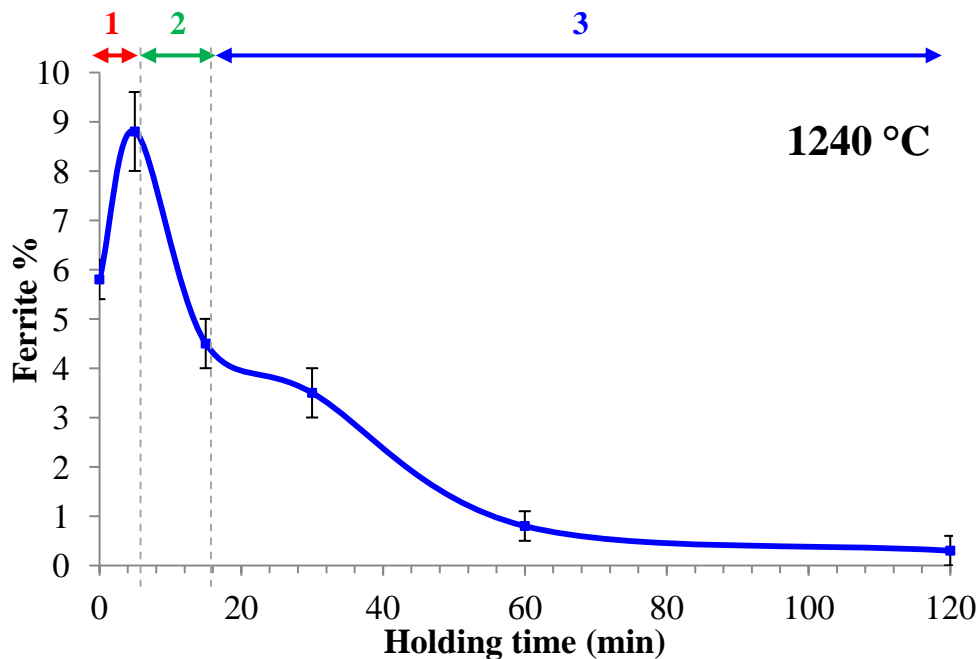


Figure III. 14: The three regimes of the dissolution of vermicular ferrite at 1240°C.

Each stage is examined in detail in the following paragraphs:

#### Early growth (stage1):

Ferrite fraction initially increases until reaching 9% after 5 min annealing. This ferrite fraction does not necessarily correspond to the maximum ferrite growth, the latter might be reached earlier.

As it has been mentioned in Chapter I, the growth of ferrite at the initial stage of the transformation was observed in the dissolution of ferrite sheets in Fe-Cr-Ni  $\gamma/\delta/\gamma$  diffusion

couples experimentally studied by Kajihara *et al.* [35][48]. It has been shown that it is possible to explain the initial growth of ferrite as a direct consequence of the early variation of solute gradients in ferrite coupled to higher solute diffusivity than in austenite.

In the present case, we will show in Chapter V, §III.2.b *Effect of solute gradients*, that, by numerical modeling, the early growth of ferrite in the studied microstructure cannot be explained on the same basis as in Kajihara's works. An alternative mechanism will be suggested.

### **Dissolution (stages 2 and 3)**

In order to get more insight into the abrupt decrease of the dissolution rate at 15 minutes, the evolution of the morphology of ferrite particles was analyzed. A typical sequence of micrographs illustrating the microstructural changes that occur on annealing at 1240°C is shown in Figure III. 15. The progressive breakup of ferritic dendrites and their subsequent spheroidization can be clearly noticed: at the beginning of the transformation the secondary arms split up from the dendrite and dissolve very rapidly until they disappear after 15 min. The remaining particles, corresponding to the crossing of dendritic arms, become rather spherical and are regularly located at the former intersection of primary and secondary dendrite arms.

This analysis is quantitatively assessed using the circularity shape descriptor whose definition is given in Chapter II. Figure III. 16 shows the distribution of the circularities of ferrite particles for each annealing time at 1240°C. Low-circularity particles are rather elongated and high-circularity ones are rather spherical. In the as-cast microstructure the population of ferrite particles is bimodal, with a predominance of elongated ones (Figure III. 16.a): elongated particles correspond to residual ferritic dendrites or fragments of dendrites, while circle-like ones mainly correspond to dendrite arms that are cross-sectioned by the plane of the figure. As the transformation proceeds, the density of elongated particles decreases in favor of spherical ones and after 15 min, circularity histogram shows that elongated particles almost completely disappeared. In the subsequent dissolution stage ferrite continues its dissolution as spheroid particles.

It can be concluded from these analyses that the rapid dissolution regime (5 to 15 min) is dominated by the dissolution of dendrite secondary arms. Subsequently, the dissolution of dendrite arms intersections corresponds to the low dissolution regime occurring from 15min onwards. This conclusion is assessed by the same circularity analysis at the other annealing temperatures, which can be found in Appendix A.

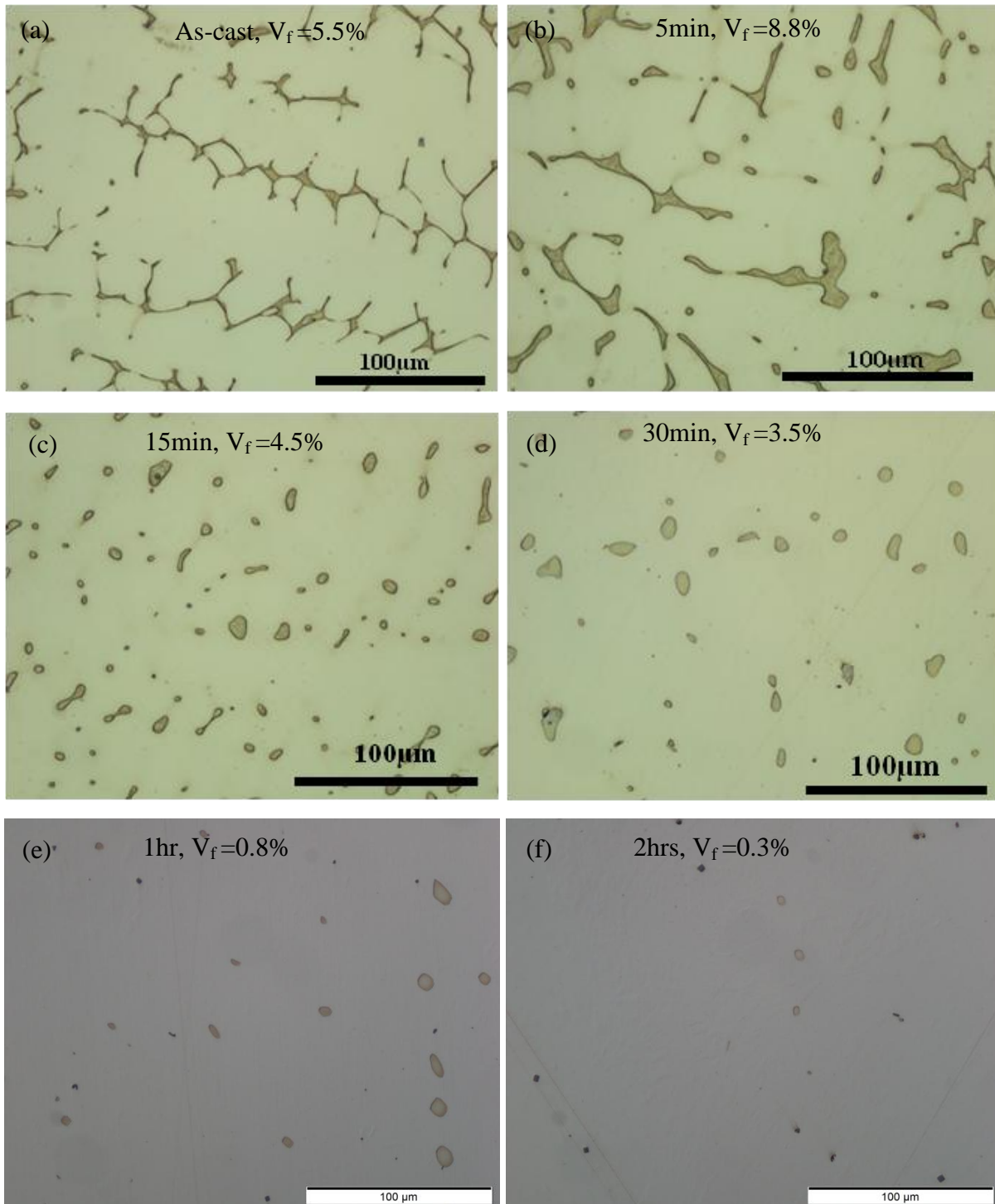
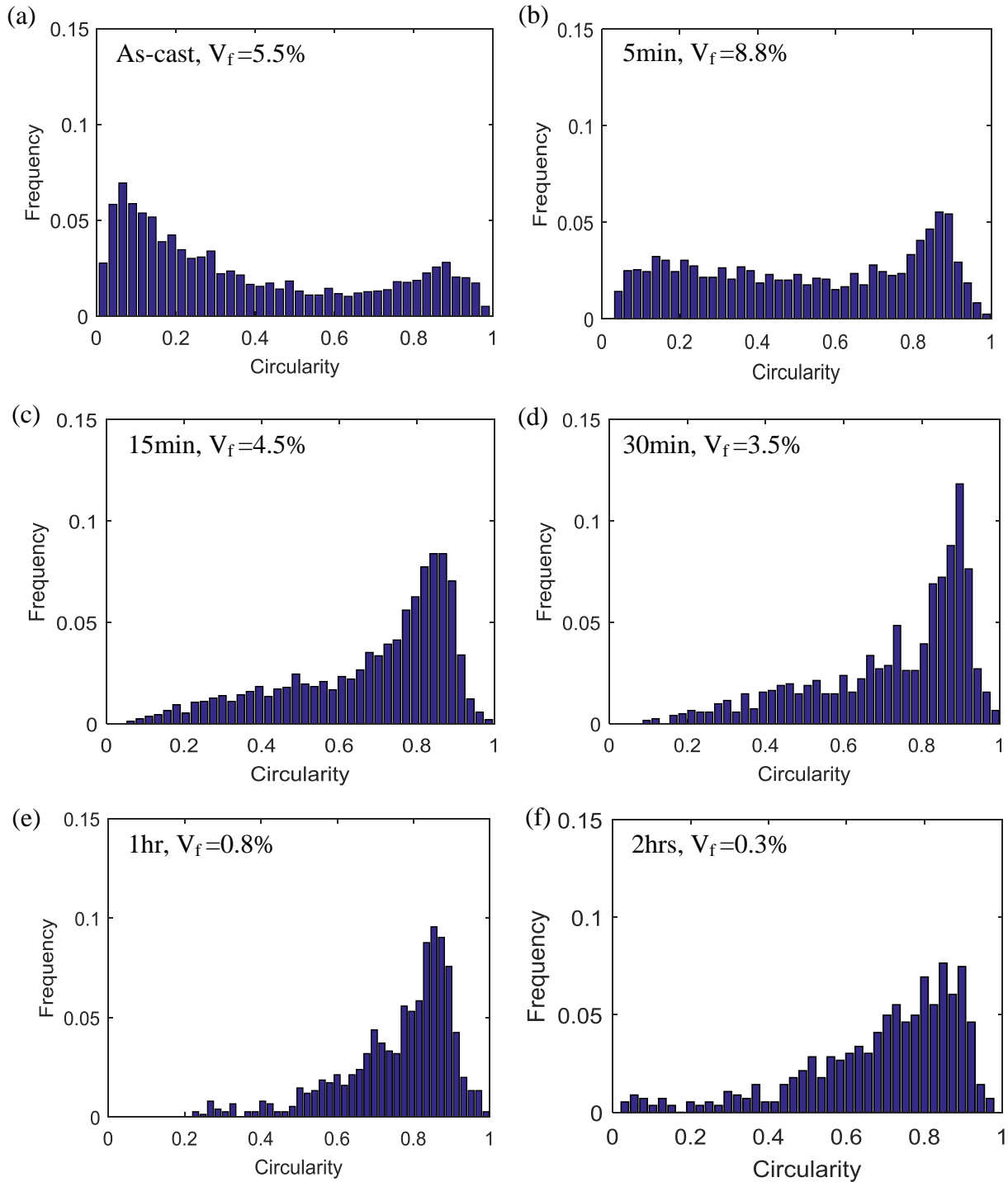


Figure III. 15: The evolution of the morphology of the vermicular ferrite particles during its dissolution at 1240°C (a) in the as-cast state, (b) after 5min, (c) after 15min, (d) after 30min, (e) after 1hr and (f) after 2hrs.



**Figure III. 16:** Distribution of the circularity of the vermicular ferrite particles during its dissolution at 1240°C (a) in the as-cast state, (b) after 5min, (c) after 15min, (d) after 30min, (e) after 1hr and (f) after 2hrs.

### I.3.c. Dissolution of lathy ferrite in the centre of the ingot

Unlike the vermicular type, the dissolution kinetics of central lathy does not always exhibit the initial growth stage. At the highest (1300°C and 1346°C) and the lowest (1140°C) temperatures, the growth stage has been evidenced after 5 min annealing, while it was not observed at intermediate temperatures (1200°C, 1240°C, 1260°C et 1280°C). This does not

state that ferrite growth did not occur at these intermediate temperatures, one possibility being that it was so rapid that it could not be observed after 5 minutes annealing.

### I.3.d. Overall transformation kinetics

The overall dissolution kinetics of vermicular and central-lathy ferrite is shown in the Figure III. 17. The evolution of ferrite fraction as a function of temperature is shown at different holding times. A vertical line representing the A4 temperature of the ternary alloy, as calculated with CEQCSI and the Ptimec-Miettinen module, is superimposed on graph (real A4 temperature lies between 1300°C and 1346°C).

For a given holding time, the remaining ferrite fraction is generally more elevated at lower (1140°C) and higher (1300°C-1346°C) temperatures, while it is the lowest at intermediate ones. For vermicular ferrite, the transformation is the fastest at 1240°C and for central-lathy one it is the fastest at 1240-1280°C. The low transformation rate at 1140°C is due to slow diffusion of Cr and Ni, while it is caused by small driving force of dissolution at 1300°C.

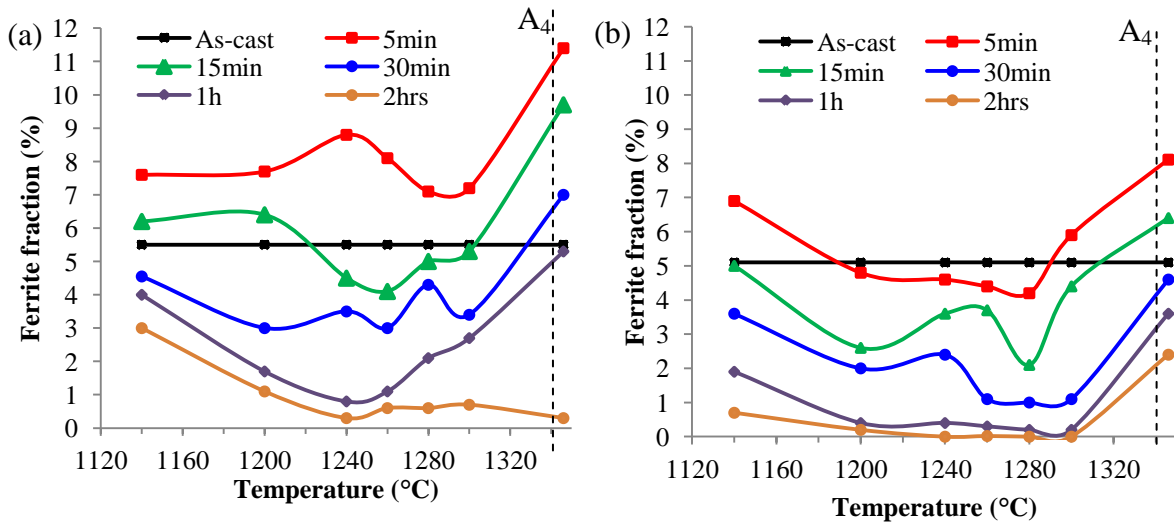


Figure III. 17: Evolution of ferrite fraction with temperature at different holding times for (a) vermicular and (b) central-lathy ferrite. Vertical dashed lines represent the A4 temperature of the Fe-17.3%Cr-9.4%Ni alloy as calculated by the CEQCSI software and the Ptimec-Miettinen module.

## II. Ferrite dissolution in the multilayered microstructures

In addition to the reduced number of diffusing solutes (Cr and Ni), the multilayered microstructures are designed with planar  $\alpha/\gamma$  interfaces where the concentration fields in both ferrite and austenite can be easily described by the 1D phase transformation model that will be developed in chapter IV.

In the next paragraph, the elaboration steps of such microstructures are first presented. Then the microstructure after each step is characterized and then submitted to high temperature heat treatments in order to establish the kinetics of ferrite dissolution.

## II.1. Elaboration of the multilayered microstructures

The chemical composition of ferrite and austenite in the multilayered microstructures was chosen to be representative of those of the ingot-cast alloy (see Table III. 4). A single phase ferritic and a single phase austenitic alloys of the ternary Fe-Cr-Ni system were cast as 50 kg ingots in APERAM Imphy Research Center. Their chemical compositions are given in Table III. 6.

**Table III. 6: Composition of the ferritic and austenitic alloys used in the elaboration of the multilayered microstructure.**

Grade	Mn wt. %	P wt. %	Si wt. %	Ni wt. %	Cr wt. %	Cu wt. %	Mo wt. %	V wt. %	Ti wt. %	Co wt. %	N ppm	C ppm	S ppm	O <sub>2</sub> ppm
Ferritic	0.020	0.005	0.019	<b>2.91</b>	<b>25.45</b>	≤ 0.001	0.002	0.010	0.005	0.002	14	76	11	78
Austenitic	≤ 0.002	0.006	0.006	<b>12.00</b>	<b>16.83</b>	≤ 0.001	0.003	0.002	≤ 0.001	0.003	14	93	10	38

Thermodynamic calculations show that, at temperatures ranging from 650°C to 1400°C, both alloys are thermodynamically stable, as shown in Figure III. 18.

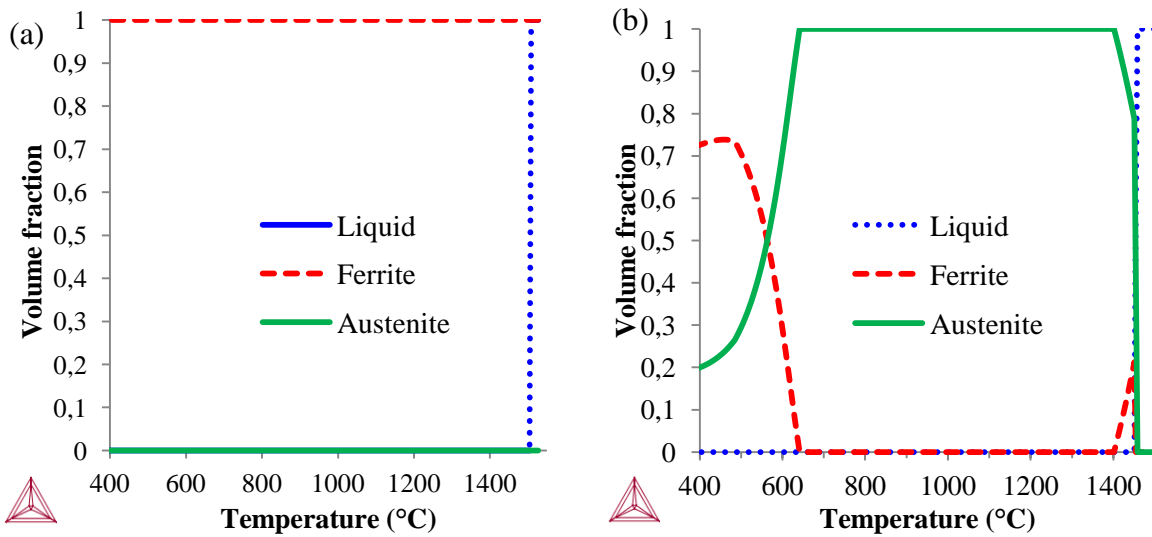


**Figure III. 18 : Phase equilibria calculated with ThermoCalc® and the TCFE6 database for (a) the ferritic alloy (w(Cr)=25.4%, w(Ni)=2.9%), (b) the austenitic alloy (w(Cr)=16.8%, w(Ni)=12%).**

Blocks of ferrite (20 x 50 x 120 mm<sup>3</sup>) and austenite (40 x 50 x 120 mm<sup>3</sup>) were cut from the ingots and transformed into sheets by means of hot and cold rollings. The hot rolling was performed after 30 min homogenization at 1200°C, allowing to reduce the thickness of blocks by a factor of 10. An overview of both alloy microstructures at this stage is given in Figure III. 19. Afterwards sheet surfaces were cleaned by sanding and subsequent pickling with a mixture of HF and HNO<sub>3</sub> acids in order to remove surface oxides. A cold rolling is then applied (50% thickness reduction) in order to reach a final thickness of 2 and 0.5mm for austenite and ferrite sheets respectively. After recrystallisation annealing, plate specimens with 80mm x 50mm dimensions were extracted from the sheets by machining and edges were rectified by milling operations. Surface roughness R<sub>a</sub> of the plates is ensured to be lower than 1µm which is essential to reach a strong bonding between plates during the Hot Isostatic Pressing (HIP).

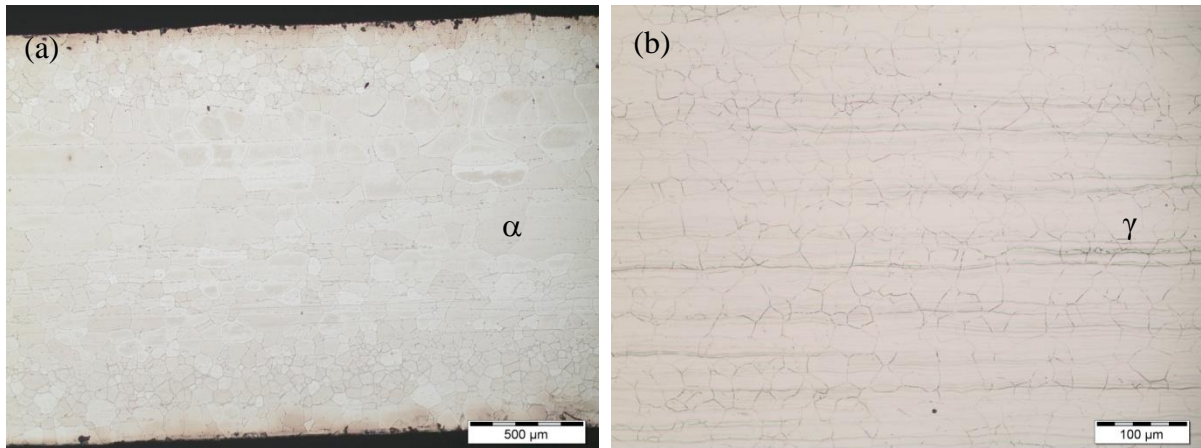


**Figure III. 19:** Microstructure of the (a) ferritic and (b) austenitic Fe-Cr-Ni alloys after casting followed by a first hot rolling and a recrystallisation heat treatment (Electronitric etching). Macroseggregations in the austenite alloy appears as long horizontal bands.

The fabrication of the multilayered microstructures includes a series of diffusion-bonding steps followed by thickness reductions by hot and cold rollings. The reduction steps are intended to obtain final ferrite thicknesses comparable to those of the residual ferrite ( $\sim 1\mu\text{m}$  to  $5\mu\text{m}$ ) in as-cast microstructure of the ingot-cast alloy. The elaboration step are as following:

- **Hot Isostatic Pressing 1:** a sketch of the stack is shown in Figure III. 20.a. The stack was made by alternating 14 plates of austenite and ferrite, corresponding to a ferrite fraction of 20% and a global composition of 18.5wt.%Cr-10.2wt.%Ni. Before stacking, sheets were first cleaned with acidic solution to remove residual surface oxides. The stack was then sealed in a container made of 304L stainless steel, under vacuum in order to avoid any contamination from the ambient environment. The stack was subsequently submitted to the Hot Isostatic Pressing (HIP) cycle shown in Figure III. 20.b which includes a plateau of  $42 \pm 10$  min at  $1000 \pm 10^\circ\text{C}$  and under a pressure of  $1400 \pm 10$  bar. The HIP technique was used to ensure strong bonding between neighboring plates without passing through the liquid domain and to maintain planar interfaces. The hot isostatic pressing as well as the cleaning and the sealing were performed at CEA-LITEN, Grenoble.

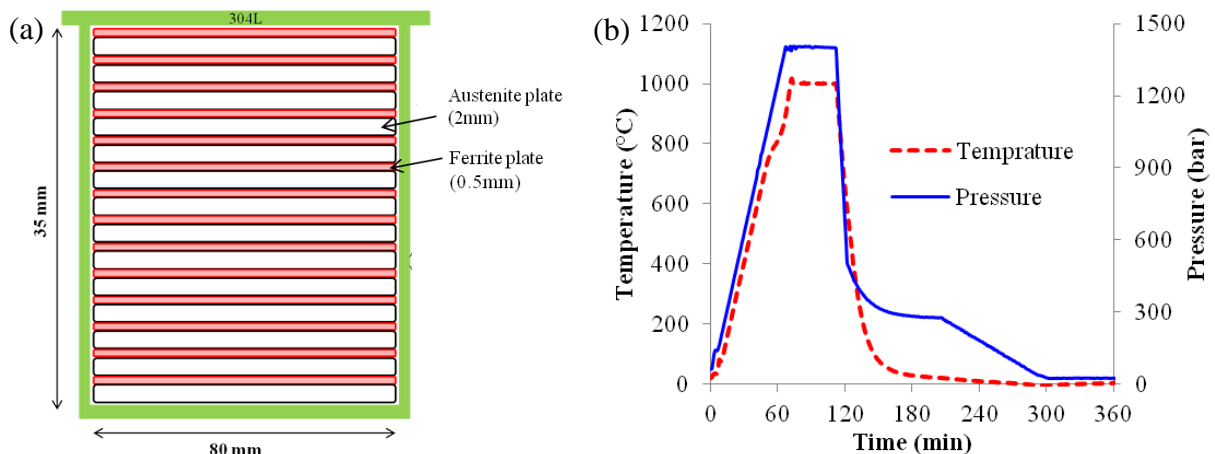


**Figure III. 20:** (a) Schematic of the initial stack. (b) Temperature and pressure cycles during the hot isostatic pressing.

- **Hot rolling 1:** the thickness of the stack was then reduced from 35mm to 6mm by hot rolling after furnace heating at 1050°C during 120min. In order to avoid contamination by nitrogen that may diffuse from the 304L container, upper and lower parts of the container were removed prior to hot rolling. Peripheral parts are kept in order to ensure cohesion of the stack during rolling.
- **Cold rolling 1:** The stack was afterwards submitted to recrystallisation annealing at 1050°C for 1min and then cold rolled to a thickness of 3.5mm.
- **Hot Isostatic Pressing 2:** five plate specimens (80 x 50 x 3.5mm) were cut from the cold rolled stack, piled up and then diffusion-bonded by a second HIP cycle using the same thermo-mechanical conditions as in Figure III. 20.b. The height of the second stack is 17.5mm.
- **Hot rolling 2:** the hipped stack was submitted to a second hot rolling after 30min at 1050°C and the resultant thickness is 3.8mm.
- **Cold rolling 2:** after cleaning and recrystallisation heat treatment, the stack thickness was finally cold rolling to a final thickness of 1.8mm.

The sketch of Figure III. 21 summarizes the processing steps of the multilayered microstructures.

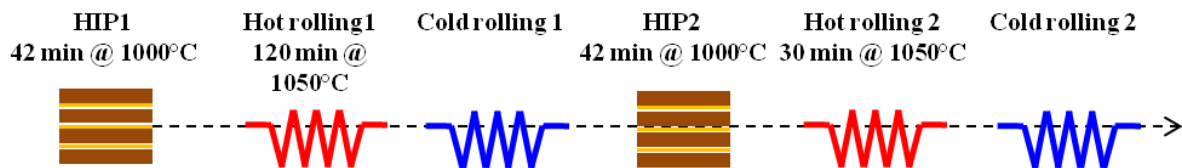


Figure III. 21: Schematic of the processing steps of the multilayered microstructure. Four microstructures thicknesses are considered: after the first hot rolling (HR1), after the first cold rolling (CR1), after the second hot rolling (HR2) and after the second cold rolling (CR2).

After each reduction step, the microstructure was characterized in the as-received state and the dissolution of ferrite was investigated afterwards. A piece of material like the one shown in Figure III. 22 was extracted from each stack. Observations were performed along the rolling direction, *i.e.* in the (ND, TD) plan. It is to be noticed that microstructures after HIP1 and HIP2 are not characterized since hipped assemblies are directly hot rolled without sample extraction prior to hot rolling.

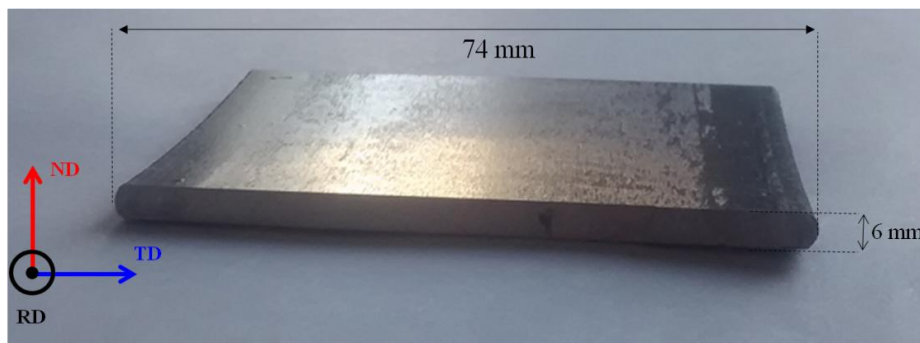


Figure III. 22: Example of a piece of material extracted from the stack after the first hot rolling. The multilayered microstructure is observed in the cross section of the piece (the (TD, ND) plane).

## II.2. Microstructures in the as-received states

### II.2.a. Microstructure after the first hot rolling (HR1)

Figure III. 23.a shows a typical cross section of the stack after the first hot rolling, followed by a recrystallisation heat treatment of 1 min at 1100°C. In the microstructure revealed by electro-nitric etching, austenite bands are clearly colored, while ferrite ones possess different colorings owing to the variety of grain orientations. The dark band at the bottom of the stack corresponds to the remaining part of the container used for the hot isostatic pressing. For easy identification, ferrite and austenite bands will be numbered from 1 to 14 starting from the bottom.

The thickness of ferrite and austenite bands is not homogeneous throughout the stack: central bands are the thinnest while upper and lower ones are the thickest. Figure III. 23.b and c show the variation of ferrite and austenite thicknesses with respect to their position in the stack. They increase by factor one to three from the center to the edge. It can be noted that ferrite bands 4 to 9 have roughly the same average thickness of 66  $\mu\text{m}$ .

Composition profiles of Cr and Ni in ferrite band 7 are shown in Figure III. 24. Ferrite is slightly enriched in Ni and depleted in Cr in the vicinity of the interface. This is due to the interdiffusion of Ni and Cr owing to the successive heating cycles during hot isostatic pressing and hot rolling. In the same fashion a composition gradient of Ni is established in austenite but at a much smaller extent due to a less important diffusivity ( $D^\gamma/D^\delta \approx 1/100$  at 1000°C, according to MOB2 mobility database [72]).

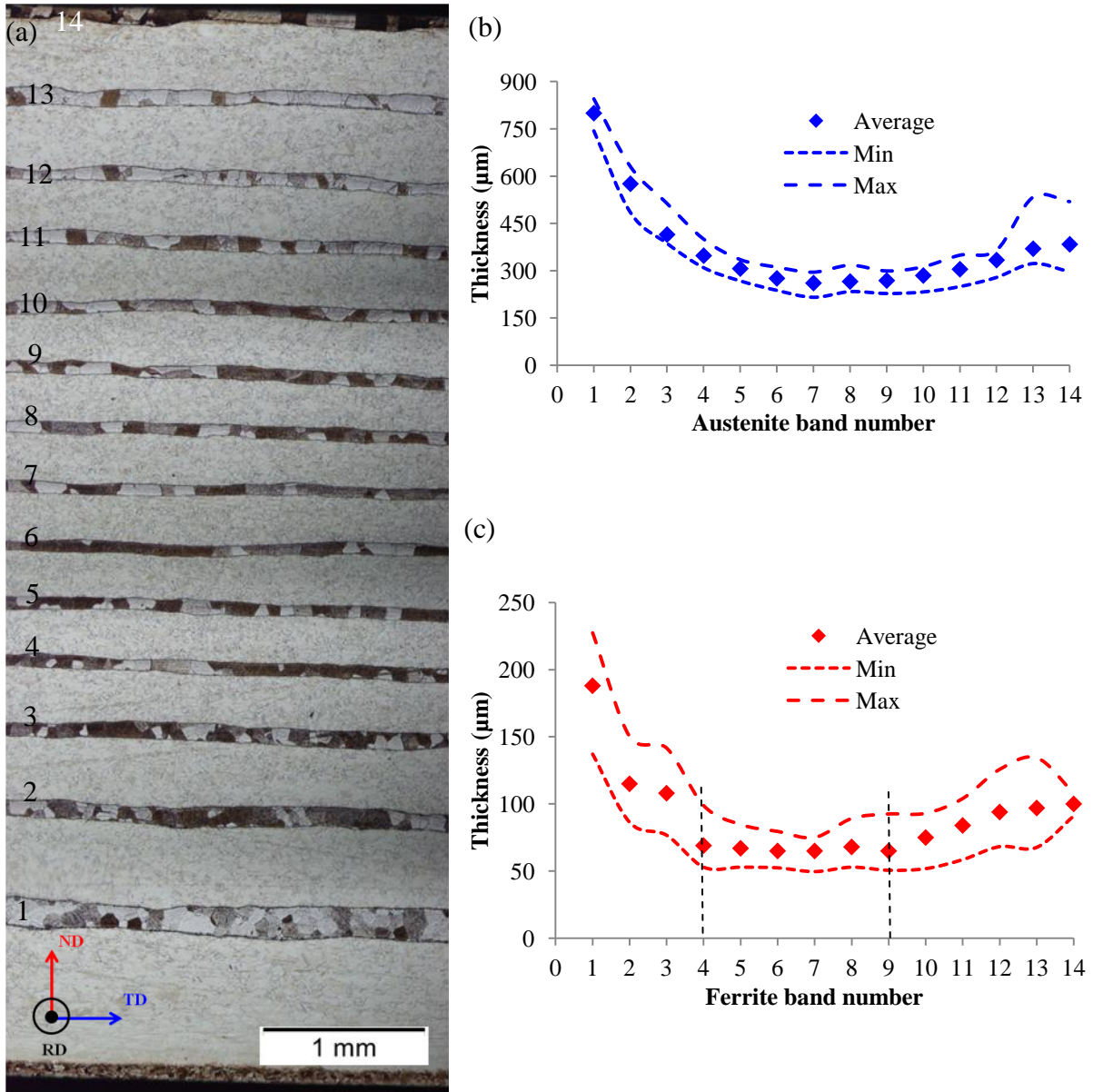


Figure III. 23: (a) Cross section of the stack in the HR1 state followed by a recrystallisation heat treatment (electro-nitric etching). Average, minimum and maximum thicknesses of (b) austenite and (c) ferrite bands with respect to their position in the stack.

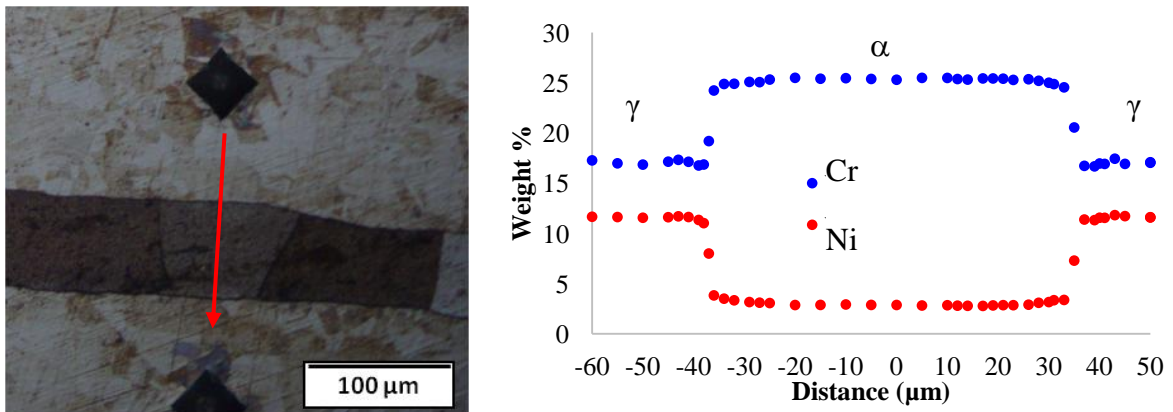


Figure III. 24: Composition profiles of chromium and nickel measured by EPMA across ferrite band 7 in the multilayered microstructure in the HR1 state (Electronitric etching).

### II.2.b. Microstructure after the first cold rolling (CR1)

The microstructure after CR1 and a recrystallisation heat treatment of 1min at 1050°C is shown in Figure III. 25.a. As in the HR1 state, ferrite thicknesses are not homogeneous throughout the stack (Figure III. 25.b, c). Central bands (n° 4 to 9) exhibit roughly the same thickness of 42µm, except bands 6 and 7 whose thickness is 32µm. Composition profiles in ferrite band 7 are shown in Figure III. 26. As in the previous stage, Cr and Ni gradients are well established in ferrite.

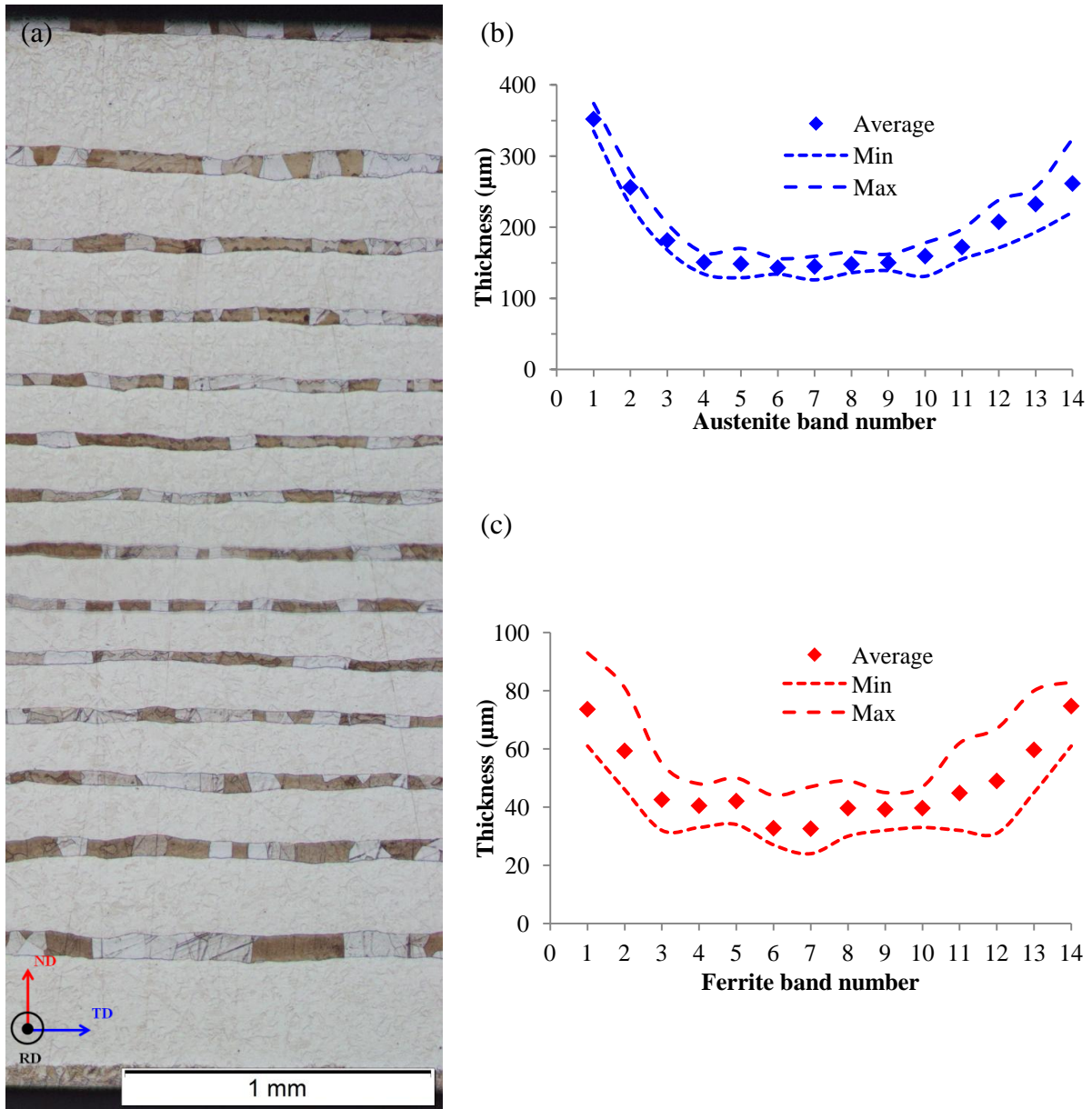


Figure III. 25: (a) Cross section of the stack in the CR1 state after recrystallisation heat treatment (Electro-nitric etching). Average, minimum and maximum thicknesses of (b) austenite and (c) ferrite bands with respect to their position in the stack.

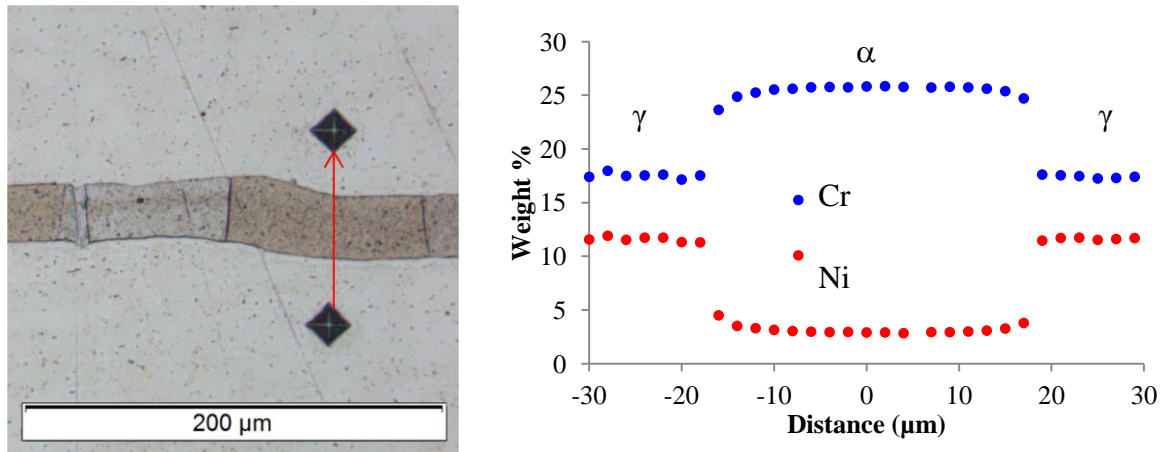


Figure III. 26: Composition profiles of chromium and nickel measured by EPMA across ferrite band 7 in the multilayered microstructure in the CR1 state (Electronitric etching).

### II.2.c. Microstructure after the second hot rolling (HR2)

Figure III. 27.a shows a cross section of the microstructure after HR2 followed by 3min recrystallisation at 1050°C. As stated before, this microstructure is made of 5 plates of the CR1 state. The bonding junctions between the these plates are either between two successive austenite bands or successive ferrite bands.

As a result of the successive rollings, ferrite bands are more undulated in comparison with the HR1 and CR1 states. Furthermore, their thicknesses are not the same from one plate to another.

For the characterization, it was chosen to focus on the microstructure of the central CR1 plate in the stack (Plate 3). Figure III. 27.b and c shows the thicknesses of ferrite and austenite bands with respect to their position in this plate. Central bands possess approximately the same thickness of 8μm for ferrite and 34μm for austenite. On the other hand, the local variation in the thickness of a given ferrite band is higher than in the previous states, as ratio between the maximum ( $\alpha_{max}$ ) and the minimum ( $\alpha_{min}$ ) thicknesses reaches a value of 4, against 2 in the previous states.

The composition profiles of Cr and Ni across ferrite bands 6 to 9 are shown in Figure III. 28. Solute profiles in ferrite are flat except at the interface. But given the additional thickness reduction, gradients are very spatially reduced and not accurately evidenced due to the low spatial resolution of EPMA.

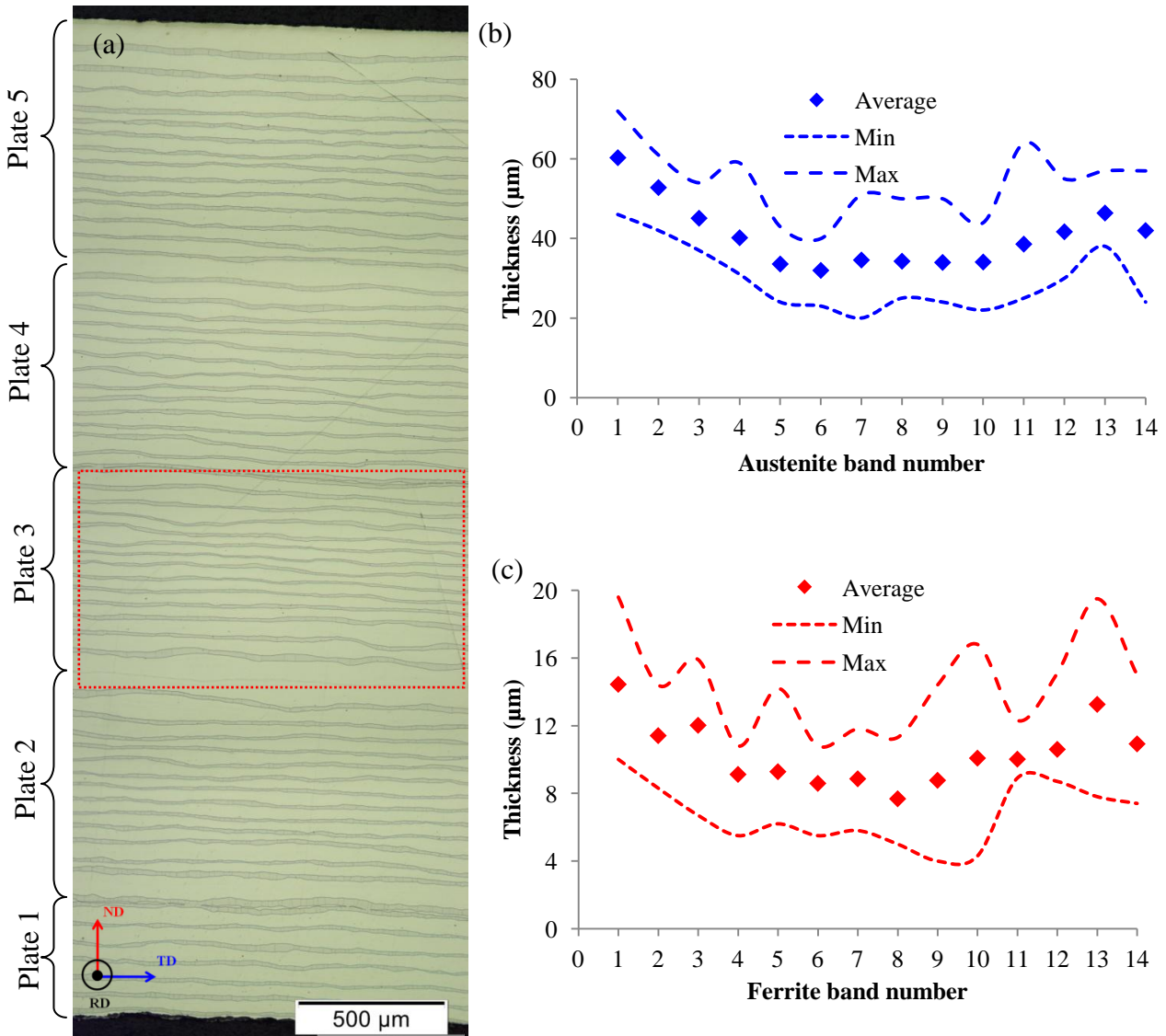


Figure III. 27: (a) Cross section of the stack in the HR2 state after recrystallisation heat treatment (Electronitric etching). The dashed rectangle refers to the plate at which characterizations were performed. Average, minimum and maximum thicknesses of (b) austenite and (c) ferrite bands with respect to their position in the central plate of the stack.

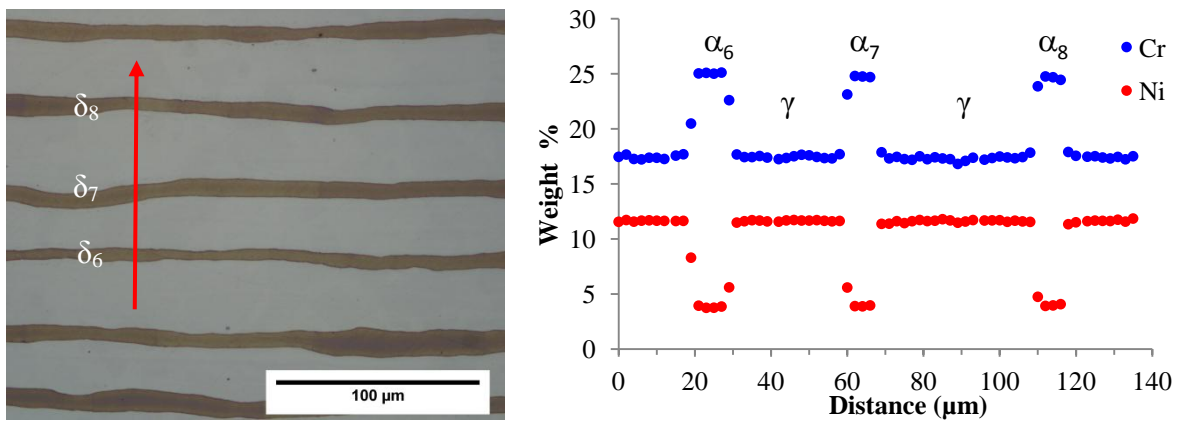


Figure III. 28: composition profiles of chromium and nickel measured by EPMA across ferrite bands 6 to 8 in the multilayered microstructure in the HR2 state (NaOH etching).

### II.2.d. Microstructure after the second cold rolling (CR2)

An overview of the stack in the as-received CR2 state is given in Figure III. 29.a. Characterizations are also carried in the central plate (Plate 3). Ferrite and austenite thicknesses as a function of their position in this plate are shown in Figure III. 29.b and c. Central bands possess a thickness of 4 $\mu\text{m}$  for ferrite and 14 $\mu\text{m}$  for austenite. Characteristic Cr and Ni profiles are plotted in Figure III. 30. In ferrite bands, composition is not accurately determined owing to their fine thickness. The effect of this uncertainty on the subsequent numerical calculations will be studied in Chapter V.

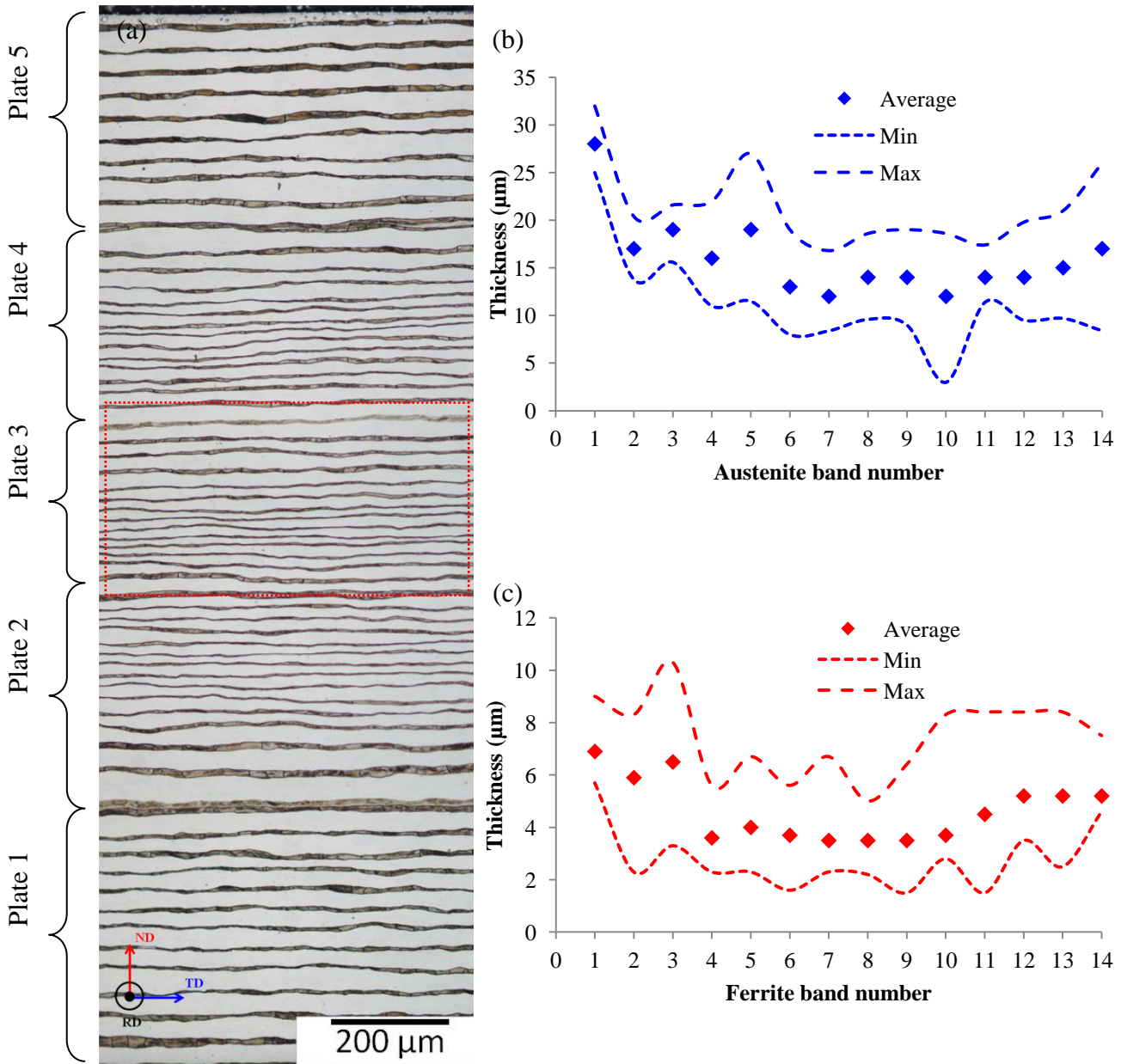


Figure III. 29 (a) Cross section of the stack in the CR2 state (Electronitric etching). The dashed rectangle in the middle refers to the plate at which characterizations were performed. Average, minimum and maximum thicknesses of (b) austenite and (c) ferrite bands with respect to their position in the central stack.

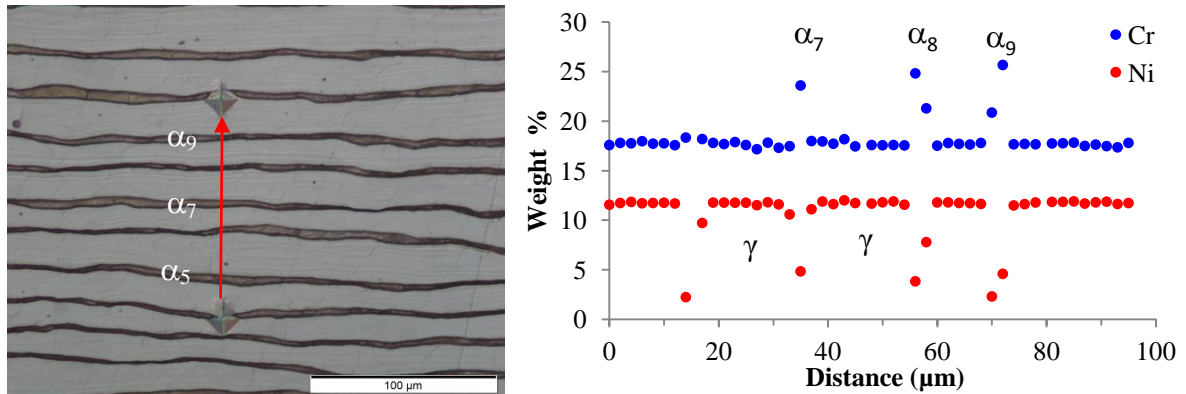


Figure III. 30: Concentration profiles of Cr and Ni in ferrite bands 5 to 9 in the multilayered microstructure at the CR2 state (Electronitric etching).

### II.2.e. Summary

Multilayered microstructures with decreasing ferrite and austenite thicknesses have been obtained by successive reduction steps of the initial stack fabricated by HIP. Ferrite and austenite bands 4 to 9 have been found to possess approximately the same thickness in each state, except in the CR1 one, where two band thicknesses were evidenced: 32 and 42 $\mu\text{m}$ . We will show in chapter V that this difference in thickness will have a determinant effect on the prediction of the kinetics of ferrite dissolution in the CR1 state. In the CR2 state, a non negligible variability of Cr and Ni contents in ferrite was observed. Retained values for future calculations are chosen in order to be consistent with those of the HR2 state. The consequences of this choice on the prediction of ferrite dissolution will later be discussed.

Dissolution study is carried after each reduction step. Only ferrite bands 6 to 9 are considered for the establishment of the dissolution kinetics. Table III. 7 lists their minimum, average and maximum thicknesses as well as their initial Cr and Ni compositions after each reduction step. It should be noted that the specified compositions are average values of EPMA profiles in both phases.

Table III. 7: Chromium and nickel compositions and average, minimum and maximum thicknesses of ferrite and austenite bands 6 to 9 at each reduction step.

	HR1	CR1	HR2	CR2
Thickness $\alpha$ ( $\mu\text{m}$ )	66 <sub>50</sub> <sup>90</sup>	32/42 <sub>24</sub> <sup>48</sup>	8 <sub>4</sub> <sup>14</sup>	4 <sub>2</sub> <sup>7</sup>
Composition $\alpha$ (wt. %)	25.3Cr - 2.9Ni	25.3Cr - 2.9Ni	25.1Cr - 3.8Ni	25.6Cr - 3.7Ni
Thickness $\gamma$ ( $\mu\text{m}$ )	268 <sub>215</sub> <sup>310</sup>	146 <sub>124</sub> <sup>175</sup>	34 <sub>20</sub> <sup>50</sup>	14 <sub>8</sub> <sup>19</sup>
Composition $\gamma$ (wt. %)	17.4Cr - 11.6Ni	17.4Cr - 11.6Ni	17.4Cr - 11.6Ni	17.6Cr - 11.7Ni

### II.3. Dissolution of ferrite bands at 1240°C: results and discussion

The dissolution of ferrite in the multilayered microstructures is performed at 1240°C, temperature at which the dissolution of vermicular ferrite was shown to be the fastest (see §I.3.d. Overall transformation kinetics). Table III. 8 lists the holding times considered for

HR1, CR1 and HR2 states. For the CR2 state an inverse approach is followed for the establishment of the kinetics of ferrite dissolution: using the characterization of the as-received CR2 state (Table III. 7), dissolution is first predicted by the numerical model and experiments are then carried out on the basis of the predictions (Chapter V).

It should be noted that prior to each annealing, samples were submitted to recrystallisation heat treatment at 1000-1050°C in order to remove any unwanted effects induced by rollings (enhanced diffusion by dislocations, crystallographic texture, etc.).

**Table III. 8: Heat treatments carried at 1240°C for stacks in the HR1, CR1 and HR2states.**

Time	5 min	10 min	15 min	30 min	1h	2h	3h	4h	24h	48h	72h	96h	164h
HR1					✓			✓	✓		✓	✓	✓
CR1		✓		✓	✓			✓	✓	✓	✓	✓	
HR2	✓		✓	✓	✓	✓	✓		✓				

### II.3.a. In the microstructure after the first hot rolling (HR1)

The evolution of the thickness of ferrite bands 6 to 9 is shown in Figure III. 31. As stated in Chapter II, the amount of ferrite was accounted for by measuring the average thickness  $\ell$  of the equivalent rectangle. At the beginning of the transformation the thickness of ferrite bands transiently increases by an amount that varies between 30% for ferrite band 6 and 100% for ferrite band 9, despite their equal initial average thicknesses (66 $\mu$ m). Then (after 4hrs), the dissolution of ferrite starts until complete disappearance after 164hrs.

Micrographs of ferrite bands at various holding times are shown in Figure III. 32. The  $\alpha/\gamma$  interface maintains its initial regularity in the early stage of the transformation (1hr). After 4hrs annealing, triple grain boundaries evolve towards an equilibrium shape driven by the balance of tension forces, as evidenced on the micrograph of Figure III. 33. Moreover, at the  $\alpha/\alpha$  grain boundaries the dissolution of ferrite is more pronounced as diffusion of solutes along the grain boundaries is faster than in the bulk (the activation energy of Cr grain boundary diffusion is 132kJ against 290kJ for volume diffusion according to [38]). The breakup of the ferrite layer along grain boundaries occurs after 72hrs annealing. The dissolution of ferrite goes on henceforth in separate ferritic islands. The grey zone indicated in Figure III. 31 refers to annealing times where ferrite dissolves as isolated grains.

At the interface, martensite can be observed. Its spatial extension is very limited at the beginning of the transformation but increases with time, as the Cr enrichment and Ni depletion of austenite spatially extend (Solute profiles across the interface are shown in Appendix B). This martensite is strain-induced owing to sample surface preparation.

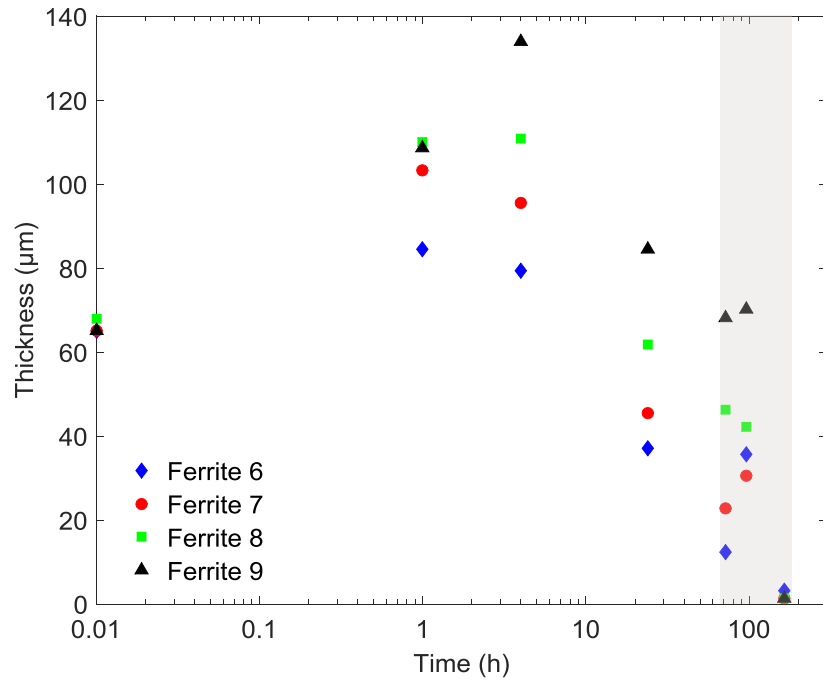


Figure III. 31: Average thickness of ferrite bands 6 to 9 with annealing time at 1240°C in the multilayered microstructure in the HR1 state. The grey zone corresponds to annealing times where ferrite layers are broken into several isolated grains.

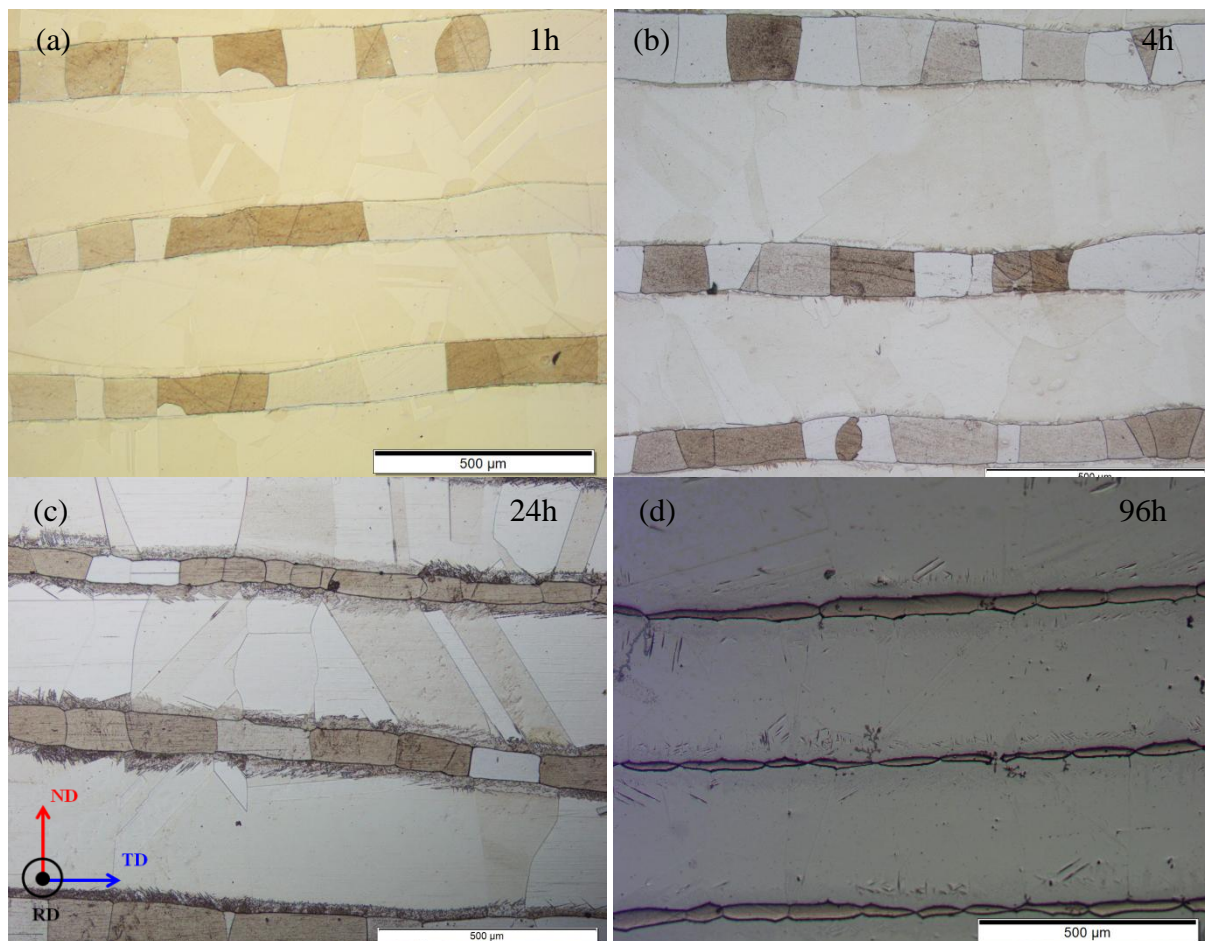


Figure III. 32: Multilayered microstructure in the HR1 state after (a) 1hr, (b) 4hrs, (c) 24hrs and (d) 96hrs holding at 1240°C (Electronitric etching).

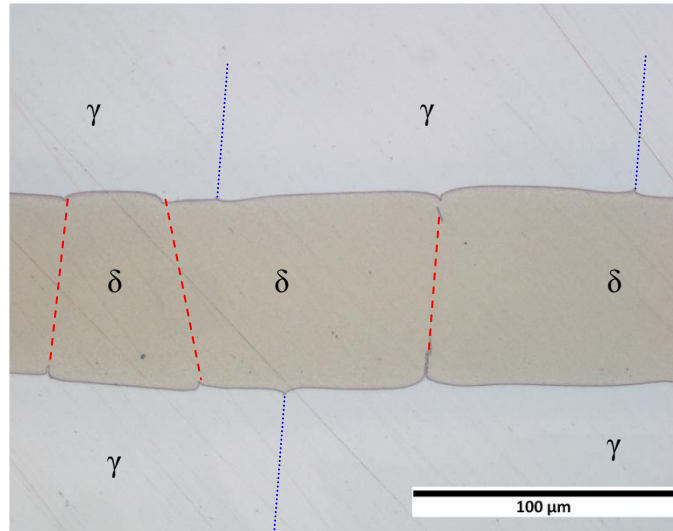


Figure III. 33: Triple junctions between ferrite and austenite grains after 4hrs holding at 1240°C and enhanced interface advancement towards ferrite at the ferritic grain boundaries. Ferrite grain boundaries are indicated with dashed lines and austenite grains boundaries are indicated with dotted lines (NaOH etching).

### II.3.b. In the microstructure after the first cold rolling (CR1)

The kinetics of ferrite dissolution in the microstructure after the first cold rolling is shown in Figure III. 34. The early ferrite growth occurs during the first 30min and dissolution ends after 96hrs heat treatment. It can be noticed that, in contrast with the HR1 state, although ferrite bands 8 and 9 are initially 10μm thicker than bands 6 and 7, the scattering between dissolution kinetics of all bands is very limited.

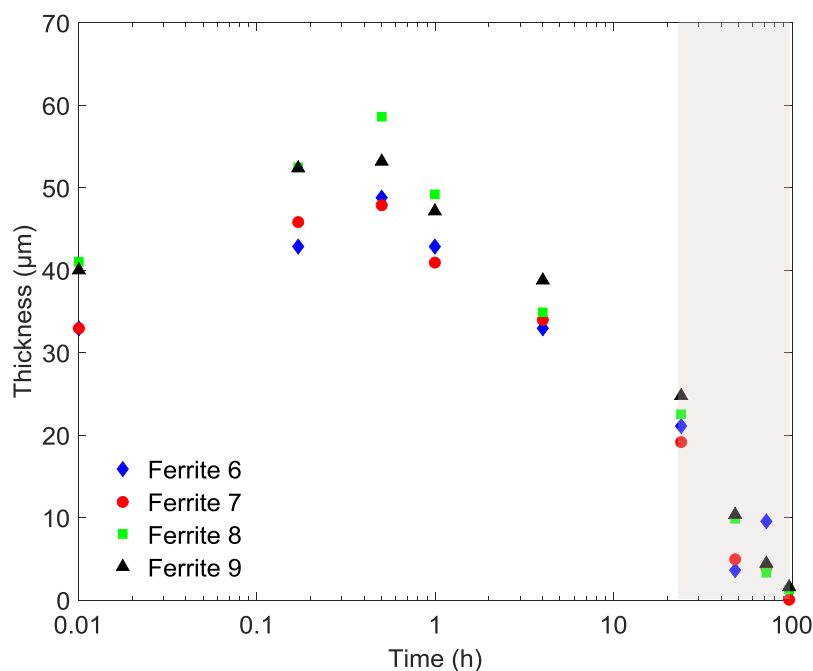


Figure III. 34: Average thickness of ferrite bands 6 to 9 with annealing time at 1240°C in the multilayered microstructure in the CR1 state. The grey zone corresponds to annealing times where the ferrite layer is broken into several particles.

The evolution of the microstructure of the stack during dissolution is shown in Figure III. 35. As in the HR1 case, the  $\alpha/\gamma$  boundary maintains its initial regularity in the early stages of the transformation. After 24hrs annealing, the first breakup of ferrite bands is observed at the ferritic grain boundaries. then ferrite continues to dissolves as separated particles. Generally, particles keep an elongated shape with sharp tips at the location of former grain boundaries and faceted interfaces in contact with the neighboring austenite grains. No spheroidization of ferrite particles has been observed, as this shape is maintained until their disappearance (see Figure III. 36 for example). At ferrite-free location, austenite grains continue their growth so that ferrite particles become, at advanced annealing times, surrounded by at most three austenite grains.

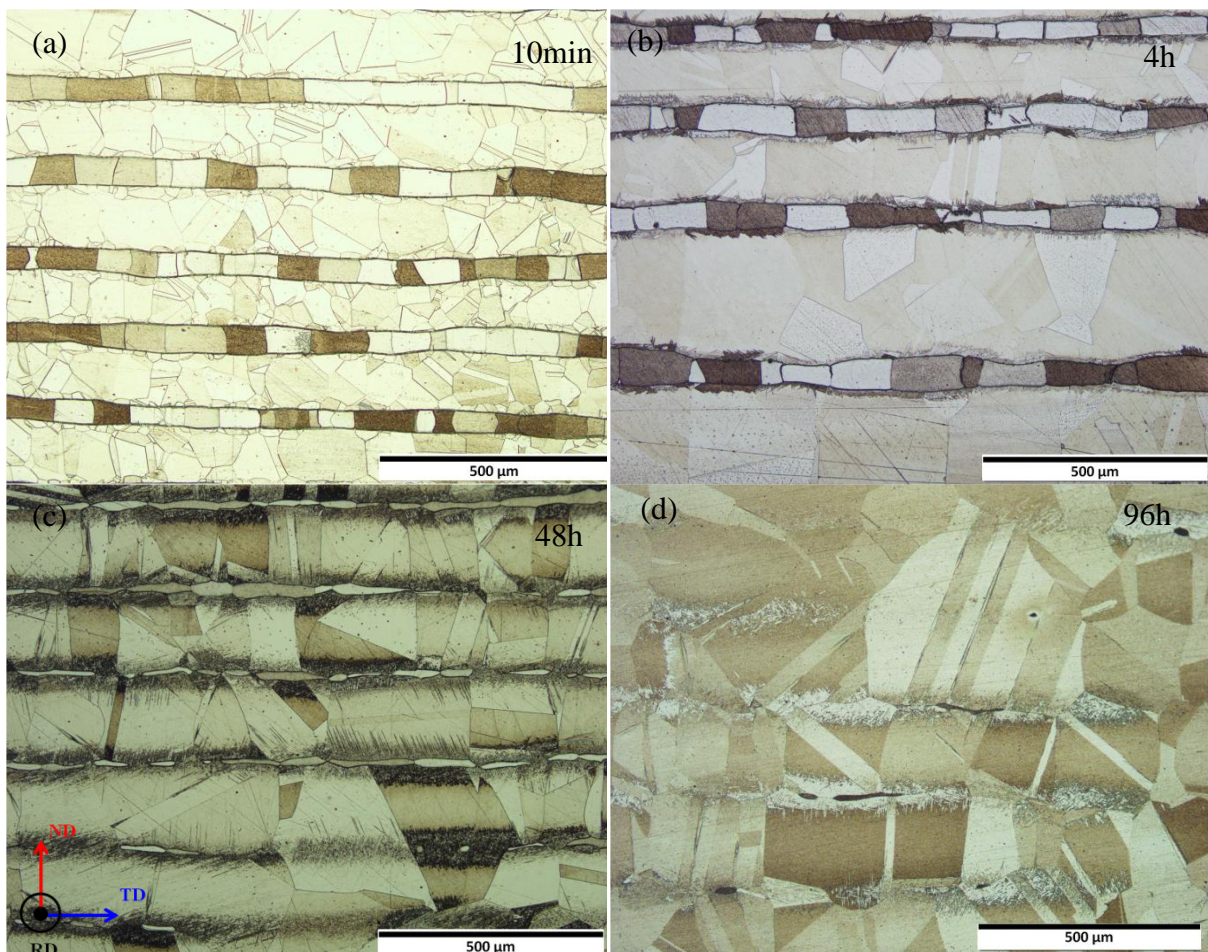
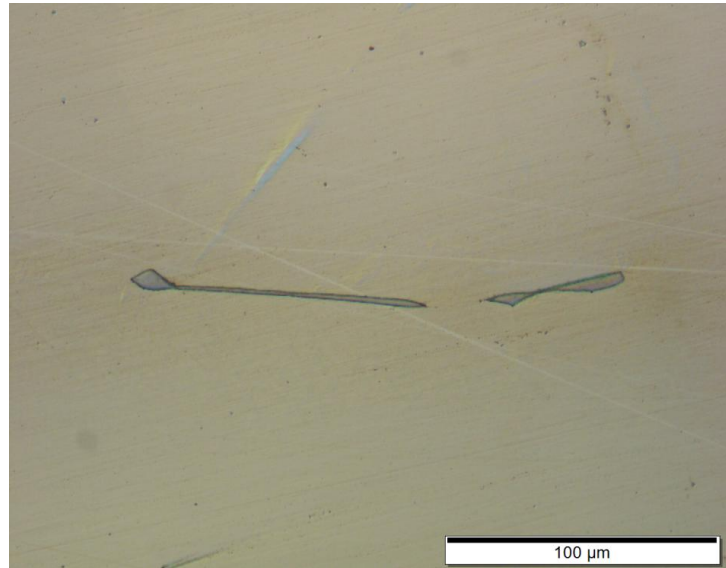


Figure III. 35: Multilayered microstructure in the CR1 state after (a) 10min, (b) 4hrs, (c) 48hrs and (d) 96hrs annealing at 1240°C (Electronitric etching).



**Figure III. 36:** Remaining ferrite grain in the multilayered microstructure in the CR1 state after 72hrs annealing at 1240°C. The ferrite particle keeps an elongated shape.

Figure III. 37 shows the concentration profiles across the ferrite particles at several annealing times. Composition profiles of Cr and Ni are already flat in ferrite except at the interface where slight Cr-enrichment and Ni-depletion are observed. Explanation of this behavior will be given in Chapter V, §II.3.c. *Interface compositions upon quenching*. In austenite, composition gradients are steep at the beginning and become gradually flat as transformation proceeds. This denotes that the  $\alpha \rightarrow \gamma$  transformation is diffusion-controlled.

However, this characteristic is only observed in the normal direction. When measured along the transversal direction between two adjacent ferrite particles (Figure III. 38), composition profiles in austenite are almost flat, though the transformation did not end yet. This observation, together with the acute morphology of ferrite tips, may suggest that the movement of the interface at the tips of ferrite particles is not diffusion-driven but rather interface-controlled. The acute shape of the tip is maintained in equilibrium as a result of the overall surface tensions exerted by the ferrite grain and the surrounding austenite grains.

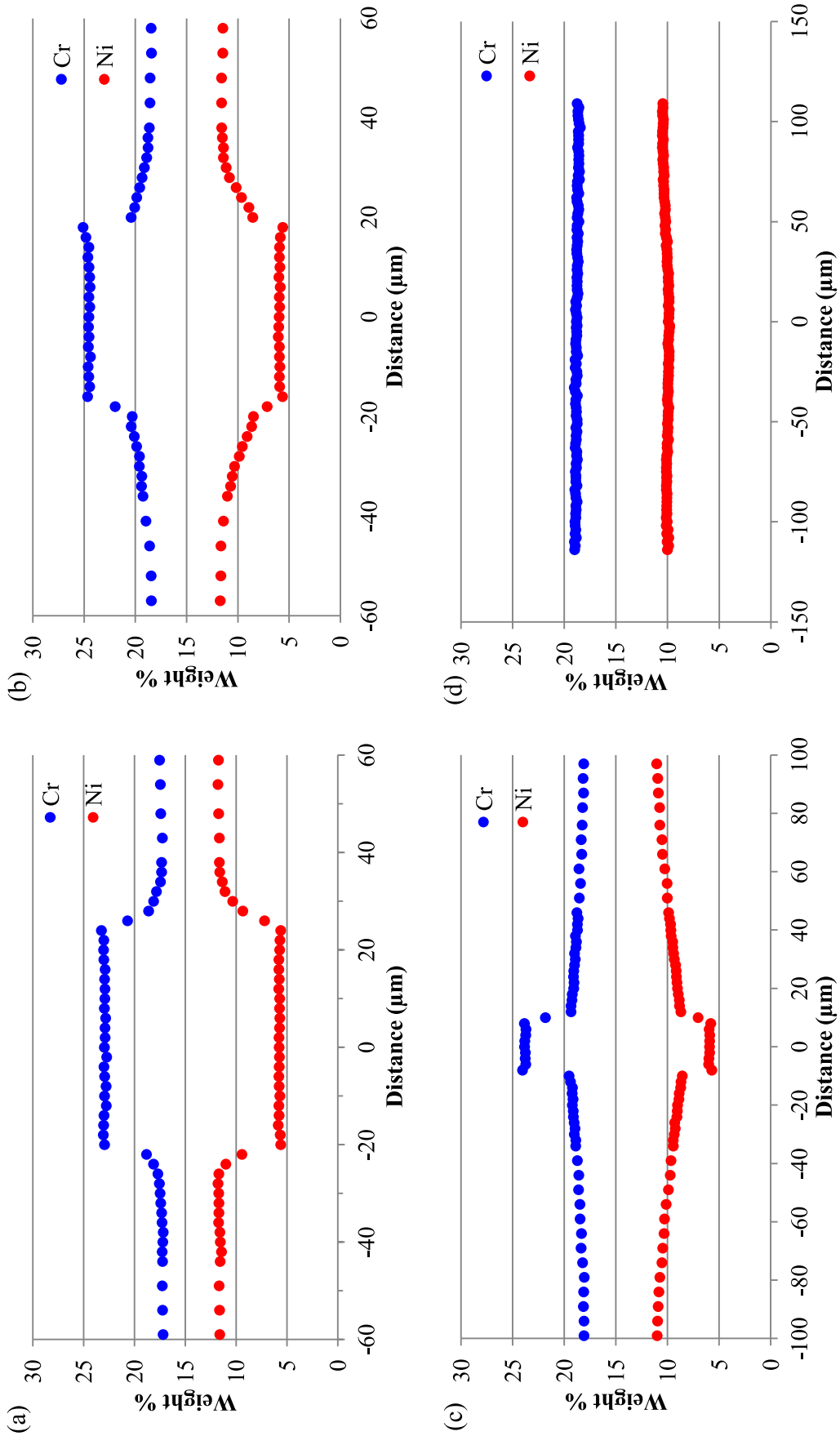


Figure III. 37: Chromium and nickel profiles in the multilayered microstructure in the CR1 state at 1240°C after (a) 10min, (b) 1hr, (c) 72hrs and (d) 96hrs.

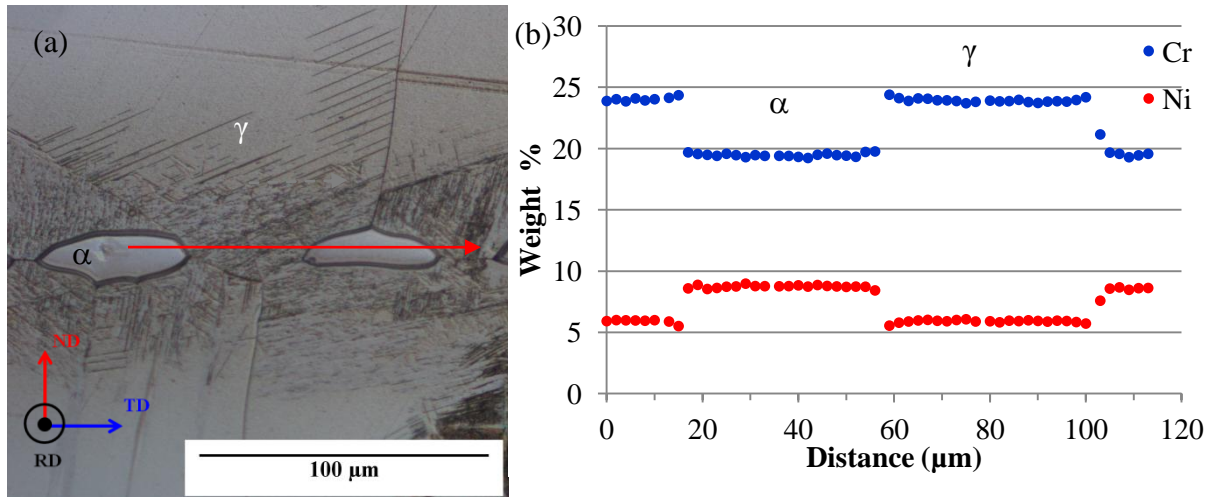


Figure III. 38: Chromium and nickel composition profiles along the transversal direction between two ferrite particles after 72hrs annealing at 1240°C in the CR1 state.

### II.3.c. In the microstructure after the second hot rolling (HR2)

Figure III. 39 shows the dissolution kinetics of ferrite bands 6 to 9 at 1240°C. The early growth of ferrite is not observed, except for ferrite band 8. The transformation ends after 3hrs approximately. Dissolution of all bands qualitatively follows the same trend but quantitative results are rather scattered. Such a dispersion is to be linked to the high local variability of the initial ferrite thickness.

The evolution of the microstructure during the dissolution is shown in Figure III. 40. Ferrite bands breakup after 15min annealing and resultant particles maintain an elongated shape parallel to the transverse direction.

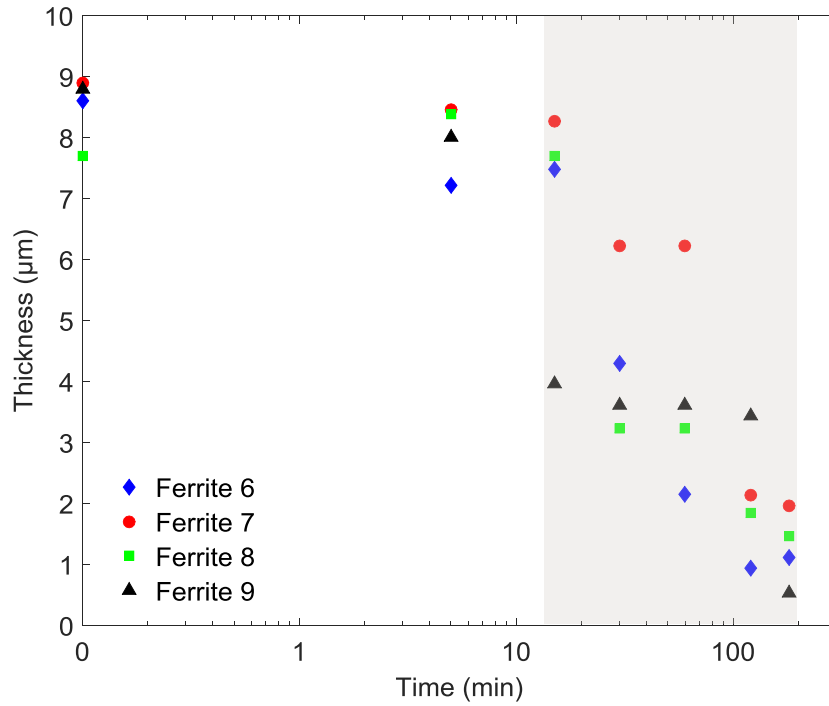


Figure III. 39: Evolution of the thickness of ferrite bands 6 to 9 with annealing time in the multilayered microstructure in the CR2 state.

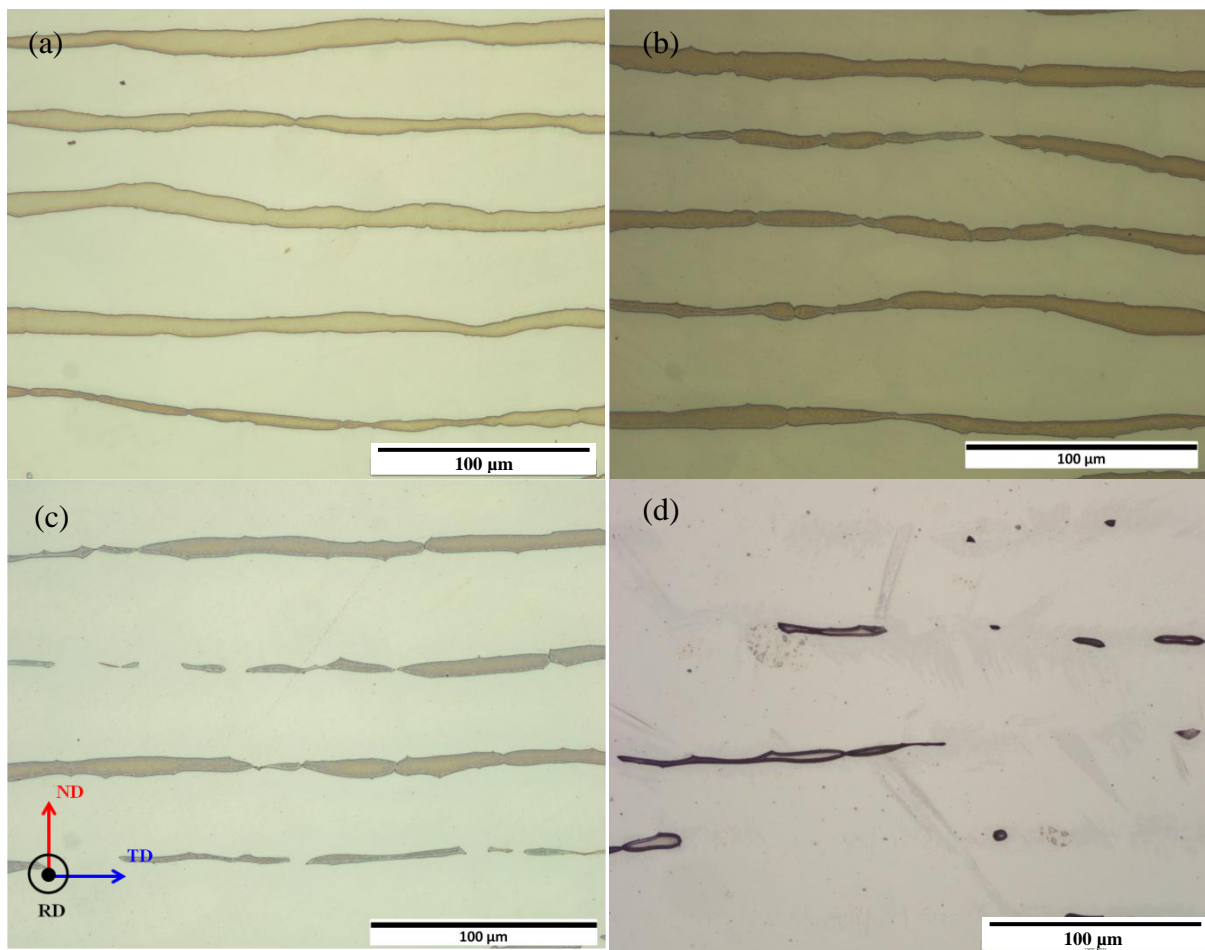


Figure III. 40: Multilayered microstructure in the HR2 state after (a) 5 min, (b) 15min, (c) 1hr and (d) 3hrs annealing at 1240°C (NaOH etching).

### II.3.d. EBSD mappings

From the micrographs shown in the previous sections, it can be noticed that the dissolution of ferrite grains does not occur at the same rate, resulting in a fast disappearance of certain grains while others are still present. Further, as stated in §II.3.b. *Microstructure after the first cold rolling*, ferrite grains do not spheroidise, but maintain an elongated shape and their tips remain acute during the transformation. The mobility of the interface was suspected not to be solely diffusion-controlled but also interface-controlled at certain locations. Among the factors affecting the mobility of the interface, the crystallographic structure of the interface is known to possibly impact the transfer of atoms across the interface.

EBSD mappings were performed in order to know whether specific orientation relationships between ferrite grains and neighboring austenite could explain the variety of interface morphologies (Figure III. 41 and 42). From the orientation relationships studied between individual ferrite grains and surrounding austenite (an example is given in Figure III. 43), it appeared that no specific orientation relationship (Kurdjumov-Sachs or Nishiyama-Wasserman type) was observed. Therefore, the assumption of the interface mobility being impacted by the crystallographic orientation between ferrite and austenite grains is not validated.

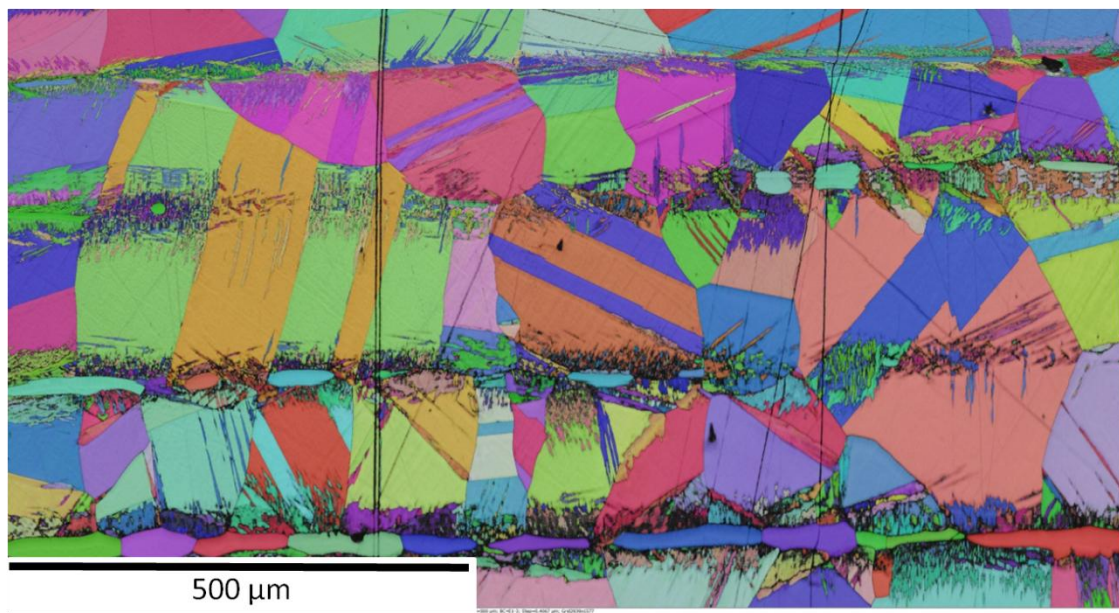


Figure III. 41: EBSD Mapping of ferrite and austenite bands in the CR1 state after 48h annealing at 1240°C.

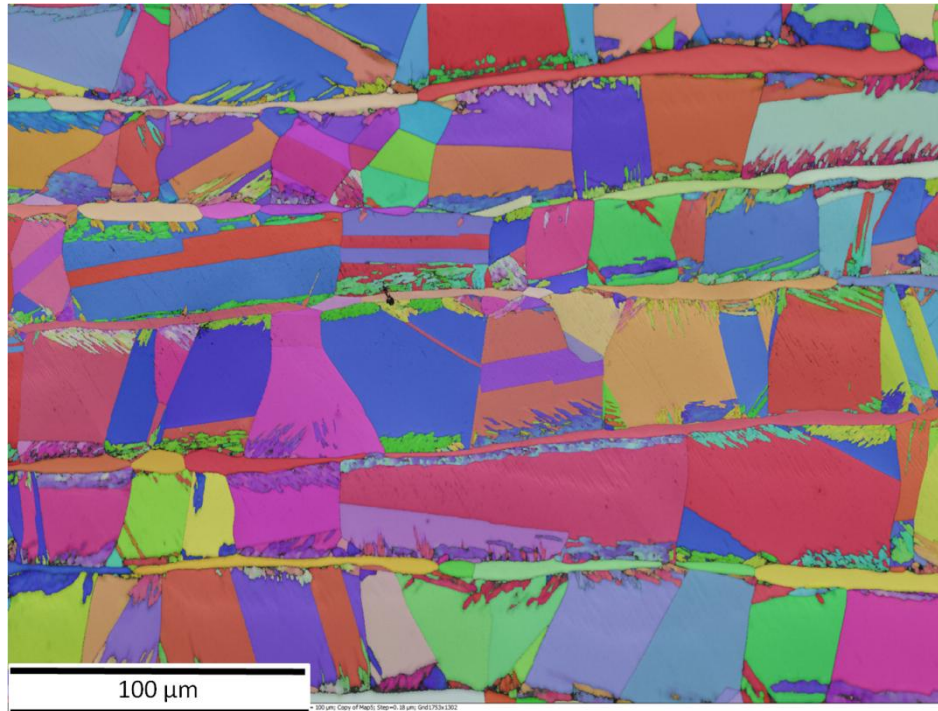


Figure III. 42: EBSD Mapping of ferrite and austenite bands in the HR2 state after 30min annealing at 1240°C.

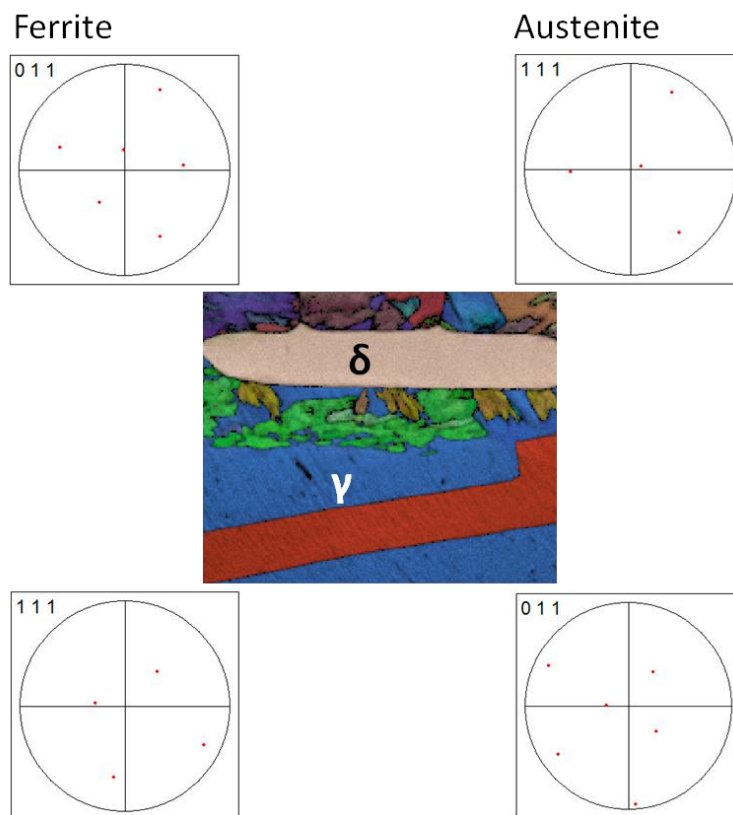


Figure III. 43: Example of a  $\langle 011 \rangle$  and  $\langle 111 \rangle$  pole figures from a grain of ferrite and one neighboring austenite grain.

### II.3.e. Estimation of interdiffusion coefficients at 1240°C

The rather planar morphology of ferrite and austenite bands provides suitable conditions for the estimation of the interdiffusion coefficients  $D_{CrCr}^Y$  and  $D_{NiNi}^Y$  from the composition profiles of Cr and Ni measured by EPMA at different holding times. The measurement methodology is based on the calculation of the diffusion length  $\ell_k$  of solute  $k$  which is known to be related to the interdiffusion coefficient  $D_{kk}^Y$  by the following equation:

$$\ell_k \approx 2\sqrt{D_{kk}^Y t} \quad (III.1)$$

where  $t$  is the holding time. Figure III. 44 sketches this measurement procedure. Eq.(III.1) holds only in semi-infinite medium. Hence estimations are only carried at annealing times where austenite bands can be considered as semi-infinite with regard to the diffusion extent of Cr and Ni. Composition profiles used for this purpose can be found in §II.2.b. In the microstructure after the first cold rolling and in Appendix B. Ten measurements of  $D_{CrCr}^Y$  and  $D_{NiNi}^Y$  are carried. Average values are  $2.7 \pm 1 \times 10^{-14}$  and  $1.1 \pm 0.5 \times 10^{-14}$  m<sup>2</sup>/s respectively (at 1240°C). Despite the lack of precision inherent to this calculation method, these values are consistent with those extracted from literature [61], [73]. They will be used in Chapter V, §III.4. Discussion in order to discuss the simulation results.

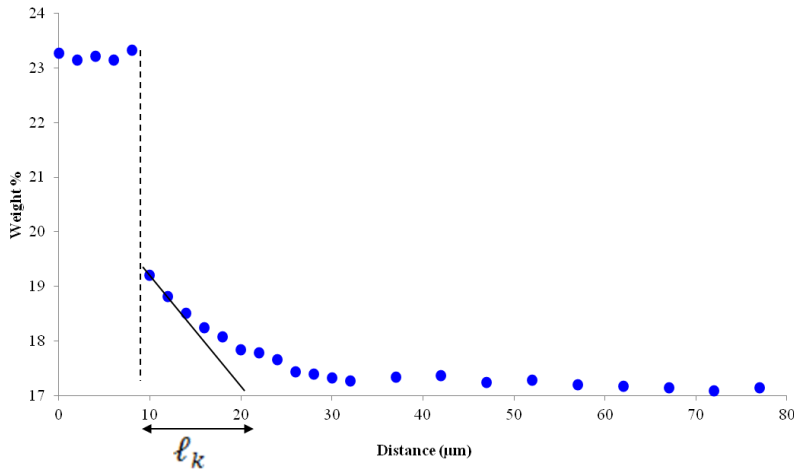


Figure III. 44: Sketch of the estimation methodology of the interdiffusion coefficients in austenite from an EPMA composition profile : a tangent line to the composition profile at the interface is first drawn and then its intersection with the distance axis yields the diffusion length  $\ell_k$ .

Table III. 9: Chromium and nickel interdiffusion coefficients in austenite at 1240°C: comparison between values experimentally determined in this study and data extracted from literature.

Cr (wt. %)	Ni (wt. %)	$D_{CrCr}$ (m <sup>2</sup> /s)	$D_{NiNi}$ (m <sup>2</sup> /s)	Source
--	14.9	--	$5.9 \times 10^{-15}$	Smithells [73]
--	9.2	--	$1.2 \times 10^{-14}$	
20	10	$4.3 \times 10^{-14}$	$1.3 \times 10^{-14}$	Vitek [61]
17.4	11.6	$2.7 \times 10^{-14}$	$1.1 \times 10^{-14}$	Experiments

### III. Summary and conclusion

In literature, the dissolution of ferrite in the Fe-Cr-Ni system or equivalent alloys was only studied at temperatures up to 1200°C. With this respect, the dissolution of ferrite in the multilayered microstructures at 1240°C and that in the cast alloy from 1240 to 1300°C provided original and complementary experimental results which can be used as reliable data for the scientific community.

The dissolution kinetics of  $\delta$ -ferrite was established in two initial microstructures of the Fe-Cr-Ni system. In the ternary Fe-17.3%Cr-9.4%Ni ingot-cast alloy, three morphologies of ferrite have been evidenced and their formation mechanisms briefly discussed. Ferrite dissolution in austenite was then studied at different temperatures ranging from 1140°C to 1346°C for each morphology. In the case of vermicular ferrite, experiments revealed that dissolution kinetics exhibits three stages: a transient growth of ferrite, followed by a high then a low rate dissolution regimes. Explanations of transient phase growth have been reported in literature [36] in the case of ferrite dissolution in  $\gamma/\alpha/\gamma$  diffusion couples. With the aid of the numerical model, it will be shown in Chapter V that the suggested growth mechanism is not suited for the case of vermicular ferrite. Instead, another mechanism will be outlined. Regarding the change in the dissolution regimes, analyses of the morphological evolution of ferrite particles using the circularity shape descriptor allowed to correlate the high rate dissolution regime to the dissolution of dendritic arms (elongated morphology) and the low rate dissolution regime to the dissolution of the coarse particles corresponding the intersections between dendritic arms (spherical morphology).

The multilayered microstructure was designed in order to study the  $\alpha \rightarrow \gamma$  transformation in a more simplified situation where  $\alpha/\gamma$  interface are planar. Using the Hot Isostatic Pressing technique, it was possible to elaborate such microstructure by bonding ferrite and austenite sheets of the Fe-Cr-Ni system. Applying successive hot and cold rollings, four initial states of the multilayered microstructure were obtained, with decreasing thicknesses of ferrite and austenite bands. Dissolution heat treatments were carried out at 1240°C where ferrite was expected to dissolve after sufficiently long annealing time. As in the case of the ternary alloy, before dissolution starts, ferrite thickness increases with annealing time at the early stage of the transformation. However, the mechanisms underlying the growth in both cases are different, as it will be shown in Chapter V. Time-evolution of Cr and Ni composition fields normal to the initial  $\alpha/\gamma$  interfaces shows that the interface movement is diffusion-controlled, whereas at some specific locations (former  $\alpha/\alpha$  boundaries) the mobility of the interface seems to be interface-controlled.

Although designed to simplify the experimental study of ferrite's dissolution, the multilayered microstructure showed a rather complex behavior when heat treated. The interface rapidly ceases to be planar, mainly at  $\alpha/\alpha$  grain boundaries where the interface movement is the most enhanced. The subsequent breakup of ferrite bands into isolated particles arises the problem of the relevance of the equivalent rectangle thickness as a quantifier of the amount of ferrite. This procedure implies that, at each annealing time, ferrite

is virtually considered as single and continuous band. Experimentally, this rapidly ceases to be the case after ferrite breakup.

In Chapter V the experimental results already collected will be analyzed using the numerical model developed in Chapter IV.

# Chapter IV

## Modeling the ferrite to austenite transformation in the Fe-Cr-Ni system

In this chapter, a numerical model of ferrite to austenite phase transformation in the Fe-Cr-Ni system is developed. In the first section, a general presentation of the problem is given, followed by a description of the thermodynamic and kinetic parameters. Under some hypothesis, governing equations are afterwards derived. A large part of this chapter is then dedicated to the numerical techniques and resolution algorithms used for modeling, after which the model will be validated on experimental results from literature.

### I. Problem description

The ferrite to austenite transformation in the ternary Fe-Cr-Ni system is modeled using a one dimensional moving-boundary model. The considered system comprises a ferrite region ( $\delta$ ) with length  $z$  adjacent to an austenite region ( $\gamma$ ) and separated from it by a sharp interface (Figure IV. 1). The overall length of the calculation cell is  $L$ . The size of the calculation domain is linked to the characteristic diffusion length which depends on the nature of the microstructure in which diffusion will be modeled. Since the interface is allowed to move, the variable  $z$  changes with time whereas  $L$  remains constant. The diffusion of Cr and Ni is treated in each region separately and both regions are coupled by appropriate conditions at the moving  $\delta/\gamma$  interface. The calculation cell has either a planar, a cylindrical or a spherical geometry. Given the high symmetry of each geometry, diffusion depends only on one coordinate,  $x$ . Calculations are performed using the finite-difference technique.

In diffusion problems, the amount of each solute is usually defined by its concentration  $c^\varphi$ , measured in mole per unit volume, which depends on both space ( $x$ ) and time ( $t$ ):  $c^\varphi = c^\varphi(x, t)$ ,  $\varphi = \delta, \gamma$ . In the framework of this study it is chosen to use the molar fraction  $X^\varphi$  as an alternative quantifier of solute amounts. It is derived from concentration  $c^\varphi$  by the formula  $X^\varphi = c^\varphi V_m^\varphi$  where  $V_m^\varphi$  is the molar volume of phase  $\varphi$ .

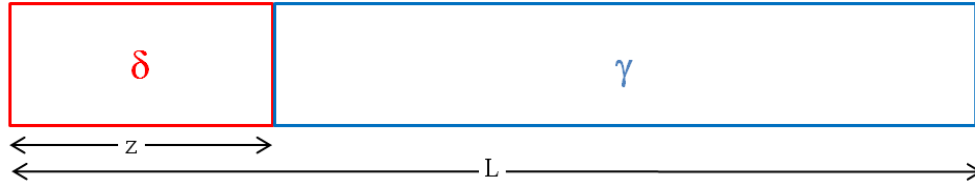


Figure IV. 1: Schematic of the calculation cell with ferrite and austenite regions separated by a moving interface located at  $z$ .

## II. Thermodynamical description and diffusion coefficients

### II.1. Coupling with phase diagram

Diffusion calculations require the use of thermodynamic data of the Fe-Cr-Ni phase diagram. Two thermodynamic databases dedicated to iron-based alloys have been used for this purpose: the Ptimec-Miettinen module in the multiphase equilibrium calculation CEQCSI software [70] developed at IRSID, and the TCFE6 database [69] with the Thermo-Calc<sup>®</sup> software [58]. The model can be coupled to these thermodynamic tools following two approaches:

- either by direct coupling to the thermodynamic software. For example, with Thermo-Calc<sup>®</sup> this can be done via the TQ interface.
- or by the tabular approach where thermodynamic data are first generated by the thermodynamical softwares and then treated as simple input data files by the model. The tabular approach has already been tested by several authors [60][75] and has been demonstrated to reduce calculation time by a factor of 10 in ternary systems and 100 in quaternary systems, in comparison to direct coupling [75].

In the framework of this project, the tabular approach was used for the thermodynamical description. Both CEQCSI and Thermo-Calc<sup>®</sup> are separately used to generate  $\delta/\gamma$  equilibrium data in the iron rich corner of the Fe-Cr-Ni phase diagram for several isothermal sections, ranging from 1000°C to 1360°C by a step of 20°C, (Appendix C). Figure IV. 2.a shows an isothermal section at 1100°C of the Fe-Cr-Ni phase diagram as calculated by Thermo-Calc<sup>®</sup> including tie lines defining interface compositions at equilibrium in the two phase  $\delta+\gamma$  region: ferrite chromium  $X_{Cr}^{\delta}$ , ferrite nickel  $X_{Ni}^{\delta}$ , austenite chromium  $X_{Cr}^{\gamma}$  and austenite nickel  $X_{Ni}^{\gamma}$ . It can be seen that the specification of Cr or Ni composition in either ferrite or austenite defines a unique tie-line and the other interface compositions can thus be determined accordingly. In the framework of this project,  $X_{Cr}^{\gamma}$  is considered as the independent variable: the phase boundaries will have to be parameterized as function of  $X_{Cr}^{\gamma}$  in order to get analytical expressions of  $X_{Cr}^{\delta}$ ,  $X_{Ni}^{\delta}$  and  $X_{Ni}^{\gamma}$  as functions of  $X_{Cr}^{\gamma}$ . For this purpose a second order polynomial fit of  $X_{Cr}^{\gamma}$  is used, as in Vitek *et al.* [61]. For example,  $X_{Cr}^{\delta}$  is expressed as:

$$X_{Cr}^{\delta} = K_1^{\delta} + K_2^{\delta} X_{Cr}^{\gamma} + K_3^{\delta} (X_{Cr}^{\gamma})^2 \quad (\text{IV.1})$$

where  $K_1^{\delta}$ ,  $K_2^{\delta}$  and  $K_3^{\delta}$  are interpolation constants. A comparison of the parameterized phase boundaries with those calculated by Thermo-Calc at 1100°C is shown in Figure IV. 2.b. The

parameterized form is in excellent agreement with the calculated boundaries. This is also verified in the temperature range 1000-1360°C (see Appendix C).

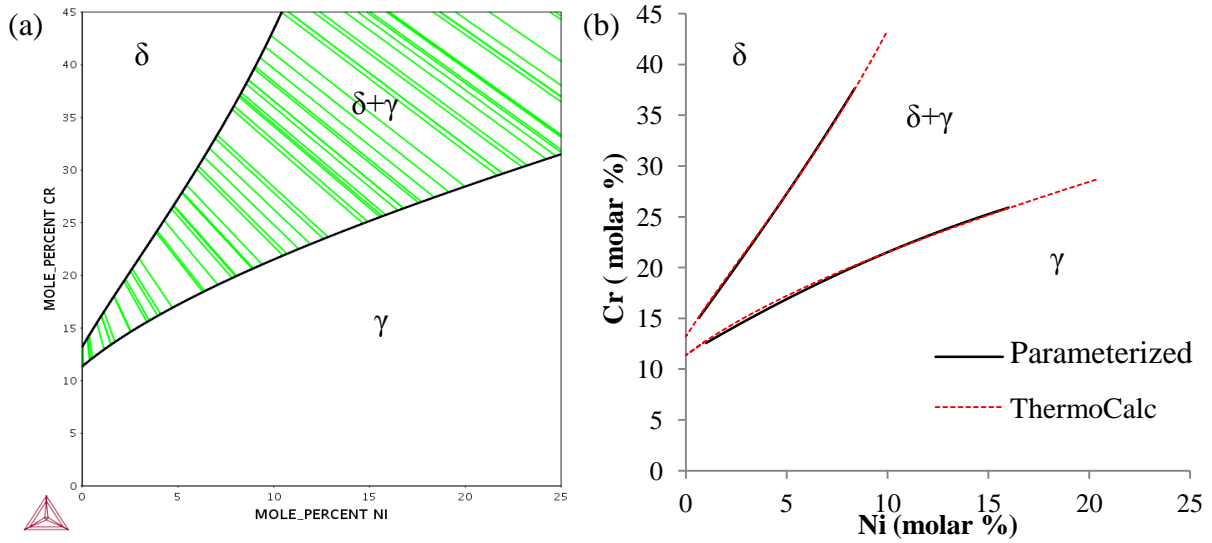


**Figure IV. 2:** (a) Isothermal section at 1100°C of the Fe-Cr-Ni phase diagram calculated by ThermoCalc® and the TCFE6 database. (b) Quadratic parameterization (solid lines) of ferrite and austenite phase boundaries compared to calculations (dashed lines).

In order to simulate non isothermal transformations, coefficients  $K_1^\delta$ ,  $K_2^\delta$  and  $K_3^\delta$  should be temperature-dependant. They are thus determined using third order polynomial interpolation of temperature [61]:

$$K_i^\varphi = a_i + b_i T + c_i T^2 + d_i T^3 \quad (\text{IV.2})$$

where T is temperature in Kelvin and  $a_i$ ,  $b_i$ ,  $c_i$  and  $d_i$  are interpolation constants. Similar expressions are derived for  $X_{Ni}^\delta$  and  $X_{Ni}^\gamma$ . Values of the constants  $a_i$ ,  $b_i$ ,  $c_i$  and  $d_i$  for each of the coefficients  $K_1^\varphi$ ,  $K_2^\varphi$  and  $K_3^\varphi$  are given in Appendix C. An example of an isothermal interpolation of the Fe-Cr-Ni phase diagram in the 1000°C-1350°C temperature range is given in Figure IV. 3. The quality of the fitting is very satisfying and no numerical oscillation due to the interpolation are observed. On the same graph, an example of the evolution of interface compositions during a non-isothermal cycle is also shown.

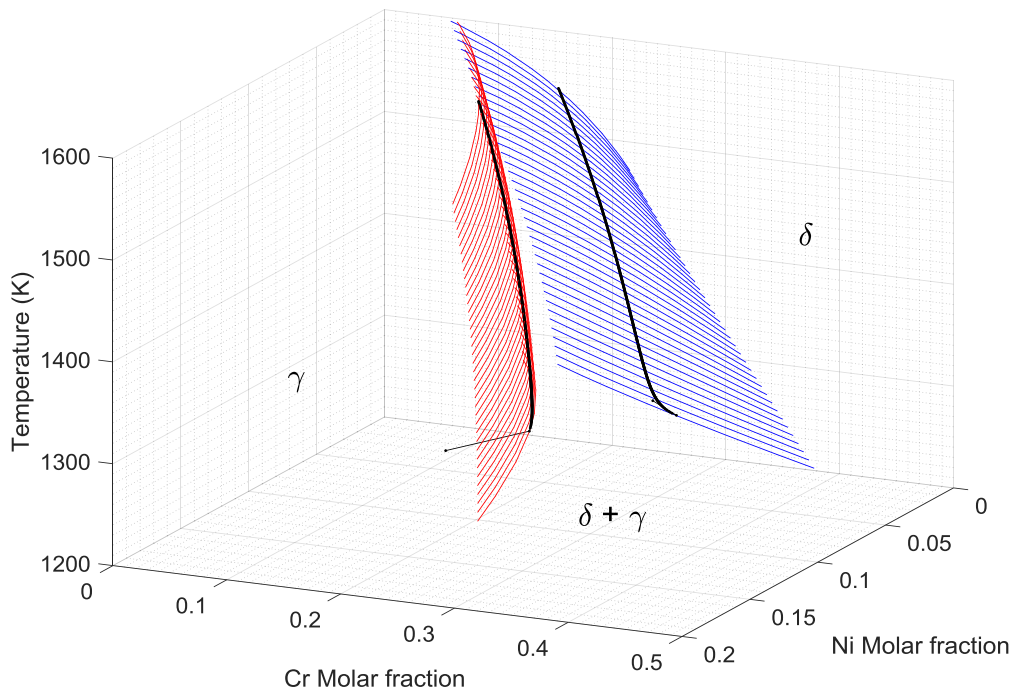


**Figure IV. 3: Interpolation of the Fe-Cr-Ni phase diagram between 1273K (1000°C) and 1622K (1350°C) using the parameterization equations (Eqs. IV.1 and IV.2). Black lines correspond to interface compositions during a heating ramp.**

## II.2. Interdiffusion coefficients

Extensive data are available in literature for the interdiffusion coefficients of Cr and Ni in the Fe-Cr-Ni system [36], [55], [73], but values that are function of temperature are often limited, especially in ferrite. In this project, it is required to use temperature-dependent interdiffusion coefficients in order to :

- simulate the dissolution of  $\delta$ -ferrite in the ingot-cast alloy that was experimentally studied at several temperatures (Chapter III).
- apply the model to non-isothermal heating cycles as it will be shown in Chapter V.

The MOB2 mobility database [72] used with the DICTRA<sup>®</sup> software [58] provides the required diffusion parameters. Preliminary studies have shown that interdiffusion coefficients extracted from MOB2 are consistent with experimentally determined ones obtained from literature [35][74], which gives reliability in them.

In Appendix D, preliminary MOB2 calculations have shown that it is appropriate to consider coupled interdiffusion terms as negligible compared to main ones at temperatures above 1100°C. In addition, for the sake of simplicity, we will consider main interdiffusion coefficients  $D_{kk}^{\varphi}$  as independent of composition. Therefore, their only dependence is on temperature via the Arrhenius equation:

$$D_{kk}^{\varphi} = D_0 \exp\left(-\frac{Q}{RT}\right)$$

where  $D_0$  and  $Q$  are the frequency factor and the activation energy related to solute  $k = Cr, Ni$  in phase  $\varphi = \delta, \gamma$ .

### III. Model hypotheses

In literature, the  $\delta \rightarrow \gamma$  transformation in the Fe-Cr-Ni system is generally modeled under the following simplifying hypotheses which will be considered in the present work [49][52][61]:

1. **The transformation is diffusion-controlled:** equilibrium is assumed to hold locally at the interface. Compositions on both sides of the interface can therefore be read from the phase diagram of the Fe-Cr-Ni system. This assumption was experimentally substantiated by Kajihara *et al.*[56] in their work on ferrite dissolution in  $\gamma/\delta/\gamma$  diffusion couples of the Fe-Cr-Ni system at 1100°C. This hypothesis implies that neither capillarity effects nor solute attachments to the interface are considered.
2. **Ferrite and austenite possess the same molar volume  $V_m$ :** according to Bobadilla *et. al* [18] an empirical calculation of the molar volume of ferrite and austenite in the Fe-Cr-Ni at 1200°C yields  $V_m^{\delta} = 7.39 \text{ cm}^3/\text{mol}$  and  $V_m^{\gamma} = 7.34 \text{ cm}^3/\text{mol}$ , *i.e.* a relative difference of less than 1%. These empirical calculations are supported by calculations with the ThermoCalc<sup>®</sup> software and the TCFE6 database. This simplifying assumption can therefore be regarded as appropriate.
3. **Coupled diffusion between Cr and Ni is negligible** (see Appendix D).
4. **Interdiffusion coefficients are independent of compositions:** given the difficulty of taking into account their variation with composition, the interdiffusion coefficients are assumed constant in the model. This hypothesis is generally not true as was demonstrated by preliminary calculations of Appendix D.

### IV. Constitutive equations

In this section, the equations describing solute diffusion will be derived under the hypotheses formulated above.

Solute flux under composition gradient is expressed using Fick's first law. Given that coupled interdiffusion coefficients are negligible compared to main ones, diffusion flux  $J_k^{\varphi}$  of solute  $k$  ( $k = Cr, Ni$ ;  $\varphi = \delta, \gamma$ ) is related only to its composition gradient:

$$J_k^{\varphi} = -D_{kk}^{\varphi} \frac{\partial X_k^{\varphi}}{\partial x} \quad (\text{IV.3})$$

where  $D_{kk}^{\varphi}$  is the main interdiffusion coefficient of solute  $k$  in phase  $\varphi$ . By combining Fick's first law with the continuity equation, which expresses solute conservation, volume diffusion in ferrite and austenite is described by Fick's second law:

$$\frac{\partial X_k^{\varphi}}{\partial t} = \frac{1}{x^n} \frac{\partial}{\partial x} \left( x^n D_{kk}^{\varphi} \frac{\partial X_k^{\varphi}}{\partial x} \right) \quad (\text{IV.4})$$

where  $n = 0, 1$  and  $2$  for planar, cylindrical and spherical geometries respectively. Since main interdiffusion coefficients  $D_{kk}^\varphi$  in both ferrite and austenite are assumed independent of composition, and then of distance  $x$ , Fick's second law can be written, by further developments:

$$\frac{\partial X_k^\varphi}{\partial t} = \frac{nD_{kk}^\varphi}{x} \frac{\partial X_k^\varphi}{\partial x} + D_{kk}^\varphi \frac{\partial^2 X_k^\varphi}{\partial x^2} \quad (\text{IV.5})$$

Under diffusion fluxes of Cr and Ni in ferrite and austenite, the  $\delta/\gamma$  interface should move in order to bring the system to global equilibrium (Figure IV. 4). The interface movement should respect the conservation of the quantity of Cr and Ni transferred at the interface, which implies that the net flux of solute  $k$  across the interface,  $J_k^\delta - J_k^\gamma$ , should be balanced by the growth or the shrink of the  $\delta$  phase. This is expressed by the mass balance equation at the  $\delta/\gamma$  interface for both Cr and Ni:

$$\left\{ \begin{aligned} (X_{Cr}^{\delta/\gamma} - X_{Cr}^{\gamma/\delta}) \frac{dz}{dt} \Big|_{Cr} &= D_{CrCr}^\gamma \frac{\partial X_{Cr}}{\partial x} \Big|^\gamma - D_{CrCr}^\delta \frac{\partial X_{Cr}}{\partial x} \Big|^\delta \\ (X_{Ni}^{\delta/\gamma} - X_{Ni}^{\gamma/\delta}) \frac{dz}{dt} \Big|_{Ni} &= D_{NiNi}^\gamma \frac{\partial X_{Ni}}{\partial x} \Big|^\gamma - D_{NiNi}^\delta \frac{\partial X_{Ni}}{\partial x} \Big|^\delta \end{aligned} \right. \quad (\text{IV.6.a})$$

$$\left\{ \begin{aligned} (X_{Cr}^{\delta/\gamma} - X_{Cr}^{\gamma/\delta}) \frac{dz}{dt} \Big|_{Cr} &= D_{CrCr}^\gamma \frac{\partial X_{Cr}}{\partial x} \Big|^\gamma - D_{CrCr}^\delta \frac{\partial X_{Cr}}{\partial x} \Big|^\delta \\ (X_{Ni}^{\delta/\gamma} - X_{Ni}^{\gamma/\delta}) \frac{dz}{dt} \Big|_{Ni} &= D_{NiNi}^\gamma \frac{\partial X_{Ni}}{\partial x} \Big|^\gamma - D_{NiNi}^\delta \frac{\partial X_{Ni}}{\partial x} \Big|^\delta \end{aligned} \right. \quad (\text{IV.6.b})$$

Eqs. (IV.6.a) and (IV.6.b) are valid under the assumption  $V_m^\delta = V_m^\gamma$ . The quantities  $X_k^{\delta/\gamma}$  and  $X_k^{\gamma/\delta}$  are the molar fractions of solute  $k$  on the ferritic and the austenitic sides of the interface. They should be directly read from the phase diagram since local equilibrium is assumed to hold at the interface. The quantities  $\frac{dz}{dt} \Big|_{Cr}$  and  $\frac{dz}{dt} \Big|_{Ni}$  are the migration rates of the interface caused by the diffusion fluxes of Cr and Ni respectively. Since there is a unique  $\delta/\gamma$  interface, they must satisfy:

$$\frac{dz}{dt} \Big|_{Cr} = \frac{dz}{dt} \Big|_{Ni} = \frac{dz}{dt} \quad (\text{IV.7})$$

Therefore, the resolution of the mass-balance equations must be carried under the constraint of the equality of the migration rates  $\frac{dz}{dt} \Big|_{Cr}$  and  $\frac{dz}{dt} \Big|_{Ni}$  and under the hypothesis of local equilibrium at the interface.

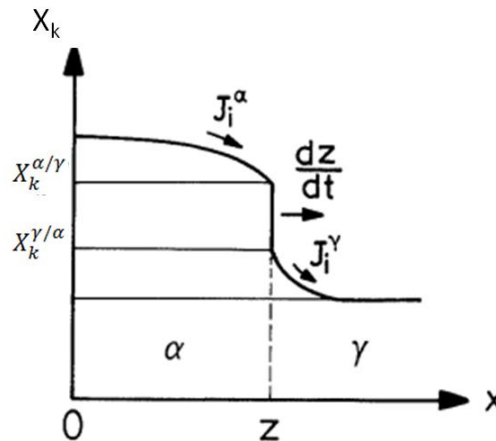


Figure IV. 4: Schematic composition profile of a solute across the moving  $\alpha/\gamma$  interface [36].

The overall amount of solutes in the calculation cell must be conserved. Therefore at the boundaries of the calculation cell there should be no flux of matter. Homogeneous Von Neumann boundary condition is thus applied:

$$\left. \frac{dX_k}{dt} \right|_{x=0} = \left. \frac{dX_k}{dt} \right|_{x=L} = 0 \quad (\text{IV.8})$$

## V. Numerical techniques

### V.1. Variable grid spacing

Each phase region has a fixed number of grid points  $x_i$  ( $i = 1, \dots, N$ ). The first and last grid points are initially set to coincide with the region's boundaries (Figure IV. 5).

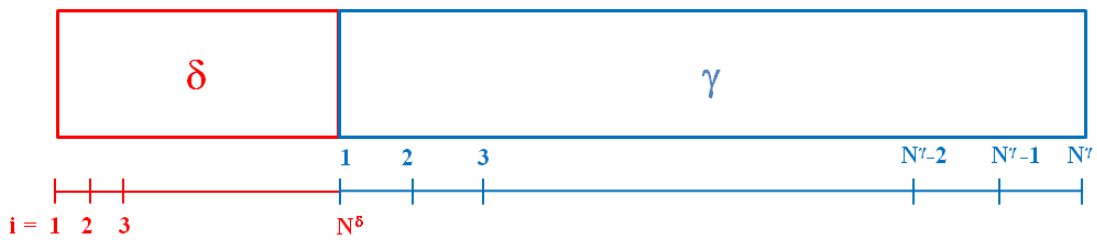


Figure IV. 5: Sketch of the grid point network in both ferrite and austenite.

In moving boundary problems, where the interface position varies in time, the use of a fixed space meshing does not lead to an easy tracking of the interface, since the latter does not necessarily coincide with a grid point. An alternative solution is to use a variable grid spacing that allows to locate the interface at a grid point. This approach was first introduced by Murray *et al.* [53] and then was widely used in problems where phase transformation involves a moving interface [48][50][51]. In the variable grid spacing method, each phase is subdivided into a fixed number of grid spacings (or equivalently a fixed number of grid points). The size of the grid spacings varies with the movement of the interface. It expands for a growing phase, while it diminishes for a shrinking phase (Figure IV. 6). Therefore the location  $x_i$  of grid point  $i$  varies with time and the addition of a term that accounts for the change in composition resulting from the grid point movement, regardless of any diffusion effect, is required. This is accounted for through the total time derivative of the composition:

$$\frac{dX_k^\varphi}{dt} = \frac{\partial X_k^\varphi}{\partial x} \frac{dx_i}{dt} + \frac{\partial X_k^\varphi}{\partial t} \quad (\text{IV.9})$$

For each grid point  $i$ , the travel rate  $\frac{dx_i}{dt}$  is proportional to the interface velocity  $\frac{dz}{dt}$  by its relative distance to the interface. It is written

$$\frac{dx}{dt} = \frac{x_i}{z} \frac{dz}{dt} \quad (\text{IV.10.a})$$

in the ferrite region and

$$\frac{dx}{dt} = \frac{L - x_i}{L - z} \frac{dz}{dt} \quad (\text{IV.10.b})$$

in the austenite region. Finally, with the incorporation of the grid movement, the diffusion equation (IV.5) becomes the diffusion-transport equation

$$\frac{dX_k^\delta}{dt} - D_{kk}^\delta \frac{\partial^2 X_k^\delta}{\partial x^2} - \frac{x_i dz}{z dt} \frac{\partial X_k^\delta}{\partial x} - \frac{nD_{kk}^\delta}{x_i} \frac{\partial X_k^\delta}{\partial x} = 0 \quad (\text{IV.11.a})$$

in ferrite, and

$$\frac{dX_k^\gamma}{dt} - D_{kk}^\gamma \frac{\partial^2 X_k^\gamma}{\partial x^2} - \frac{L - x_i dz}{L - z dt} \frac{\partial X_k^\gamma}{\partial x} - \frac{nD_{kk}^\gamma}{x_i} \frac{\partial X_k^\gamma}{\partial x} = 0 \quad (\text{IV.11.b})$$

in austenite. These equations can be regarded as a combination of a temporal term, a diffusion term, a transport term and a term that accounts for the geometry of the calculation cell.

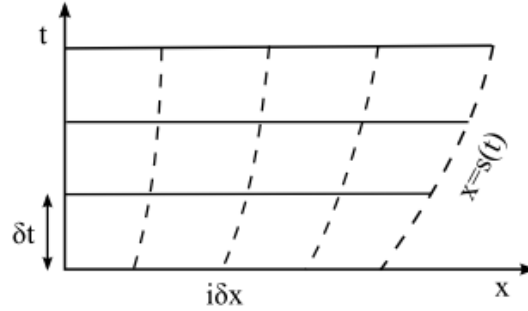


Figure IV. 6: Deformation of a one dimensional mesh according to the Murray-Landis method.

## V.2. Numerical schemes

In this section we present the numerical schemes used to derive the finite difference form of the constitutive equations. Depending on the position of the grid point in the calculation domain, appropriate schemes will be used. In the followings, the subscripts  $k$  and  $\varphi$  are dropped in order to lighten the equations.

### V.2.a. Volume diffusion at internal grid points

Eqs.(IV.11.a) and (IV.11.b) express volume diffusion which is treated at internal grid points  $i = 2, \dots, N - 1$  ( $N = N^\delta, N^\gamma$ ) in each region respectively. Finite-difference formulation of first and second space derivatives are approximated with the following equations that take into account a non-uniform grid spacing [76]:

$$\frac{\partial X_i}{\partial x} = \frac{\Delta x_-^2 X_{i+1} - (\Delta x_+^2 - \Delta x_-^2) X_i - \Delta x_+^2 X_{i-1}}{\Delta x_- \Delta x_+ (\Delta x_- + \Delta x_+)} - \frac{1}{6} \Delta x_- \Delta x_+ \frac{\partial^3 X_i}{\partial x^3} + \mathcal{O}(\Delta x^3) \quad (\text{IV.12})$$

$$\frac{\partial^2 X_i}{\partial x^2} = \frac{\Delta x_- X_{i+1} - (\Delta x_- + \Delta x_+) X_i + \Delta x_+ X_{i-1}}{\frac{1}{2} \Delta x_- \Delta x_+ (\Delta x_- + \Delta x_+)} - \frac{1}{3} (\Delta x_+ - \Delta x_-) \frac{\partial^3 X_i}{\partial x^3} + \mathcal{O}(\Delta x^2) \quad (\text{IV.13})$$

where

$$\Delta x_- = x_i - x_{i-1} \text{ and } \Delta x_+ = x_{i+1} - x_i$$

The first derivative is approximated with a parabola that passes through  $X_{i-1}$ ,  $X_i$  and  $X_{i+1}$ . Its local truncation error is second order. The formulation of the second derivative is only first order accurate since it contains a term proportional to  $(\Delta x_+ - \Delta x_-)$ . For a uniform grid spacing both approximations equal the second order central difference approximations

$$\frac{\partial X_i}{\partial x} = \frac{X_{i+1} - X_{i-1}}{2\Delta x} + \mathcal{O}(\Delta x^2) \quad (\text{IV.14})$$

$$\frac{\partial^2 X_i}{\partial x^2} = \frac{X_{i+1} - 2X_i + X_{i-1}}{\Delta x^2} + \mathcal{O}(\Delta x^2) \quad (\text{IV.15})$$

In order to obtain the finite difference form of Eqs.(IV.11), the Crank-Nicolson discretization scheme [77] is used and Eqs.(IV.12) and (IV.13) are inserted into Eqs.(IV.11). For more details, the reader can refer to appendix E. The final finite difference form is then arranged into the following linear form:

$$A_i X_{i-1}^{t+1} + B_i X_i^{t+1} + C_i X_{i+1}^{t+1} = D_i X_{i-1}^t + E_i X_i^t + F_i X_{i+1}^t \quad (\text{IV.16})$$

where, for each internal grid point, the coefficients  $A_i, B_i, C_i$  and  $D_i, E_i, F_i$  are functions of the time-step, the grid spacings and interdiffusion coefficients at times  $t$  and  $t + 1$  respectively. This set of linear equations is arranged into the following matrix form:

$$M^{t+1} X^{t+1} = M^t X^t \quad (\text{IV.17})$$

where  $M^{t+1}$  and  $M^t$  are tri-diagonal matrixes composed of  $A_i, B_i, C_i$  and  $D_i, E_i, F_i$  terms respectively. This equation is solved by the TriDiagonal Matrix Algorithm (TDMA), which is a variant of the Gauss pivot elimination for tri-diagonal matrixes [77]. Details of the discretization scheme are provided in Appendix E and the choice of the Crank-Nicolson method will be explained in §V.5. *Stability treatments*.

### V.2.b. Fluxes at the interface

Solute fluxes at the interface, *i.e.* at grid points  $N^\delta$  in ferrite ( $X_{N^\delta} = X^{\delta/\gamma}$ ) and 1 in austenite ( $X_1 = X^{\gamma/\delta}$ ), are approximated with a three-point decentered Taylor expansions which are second order accurate. They are given by the following equations:

$$J^\delta = -D^\delta \frac{(X_{N^\delta-2} - 4X_{N^\delta-1} + 3X_{N^\delta}^{\delta/\gamma})}{2\Delta x_\delta} + \mathcal{O}(\Delta x_\delta^2) \quad (\text{IV.18.a})$$

in ferrite, and

$$J^\gamma = -D^\gamma \frac{(-3X^{\gamma/\delta} + 4X_2 - X_3)}{2\Delta x_\gamma} + \mathcal{O}(\Delta x_\gamma^2) \quad (\text{IV.18.b})$$

in austenite.

### V.2.c. Boundary conditions

At each boundary ( $x_1 = 0$  and  $x_{N^\gamma} = L$ ) the grid is enlarged with a virtual node (Figure IV. 7). The distance between the virtual node to the boundary node is  $\Delta x_1 = x_2 - x_1$  in ferrite and  $\Delta x_{N-1} = x_N - x_{N-1}$  in austenite. The zero flux condition implies that composition at virtual node 0 equals that at node 2 in ferrite and similarly, the composition at node  $N^\gamma - 1$  equals that at virtual node  $N^\gamma + 1$  in austenite, for each solute. These conditions ensure that gradients are set to zero at boundary nodes (1,  $N^\gamma$ ) of the system. It should be noted that this approximation is only first order accurate.



Figure IV. 7: Schematic of the virtual points at the (a) left and (b) the right boundaries of the calculation cell.

### V.3. Grid points distribution

With the expressions of the first and second derivatives in Eqs.(IV.12) and (IV.13), it is possible to test a variety of grid distributions and select the most appropriate one for the problems treated in this PhD work. The use of a uniform grid distribution provides second order accuracy but solutions are found to depend on the number of grid points in austenite (Appendix F). To lift this dependency, either a high number of grid points, which is time-consuming, or a finer mesh near the interface is required. The geometrical distribution is well suited for this purpose since grid spacings are very fine near the interface, which is convenient to capture solute gradient, while they become coarser near the boundaries, where gradients are low. However, due to the non-uniform grid spacings, the geometrical meshing is only first order accurate (see Eq.(IV.13)) and leads in the present case to a considerable deviation from perfect solute mass conservation, making the results less reliable (see Appendix F). The concept of deviation from mass conservation will be addressed in §VI.1. Model validation.

In this paragraph we present a new approach that allows to produce mesh-insensitive results, with high accuracy and using a reasonably low number of grid points. A meshing distribution called "double-uniform" is used for this purpose. An example of such a meshing in the austenite region is sketched in Figure IV. 8. Austenite is subdivided into two complementary zones: a dense meshing zone and a coarse meshing zone. The first zone is located near the interface with a dense meshing containing  $M$  grid points ( $M < N$ ). It is designed to capture solute gradients near the interface, especially when they are very steep at the beginning of the transformation. Far from the interface where gradients are generally low, the coarse grid spacing is used ( $N - M + 1$  grid points). Coarse and dense meshings are connected at grid point  $M$ . Overall, the double-uniform meshing is second order accurate except at grid point  $M$  where grid spacing changes from a fine one to a coarse one.

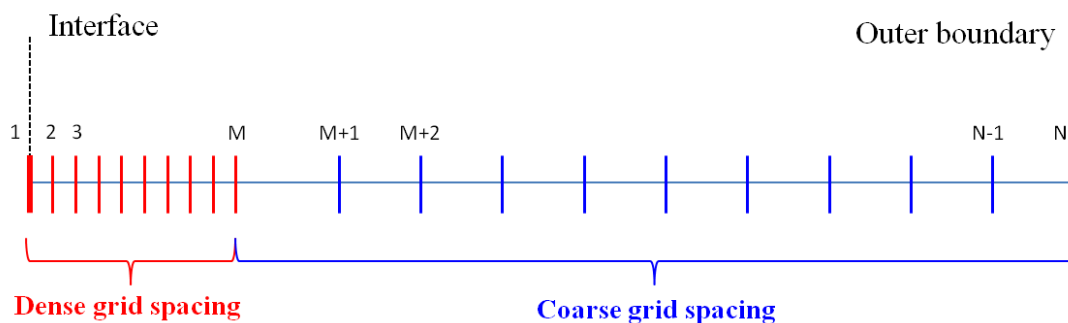
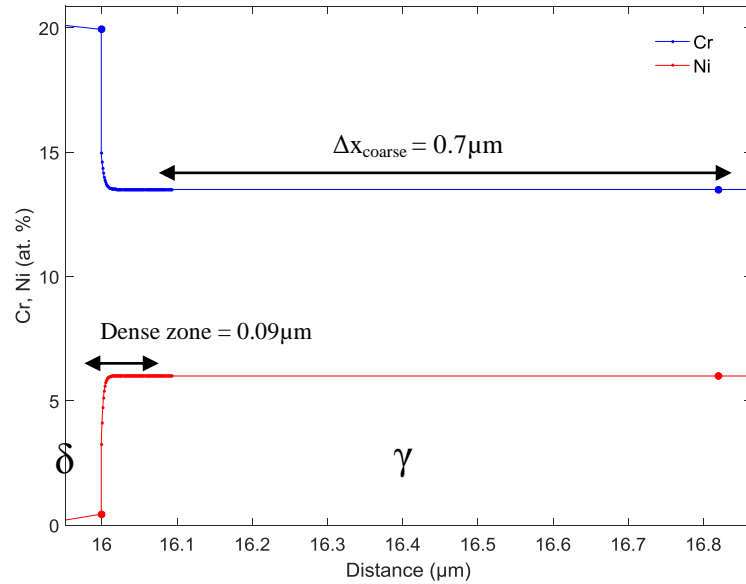


Figure IV. 8: Double-uniform meshing in the austenite region; dense meshing zone near the interface and coarse meshing zone in the rest of the region.

As the transformation proceeds, solute gradients become less steep and more spatially expanded. Therefore the grid spacing and the spatial extension of each zone have to evolve with time. This is performed according to the following procedure:

- i. Initially the length of the dense meshing zone  $l_0^{dense}$  corresponds to the diffusion length of the fastest solute in austenite for an initial time-step  $dt_0$ , *i.e.*  $l_0^{dense} = 2\sqrt{\max(D_{Cr}, D_{Ni})dt_0}$ . In the studied cases, for  $dt_0 = 0.1s$  the initial length is lower than  $0.1\mu m$ . The initial dense grid spacing is subsequently defined by  $\Delta x_0^{dense} = \frac{l_0^{dense}}{M-1}$ . The rest of the austenite region corresponds to the coarse meshing zone which is subdivided over  $N - M$  equally spaced meshes.
- ii. At the beginning of the transformation, to ensure that solute gradients remain located in the dense meshing zone, the initial time-step  $dt_0$  should be reduced to an appropriate value (divided by 100 in this study), so that diffusion length of solutes do not exceed the extent of the dense zone (see Figure IV. 9 for example).



**Figure IV. 9:** Example of dense and coarse meshings in austenite ( $\gamma$ ) at the initial temporal iteration  $t=0.001s$ . The length of the dense meshing is  $0.09\mu m$  while the size of the coarse grid spacing is  $0.7\mu m$ . The total size of austenite is  $73\mu m$  (case of the microstructure in the CR1 state).

- iii. In order to avoid abrupt slope changes at the transition from fine to coarse meshing at grid point M, it is considered appropriate to maintain the location of grid point M far from the extension of solute gradients. For this reason the length of the dense part is always kept a least twice larger than the diffusion length of solutes. When the diffusion length of the fastest solute exceeds half the length of the dense zone  $l_0^{dense}$  (this is called the size doubling criterion), the latter is doubled in size and so is the fine grid spacing. Solute profiles before size doubling are interpolated over the new grid points with spline interpolation (Figure IV. 10). In the same fashion, the coarse meshing is contracted and the correspondent solute profiles are also spline-interpolated on the new coarse meshing.

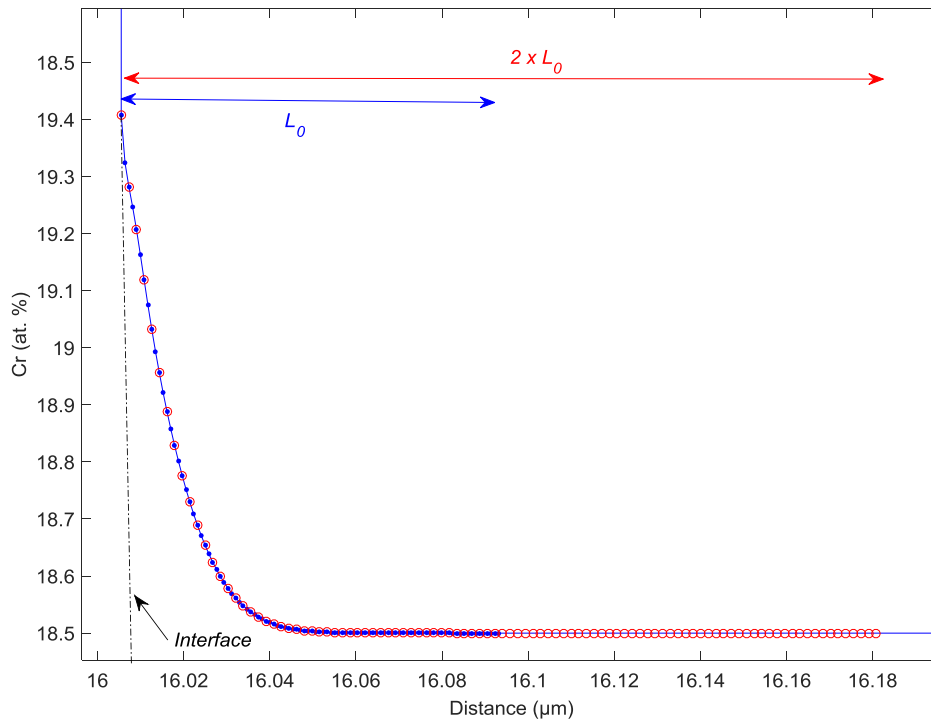


**Figure IV. 10:** Doubling of the length of the dense meshing zone in austenite and interpolation of the chromium profile in austenite on the new meshing in the dense zone. The dense meshing prior to size doubling is in blue and new one is in red. The interface is located at 16.01  $\mu\text{m}$ .

- iv. The last step (iii) is repeated each time the size doubling criterion is satisfied, as long as the new length of the dense zone does not exceed the austenite size. In such a case, the dense part will then be extended over the whole austenite region (the coarse meshing disappears). Grid spacings will be adapted accordingly and solute profiles will be redefined over the new grid points distribution.

Extensive numerical experiments have shown that, with the double-uniform meshing, numerical results become insensitive to the meshing size (Appendix F). This method is then validated and is henceforth used in all simulations.

#### V.4. Calculation algorithm

The general algorithm of calculation is shown in the flowchart of Figure IV. 12. It comprises four stages:

- **Stage 1:** *updating the mesh*  
At the beginning of each time step (time  $t + 1$ ), if a double-uniform meshing is used, the length and the grid spacing of the dense and coarse zones in the austenite phase region are updated if required.
- **Stage 2:** *calculation of physical quantities*  
Temperature, thermodynamic data and interdiffusion coefficients are updated if transformation involves a non-isothermal heating cycle.
- **Stage 3:** *resolution of constitutive equations*

Eqs.(IV.11) are coupled at the interface through Eqs.(IV.6): the velocity of the interface  $\frac{dz}{dt}$  depends on solute gradients on both sides of the interface, which result from the resolution of Eqs.(IV.11). Simultaneously, Eqs.(IV.11) include a transport term proportional to  $\frac{dz}{dt}$ . The latter must be known a priori to resolve Eqs.(IV.11). It appears thus that Eqs.(IV.6) and (IV.11) are interlinked.

A first method of resolution is to resolve, at each time step, Eqs.(IV.6) by taking gradients at the interface from the last time step. The resultant  $\frac{dz}{dt}$  is then injected in Eqs.(IV.11) and diffusion profiles in both phases are computed. This makes the method inherently explicit and dependent on the size of time step.

The method adopted here is to cast these equations into a nominally linear form and an iterative procedure will be used to solve them. In the following, the superscripts *iter-1* and *iter* refer respectively to values at the former and at the current iteration in the iterative loop:

**1. Initialization:** before the starting of the iteration loop, values of  $\frac{dz}{dt}$ ,  $X_{Cr}^\delta$ ,  $X_{Ni}^\delta$ ,  $X_{Cr}^\gamma$  and  $X_{Ni}^\gamma$  and solute profiles in ferrite and austenite at the previous time step (*t*) are used as initial guesses (*iter* = 0) to start the iteration procedure.

**2. Mass balance at the interface (Eqs.(IV.6)):** this step aims at determining the velocity  $\frac{dz}{dt}$  and the compositions at the interface  $X_{Cr}^{\delta/\gamma}$ ,  $X_{Ni}^{\delta/\gamma}$ ,  $X_{Cr}^{\gamma/\delta}$  and  $X_{Ni}^{\gamma/\delta}$  for iteration *iter*. The interface compositions are determined by requiring that the two phases are in local equilibrium. With the aid of the tie-line relations, only one solute composition is independent. As mentioned earlier,  $X_{Cr}^{\gamma/\delta}$  is chosen as the independent composition. The determination of the interface compositions and velocity is performed according to the following steps: given a composition profile from the previous iteration *iter-1*:

- An initial interface composition  $X_{Cr}^{\gamma/\delta}|^{iter}$  is selected.
- The rest of interface compositions  $X_{Ni}^{\gamma/\delta}|^{iter}$ ,  $X_{Ni}^{\delta/\gamma}|^{iter}$  and  $X_{Cr}^{\delta/\gamma}|^{iter}$  are calculated using the parameterized form of the phase diagram.
- Solute fluxes  $J_{Cr}^{\delta,iter}$ ,  $J_{Cr}^{\gamma,iter}$ ,  $J_{Ni}^{\delta,iter}$ ,  $J_{Ni}^{\gamma,iter}$  are calculated using Eqs.(IV.19). Since neighboring grid points, *i.e.*  $X_2^\gamma$ ,  $X_3^\gamma$ ,  $X_{N-1}^\delta$  and  $X_{N-2}^\delta$  are not already known at iteration *iter*, their values are thus taken from the previous iteration *iter - 1*:

$$J_{Cr}^{\delta,iter} = -D^\delta \frac{X_{N-2}^\delta|^{iter-1} - 4X_{N-1}^\delta|^{iter-1} + 3X_{Cr}^{\delta/\gamma}|^{iter}}{2\Delta x_\delta} \quad (IV.19.a)$$

$$J_{Cr}^{\gamma,iter} = -D^\gamma \frac{-3X_{Cr}^{\gamma/\delta}|^{iter} - X_3^\gamma|^{iter-1} + 4X_2^\gamma|^{iter-1}}{2\Delta x_\gamma} \quad (IV.19.b)$$

- Interface velocities  $\frac{dz}{dt}_{Cr}^{iter}$  and  $\frac{dz}{dt}_{Ni}^{iter}$  are calculated based on Eqs.(IV.6).
- If the calculated velocities are equal to a certain prescribed tolerance  $\varepsilon$  ( $\varepsilon < 10^{-12}$ ), the tested values of interface compositions are retained.

Otherwise another interface composition is chosen and the steps (b) to (d) are repeated until interface velocities agree to the desired tolerance.

The selection of the interface compositions in (a) is performed in either two ways:

**(a.1)** At the first time step, initial interface compositions do not necessarily satisfy the local equilibrium condition. They depend on the initial profiles the user defined. Therefore the interface compositions that match the local equilibrium condition are not known a priori and thus the research of the future interface compositions will have to be carried out in the whole range of compositions ( $X_{Cr}^{\gamma/\delta}$  will be varied from 0 to 1). The composition range [0,1] is subdivided into n (n=100) subdivisions and the velocities are calculated at each subdivision value. An example of such procedure is given in Figure IV. 11 where it is shown the evolution of  $\left| \frac{\frac{dz}{dt_{Cr}} - \frac{dz}{dt_{Ni}}}{\frac{dz}{dt_{Cr}}} \right|$  as function of  $X_{Cr}^{\gamma/\delta}$ . Three  $X_{Cr}^{\gamma/\delta}$  values are potential solutions for the equation  $\frac{dz}{dt_{Cr}} = \frac{dz}{dt_{Ni}}$ . For each value, the rest of the correspondent interface compositions are calculated and unphysical ones are eliminated (Table IV. 1). By unphysical we refer to compositions that are negative or exceed 1. As a result, only one value of  $X_{Cr}^{\gamma/\delta}$  is retained.

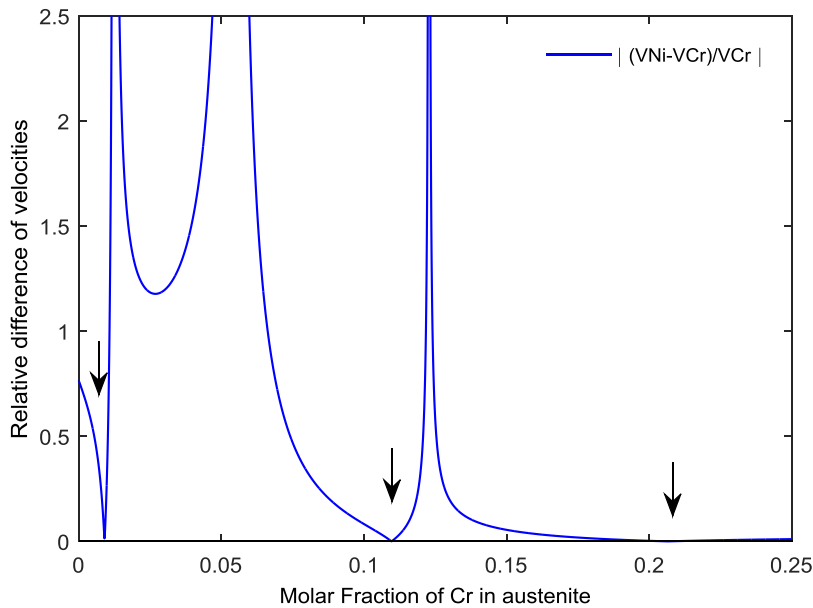


**Figure IV. 11:** Relative difference between Ni and Cr velocities as function of  $X_{Cr}^{\gamma/\delta}$  at the first time step. The arrows point to the composition values of  $X_{Cr}^{\gamma/\delta}$  corresponding to local minima values of the relative velocity difference.

**Table IV. 1:** Calculated values of the rest of interface compositions. Underlined values are not physical hence not retained. Bold ones are accepted.

Minima $\Delta V/V$	$X_{Cr}^{\gamma/\delta}$	$X_{Cr}^{\delta/\gamma}$	$X_{Ni}^{\delta/\gamma}$	$X_{Ni}^{\gamma/\delta}$
0.0136	0.009	0.005	<u>-0.06</u>	<u>-0.06</u>
0.0004	0.109	0.12	0.0001	<u>-0.003</u>
0.00001	<b>0.206</b>	<b>0.275</b>	<b>0.064</b>	<b>0.11</b>

(a.2) At further time steps, since interface compositions vary progressively, their values at time  $t$  are to be looked for only in the neighborhood of the interface compositions at time  $t - 1$ .

In order to accelerate the research of the interface velocity, the Newton-Raphson method was used. It permits to reach the desired accuracy after less than 10 iterations. To ensure stability of this algorithm one has to start from a first guess  $X_{Cr}^{(0)}$  that lies near the solution  $X_{Cr}^{(*)}$  of the mass balance equations system. This is treated in either two ways:

- In the initial time-step the first guess  $X_{Cr}^{(0)}$  will be taken at the minimum of the  $\left| \frac{\frac{dz}{dt_{Cr}} - \frac{dz}{dt_{Ni}}}{\frac{dz}{dt_{Cr}}} \right|$  curve as it has been shown in (a.1) (Figure IV. 11).
- At later time steps, the interface composition at the last time step  $t$  will be considered as the first guess.

At the end of this stage, the velocity  $\frac{dz^{t+1,iter}}{dt}$  and interface compositions at iteration  $iter$  are known.

- 3. Grid points positions** are redistributed in both phase regions according to the new position of the interface  $z^{t,iter}$ . A new grid spacing is calculated in ferrite and austenite:  $\Delta x_{\delta}^{iter}$  and  $\Delta x_{\gamma}^{iter}$ .
- 4. Volume diffusion:** once the state at the interface has been established, diffusion equation is solved in order to determine the new composition profiles  $X^{\delta,iter}$  and  $X^{\gamma,iter}$  corresponding to the new Dirichlet boundary conditions fixed by new compositions at the interface,  $X^{\delta/\gamma,iter}$  and  $X^{\gamma/\delta,iter}$ . This is done by inverting the diffusion-transport equations (IV.11.a) and (IV.11.b).
- 5. Convergence:** the iteration loop ends when values at  $iter$  are sufficiently close to those at  $iter - 1$ . The convergence criterion is

$$\left| \frac{\frac{dz^{iter}}{dt} - \frac{dz^{iter-1}}{dt}}{\frac{dz^{iter-1}}{dt}} \right| < \varepsilon$$

where  $\varepsilon$  is set to  $10^{-5}$ .

- **Stage 4:** once convergence is reached and a consistent solution is obtained, the fraction of ferrite in the cell is calculated and conditions for transformation ending are checked. Transformations ends in one of the following ways:
  - by ferrite dissolution ( $f^{\delta} < 0.1\%$ ) or austenite dissolution ( $f^{\delta} > 99.9\%$ ) if the global composition of the calculation cell lies in the ferritic or austenitic domain, respectively.
  - or by the flattening of the composition profiles if the equilibrium lies in the two-phase  $\delta+\gamma$  domain.

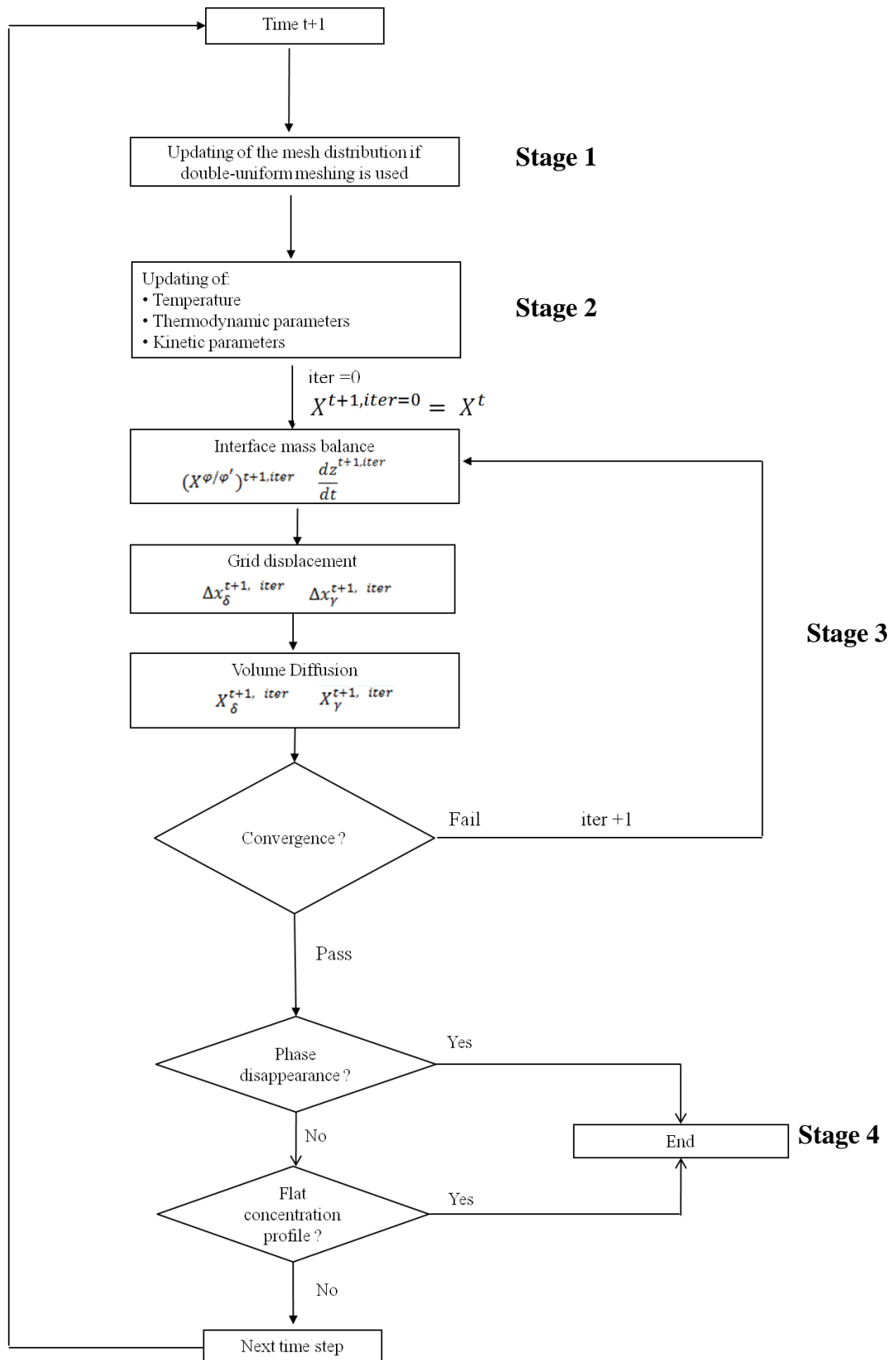


Figure IV. 12: Flowchart of the resolution algorithm.

## V.5. Stability treatments

Stability of numerical schemes is an issue that has to be correctly addressed. Unstable schemes lead to non physical solutions and to a loss of accuracy resulting in deviation from perfect solute mass conservation which is detrimental to the reliability of the calculations. Two kinds of instability were identified for the diffusion-transport equation [78][79]:

### V.5.a. Temporal instability

Solutions of Eqs.(IV.11) can be obtained using several numerical methods. The explicit methods evaluate solutions at current time ( $t + 1$ ) in terms of known quantities of the previous time ( $t$ ). These methods, though cheap in calculation time, are known to produce numerical instabilities if large time steps  $\Delta t$  are used [78], *i.e.* if

$$\frac{D\Delta t}{\Delta x^2} > \frac{1}{2} \quad (\text{IV.20})$$

In practice, this implies to always use bounded values of time steps that can be impractically small when  $\Delta x$  decreases (this is often the case in diminishing phase regions). To avoid the constraint on  $\Delta t$  without losing stability, implicit schemes are generally used. They evaluate the state of the system at current time ( $t + 1$ ) in terms of known quantities at the previous time ( $t$ ) plus the unknown ones of the current time ( $t + 1$ ). Though requiring more computational effort, implicit methods are unconditionally stable.

In the present study, the Crank-Nicolson scheme is used. This scheme is unconditionally stable and provides second order time accuracy. More details on the discretization schemes can be found in Appendix E.

### V.5.b. Spatial instability

The incorporation in the diffusion equation of the transport term that accounts for grid movement can give rise to "spatial instabilities" if the diffusion  $D$  is dominated by convection  $\frac{dz}{dt}$ . The Péclet grid number:

$$Pe = \frac{dz \Delta x}{dt D} \quad (\text{IV.21})$$

reflects the degree to which convection dominates diffusion. In case  $Pe > 2$ , numerical wiggles (or oscillations) will develop near the interface if the first derivative of composition is expressed with a centered Taylor approximation:

$$\frac{\partial X_i}{\partial x} = \frac{X_{i+1} - X_{i-1}}{2\Delta x} + \mathcal{O}(\Delta x^2) \quad (\text{IV.22})$$

Figure IV. 13 gives an example of such oscillations. This situation generally occurs at the very beginning of the transformation where the interface velocity is very high as a result of very steep solute gradients at the interface. When gradients become less steep, oscillations vanish and the central scheme becomes stable. A detailed mathematical explanation of these oscillations is supplied in Appendix G. These oscillations indicate that the mesh size is not sufficiently fine to correctly represent solute gradients in the vicinity of the interface. To

eliminate them, one immediate solution is to reduce the grid size  $\Delta x$  at least near the interface to capture the solution. However this approach is not pertinent since it lengthens the calculations as the number of grid points will have to increase and most importantly because, in our case, the finer is the grid size near the interface, the higher are diffusion fluxes and so is the interface velocity. As a result the oscillations will appear again.

A cure for the unwanted oscillations is to approximate derivative of composition by upwind differences instead of centered ones. The upwind difference is written:

$$\frac{\partial X_i}{\partial x} = \frac{X_i - X_{i-1}}{\Delta x} + \mathcal{O}(\Delta x) \text{ if } \frac{dz}{dt} > 0 \quad (\text{IV.23.a})$$

$$\frac{\partial X_i}{\partial x} = \frac{X_{i+1} - X_i}{\Delta x} + \mathcal{O}(\Delta x) \text{ if } \frac{dz}{dt} < 0 \quad (\text{IV.23.b})$$

With this scheme, spatial stability is ensured, as shown in Figure IV. 13, regardless of the Péclet value and no finer meshing is needed at the interface.

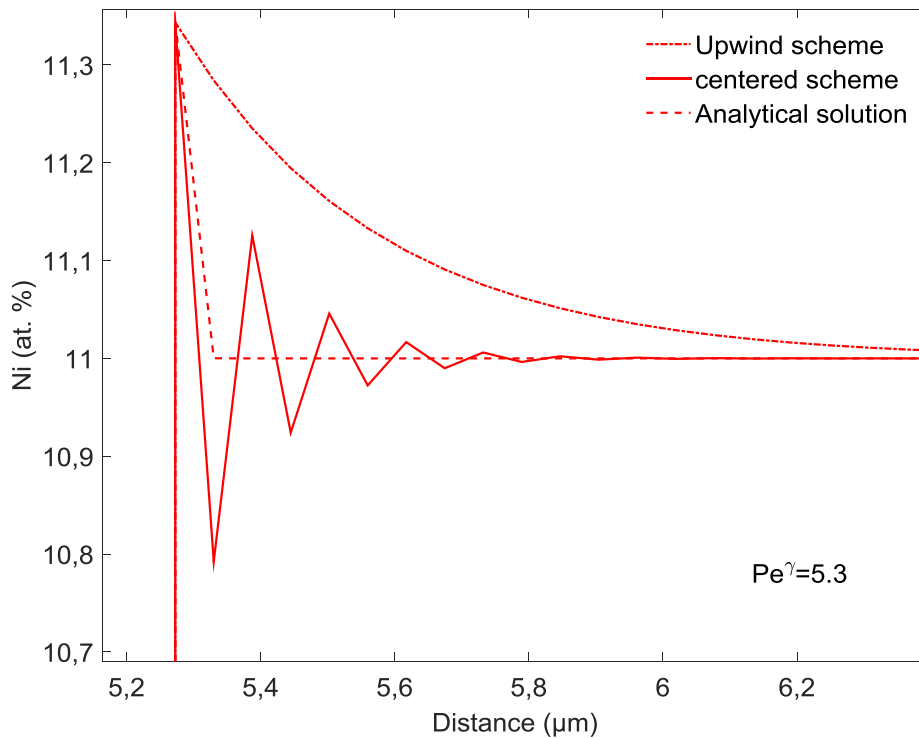


**Figure IV. 13: Numerical instabilities developed in the centred scheme when  $Pe > 2$  while the upwind scheme remains stable.**

### V.5.c. Artificial diffusion [80]

By choosing the upwind scheme, spatial instabilities in convection-dominated problems are eliminated but at the cost of a decrease in space precision as truncation error becomes only first order (Eqs.(IV.23)). Compared to an analytical solution which is exact at grid nodes, upwind scheme leads to an exaggerated diffusion (Figure IV. 13) which is solely due to the finite-difference approximation, not to the actual physics of the problem [80]. On the

contrary, centered scheme slightly underestimates diffusion. Explanation of both phenomena can be found in Appendix H.

This over-diffusion problem can be eliminated by constructing a new optimized scheme which combines central (underdiffusing) and upwind (overdiffusing) schemes. In an equivalent way, this solution is constructed by adding the proper amount of artificial diffusion  $\bar{D}$  to the central difference scheme in order to recover the analytical solution at the grid points [80]. The modified diffusion-transport equation writes (in the planar case):

$$\frac{\partial X}{\partial t} - (D + \bar{D}) \frac{\partial^2 X}{\partial x^2} - \frac{\partial X}{\partial x} \frac{\partial x}{\partial t} = 0 \quad (\text{IV.24})$$

where

$$\bar{D} = \frac{dz}{dt} \frac{\Delta x}{2} \bar{\xi} \quad (\text{IV.25})$$

$$\bar{\xi} = \coth\left(\frac{Pe}{2}\right) - \frac{2}{Pe} \quad (\text{IV.26})$$

$$Pe = \frac{dz}{dt} \frac{\Delta x}{D} \quad (\text{IV.27})$$

where  $\frac{dz}{dt}$ ,  $Pe$ ,  $\Delta x$  are the interface velocity, the Péclet number and the grid spacing respectively. The solution of the modified diffusion-transport equation is stable for all Péclet numbers and is second order accurate.

The analytical expression of the artificial diffusion coefficient is only known for diffusion-transport equations where the diffusion coefficient  $D$  and the transport term  $\frac{dz}{dt}$  are **constant** and the **geometry is planar**. In the present problem, the transport term is proportional to the distance of the grid point to the interface and the geometry may either be planar, cylindrical or spherical. In such cases, the analytical expression of the artificial diffusion coefficient is not known. Thus the accuracy of the correction is not theoretically proven and thus numerical errors may not be as reduced as in the case of planar geometry and constant transport term.

## VI. Model validation

### VI.1. Comparison with Vitek's numerical results

The present model was compared to numerical simulations of ferrite to austenite transformation in stainless steel welds at 1100°C performed by Vitek *et al.*[61]. The size and the composition of ferrite and austenite are specified in Table IV. 2. As in the Vitek's work, the number of grid points is fixed to 20 in ferrite and 780 in austenite and the time step is initially set to 0.0005s and is allowed to increase at each time iteration by 0.2% until reaching the maximum allowed value of 1s. Calculations are performed in the planar geometry with the Crank-Nicolson difference scheme and a uniform mesh distribution.

**Table IV. 2: Initial ferrite and austenite compositions and sizes and grid-point numbers used in the calculations [61].**

Phase	Cr (wt.%)	Ni (wt.%)	Size ( $\mu\text{m}$ )	Grid points
Ferrite	30	4.5	0.5	20
Austenite	21	11	4.5	780
Total	21.9	10.35	5	800

In Vitek's work, the phase boundary of the ferrite and austenite in the Fe-Cr-Ni are calculated using the Thermo-Calc software and the TCFE thermodynamic database [81]. they are given in terms of chromium and nickel weight fraction. The fitting parameters of the phase boundaries are given by the following expressions,  $x_{Cr}^{\gamma/\delta}$  being chosen as the independent variable of the fitting:

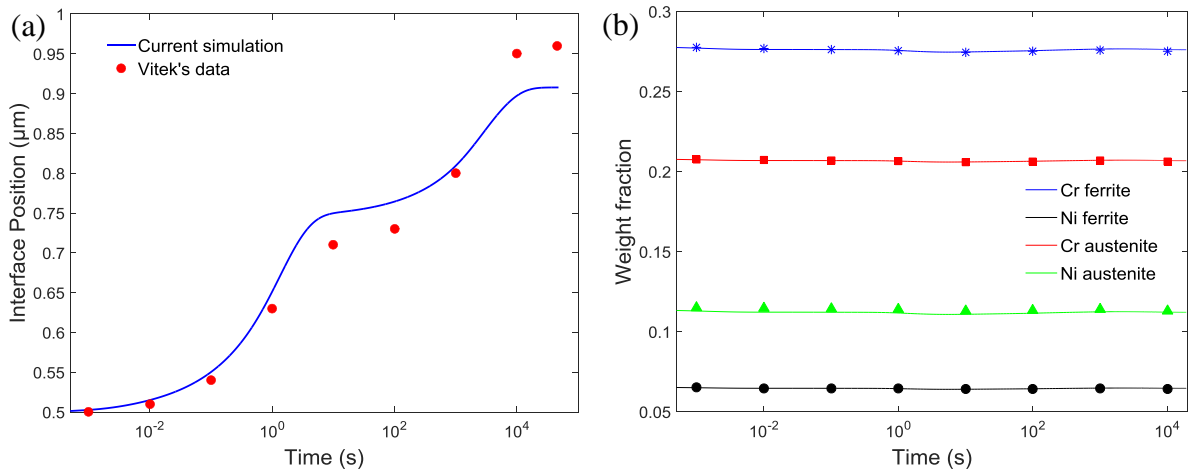
$$\begin{cases} x_{Cr}^{\delta/\gamma} = -0.00316 + 0.95430 x_{Cr}^{\gamma/\delta} + 1.91493 (x_{Cr}^{\gamma/\delta})^2 \\ x_{Ni}^{\delta/\gamma} = -0.06670 + 0.58053 x_{Cr}^{\gamma/\delta} + 0.26323 (x_{Cr}^{\gamma/\delta})^2 \\ x_{Ni}^{\gamma/\delta} = -0.06227 + 0.18753 x_{Cr}^{\gamma/\delta} + 3.16987 (x_{Cr}^{\gamma/\delta})^2 \end{cases}$$

The interdiffusion coefficients of Cr and Ni in austenite and ferrite are given in Table IV. 3.

**Table IV. 3: Interdiffusion coefficients of chromium and nickel in ferrite and austenite at 1100°C, extracted from [61].**

	$D_{CrCr}$ ( $\text{m}^2/\text{s}$ )	$D_{NiNi}$ ( $\text{m}^2/\text{s}$ )
Ferrite	1.48 e-13	1.13 e-13
Austenite	3.92 e-15	1.15 e-15

Figure IV. 14.a shows the evolution of the ferrite size with respect to the aging time. Solid symbols are extracted from Vitek's calculations at different times while the continuous curves represent current simulation. Both simulations predict the same evolution trend and transformation's duration. A slight underestimation by the current simulation is observed at the final stage of the transformation. The interface compositions predicted by the current model are also consistent with those calculated in [61].


**Figure IV. 14: (a) Interface position with time. (b) Interface compositions as a function of the aging time. Continuous lines represents the current simulation while solid symbols are extracted from [61].**

The problem of mass conservation is addressed in the present study. Generally the reliability and the accuracy of the calculations can be measured by the deviation from initial solute content. In this model, average Cr and Ni contents in the whole system are calculated at each time step using the trapezoidal integration method. The global relative variation of the average chromium and nickel contents is considered as a measure of the deviation from mass conservation. This criterion will be used to test the performances of the algorithm, in particular the effect of:

- the non iterative scheme (or explicit scheme).
- the iterative scheme.
- the iterative scheme plus the artificial diffusion.

Figure IV. 15 shows the evolution of the average Cr and Ni as function of time with the three schemes. Global mass deviation in each case is recapitulated in Table IV. 4 (In [61], it is kept under 0.02%). When the non-iterative scheme is used, the variation of the average contents seems to be correlated to the movement of the interface as it can be seen by comparison to Figure IV. 14: the variation of the average content is higher as the interface movement is faster (from 0 to 1s for example) and slower when the interface moves slower (from 1 to 100s). The use of the iterative resolution permits to reduce by half the average mass loss (0.17% for Cr) as can be seen in Table IV. 4. With the incorporation of the artificial diffusion mass deviation is further reduced to reach 0.03 % for Cr.

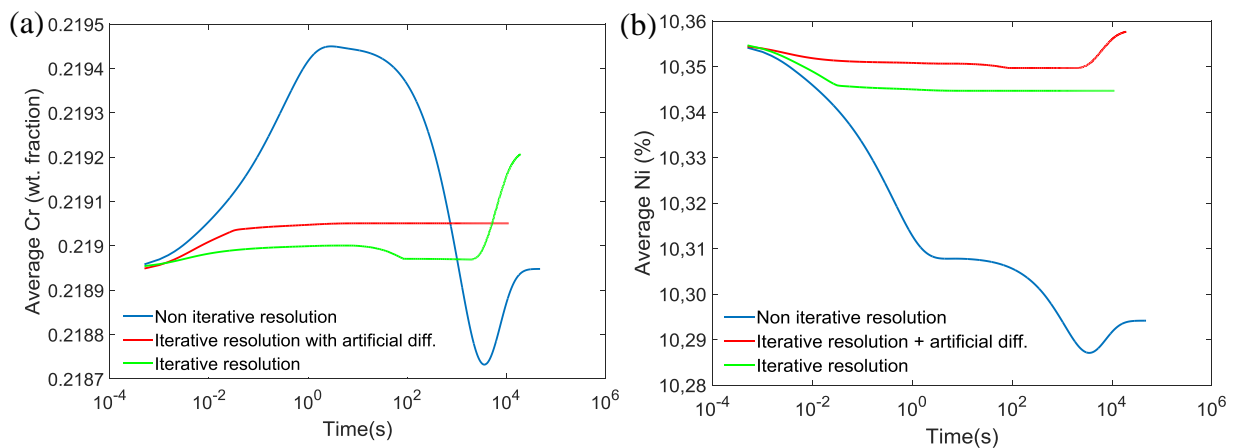


**Figure IV. 15:** Average composition of (a) chromium and (b) nickel as function of time using the non-iterative, the iterative and the iterative plus artificial diffusion scheme.

**Table IV. 4:** Relative variation of the average chromium and nickel contents with non-iterative, iterative and iterative plus artificial diffusion schemes.

	Relative variation of average content (%)		
	Non iterative resolution	Iterative resolution	Iterative resolution with artificial diffusion
Cr	0.3	0.17	0.03
Ni	-0.8	-0.32	-0.05

In conclusion, the model has shown capability in predicting a phase transformation kinetics close to Vitek's simulation [61]. On the other side, these numerical experiments have shown the importance of using iterative resolution and artificial diffusion in reducing the deviation from solute mass conservation.

## VI.2. Comparison to the experiments of Kajihara

The model was also applied to the dissolution of ferrite in  $\gamma/\alpha/\gamma$  diffusion couples of the ternary Fe-Cr-Ni reported by Kajihara *et al.*[36] (Figure IV. 16). Phase compositions and initial sizes are given in Table IV. 5. All diffusion couples were annealed at 1100°C. The thermodynamical description is derived from the experimental work of Hasebe *et al.* [54]. In [36],  $X_{Ni}^{\delta/\gamma}$  is considered as the independent variable in the parameterization of the isothermal section of the phase diagram. In this study, since  $X_{Cr}^{\gamma/\delta}$  is taken as the independent interface composition, the parameterization in [36] is rewritten as function of  $X_{Cr}^{\gamma/\delta}$  (Figure IV. 16.b).

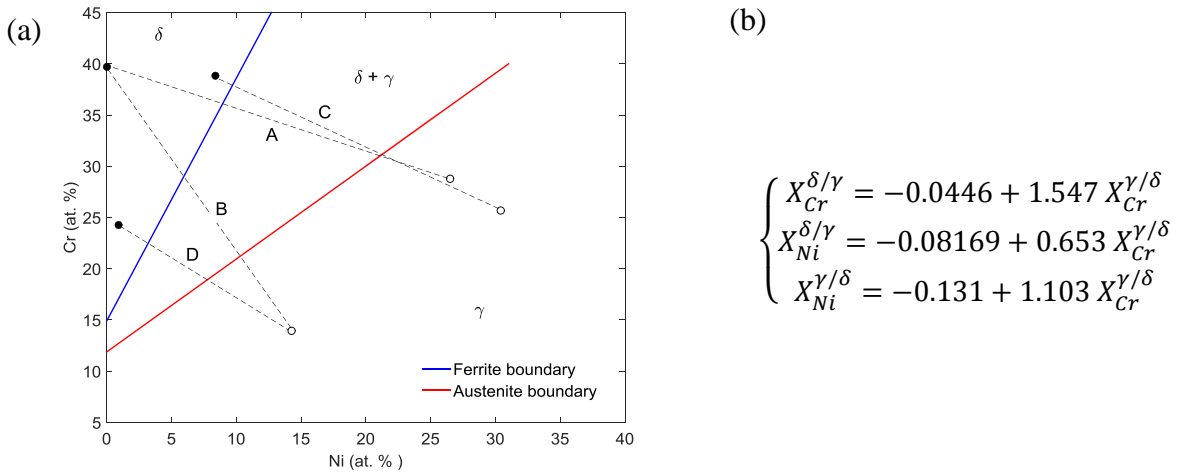


**Figure IV. 16:** (a) Composition pairs of the diffusion couples A, B, C and D plotted in the isothermal section at 1100°C of the Fe-Cr-Ni phase diagram [36]. (b) Interpolation functions of the austenite and ferrite phase boundaries.

Interdiffusion coefficients are those used by Kajihara *et al.* [36] in their numerical analysis as adjustable variables to fit calculations to the experimental results (Table IV. 6).

**Table IV. 5:** Composition of ferrite and austenite phases in  $\gamma/\alpha/\gamma$  diffusion couples of the Fe-Cr-Ni system, as extracted from [36].

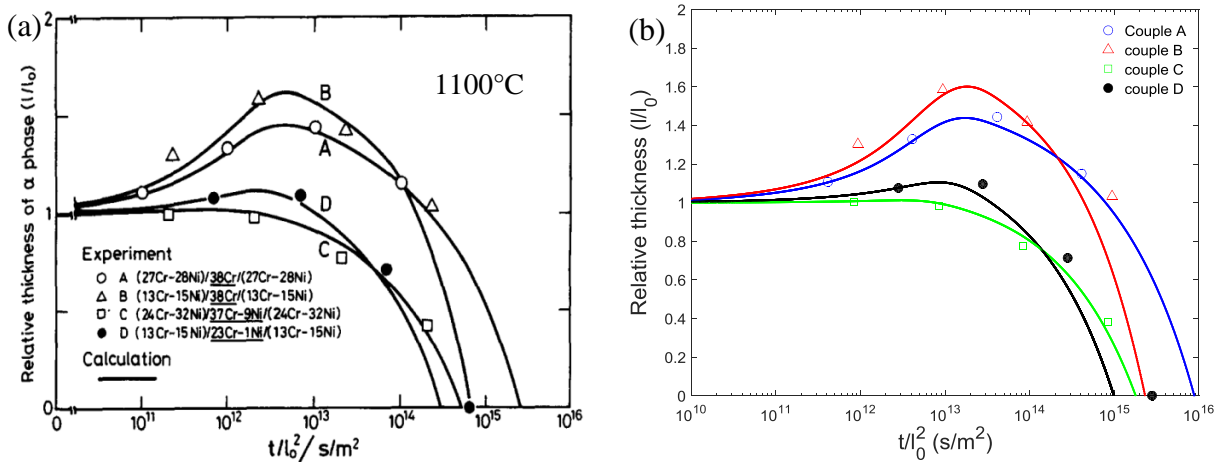
Diffusion couple	Composition (wt. %)		Thickness ( $\mu\text{m}$ )	
	$\alpha$ phase	$\gamma$ phase	$\alpha$ phase	$\gamma$ phase
A	38 Cr	27 Cr, 28 Ni	187	2000
B	38 Cr	13 Cr, 15 Ni	124	2000
C	37 Cr, 9 Ni	24 Cr, 32 Ni	130	2000
D	23 Cr, 1 Ni	13 Cr, 15 Ni	71	2000

**Table IV. 6: Interdiffusion coefficients of chromium and nickel in ferrite and austenite of the ternary Fe-Cr-Ni diffusion couples at 1100°C [49].**

Diffusion couple	$\alpha$ phase		$\gamma$ phase	
	$D_{CrCr}$ (m <sup>2</sup> /s)	$D_{NiNi}$ (m <sup>2</sup> /s)	$D_{CrCr}$ (m <sup>2</sup> /s)	$D_{NiNi}$ (m <sup>2</sup> /s)
A	$1.8 \cdot 10^{-13}$	$1.4 \cdot 10^{-13}$	$3.7 \cdot 10^{-15}$	$1.2 \cdot 10^{-15}$
B	$1.8 \cdot 10^{-13}$	$1.4 \cdot 10^{-13}$	$4.3 \cdot 10^{-15}$	$1.3 \cdot 10^{-15}$
C	$1.8 \cdot 10^{-13}$	$1.4 \cdot 10^{-13}$	$3.7 \cdot 10^{-15}$	$1.1 \cdot 10^{-15}$
D	$1.2 \cdot 10^{-13}$	$0.9 \cdot 10^{-13}$	$3.6 \cdot 10^{-15}$	$1.1 \cdot 10^{-15}$

In their numerical calculations, Kajihara *et al.* [36] used the finite difference technique combined to a flexible grid system. The meshing size evolves geometrically from the cell boundary to the interface. To solve the finite difference equation the Crank-Nicolson scheme was utilized. The numerical results they obtained are given in Figure IV. 17.a. Calculations obtained with the present numerical model are shown in Figure IV. 17.b and compared to the experimental results. In both figures, the relative thickness of ferrite sheets to the initial thickness  $l_0$  is used in order to make direct comparisons among the four sets of experimental data. Very satisfying agreement is reached between present calculations and Kajihara's experiments and calculations. It can then be deduced that the use of the dense meshing near the interface (present calculation) gives similar results as with the geometrical meshing (Kajihara's calculation).

Figure IV. 18 shows experimental and calculated Cr and Ni profiles in couple A after 1hr 10hrs 100hrs and 1000hrs annealing. The agreement between calculations and experiments is also very satisfactory.


**Figure IV. 17: Time-evolution of the thickness of ferrite sheets in the  $\gamma/\alpha/\gamma$  diffusion couples of the Fe-Cr-Ni system as calculated (a) by Kajihara [36] and (b) the current model. Experimental results are superimposed as solid symbols.**

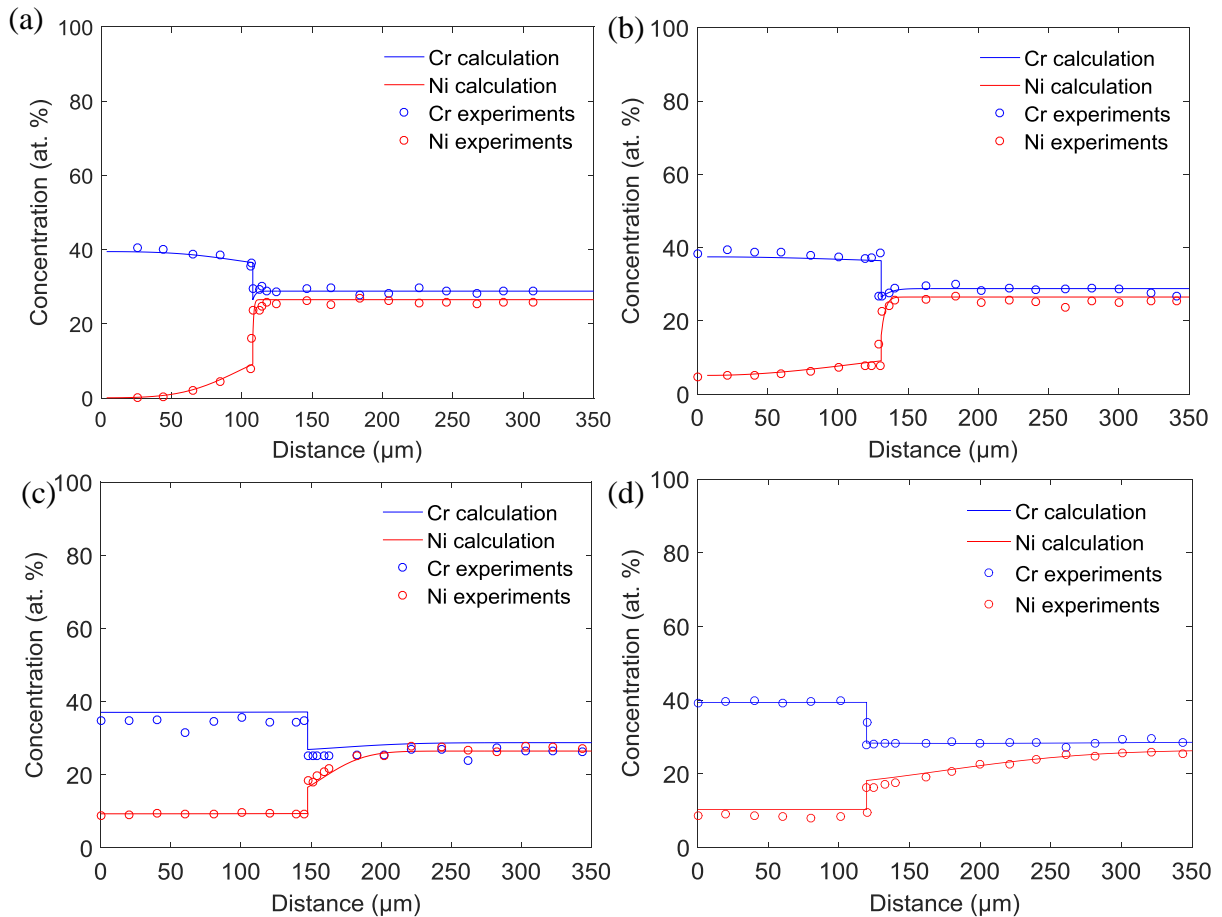


**Figure IV. 18:** Experimental and calculated composition profiles for diffusion couple A after (a) 1hr, (b) 10hrs, (c) 100hrs and (d) 1000hrs (Experimental results from [36]).

Deviation from perfect mass conservation was also checked in this case. Present calculations were accompanied with a very small mass loss (less than 0.1% relative) as can be shown in Table IV. 7.

**Table IV. 7:** Deviation from mass conservation of chromium and nickel during the simulation of ferrite dissolution in diffusion couples A to D.

	A	B	C	D
Average Cr	-0.09%	0.1%	0.005%	0.01%
Average Ni	-0.03%	0.02%	-0.02%	-0.03%

Overall, it has been shown that the model was able of predicting ferrite dissolution in the case of Fe-Cr-Ni diffusion couples. Besides, the numerical techniques used in the present development have proven to be efficient in conserving, to a very satisfying extent, solute quantities during the simulation. In Chapter V, we will reiterate the same calculations, but using the TCFE6 and Ptimec-Miettinen modules in order to compare them.

## VII. Conclusions and perspectives

A numerical model has been developed in order to simulate ferrite dissolution in the ternary Fe-Cr-Ni system. Diffusion is treated in a one dimensional calculation cell with the finite difference technique and using the adaptative meshing method for the tracking of the interface. Simulations can be performed in the planar, spherical and cylindrical geometries. The movement of the interface diffusion controlled, as equilibrium is assumed to hold locally at the interface. Thermodynamical descriptions of the Fe-Cr-Ni phase diagram are interpolated on thermodynamic data extracted from appropriate databases.

Several numerical challenges have been addressed in the course of this development. Of the most importance is the deviation from perfect mass conservation of Cr and Ni in the calculation cell that makes calculations less reliable. The use of an iterative resolution of the governing equations as well as the addition of an artificial diffusion coefficients have shown that mass loss can be lowered under to 0.1%. This performance was only achieved in the planar geometry. In cylindrical and spherical ones, it will be shown in Chapter V that deviation from mass conservation is not negligible and can considerably impact the model predictions. Some improvements need thus to be achieved with this regard.

The issue of the sensitivity of the calculation results to the number of grid points in austenite was also addressed. The use the double-uniform meshing in austenite permitted to obtain mesh-insensitive results with a relatively low number of grid points.

In developing this model, several numerical techniques have been tried and their efficiency discussed. In Table IV. 8 we list these techniques as well as their advantages and drawbacks.

Table IV. 8: Numerical techniques encountered in the development of the model: advantages and drawbacks.

Technique	Advantages	Drawbacks
<b>Meshing</b>		
Uniform	<ul style="list-style-type: none"> <li>- 2<sup>nd</sup> order precision.</li> </ul>	<ul style="list-style-type: none"> <li>- Results depend on meshing.</li> <li>- Time consuming if high grid number.</li> </ul>
Geometric	<ul style="list-style-type: none"> <li>- Fine meshing near the interface.</li> <li>- Gradients are properly taken into account.</li> <li>- No need for a high number of grid points.</li> </ul>	<ul style="list-style-type: none"> <li>- 1<sup>st</sup> order precision.</li> <li>- Considerable mass loss.</li> </ul>
Double-uniform	<ul style="list-style-type: none"> <li>- Gradients are properly taken into consideration.</li> <li>- 2<sup>nd</sup> order at interior nodes.</li> <li>- Results are independent on meshing</li> <li>- No need for a high number of grid points.</li> </ul>	<ul style="list-style-type: none"> <li>- 1<sup>st</sup> order at the node where grid spacing abruptly changes.</li> </ul>
<b>Numerical schemes</b>		
Centered	<ul style="list-style-type: none"> <li>- Unstable results if <math>Pe &gt; 2</math></li> <li>- 2<sup>nd</sup> order accurate</li> </ul>	<ul style="list-style-type: none"> <li>- Slightly underestimates diffusion</li> </ul>
Upwind	<ul style="list-style-type: none"> <li>- Stable for all values of <math>Pe</math></li> <li>- 1<sup>st</sup> order accurate.</li> </ul>	<ul style="list-style-type: none"> <li>- Overestimates diffusion.</li> <li>- Increases mass loss.</li> </ul>
Artificial diffusion + centered	<ul style="list-style-type: none"> <li>- Stable for all values of <math>Pe</math>.</li> <li>- Diffusion is not overestimated nor underestimated.</li> <li>- Reduces mass loss.</li> </ul>	<ul style="list-style-type: none"> <li>- Artificial diffusion known only for the planar geometry.</li> <li>- No mass loss reduction in cylindrical and spherical geometries.</li> </ul>
Three-point decentered	<ul style="list-style-type: none"> <li>- 2<sup>nd</sup> order accurate at first and last grid points in each phase region</li> </ul>	
<b>Other techniques</b>		
Murray-Landis	<ul style="list-style-type: none"> <li>- Allows to easily track the interface.</li> <li>- Easier management of the meshings in <math>\delta</math> and <math>\gamma</math> regions.</li> </ul>	<ul style="list-style-type: none"> <li>- Introduces a transport term in the diffusion equation.</li> <li>- Contributes to mass loss.</li> </ul>
Iterative loop	<ul style="list-style-type: none"> <li>- Allows to solve a system of coupled equations</li> <li>- Reduce the mass loss</li> </ul>	<ul style="list-style-type: none"> <li>- Lengthens the calculations.</li> </ul>

## Chapter V

# Application of the model to analyze ferrite dissolution in the Fe-Cr-Ni cast and multilayered microstructures

In Chapter III, the dissolution of ferrite was first studied in the ingot-cast Fe-17.3%Cr-9.4%Ni alloy. Characteristic features of the dissolution were outlined: early ferrite growth followed by two dissolution regimes accompanied by a change in the morphology of ferrite particles. In a second step, with the designed multilayered microstructures, the dissolution of ferrite was established for several initial states, corresponding to an increasingly thinner ferrite and austenite bands.

In the present chapter, the numerical model developed in Chapter IV is used to analyze these experimental results. The structure of the chapter is threefold. First, by preliminary numerical analysis the relevance of the available thermodynamic databases for the description of the experimentally studied Fe-Cr-Ni systems is assessed. Second, ferrite dissolution in the multilayered microstructure is analyzed and calculation results are discussed under the light of the experimental data.

Once thermodynamical and kinetics data validated on these simple cases, the dissolution of vermicular ferrite in the as-cast ingot is finally simulated with an original modeling approach in which diffusion is treated in a combination of cylindrical and spherical geometries representing the complex morphology of the  $\delta/\gamma$  interface of vermicular ferrite. Mechanisms underlying ferrite's initial growth and its dissolution rate change are enlightened. Relevant parameters of the calculations are outlined and their effect on the dissolution kinetics is fully studied.

### I. Review of the Kajihara experiments

In Chapter IV, the model was successfully applied for the prediction of ferrite dissolution in the Fe-Cr-Ni diffusion couples experimentally studied by Kajihara *et al.* [36] at 1100°C (Figure IV. 16). The excellent agreement between experimental results and calculations is partly due to the proper choice of the thermodynamic description, derived from the experimental works of Hasebe *et al.* [54], and the interdiffusion coefficients deduced by fitting calculations to experiments [56].

Kajihara's experiments provide valuable results to test the relevance of the TCFE6 database [69] and the Ptimec-Miettinen module at 1100°C. Previous calculations were then reiterated with these two thermodynamic descriptions. Corresponding results are compared to those obtained with Kajihara's thermodynamic description in Figure V. 1. With the TCFE6 database, the dissolution kinetics of all ferrite sheets are similar to those obtained with the thermodynamic description of Kajihara. On the contrary, the use of the Ptimec-Miettinen module leads to more discrepancies though the general tendency is quite the same. Discrepancies are observed especially in couples A and B, where the growth of ferrite is too low and its shrinking rate is too high.

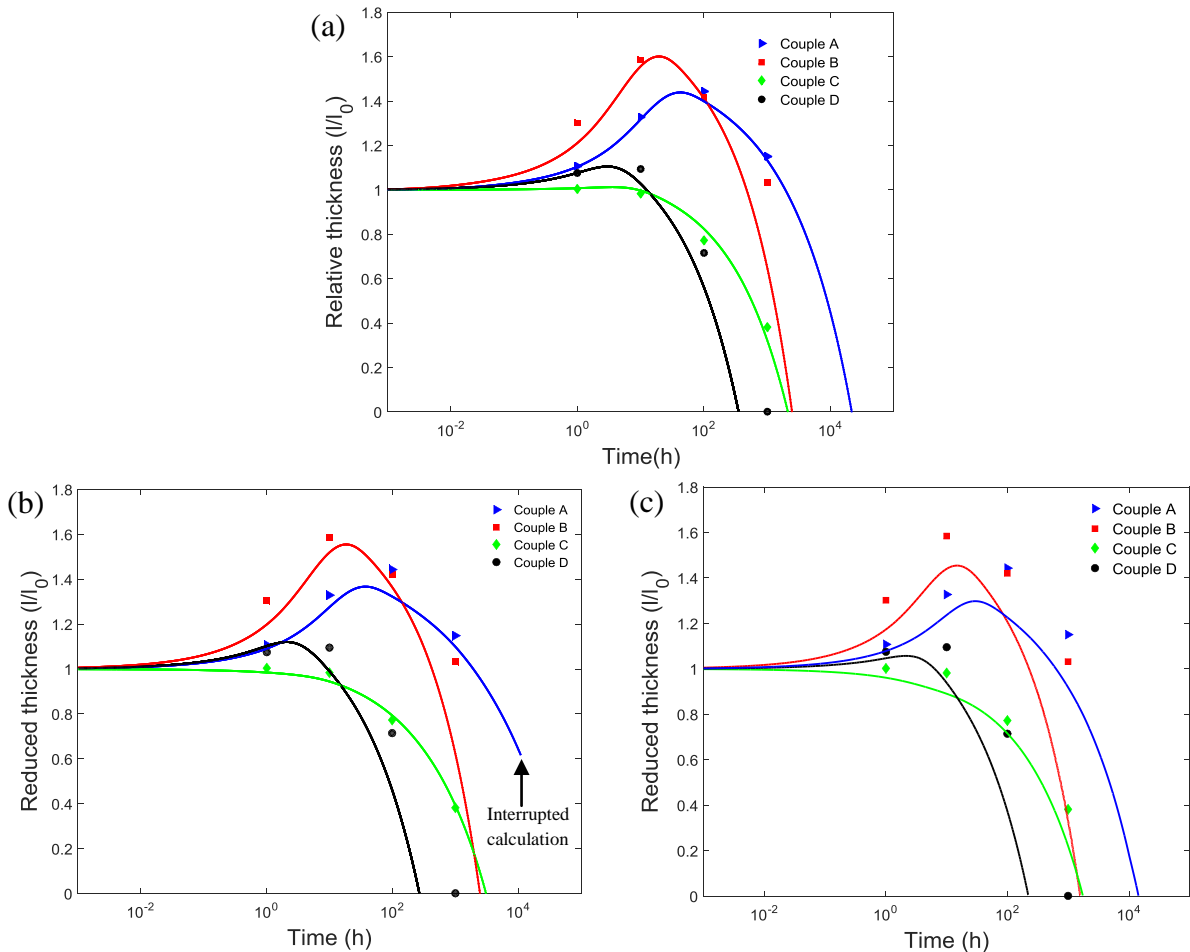


**Figure V. 1:** Time-evolution of the thickness of ferrite sheets in the  $\gamma/\delta/\gamma$  diffusion couples of the Fe-Cr-Ni system experimentally studied by Kajihara *et al.* [36]. Experimental results (solid symbols) are compared to calculations (solid lines) with the present model using (a) the Kajihara's description of the isothermal section of the Fe-Cr-Ni system at 1100°C, (b) the TCFE6 database and (c) the Ptimec-Miettinen module. Diffusion coefficients are those used in [36].

In order to understand these various behaviors, isothermal sections at 1100°C of the Fe-Cr-Ni phase diagram calculated with TCFE6 and Ptimec-Miettinen are compared to the one obtained from Kajihara (Figure V. 2). The compositions pairs of diffusion couples are plotted as well. TCFE6 and Kajihara descriptions yield similar approximations of  $\alpha/(\alpha+\gamma)$  and

$\gamma/(\alpha+\gamma)$  phase boundaries and this explains the similar dissolution calculations. With the Ptimec-Miettinen description, the positions of phase boundaries are quite different:

- the ferrite phase boundary is closer to the initial ferrite compositions. As a consequence, solute gradients that develop in ferrite at the early stage of the transformation are smaller, which explains why the extent of ferrite growth is less important with Ptimec-Miettinen calculations.
- the austenite phase boundary is more remote from initial austenite compositions. The established solute gradients in austenite are thus higher, which enhances solute fluxes at the interface resulting in a more rapid shrinking of ferrite, as can be clearly seen in Figure V. 1.c.

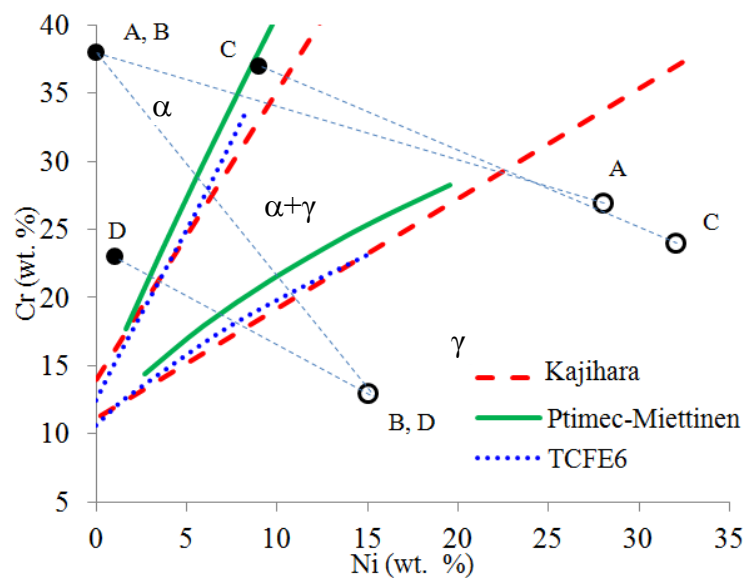


Figure V. 2: Isothermal sections at 1100°C of the Fe-Cr-Ni phase diagram calculated using the TCFE6 database and the Ptimec-Miettinen module and compared to the Kajihara description extracted from [36]. Composition pairs of  $\gamma/\alpha/\gamma$  diffusion couples are also plotted.

Therefore it can be concluded that, at 1100°C, the TCFE6 thermodynamic description is more suited than the Ptimec-Miettinen one to describe ferrite to austenite transformation for the Fe-Cr-Ni alloys under consideration. This calculation demonstrates that both TCFE6 and Ptimec-Miettinen thermodynamic descriptions are not adequate on the whole temperature range. Therefore we will have to verify in the next parts the adequacy of the thermodynamic description at each temperature at which calculations will be conducted. This has to be taken into account for calculation under anisothermal conditions. Furthermore, this result shows that even in the simple Fe-Cr-Ni system, there is a need for a better thermodynamic description.

## II. Ferrite dissolution in the multilayered microstructure at 1240°C

### II.1. Design of the simulations

#### II.1.a. Thermodynamic description

The model is applied to analyze the  $\alpha \rightarrow \gamma$  transformation in the multilayered microstructures. In order to choose the proper thermodynamic description to be used in simulations, the overall composition of the stack is superimposed on the isothermal section of the Fe-Cr-Ni phase diagram at 1240°C, computed using the Ptimec-Miettinen module and the TCFE6 database (Figure V. 3). The composition of the stack falls into the two-phase  $\alpha+\gamma$  region according to TCFE6. This database is therefore not suited since experiments of chapter III have shown that dissolution is complete at this temperature. Since the Ptimec-Miettinen description predicts a fully austenitic equilibrium at 1240°C, it will hence be used for the computation of our experiments at this temperature.

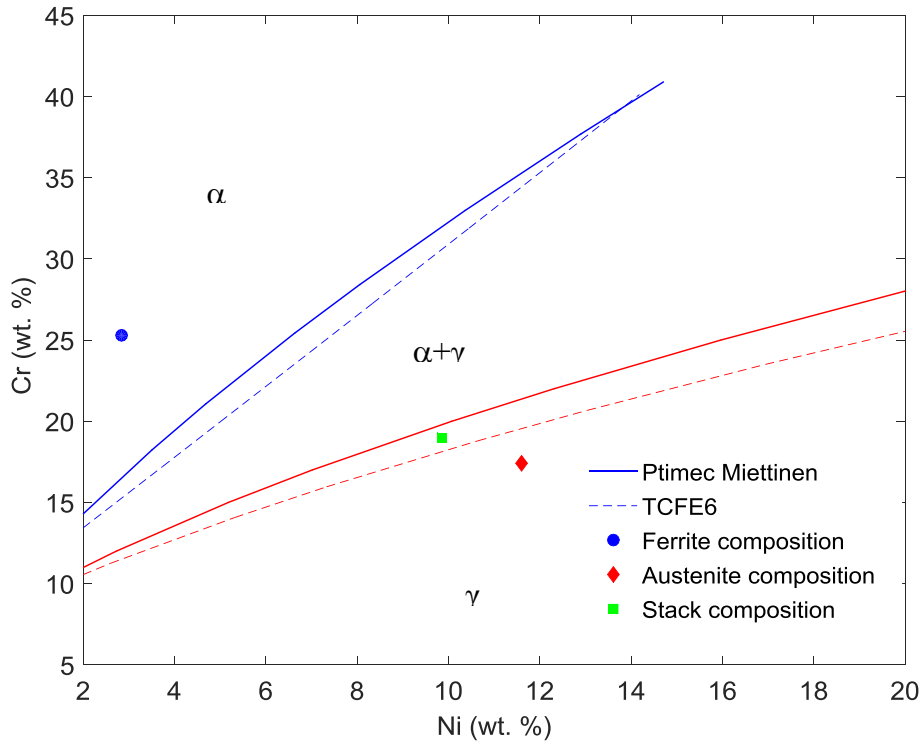


Figure V. 3: : Composition of ferrite, austenite and the whole stack superimposed on the isothermal section of the Fe-Cr-Ni phase diagram at 1240°C calculated using the Ptimec-Miettinen module (solid lines) and the TCFE6 database (dashed lines).

#### II.1.b. Interdiffusion coefficients

Interdiffusion coefficients of Cr and Ni in ferrite and austenite are calculated using DICTRA<sup>®</sup> software and MOB2 mobility database [72]. Given that the microstructure in all states possess approximately the same Cr and Ni contents (Chapter III, §II.2.e. Summary), only one set of interdiffusion coefficients will be used for all simulations for the sake of

simplicity. The interdiffusion coefficients are computed at ferrite and austenite compositions in the as-received HR1 state (Table V. 1).

**Table V. 1: Interdiffusion coefficients of chromium and nickel in ferrite and austenite computed by DICTRA<sup>®</sup> software and MOB2 database [72].**

	Composition (wt. %)	$D_{CrCr}$ (m <sup>2</sup> /s)	$D_{NiNi}$ (m <sup>2</sup> /s)
Ferrite	25.3 Cr - 2.9 Ni	$9.3 \cdot 10^{-13}$	$1.2 \cdot 10^{-12}$
Austenite	17.4 Cr - 11.6 Ni	$2.2 \cdot 10^{-14}$	$1.0 \cdot 10^{-14}$

### II.1.c. Design of the calculation cell

In chapter III, it has been shown that, in each state (HR1, CR1, HR2 and CR2), ferrite and austenite bands 6 to 9 possess similar thicknesses. The average value of these thicknesses will thus be considered as a characteristic size of ferrite and austenite bands in the calculation cell. Given the planar symmetry of the multilayered microstructures, the diffusion problem is solved in a representative elementary volume (REV) composed of half the thicknesses of ferrite and austenite bands, as shown in Figure V. 4.a. Supplementary calculations are carried with the minimum and maximum ferrite half thicknesses in order to take into account the local variation of the thickness of ferrite bands in the numerical predictions.

The calculation cell used for the simulations is shown in Figure V. 4.b. The ferrite region is meshed with 20 equally separated grid points. It is to be noted that the meshing size in ferrite has no significant influence on the dissolution calculations (Appendix F). Finer mesh near the interface is therefore not needed. On the contrary, in austenite, double-uniform meshing with 200 grid points is used in order to obtain mesh insensitive results. This mesh comprises 100 equally spaced grid points in the vicinity of the interface to capture Cr and Ni gradients and a coarser mesh with 100 grid points in the rest of the domain.

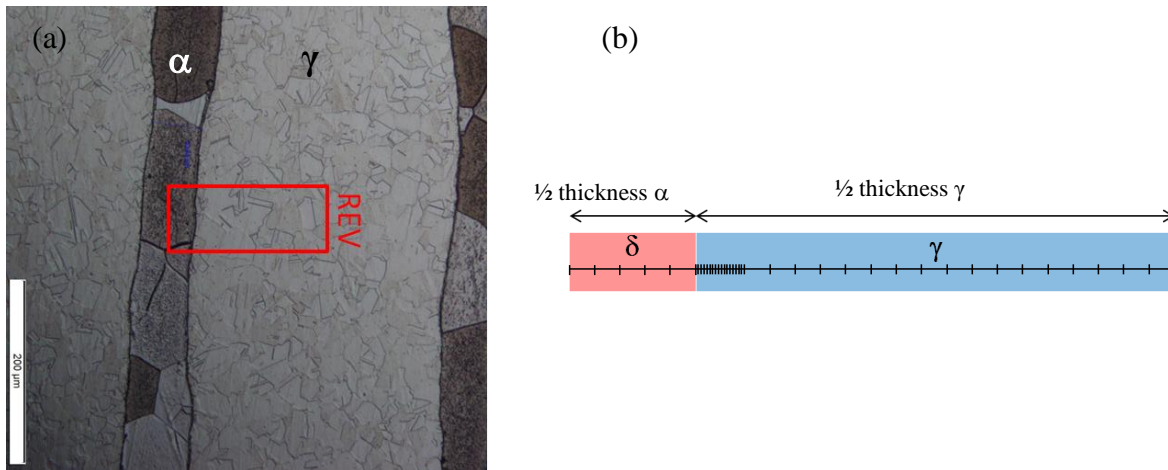


**Figure V. 4: (a) Representative elementary volume (REV) used in calculations of the dissolution of ferrite bands at 1240°C. (b) Calculation cell with meshing distribution in ferrite and austenite regions.**

Composition profiles of Cr and Ni in ferrite and austenite in the as-received states (*Chapter III, §II.1. Microstructures in the as-received states*) are flat except in the vicinity of the interface where gradients are established at a small extent owing to the HIP and HR thermal cycles. For simplicity, it has been decided to assume flat composition profiles in each phase region of the calculation cell. The effect of solute gradients on the dissolution kinetics will be discussed in the next *§II.3. Discussion*.

## II.2. Application to ferrite dissolution

### II.2.a. After the first hot rolling (HR1)

The input parameters for simulations are listed in Table V. 2: initial Cr and Ni compositions in ferrite and austenite as well as their half thicknesses in the as-received state.

**Table V. 2: Initial chromium and nickel compositions and average half thicknesses of ferrite and austenite phase regions in the HR1 state. Minimum and maximum half-thickness of ferrite are listed as well.**

	Cr (wt. %)	Ni (wt. %)	½ thickness (µm)
Ferrite	25.3	2.9	33 <sup>45</sup> <sub>25</sub>
Austenite	17.4	11.6	134

Calculated dissolution kinetics of ferrite bands with the minimum, average and maximum thicknesses are shown in Figure V. 5. The experimental dissolution of ferrite bands 6 to 9 are superimposed as well. The model reproduces quite well the general tendency of the observations: with the average ferrite thickness the dissolution is predicted to occur after 177h against 164h by experiments and the initial growth is quantitatively reproduced only for ferrite band 6 but seems underestimated for bands 7 to 9. Minimum and maximum thickness calculations permit to envelop the scattering of the experimental results but should be considered for the prediction calculations.

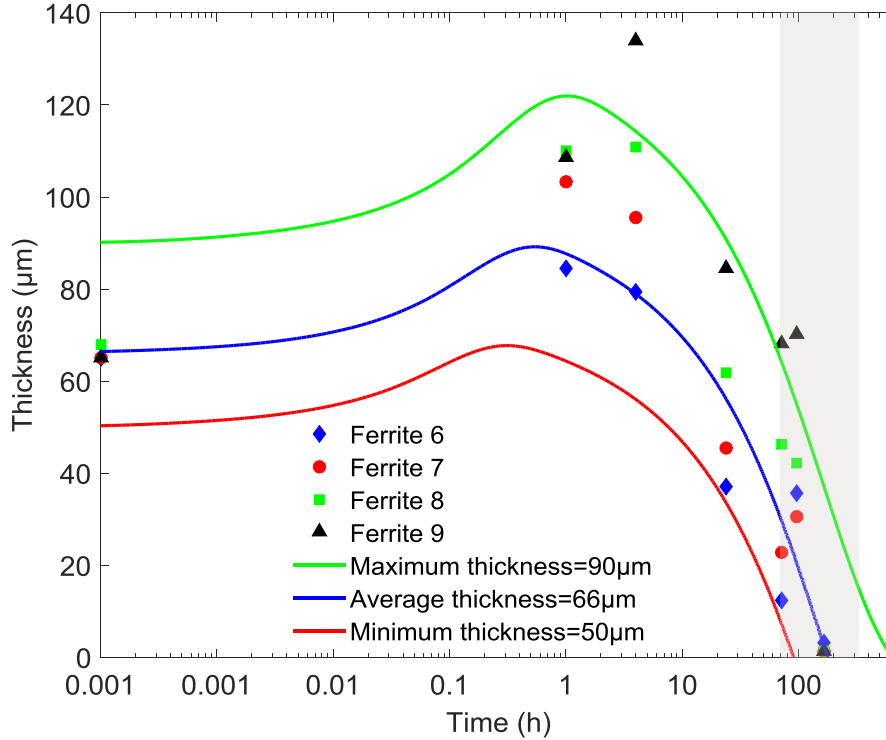


**Figure V. 5: Experimental and computed ferrite thickness as a function of the annealing time at 1240°C in the microstructure in the HR1 state. Calculations are carried with the minimum, average and maximum ferrite thicknesses.**

Computed composition profiles in ferrite and austenite are compared to EPMA results in Figure V. 6. Excellent agreement between calculated and observed Ni profiles is obtained at each annealing time. This makes the chosen  $D_{NiNi}^Y$  in simulations appear to be very adequate, though  $D_{NiNi}^Y$  was initially supposed not to depend on composition (see Appendix D). Further, computed Ni compositions at the ferritic and austenitic sides of the interface are consistent with the experiments, a result that makes the use of the Ptimec-Miettinen module more pertinent.

Regarding Cr profiles, agreement between computations and experiments is also satisfactory but at a lesser extent. In fact after 1hr and 72hrs annealings, computed gradients in austenite are less steep than EPMA results. This is explained twofold: by the choice of  $D_{CrCr}^Y$  that seems to slightly overestimate the real diffusion of Cr in austenite and by the underestimated solubility of Cr in austenite as it can be seen in Figure V. 6.a, c. On the other side, the model overestimates Cr profiles in ferrite after 4hrs and 96hrs annealings, which is due to the used thermodynamic description that raises the solubility limit of Cr in ferrite.

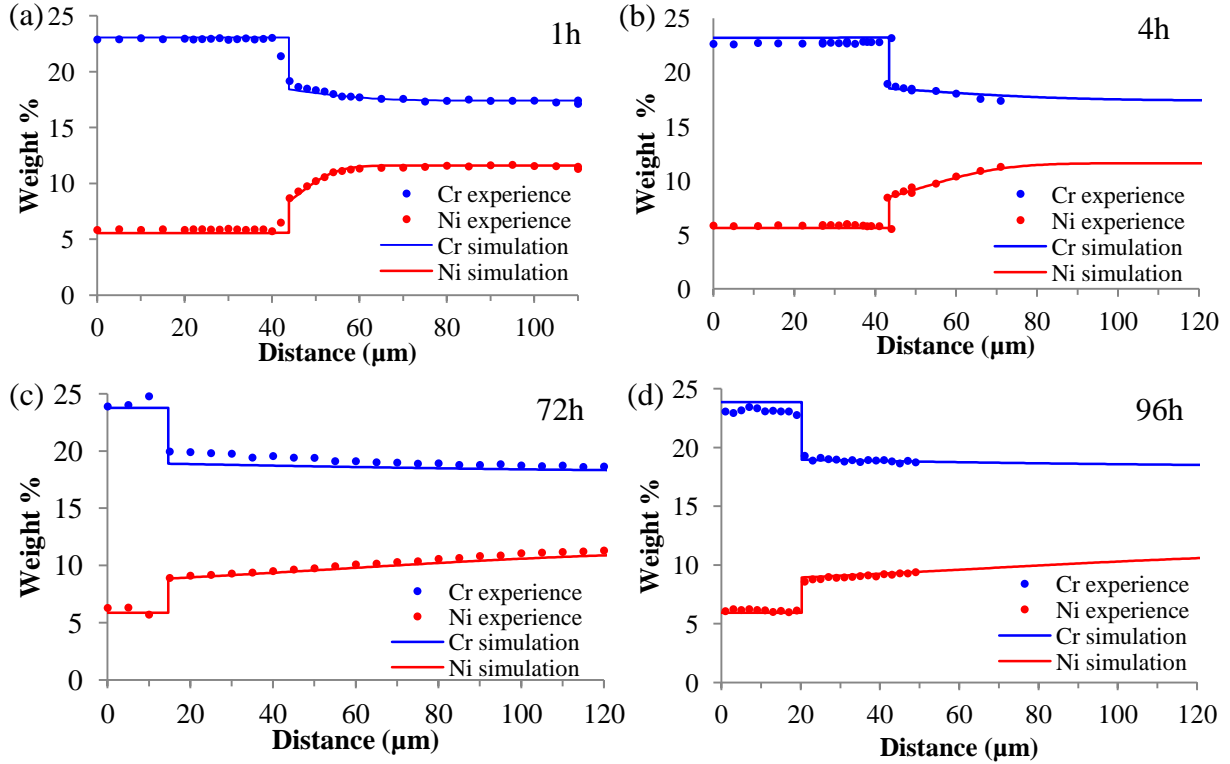


**Figure V. 6:** Experimental and computed composition profiles normal to the  $\alpha/\gamma$  interface in the multilayered microstructure in the HR1 state after (a) 1hr, (b) 4hrs, (c) 72hrs and (d) 96hrs annealings at 1240°C.

In Figure V. 7 measured compositions of Cr and Ni at the interface are reported on the isothermal section of the Fe-Cr-Ni phase diagram at 1240°C. Ptimec-Miettinen and TCFE6 descriptions are superimposed for comparison. With regard to the EPMA results, the TCFE6 description is not suited since the  $\gamma/(\alpha+\gamma)$  phase boundary is largely shifted towards higher Ni and lower Cr solubility in austenite. This provides thus additional experimental evidence for the inadequacy of the TCFE6 database for thermodynamic description of the present system at 1240°C. On the contrary, the Ptimec-Miettinen description is in very satisfactory agreement with experiments. As stated in the previous paragraph, the Cr solubility in ferrite slightly overestimates the experimental measurements. On the other side, the  $\gamma/(\alpha+\gamma)$  phase boundary is well positioned with respect to the measured compositions at the interface, though it slightly overestimate Ni solubility and underestimates Cr solubility. This shift in solubility should be kept in perspective as the measurement of interface compositions is not very accurate, given the low spatial resolution of the EPMA (2 $\mu\text{m}$ ). In addition, the interaction volume (under an acceleration voltage of 15-20keV) is on the order of 1 $\mu\text{m}^3$  for relatively heavy elements like Fe, Cr and Ni. Accordingly, if the probe falls on the  $\delta/\gamma$  interface, measurements can be altered by the surrounding elements from the other phase.

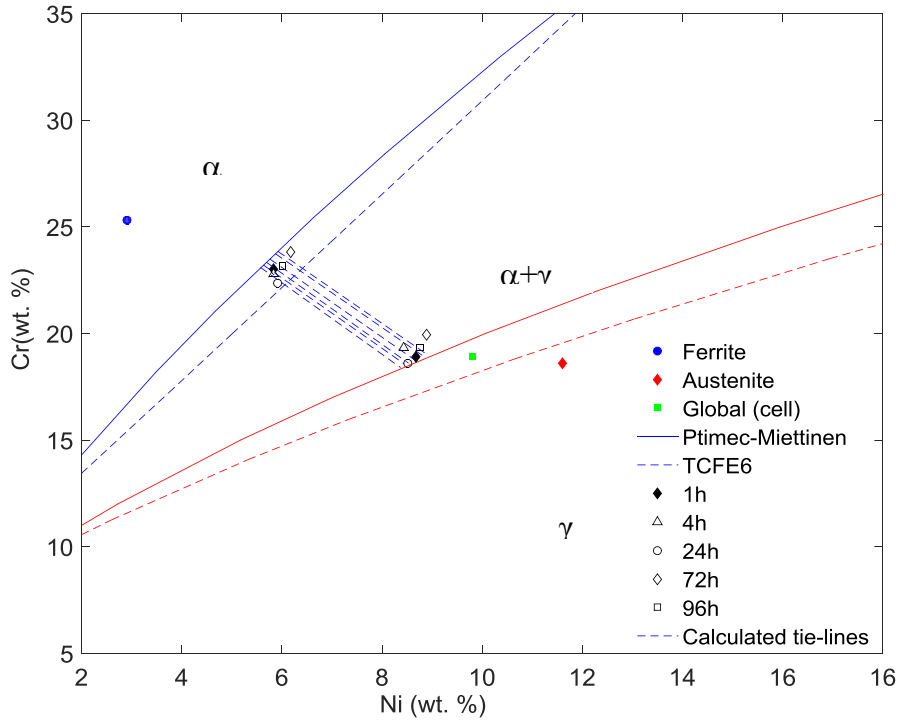


**Figure V. 7:** Chromium and nickel compositions at the  $\alpha/\gamma$  interface during ferrite dissolution in the HR1 state at 1240°C. The calculated tie lines (dashed blue lines) are compared to experimental results and superimposed on the ferritic and austenitic phase boundaries calculated using the Ptimec-Miettinen module (solid lines) and the TCFE6 thermodynamic database (dashed lines).

As a complementary validation of this model, the deviation from perfect mass conservation of Cr and Ni was checked and is presented in Figure V. 8. The relative mass loss is -0.06% for Cr and -0.03% for Ni, which is considered as very satisfactory.

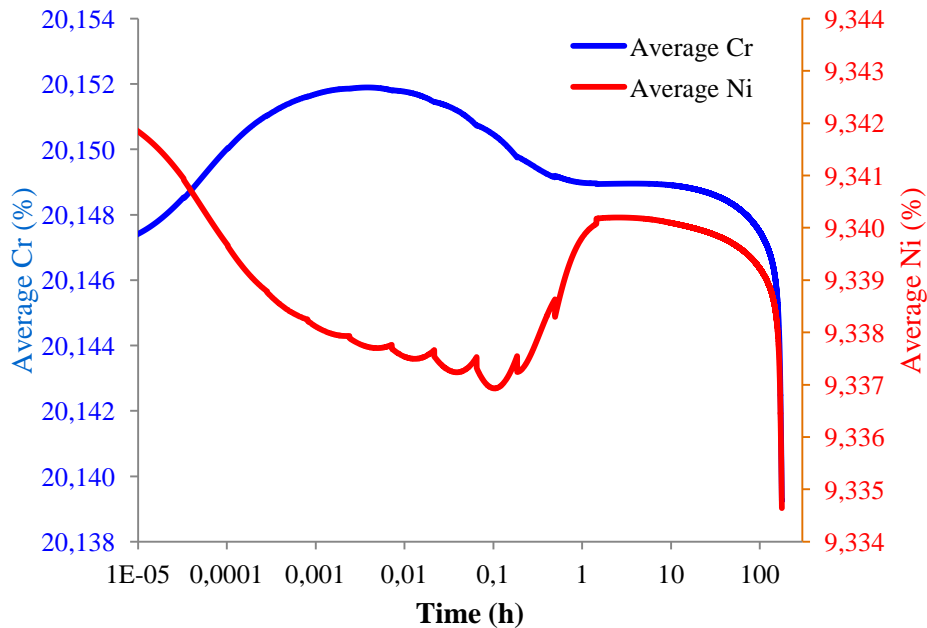


**Figure V. 8:** Relative deviation from perfect mass conservation of chromium and nickel in the simulation of ferrite dissolution ion the HR1 microstructure at 1240°C.

### II.2.b. After the first cold rolling (CR1) and the second hot rolling (HR2)

The initial Cr and Ni profiles as well as half thicknesses of ferrite and austenite in the CR1 and HR2 states are listed in Table V. 3.

**Table V. 3: Initial chromium and nickel compositions and average half thicknesses of ferrite and austenite phase regions in the CR1 and HR2 states. In the CR1 state, two ferrite initial thicknesses are considered in calculations.**

State	Phase	Cr (wt. %)	Ni (wt. %)	½ thickness (µm)
CR1	Ferrite	25.3	2.9	16/21 <sub>12</sub> <sup>24</sup>
	Austenite	17.4	11.6	73
HR2	Ferrite	25.1	3.8	4.4 <sub>2</sub> <sup>7</sup>
	Austenite	17.4	11.6	17

In CR1, half-thicknesses of ferrite bands 6 to 9 are not equal: 16µm (ferrite 6 and 7) and 21µm (ferrite 8 and 9, see Figure III. 25.c). Although non negligible, this difference in thickness did not significantly impact the experimental dissolution kinetics of ferrite bands 6 to 9, as the scattering in ferrite thicknesses is very limited from one band to the other (Figure III. 34). In the present simulations, calculations will however be carried out with both initial thicknesses and the most appropriate one will then be chosen.

Figure V. 9 shows the evolution with time of ferrite thickness as predicted by the simulation, in comparison with the experimental results in the CR1 state. With the half-thickness of 16µm, the general dissolution tendency is qualitatively well reproduced, though complete dissolution is predicted to occur after 46hrs against 96hrs experimentally. Better prediction is however obtained with 21µm as complete dissolution is expected after 98hrs. This result shows the sensitivity of the calculations to the input parameters: here we considered an increase of 30% in the initial half-thickness of ferrite and the resultant dissolution duration is doubled.

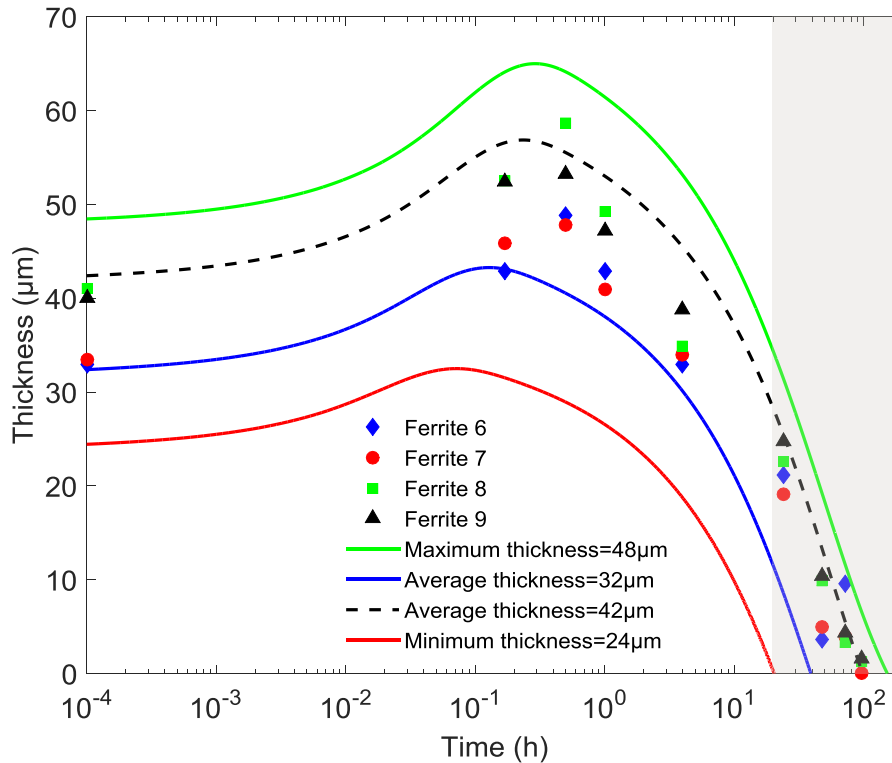


**Figure V. 9** Experimental and computed relative ferrite thickness as a function of the annealing time at 1240°C in the CR1 state.

For the HR2 state, it is to be noticed that the amount of Cr and Ni in ferrite in the HR2 state are respectively slightly lower and higher than those in the CR1, because of the additional HIP and HR cycles the HR2 microstructures undergone. Dissolution calculations (Figure V. 10) are in good agreement with experimental data as dissolution ends after 3h in both cases. The scattering of the experimental data is well enveloped by dissolution curves corresponding to minimum and maximum ferrite thicknesses. The growth stage of ferrite is not experimentally assessed since, as shown by calculations, it ends at a much earlier time than the first measurement of ferrite thickness (5min).

It can be remarked that the spread between the upper and lower dissolution curves is becoming larger as the scale of the microstructure is reduced by successive rollings: in the HR1 and CR1 states, this spread can be measured by the ratio between the lower and the upper dissolution durations which equals  $t_{max}/t_{min}$  7 and 7.5 respectively for an initial ratio between maximum and minimum ferrite thicknesses of 1.4 in both states. In the HR2 state, with the maximum ferrite thickness, the global composition of the calculation cell lies in the  $\alpha+\gamma$  region of the phase diagram at 1240°C as final thickness stabilizes at approximately 2 $\mu$ m (Figure V. 10). This stems from the fact that, since the variation of local ferrite thickness in the as-received HR2 state is nearly twice as high as in the HR1 and CR1 states (2.5 against 1.4), simulation with the maximum thickness elevates fraction of ferrite in the calculation cell from the initial 20% to 30% and the whole system is thus brought to the  $\alpha+\gamma$  equilibrium.

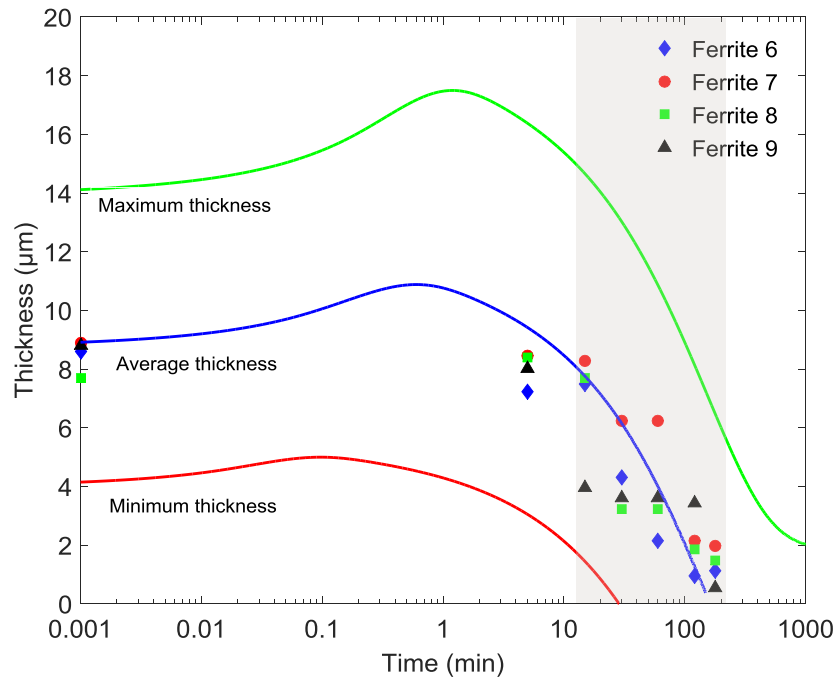


**Figure V. 10: Experimental and computed relative ferrite thickness as a function of the annealing time at 1240°C in the HR2 microstructure.**

Computed composition profiles are compared to EPMA results in Figure V. 11 and Figure V. 12 for the CR1 and the HR2 states respectively. Like the HR1 state, calculated profiles are in very good agreement with the experiments, especially in the case of Ni. A slight steepness in Cr gradients in austenite is still observed in computed Cr profiles, which may suggest a rather overestimated  $D_{CrCr}^{\gamma}$  in calculations.

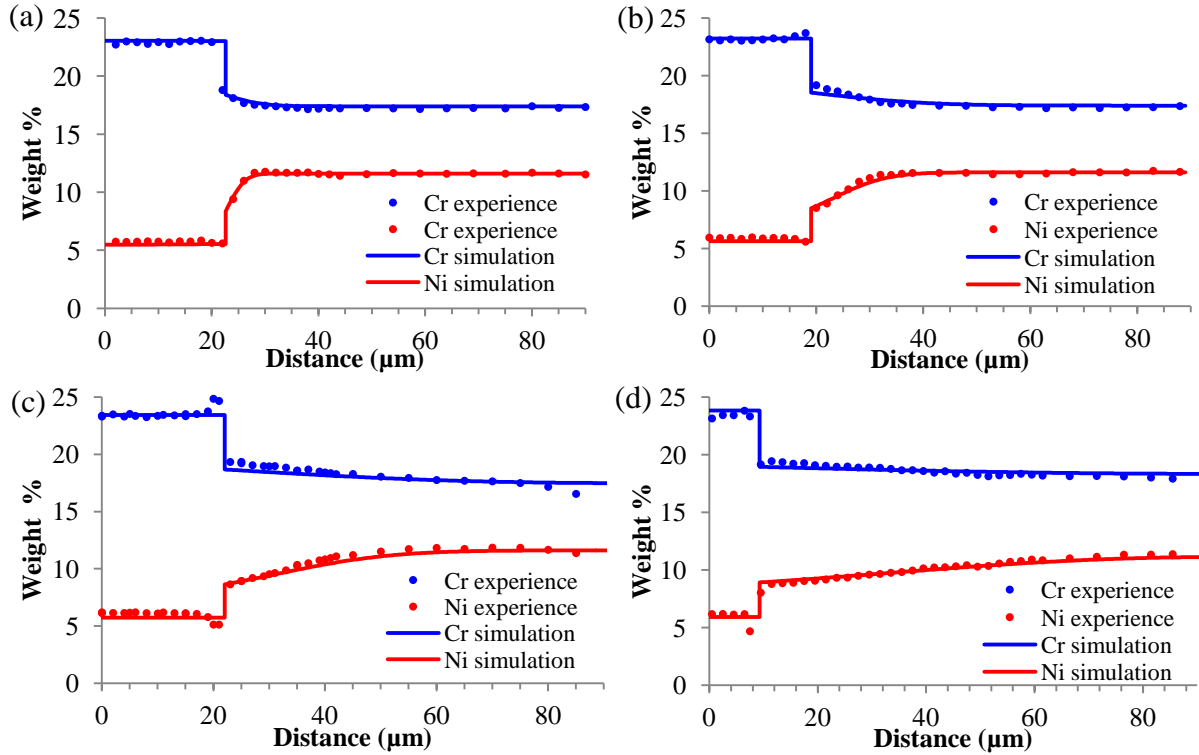


Figure V. 11: Experimental and computed composition profiles normal to the  $\alpha/\gamma$  interface in the multilayered microstructure at the CR1 state after (a) 10 min (b) 1hr, (c) 4hrs and (d) 24hrs annealings at 1240°C.

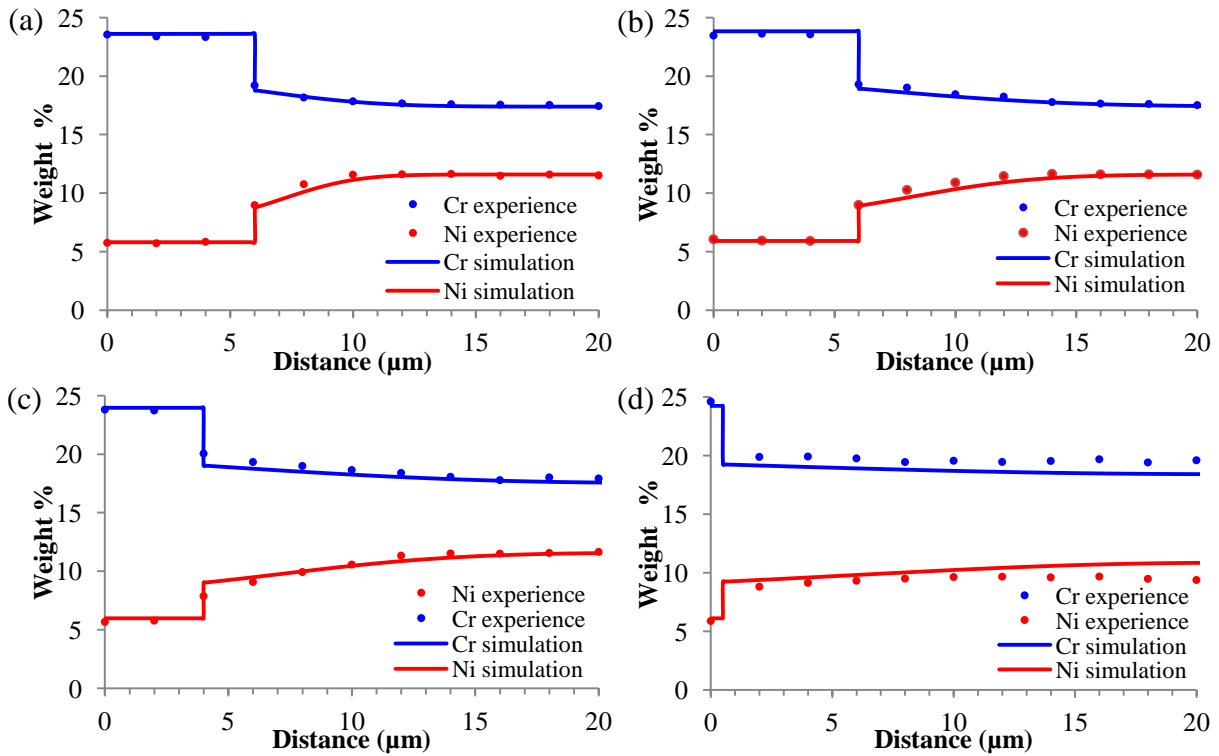
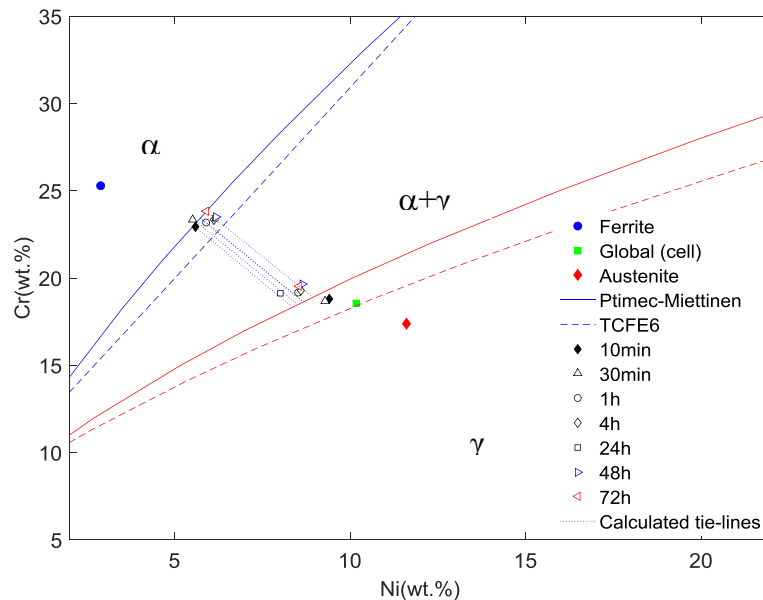
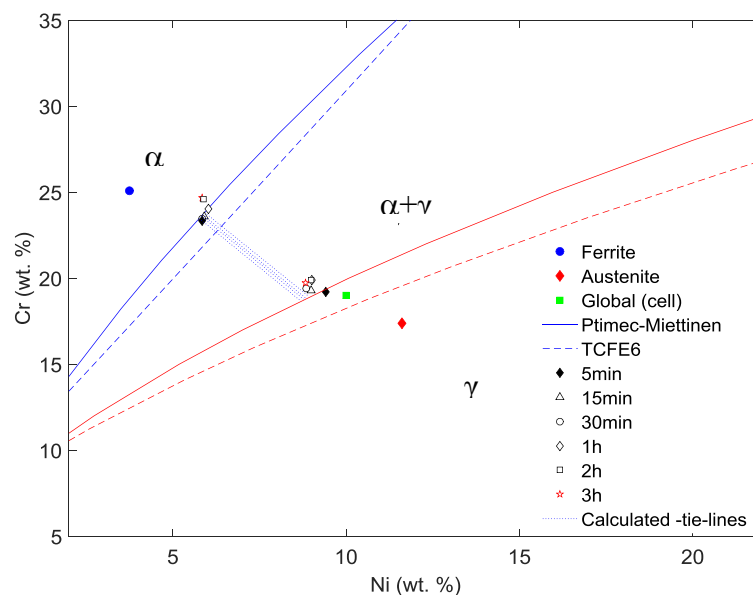


Figure V. 12: Experimental and computed composition profiles normal to the  $\alpha/\gamma$  interface in the multilayered microstructure at the HR2 state after (a) 5min (b) 15min, (c) 30min and (d) 2hrs annealings at 1240°C.

Computed tie-lines are compared to experiments in Figure V. 14 and 12. Agreement is excellent on the ferrite phase boundary, while in austenite a slight shift towards higher Ni and lower Cr solubilities is to be noticed. Knowing that this shift is to be considered in relative terms, because EPMA measurement are not very resolute, it is clear that the Ptimec-Miettinen thermodynamic description of the Fe-Cr-Ni phase diagram at 1240°C is very satisfactory.



**Figure V. 13: Chromium and nickel compositions at the  $\alpha/\gamma$  interface during ferrite dissolution in the (a) CR1 state at 1240°C. The calculated tie lines (dotted blue lines) are compared to experimental results and superimposed on the ferritic and austenitic phase boundaries calculated using the Ptimec-Miettinen module (solid blue lines) and the TCFE6 thermodynamic database (dashed blue lines).**



**Figure V. 14: Chromium and nickel compositions at the  $\alpha/\gamma$  interface during ferrite dissolution in the HR2 state at 1240°C. The calculated tie lines (dotted blue lines) are compared to experimental results and superimposed on the ferritic and austenitic phase boundaries calculated using the Ptimec-Miettinen module (solid blue lines) and the TCFE6 thermodynamic database (dashed blue lines).**

### II.2.c. After the second cold rolling (CR2)

Up to now, the developed model was able to predict the kinetics of ferrite dissolution in the Kajihara's experiments and in the multilayered microstructures in the HR1, CR1 and HR2 states. At this stage, it was chosen to perform the modeling prior to the experimental work, on the basis of the characterization of the as-received CR2 state. Initial phase compositions and sizes are shown in Table V. 4.

**Table V. 4: Initial chromium and nickel compositions and average half thicknesses of ferrite and austenite phase regions in the CR2 state. Minimum and maximum half-thickness of ferrite are listed as well.**

	Cr (wt. %)	Ni (wt. %)	½ thickness (µm)
Ferrite	25.6	3.7	$1.8_1^{3.5}$
Austenite	17.6	11.7	7

Predicted kinetics of ferrite dissolution are shown in Figure V. 15.a and complete dissolution is expected to occur after 30min. Then, experimentally, dissolution was initially investigated for 30min, but ferrite bands 6 to 9 appear not completely dissolved (Figure V. 17.a). The experimental dissolution kinetics was then established for various other holding times (Figure V. 15) and shows that the end of the dissolution occurs after between 1 and 1.5hr as shown in the micrographs of Figure V. 17.b. Nevertheless, scattered experimental results are well enveloped by dissolution calculations with minimum and maximum thicknesses. This discrepancy is caused by the high variability encountered in the measurement of the average band thicknesses and initial Cr and Ni contents in ferrite (*Chapter III, §II.2.d. Microstructure after the second cold rolling*). The sensitivity of the prediction to both parameters will be discussed in *§II.3. Discussion*.

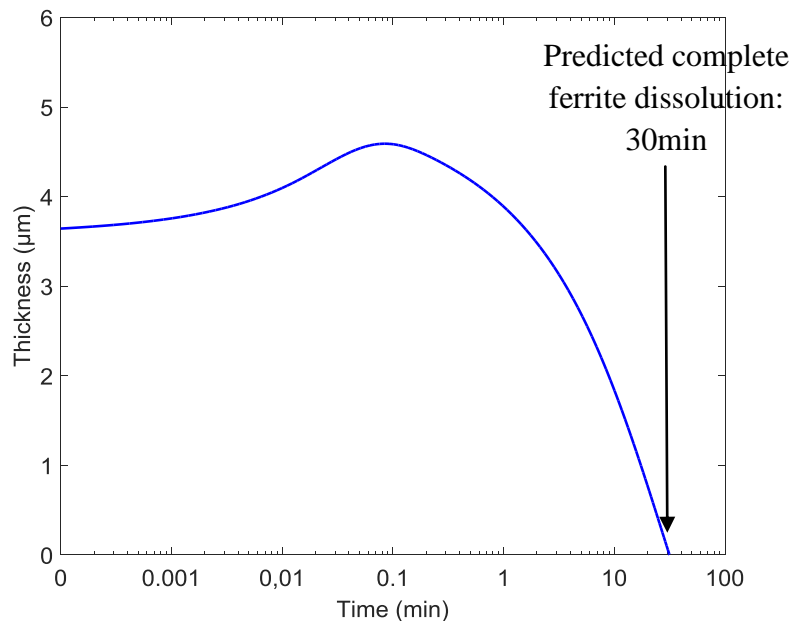


**Figure V. 15: Predicted dissolution kinetics of ferrite in the CR2 state using the average thickness value (3.6µm). Predicted dissolution is complete after 30min.**

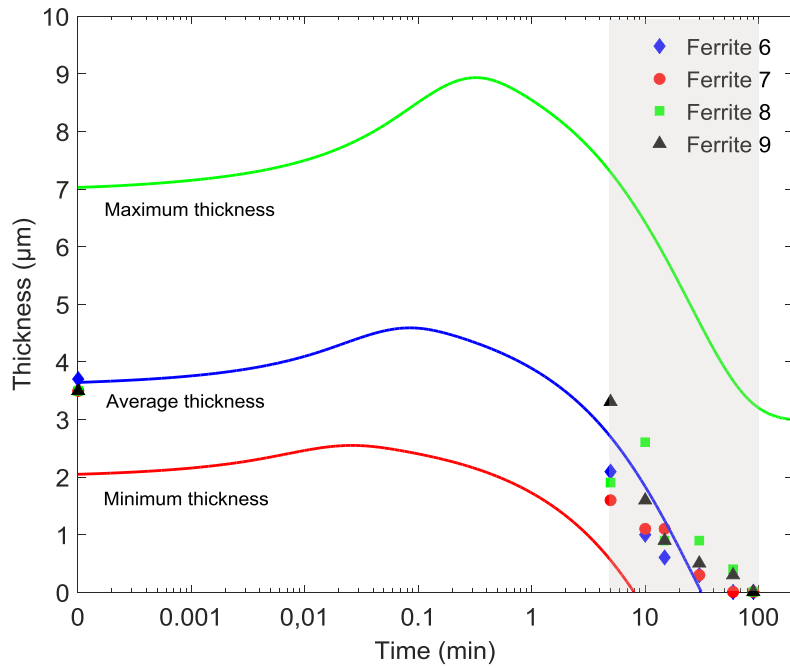


Figure V. 16: Experimental and computed ferrite thickness as a function of the annealing time at 1240°C in the CR2 microstructure.

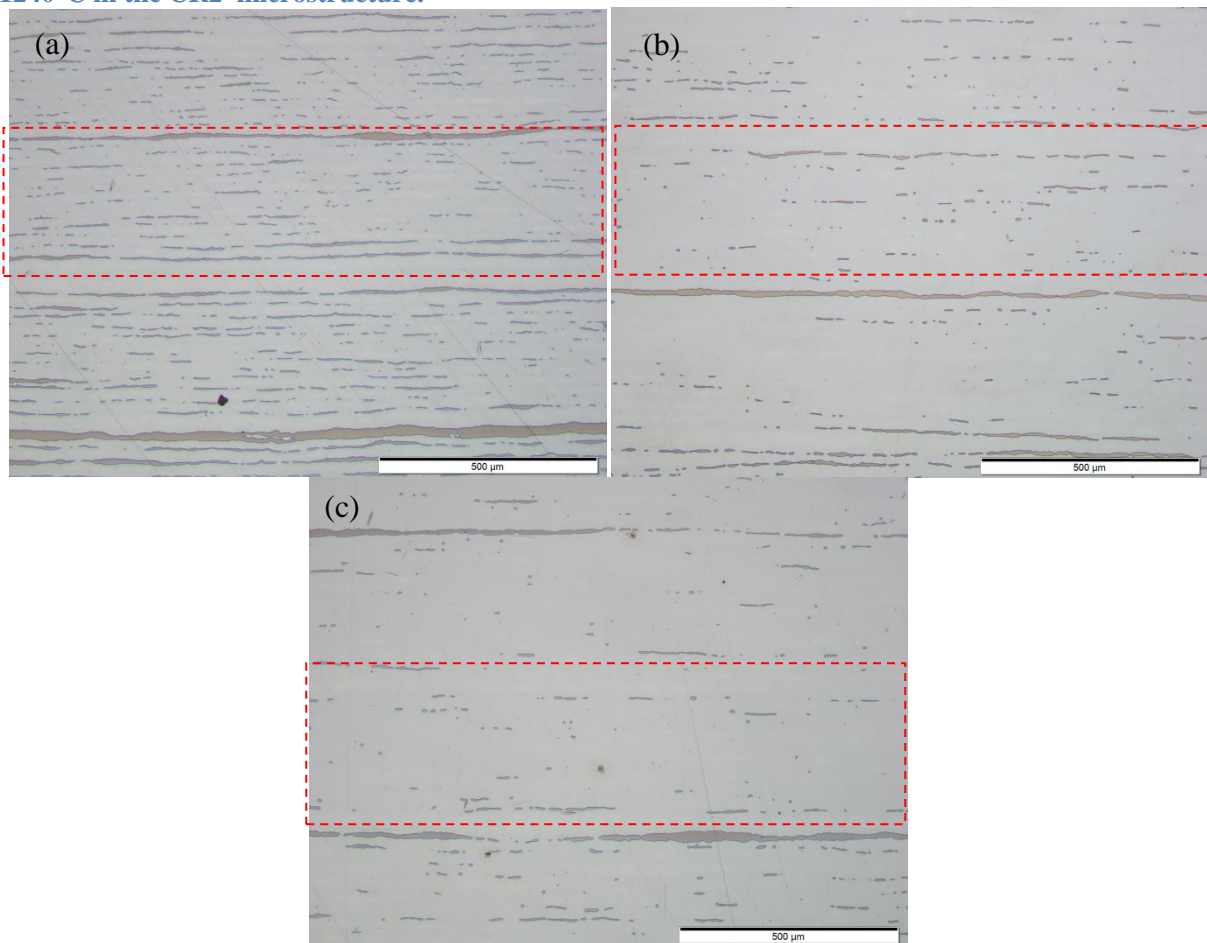


Figure V. 17: Multilayered microstructure in the CR2 state after (a) 30 min, (b) 1hr and (c) 1.5hr annealings at 1240°C (NaOH etching). Dissolution of ferrite was investigated in ferrite bands 6 to 9 in the central plate in each microstructure (dashed rectangle).

## II.3. Discussion

### II.3.a. Early growth of ferrite

The transient growth of ferrite at the early stage of the transformation is evidenced in the microstructures at the HR1 and CR1 states. This thickening behavior has been qualitatively explained by Kajihara *et al.* [36] in their experimental study of ferrite dissolution in Fe-Cr-Ni diffusion couples (Chapter I). The growth of ferrite comes as a direct result of a sufficiently high Cr and Ni gradients in ferrite coupled to a high  $D^\alpha/D^\gamma$  ratio ( $\approx 30$  at 1240°C, see Appendix D). It occurs if the criterion:

$$\frac{\Delta X_k^\alpha}{\Delta X_k^\gamma} > \sqrt{\frac{D_{kk}^\gamma}{D_{kk}^\alpha}} \quad (\text{V.1})$$

is satisfied, where  $\Delta X_k^\alpha$  and  $\Delta X_k^\gamma$  are the gap in composition at the beginning of the transformation between the interface and the bulk in ferrite and austenite respectively and  $D_{kk}^\alpha$  and  $D_{kk}^\gamma$  are interdiffusion coefficients of solute k in ferrite and austenite respectively (Figure V. 18). In the present microstructures this criterion is satisfied and the growth of ferrite is predicted by modeling even though, in the HR2 and CR2 states, early growth was not experimentally evidenced since it occurs over times less than 1 min.

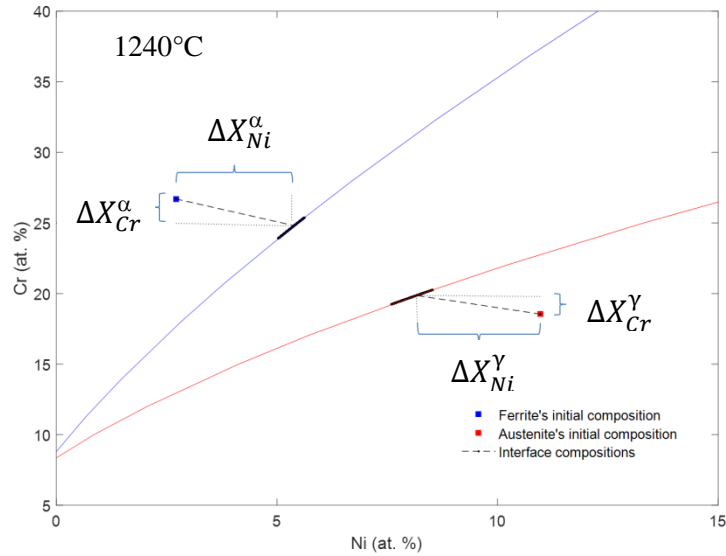


Figure V. 18: Schematics of the gap of composition between interface and bulk in ferrite and austenite at the beginning of the transformation superimposed on the isothermal section of the Fe-Cr-Ni phase diagram at 1240°C.

### II.3.b. Dissolution of ferrite

Table V. 5 summarizes the predicted and the experimental dissolution durations of ferrite in the HR1, CR1, HR2 and CR2 states. It shows that numerical computations performed with average ferrite thicknesses successfully predicted the dissolution kinetics of ferrite bands in the HR1, CR1 and HR2 states, whereas in the CR2 state, they underestimated the dissolution duration by factor of 2.

**Table V. 5: Comparison between experimental and calculated dissolution durations of ferrite at the HR1, CR1, HR2 and CR2 states.**

Duration (h)	HR1	CR1	HR2	CR2
1/2 thickness $\alpha$ ( $\mu\text{m}$ )	33	21	4.4	1.8
Experimental dissolution (h)	164	96	3	1
Calculated dissolution (h)	177	98	3	0.5

In the next paragraphs we will analyze these computational results in view of the relevance of the input parameters and the hypotheses underlying the numerical model.

### **i. Relevance of the input parameters**

#### **i.1. Sensitivity to the initial thickness of ferrite**

This parameter has the highest impact on the quantitative predictions of the numerical model. The CR1 and CR2 cases are illustrative. In the CR1 case, calculations have shown that with ferrite half-thicknesses of 16 $\mu\text{m}$  and 21 $\mu\text{m}$  dissolution durations is doubled.

As for the CR2 case, the discrepancy between calculations and experiments (Table V. 5) should be kept in perspective with the fact that, given the very fine thickness of ferrite bands in this state, measurements uncertainties may greatly affect its average value in the as-received state (1/2 thickness = 1.8  $\mu\text{m}$ ). To demonstrate this, supplementary calculations are carried out with initial ferrite half-thicknesses of 1.9 and 2 $\mu\text{m}$  and corresponding results are compared to the initial simulation in Figure V. 19. The predicted end of the transformation increases from 30 to 42min when initial thickness increases to 1.9 $\mu\text{m}$  and reaches 50min for 2 $\mu\text{m}$ . It is thus clear that small measurement errors could significantly alter the quantitative prediction of the model in this state of the microstructure and that the initial discrepancy can relativized. Obviously, given that ferrite bands in the previous states are much thicker, the impact of these errors is less significant.

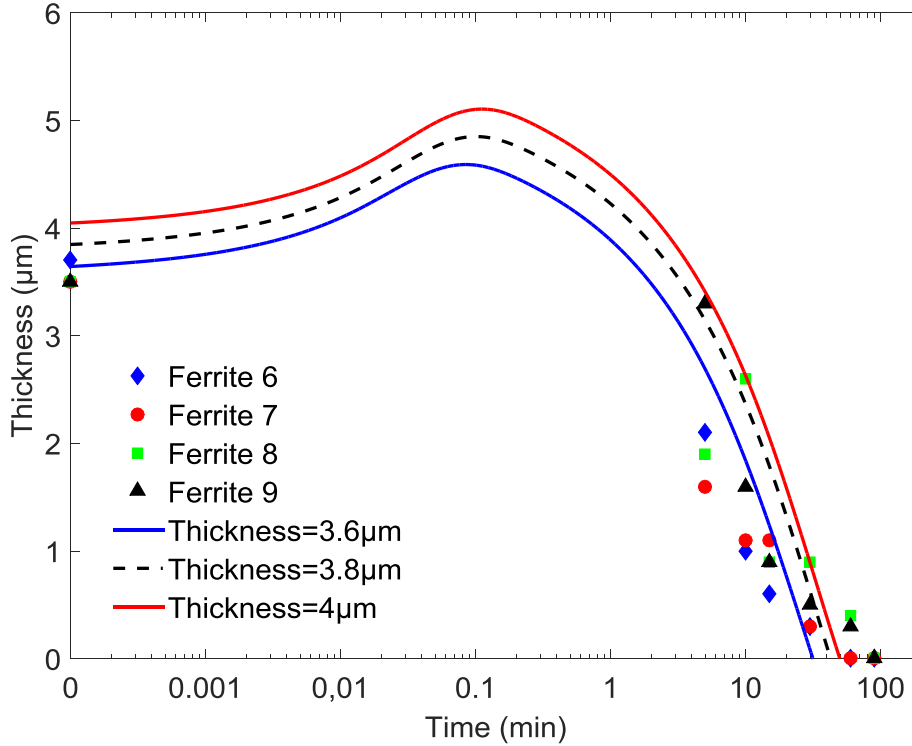


Figure V. 19: Sensitivity of the dissolution kinetics of ferrite in the CR2 state to the initial size of ferrite. Ferrite is predicted to disappear after 30min for a half-thickness of 1.8µm, after 42min for 1.9µm and after 50min for 2µm.

**i.2. CR2 state: sensitivity of the calculations to the initial ferrite composition**

It was shown in Chapter III, §II.2.d. *Microstructure after the CR2 state*, that Cr and Ni contents in ferrite bands showed a non negligible variability. The retained composition for the description of the as-received state were chosen in order to be consistent with the HR2 state (Table III. 7). The effect of composition variability on the dissolution kinetics of ferrite is tested with supplementary calculations by selecting different Cr and Ni contents from the EPMA measurements of Figure III. 30. Table V. 6 lists the used compositions and the resultant dissolution durations of ferrite. The variation in the content of Cr (-0.8%) slightly affected the dissolution of ferrite, while that of Ni (-1.4%) has a considerable impact, as dissolution is lengthened by more than 70%.

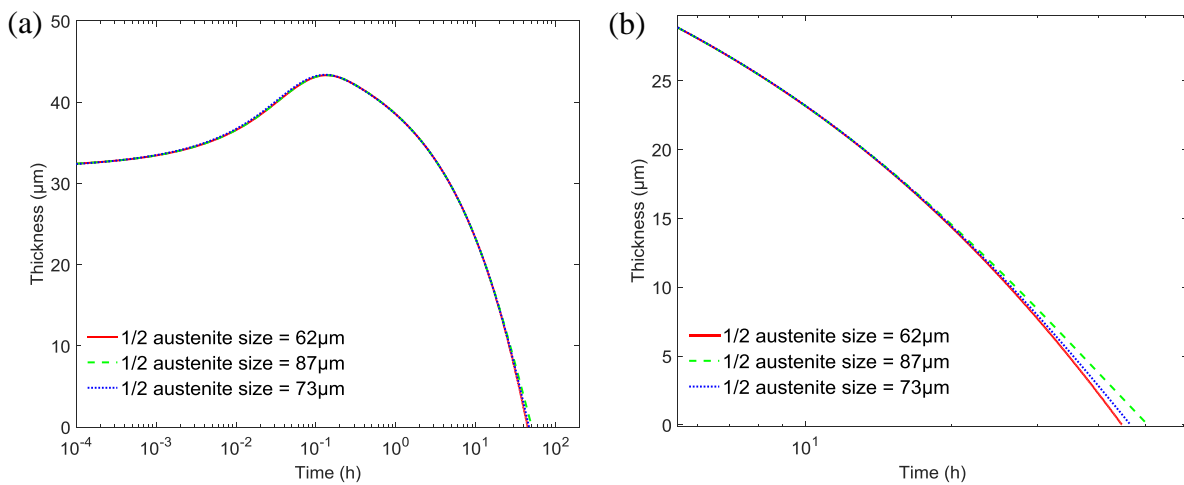
In conclusion, this impact together with that of variations initial thickness should moderate the initial discrepancy observed in the prediction of ferrite dissolution in the CR2 microstructure (§.II.2.c. *After the second cold rolling*).

Table V. 6: Possible chromium and nickel contents in ferrite bands in the CR2 microstructure and correspondent dissolution durations.

	Cr (wt. %)	Ni (wt. %)	Dissolution of
Reference case	25.6	3.7	30 min
Case 2	25.6	<b>2.3</b>	49 min
Case 3	<b>24.8</b>	3.7	32 min

### i.3. Sensitivity to the initial size of austenite

The impact of the size of austenite of the dissolution kinetics was studied with minimum ( $62\mu\text{m}$ ) and maximum ( $87\mu\text{m}$ ) half-thicknesses in the CR1 state and compared to the average value ( $73\mu\text{m}$ ) in Figure V. 20. Austenite size has a little effect on the dissolution kinetics as dissolution durations are predicted at 44h, 46h and 50h for maximum, average and minimum sizes respectively. It is to be noted that deviation between the three dissolution curves occurs only at advanced stages of the transformation (after 20h), where diffusion fields of Cr and Ni impinge in austenite (austenite is no longer considered as semi-infinite).



**Figure V. 20: (a) Dissolution kinetics of ferrite in the CR1 state for three initial austenite half sizes:  $62\mu\text{m}$ ,  $73\mu\text{m}$  and  $87\mu\text{m}$ . Ferrite's half-thickness is fixed at  $16\mu\text{m}$ . (b) The effect of the austenite size is perceptible only at advanced stages of the transformation (at the impingement).**

### i.4. Sensitivity to solute gradients in ferrite

For simplicity, simulations were carried out with initial uniform Cr and Ni contents, whereas in the as-received states, small gradients always exist at the interface due to the heating cycles of HIP and HR.

In austenite Cr and Ni composition gradients were not evidenced with EPMA measurements, given their very small spatial extent. The assumption of flat initial profiles in austenite is thus very appropriate. In ferrite, however, solute gradients are well established and their extent measures approximately  $10\mu\text{m}$  in the HR1 state (Figure III. 24),  $6\mu\text{m}$  in the CR1 state (Figure III. 25), and approximately  $2\mu\text{m}$  in the HR2 state (Figure III. 26) but not evidenced in the CR2 state (probably smaller than EPMA measurement steps).

The effect of the gradients in ferrite on the dissolution kinetics was tested on the CR1 state. Figure V. 21.a shows two initial profiles in the ferrite region: one being flat and the other taking into account the measured composition Cr and Ni gradients. The correspondent dissolution curves are compared in Figure V. 21.b. Compared to the uniform profile case, gradients contribute to lengthen the transformation from 46 to 50hrs (an increase of 9% in

dissolution's duration). This fact clearly indicates that Cr and Ni gradients in ferrite have a non negligible effect on the dissolution kinetics and that predicted dissolution of ferrite of Table V. 5 should be raised accordingly.

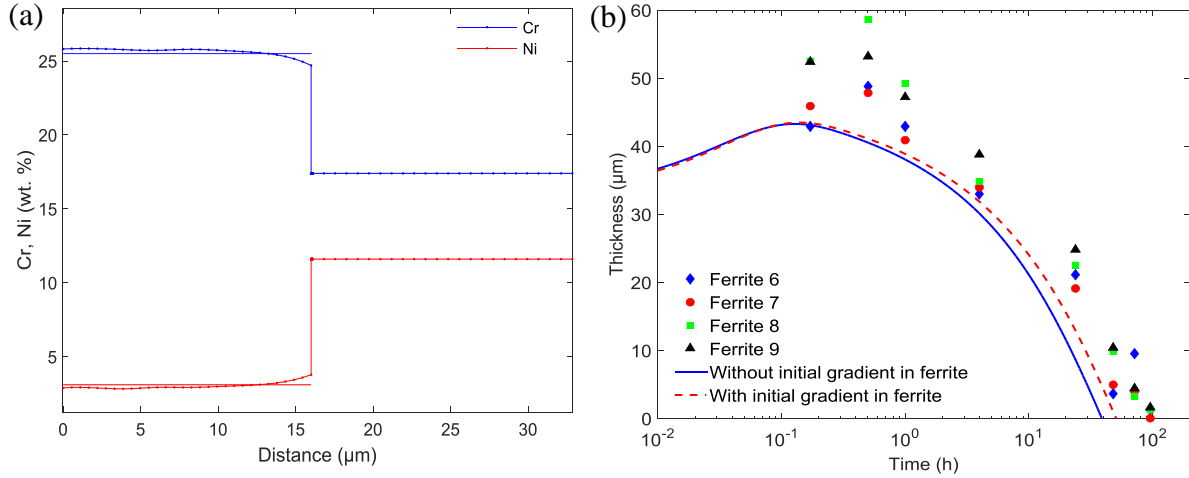


**Figure V. 21: Effect of (a) the initial composition gradients in ferrite on (b) the dissolution kinetics of ferrite in the CR1 state: with gradients dissolution occurs after 50hrs, against 46hrs without gradients.**

## **ii. The hypothesis of composition-independent interdiffusion coefficients:**

The issue of the accuracy of the interdiffusion coefficients should also be kept in perspective when considering quantitative predictions. As stated in Chapter IV, interdiffusion coefficients have been assumed to be composition-independent in the model. Actually, it is demonstrated in Appendix D that as austenite becomes enriched in Cr and depleted in Ni, *i.e.* when moving from the bulk of austenite towards the  $\alpha/\gamma$  interface, interdiffusion coefficients  $D_{CrCr}^Y$  and  $D_{NiNi}^Y$  decrease by 15% and 25% respectively. Thus, with interdiffusion coefficients used in the present simulations (Table V. 7), solute fluxes at the interface are virtually raised and, accordingly, we know that the rate of ferrite to austenite transformation is enhanced. In quantitative terms, complete ferrite dissolution can be shortened by up to 20%, in comparison with the case of the lowest possible  $D_{CrCr}^Y$  and  $D_{NiNi}^Y$  in the range of composition in austenite. This value can be regarded as the upper bound of the error committed by the composition-independence assumption. If the model were able to handle such composition dependency, the enhancement should be lower than 20% as interdiffusion coefficients will vary from the lowest to highest values in Cr and Ni composition ranges in austenite.

It can be retained from this analysis that, if composition-dependency of  $D_{CrCr}^Y$  and  $D_{NiNi}^Y$  is to be handled by the model, predicted dissolution durations of ferrite bands (Table V. 5) should be revised upwards.

In ferrite, the composition-dependency of  $D_{CrCr}^\alpha$  and  $D_{NiNi}^\alpha$  is however not necessary to be handled, since its impact on the kinetics of ferrite dissolution is negligible as demonstrated in Appendix D.

On the whole, what stems from these previous analyses is that, if the model was more refined, *i.e.* composition-dependency of interdiffusion coefficients and solute gradients in ferrite are taken into account, the calculations lead to a slower dissolution kinetics.

### **iii. Simple model vs. complex multilayered microstructure:**

Originally, the multilayered microstructures were designed to study the  $\alpha \rightarrow \gamma$  transformation in a configuration that can be easily modeled, *i.e.* with planar  $\alpha/\gamma$  interface and with Cr and Ni as the only diffusing solutes. However, experiments revealed that, in such microstructures, the transformation remains a rather complex phenomenon:

- In the model, the  $\alpha/\gamma$  interface is assumed to remain planar during all the calculation so that bulk interdiffusion in both phases depends only on the distance normal to the interface. In real microstructures, the planarity is very rapidly lost, particularly at the  $\alpha/\alpha$  grain boundaries (Figure III. 35). Thus the composition fields near the interface are more complex than expected. Besides, we may assume that upon the loss of planarity, the amount of the  $\alpha/\gamma$  interface tends to increase, compared to a planar one and dissolution would thus be expected to be more rapid than in the present predictions.

So far, the loss of planarity of the interface did not seem to be faulting the assumption of the planar interface in a sense that the model predicted quite accurately the dissolution kinetics of ferrite in all states. Or, if this is not the case, it is also possible to assume that the enhancement of the transformation rate due the loss of the interface planarity would balance the composition-dependency of interdiffusion coefficients which, as mentioned before, tends to lengthen the transformation kinetics.

- The transformation is assumed to be diffusion-controlled, which signifies that the transfer of atoms across the interface is very rapid compared to the movement of the interface. EPMA measurements normal to the  $\alpha/\gamma$  interface provided evidence for that, as solute gradients in austenite during the transformation are well developed near the interface (Figure III. 37). On the other hand, upon the breakup of ferrite bands into several isolated grains (Figure III. 35), ferrite grains preserve their elongated shape and the interfaces at the former  $\delta/\delta$  grain boundaries remain acute during dissolution. Further, measurement of Cr and Ni fields between two ferrite grains in the transversal direction (Figure III.32) show quasi-flat profiles in austenite, despite the fact that dissolution is not complete. Both facts may imply that, in the transverse direction of the multilayered microstructures, the interface is quasi stationary and that the transformation ceases to be diffusion-controlled but is probably interface-controlled. Interfacial energies between ferrite and austenite grains may play a role in such a phenomenon.

### **II.3.c. Interface compositions upon quenching**

In the measured composition profiles of the HR1 and CR1 states, it can be noticed that ferrite exhibits a slight Cr-enrichment and Ni-depletion at the interface whose extent is only few microns. An example of this observation is shown in Figure V. 22.a. These curved profiles are observed either in the early or the late stages of the transformation. They are not

characteristic of the  $\alpha \rightarrow \gamma$  transformation since profiles in ferrite flatten very rapidly, as shown experimentally and numerically (Figure V. 6). Furthermore, their very small extent indicates that they occur during a short-time process.

In the previous calculations the simulated heat treatments only comprises the isothermal holding. The heating and the quenching parts are neglected. A supplementary calculation was performed including a quench occurring after 4hrs annealing at 1240°C. The quench duration was fixed at 5s which is typical of that encountered experimentally and the temperature at the end of quenching was set to 900°C, below which we consider diffusion as negligible. Figure V. 22.b shows Cr and Ni profiles after the this heating cycle. At the ferritic side of the interface, Cr-enrichment and Ni-depletion reproduce very well the experimental results determined by EPMA (Figure V. 22.a). This composition change at the interface stems from the fact that the position of the  $\alpha/(\alpha+\gamma)$  phase boundary in the Fe-Cr-Ni phase diagram changes with decreasing temperature towards higher Cr and lower Ni solubilities.

As a conclusion, by non-isothermal calculations the model has shown that sample quenching is the cause of the composition peaks appearing at the interface.

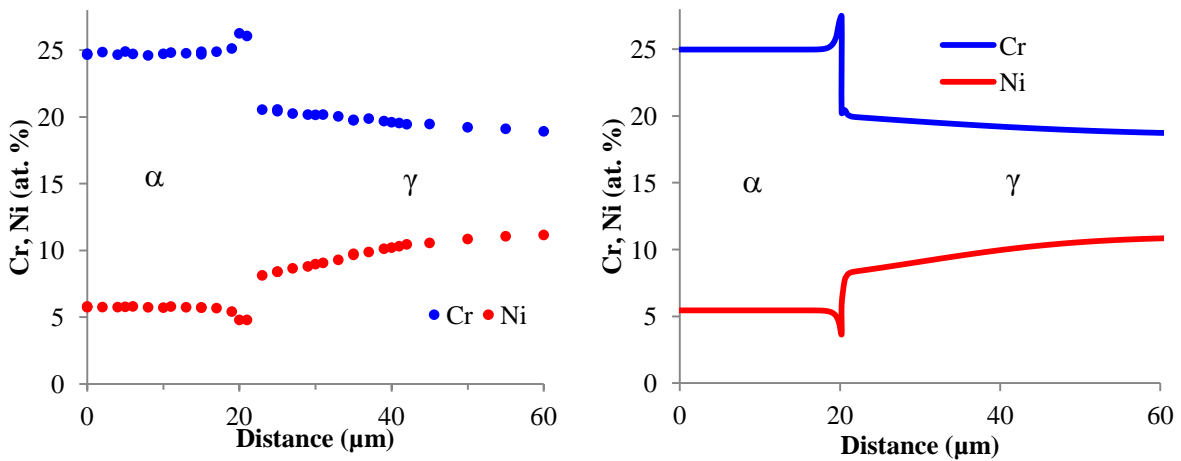


Figure V. 22: (a) Chromium enrichment and nickel depletion at the interface in the CR1 microstructure after 4hrs annealing at 1240°C. (b) Computed profiles after 4hrs annealing at 1240°C followed by a quench to 900°C at a 68°C/s rate.

### III. Ternary cast alloy: dissolution of vermicular $\delta$ -ferrite

The modeling of ferrite dissolution in the Fe-17.3%Cr-9.4%Ni alloy will only focus on the vermicular ferrite. It presents the most complex modeling situation among the morphologies encountered in the as-cast microstructure (the lathy morphology may be modeled as multilayered microstructure).

#### III.1. Design of the simulation

In contrast with the multilayered microstructures, the  $\delta/\gamma$  interface of the vermicular ferrite of the as-cast microstructure of the Fe-17.3%Cr-9.4%Ni alloy exhibits a complex morphology (Figure V. 23.a) that cannot be taken into account by the developed one dimensional model. It

is thus required to mimic it by deriving an equivalent morphology which will be a combination of simple geometries (cylinders, spheres) in which diffusion can be treated by the present 1D model.

Ferritic dendrites can be decomposed into two parts (Figure V. 23.b): elongated parts corresponding to the primary and secondary dendritic arms and coarse parts corresponding to the intersections of dendritic arms and tips of secondary arms. The elongated parts possess a rather cylindrical morphology while coarse ones can be approximated with spheres. Hence a combination of spheres and cylinders will be used to approximate the morphology of a dendritic ferrite.

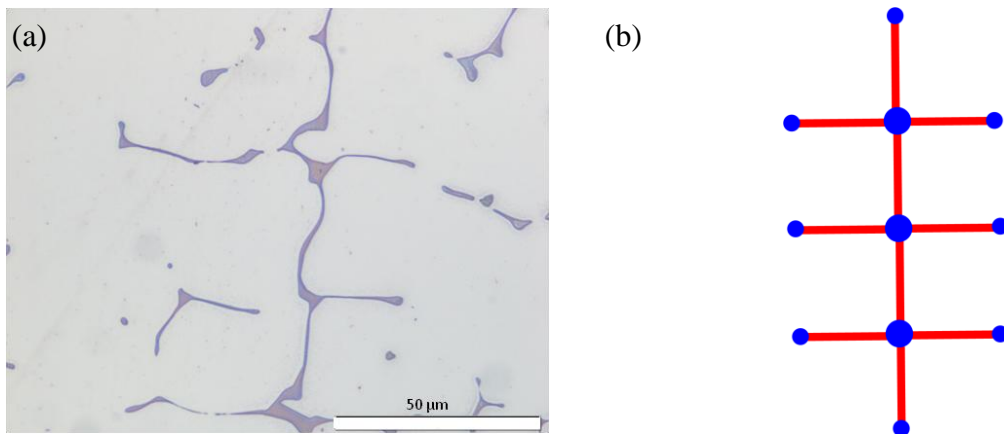


**Figure V. 23: (a) Typical morphology of dendritic ferrite in the Fe-17.3%Cr-9.4%Ni and (b) its spheres+cylinders equivalent morphology considered for diffusion calculations.**

The elongated parts are separated from the coarse ones by image analysis. Details of the separation technique can be found in Chapter II. Ferrite fraction in each population is given in Table V. 8. These fractions will be used as weights in the subsequent mixing of dissolution kinetics cylinders and spheres.

**Table V. 8: : Ferrite fraction in the elongated and massive particle populations.**

Particles	Fraction	Relative fraction
Elongated: Cylinders	2.5 %	45 %
Coarse: Spheres	3 %	55 %
Total	5.5 %	100 %

The characterization particles size was presented in Chapter II: coarse particles are mimicked by discs with equivalent areas and the latter's radii are retained as the characteristic size. Radii of the elongated particles will be described with half the width of the equivalent rectangles whose lengths are given by the Féret diameter of the particles.

Special care was paid to the description of ferrite and austenite compositions in the calculation cell. In order to obtain a more realistic description of solute compositions than a

simple linear EPMA measurements, a 2D mapping of the composition fields of Cr and Ni around a dendrite is performed with EPMA (Figure V. 24).

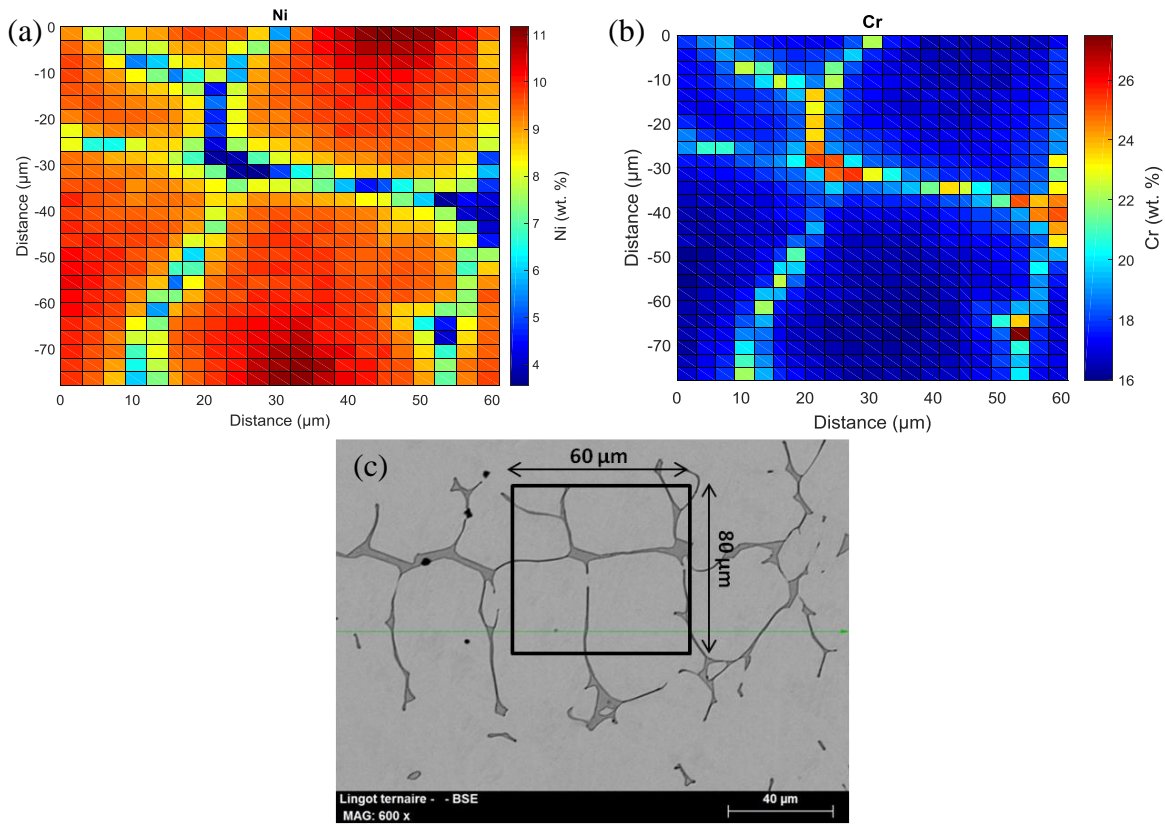


**Figure V. 24:** EPMA mapping of the composition fields of (a) nickel and (b) chromium surrounding a secondary dendritic arm and an intersection of dendritic arms. (c) SEM image of the analyzed zone.

Calculations will be performed on the basis of these raw data (particle size, composition fields, ferrite fraction). For the modeling, the question of choosing the most pertinent input parameters from these data arises: is it important to take into account ferrite's radii distribution instead of the average radius? Does solute gradients play a role in the kinetics of ferrite dissolution? Answers will be given by the preliminary calculations results of the next section.

### III.2. Preliminary results

Prior to the application of the model to the dissolution problem, numerical calculations were carried out in order to outline the relevant parameters to be used in the modeling.

#### III.2.a. Average radius versus radii distribution

In some cases it is relevant to consider only the average radius of a distribution as the representative size for calculations. This was the case for the multilayered microstructures studied previously. In this section, we propose to outline the importance of taking into account the distribution of ferrite's radii on the dissolution kinetics. Figure V. 25 shows the radii distribution of the cylindrical and spherical populations. The corresponding average radii are 0.4 μm and 1.8 μm respectively. In the population of cylinders, the average radius is in the

center of the distribution, though higher radius particles ( $r > 0.7\mu\text{m}$ ) are off the distribution. For the population of spheres the average radius is shifted towards low values, given the elevated number of tiny particles.

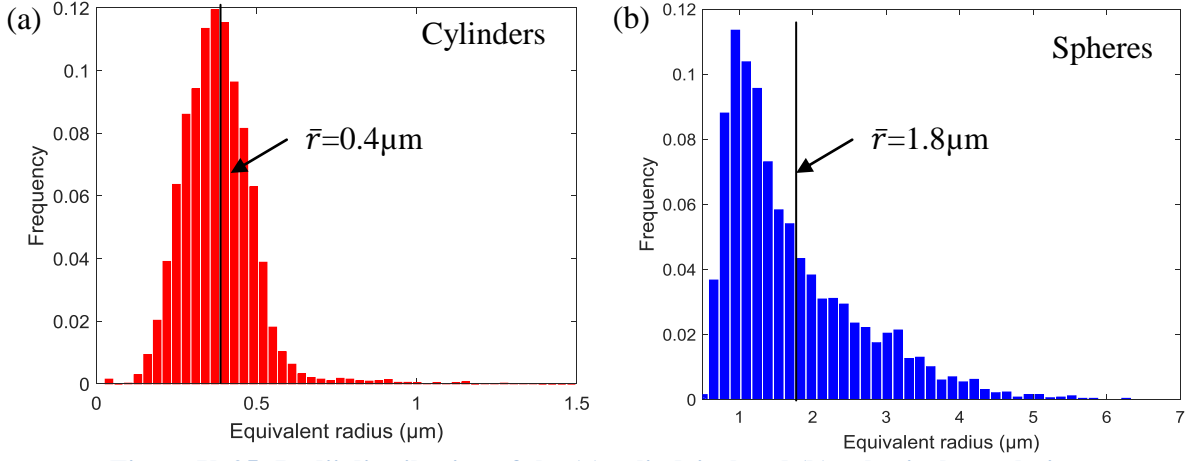


**Figure V. 25: Radii distribution of the (a) cylindrical and (b) spherical populations.**

Modeling the dissolution kinetics of ferrite in the cylindrical and spherical populations with regard to ferrite radii distribution is conducted in the following way: the range of existing ferrite radii is subdivided into four representative classes as listed in Table V. 9 and Table V. 10. For each class, the average radius  $d_i$  and the volume fraction  $w_i$  are calculated. By volume fraction it is meant the contribution of class  $i$  to the total amount of ferrite fraction and not its relative number of particles. The average kinetics  $F_\delta(t)$  is then calculated as follows:

$$F_\delta(t) = \frac{\sum_{i=1}^4 w_i \cdot f_i(t)}{\sum_{i=1}^4 w_i} \quad (\text{V.1})$$

where  $f_i(t)$  is the calculated ferrite volume fraction obtained at time  $t$  for class  $i$ . The value of  $f_i(t)$  is derived using the following formula:

$$f_i(t) = \left( \frac{d_i(t)}{L} \right)^n \quad (\text{V.2})$$

where  $d_i(t)$  is the interface position at time  $t$ ,  $n = 2$  and  $3$  for the cylindrical and spherical geometries respectively and  $L$  is the length of the calculation cell. The choice of this latter parameter will be discussed in §III.2.d.Characteristic diffusion length.

**Table V. 9: Average radius and volume fraction in each class of the cylindrical ferrite population, compared to the global average radius.**

Class (cylinders)	1	2	3	4	Global
Radius range	0 to 0.4	0.4 to 0.7	0.7 to 1.1	1.1 to 1.5	0 to 1.5
Average radius ( $\mu\text{m}$ )	0.26	0.42	0.75	1.1	0.4
Volume fraction (%)	19	66	10	5	100

**Table V. 10: Average radius and volume fraction in each class of the spherical ferrite population, compared to the global average radius.**

Class (spheres)	1	2	3	4	Global
Radius range	0 to 1.4	1.4 to 2.8	2.8 to 4.3	4.3 to 7.3	0 to 7.3
Average radius ( $\mu\text{m}$ )	1	2	3.5	5	1.8
Volume fraction (%)	17	41	34	8	100

Two kinds of calculations were performed. The first one is the classical calculation that only takes into account the average ferrite radius. The second one, as we propose in this section, considers the four-class distribution. It is important to note that, for each population, the average radius given by the four-class distribution of particles radii is exactly the same as the global average radius used in the first calculation.

Figure V. 26 shows the position of the interface with time for each class of the cylindrical and spherical population at 1240°C. Average kinetics in both populations are obtained using Eq.(V.1) and are compared to calculations with the average radii in terms of relative volume fraction  $F_\delta(t)/F_\delta(0)$  (Figure V. 27). Calculations with the radii distribution lengthen the dissolution kinetics by a factor of 2 and 3 in the cylindrical and spherical populations respectively, as particles of higher sizes are taken into account. Further, they are more consistent with experimental results of Chapter III. In fact, at 1240°C for instance, ferrite experimentally dissolves after 120min, against 90min by distribution-based simulations and 30min by calculations with average radius.

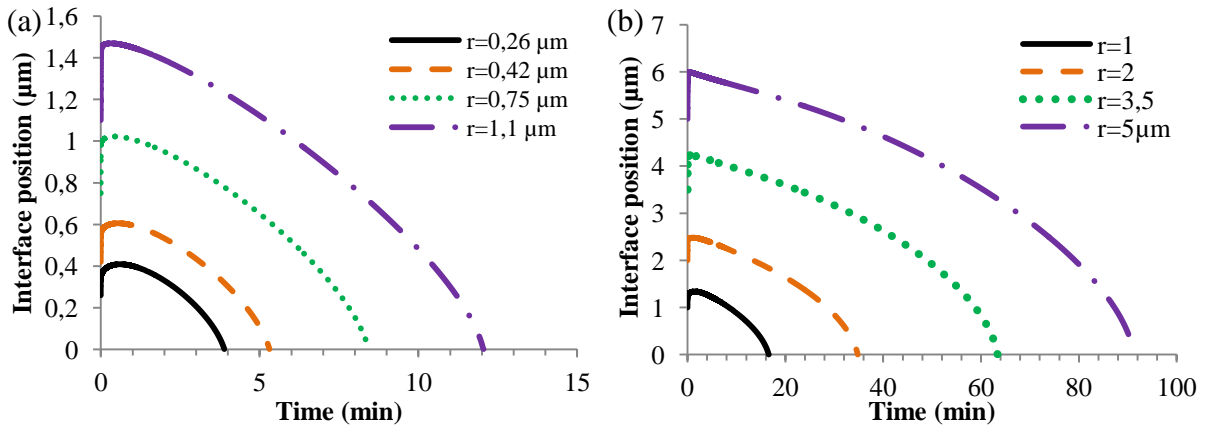


**Figure V. 26: Evolution of the interface position in each radii class of the (a) cylindrical and (b) spherical populations.**

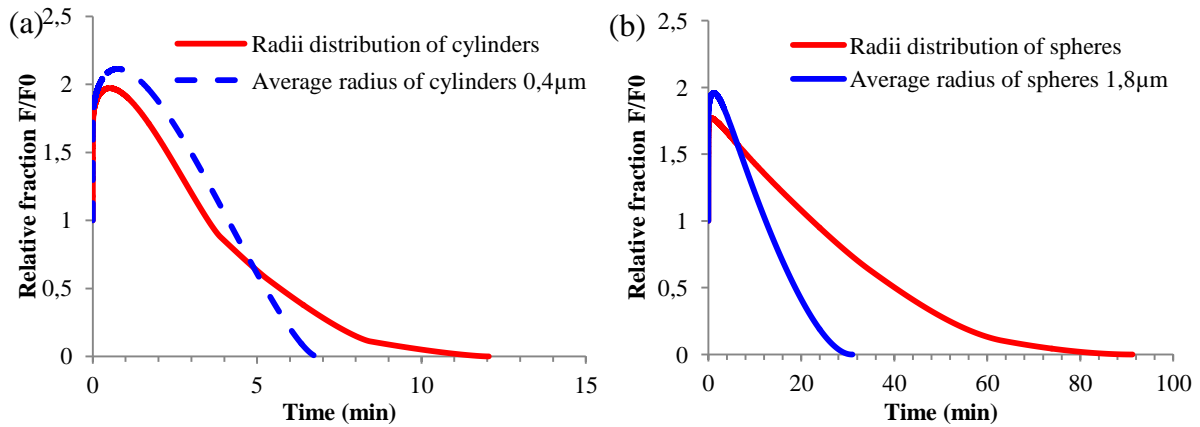


Figure V. 27: Dissolution of ferrite with an average radius versus radii distribution in the (a) cylindrical and (b) spherical populations.

This example shows that the average radius is not representative of the radii distribution, as it leads to very rapid ferrite dissolution kinetics. As a consequence, in future simulations, radii distribution will be considered instead of the average radius. It is interesting to note that the number and the extent of classes does not change the dissolution kinetics as shown in Figure V. 28. With a six-class distribution instead of four, only the end of the dissolution is delayed from 90 to 115min. But the amount of ferrite involved in this stage is very low to consider this delay as significant.

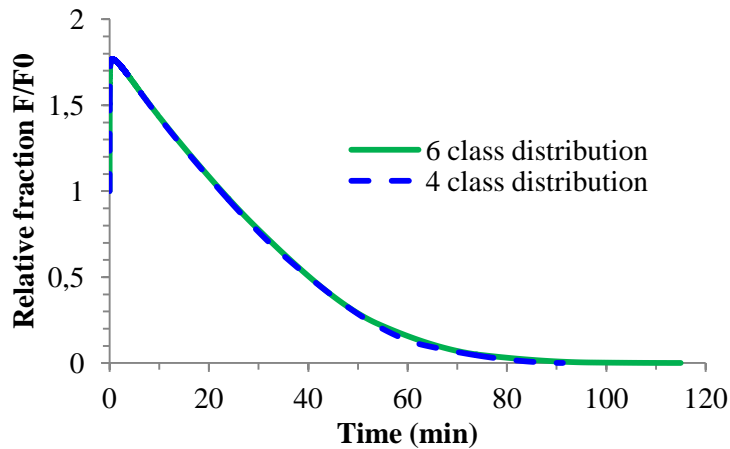


Figure V. 28: Effect of the number and the size of classes on the dissolution kinetics of ferrite in the spherical population.

### III.2.b. Effect of solute gradients

#### In ferrite

Since the size of ferrite particles is small, composition gradients cannot be measured with EPMA due to low spatial resolution of the probe ( $2\mu\text{m}$ ). They are thus evidenced by TEM-EDS measurements as shown in Figure V. 29. As it can be seen, ferrite is enriched in Cr and depleted in Ni at the interface, and this is due to the cooling of the ingot upon casting, as previously explained in §II.3. Discussion.

Based on Cr and Ni profiles of Figure V. 29, the effect of solute gradients in ferrite is studied with the following cases:

1. **Case 1.** No gradient: the average composition of the ferrite particle (28 wt.%Cr and 2.8 wt.%Ni) is set in the ferritic region of the calculation cell. Note that this composition is slightly different from that evidenced by EPMA in the Chapter III, as TEM-EDS analysis is semi-quantitative and EPMA spatial resolution is low (2 $\mu$ m).
2. **Case 2.** Linear gradient from (27.1 wt.%Cr, 3.3 wt.%Ni) at the center of ferrite to (29.3 wt.%Cr, 2.3 wt.%Ni) at the interface. The global composition of ferrite is approximately the same as in Case 1.

In the calculations, the initial size of ferrite is set to 1.3 $\mu$ m, *i.e.* half the size of the particle of Figure V. 29. The size of the cell is arbitrarily set to  $\frac{1}{2}\lambda_2$ . For the sake of simplicity initial Cr and Ni profiles in austenite are assumed flat, but the same conclusions can be drawn if real profiles are injected. Figure V. 30 shows the dissolution kinetics of ferrite in the two cases. The presence of solute gradients in ferrite has a negligible effect on the transformation kinetics, as the relative difference in the dissolution duration is only of 3%. This is explained by the fact that given the high diffusivity of Cr and Ni in ferrite, the initial gradients flatten very rapidly (< 1s) and their effect becomes not perceptible in the subsequent stages of the transformation.

Hence solute gradient in ferrite is not a pertinent parameter for the dissolution calculations. Initial ferrite profiles will therefore be considered as flat in future calculations.

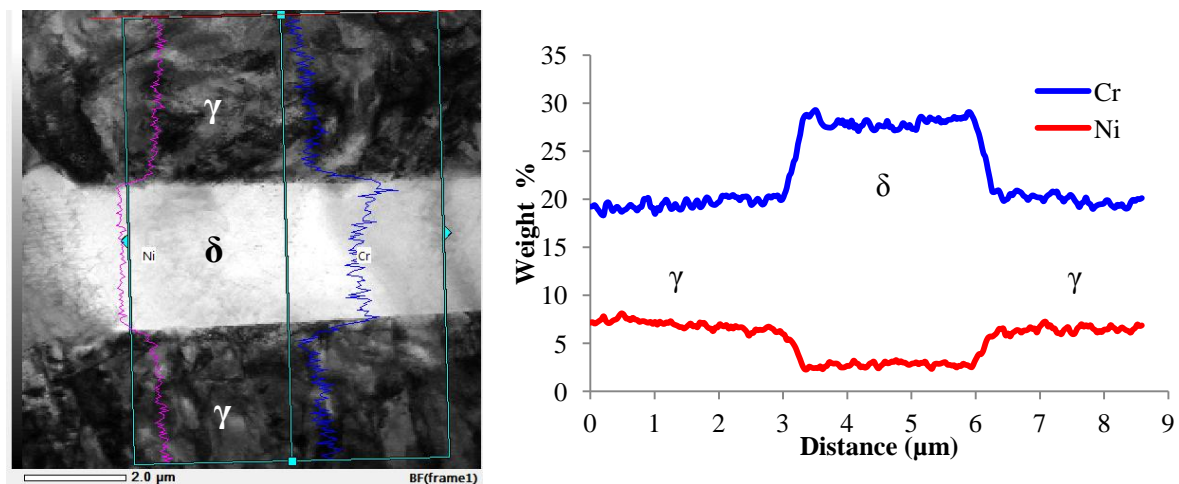


Figure V. 29: Chromium and nickel gradients in vermicular ferrite measured by TEM-EDS.

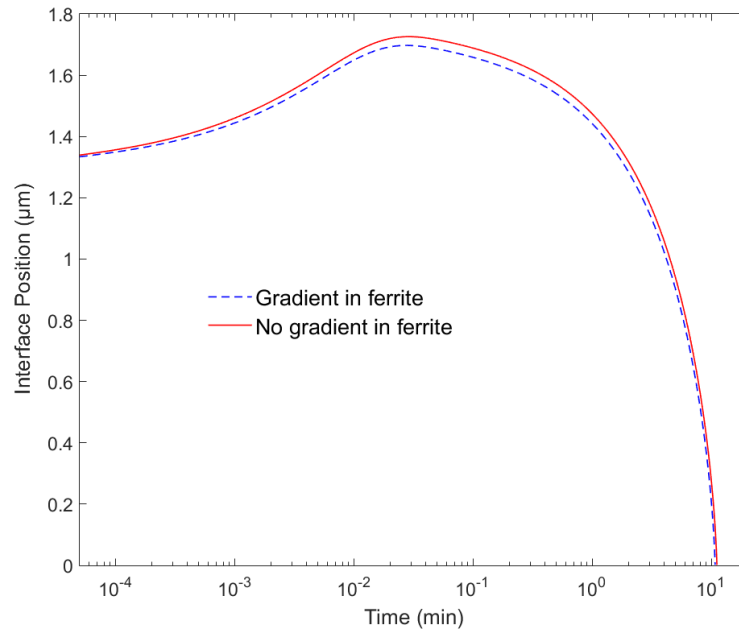


Figure V. 30: Comparison between the dissolution kinetics of a cylindrical ferrite with initial solute gradients (blue dashed line) and without solute gradients (red solid line).

### In austenite

In austenite, the effect of solute distribution is studied with the following numerical experiments: in a calculation cell representing the secondary dendritic arm of Figure V. 31 and its surrounding austenite, the austenite region is initialized either with Ni and Cr composition gradients extracted from the composition mapping of Figure V. 24, or with a flat profile having the same average composition. Both configuration are sketched in Figure V. 31. For simplicity, the gradient is assumed to vary linearly from the interface towards the right end of the calculation cell.

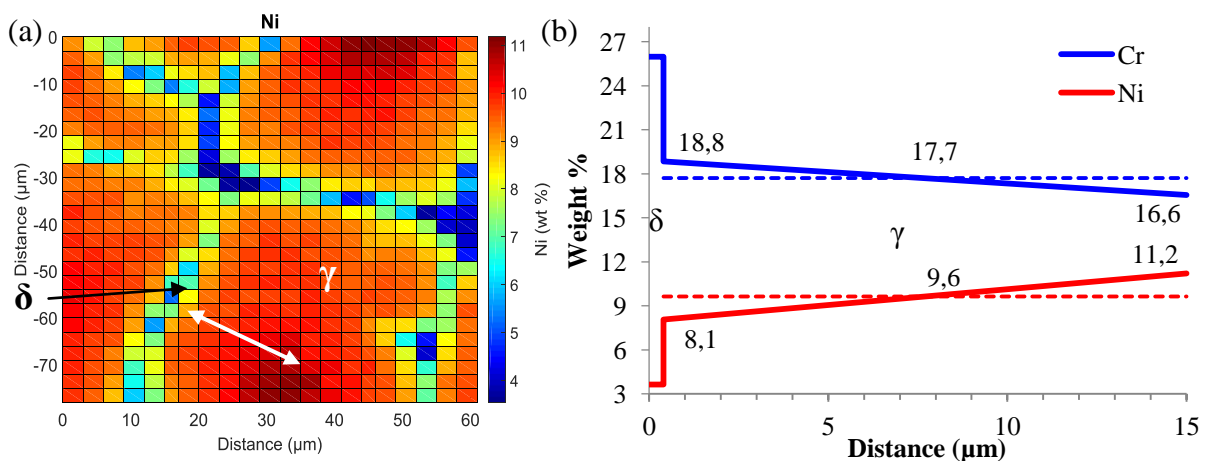
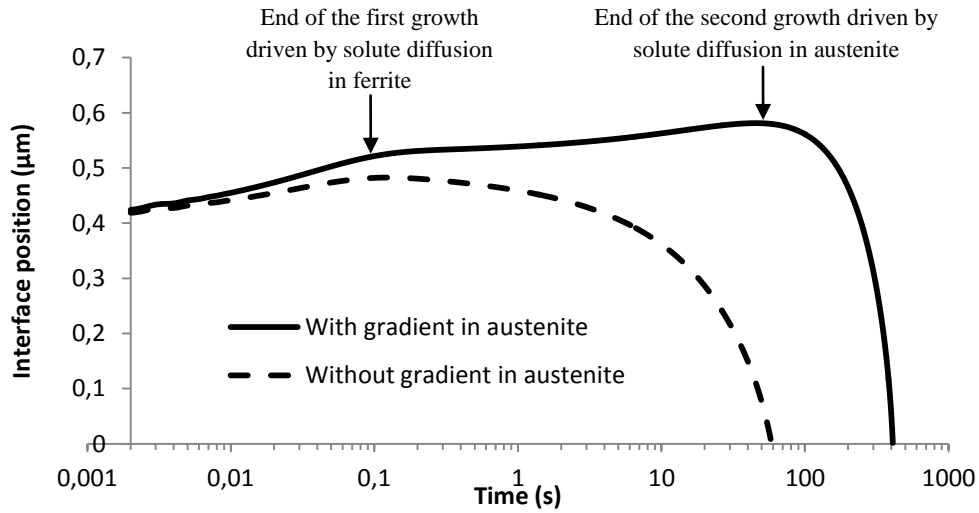


Figure V. 31: (a) Nickel EPMA mapping around a secondary dendritic arm of the Fe-17.3%Cr-9.4%Ni alloy. The double arrow refers to the nickel gradient linearized and injected in the austenite region of the calculation cell. (b) Schematic of the cylindrical calculation cell with either flat chromium and nickel profiles (dashed lines) or composition gradients (solid lines) in the austenite region.

The dissolution of ferrite in both situations is shown in Figure V. 32. The presence of solute gradients in austenite lengthens the transformation duration from 60 to 410s. The early growth of ferrite also increases from 0.1 to 42s. In the gradient-based calculations, the growth exhibits two stages, the first occurring until 0.1s and the second until 42s. The first stage is driven by solute diffusion inside ferrite resulting from the establishment of solute gradients in ferrite as interface compositions abruptly change at the first time step. Since diffusion of Cr and Ni is rapid in ferrite (see Appendix D) and the latter's size is small, Cr and Ni profiles become rapidly flat and this first regime ends at 0.1s. This stage is what Kajihara *et al.* [36] have outlined in their experimental works on ferrite dissolution in  $\gamma/\delta/\gamma$  diffusion couples of the Fe-Cr-Ni system.



**Figure V. 32: Effect of composition gradient in austenite on the dissolution kinetics of a cylindrical ferrite with the average radius of dendritic arms ( $0.4\mu\text{m}$ ).**

The next growth stage is driven by diffusion in austenite. Figure V. 33 shows a snapshot of Cr and Ni composition profiles computed during this growth stage ( $t = 10 \text{ s}$ ). The Cr profile does not decrease monotonically. Instead, a composition hump develops ahead of the interface, and leads to a negative Cr flux in austenite (flux oriented towards ferrite):

$$J_{Cr}^{\gamma} < 0 \quad (\text{V.3})$$

In the same fashion, Ni profile exhibits a plateau composition developing in front of the  $\delta/\gamma$  interface so that:

$$J_{Ni}^{\gamma} > 0 \quad (\text{V.4})$$

In addition, since Cr and Ni profiles in ferrite are already flat

$$J_{Cr}^{\delta} \cong 0 \quad (\text{V.5})$$

$$J_{Ni}^{\delta} \cong 0$$

the velocity of the  $\delta/\gamma$  interface is thus approximated by

$$V \cong \frac{-J_{Cr}^{\gamma}}{X_{Cr}^{\delta/\gamma} - X_{Cr}^{\gamma/\delta}} \cong \frac{-J_{Ni}^{\gamma}}{X_{Ni}^{\delta/\gamma} - X_{Ni}^{\gamma/\delta}} \quad (V.6)$$

Given that  $X_{Cr}^{\delta/\gamma} - X_{Cr}^{\gamma/\delta} > 0$  (and  $X_{Ni}^{\delta/\gamma} - X_{Ni}^{\gamma/\delta} < 0$ ), it can be shown that the interface migrates towards austenite, as long as  $J_{Cr}^{\gamma} < 0$  (and  $J_{Ni}^{\gamma} > 0$ ), *i.e.* when the composition hump (and plateau) exists. For such a hump to develop, the initial interface compositions at the austenitic side  $(X_{Cr}^{\gamma/\delta}, X_{Ni}^{\gamma/\delta})_{t=0}$  should lie within the  $\delta+\gamma$  domain (Figure V. 34), *i.e.* at higher Cr and lower Ni values than the operative tie-lines. This is what happens for composition profiles of Figure V. 33. On the contrary, if the initial interface compositions lie within the  $\gamma$  domain, the hump would not develop and the austenite-driven growth of ferrite will not appear. This is what occurs in the case of initial flat profiles in austenite. It should be remarked that the duration of that growth depends on the intensity of solute gradients down the hump.

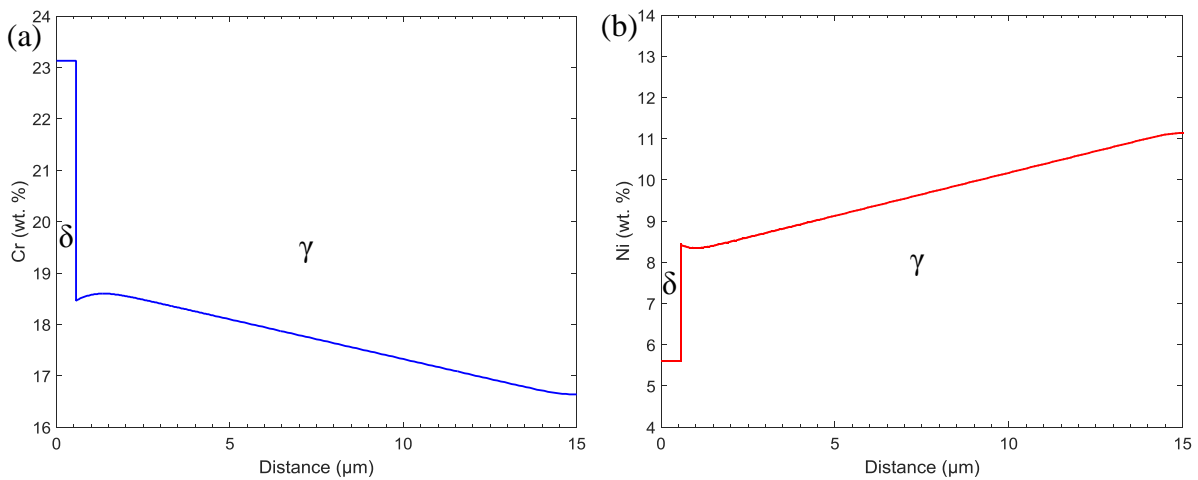


Figure V. 33: Composition profiles of (a) chromium and (b) nickel in ferrite and austenite regions after 10s at 1240°C. Case of austenite containing initial solute gradients.

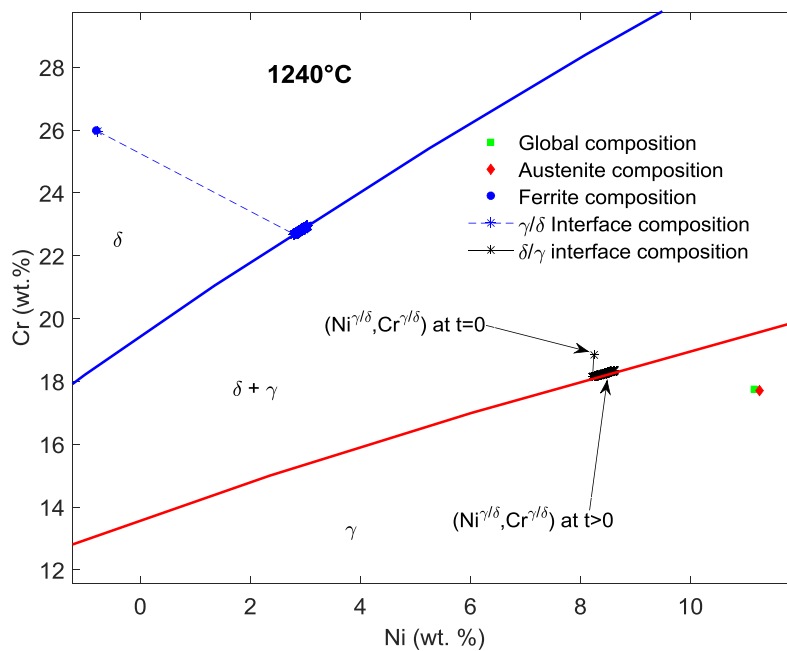


Figure V. 34: Position of the initial chromium and nickel compositions at the austenitic side of interface with regards to the  $\gamma/(\delta+\gamma)$  phase boundary and the operative tie-lines at 1240°C.

The pertinence of EPMA measurements of interface compositions may be questioned, as the resolution of the probe is not fine enough to accurately measure the real interface compositions. In order to assess the values of the interface compositions extracted from the EPMA mapping, Cr and Ni compositions fields around the  $\delta/\gamma$  interface were measured with TEM-EDS (Figure V. 35) and a very satisfying agreement with EPMA results is reached. This validates therefore the choice of the interface composition in the calculation cells and the outlined mechanism of the ferrite growth is confirmed.

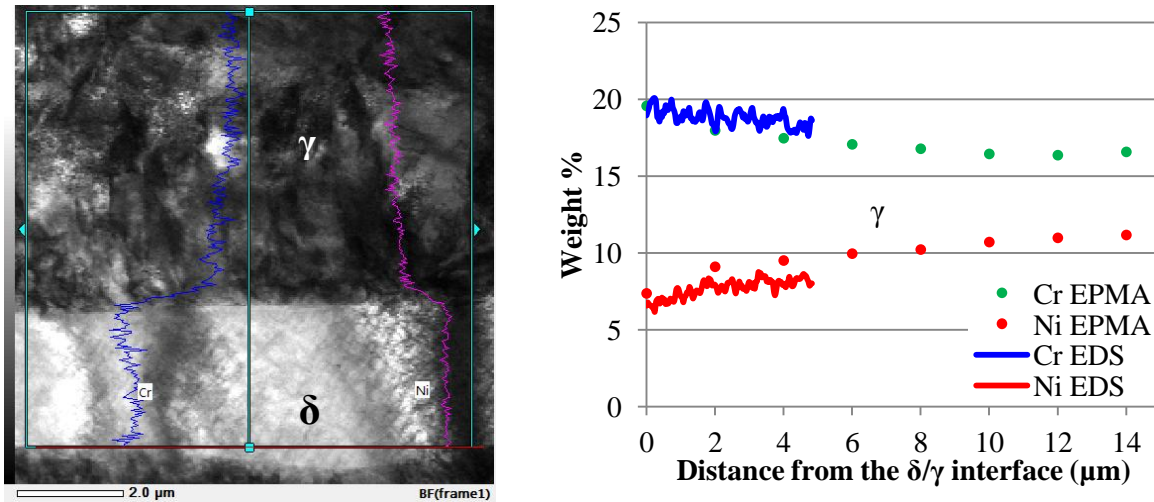


Figure V. 35: Chromium and nickel compositions at the  $\delta/\gamma$  interface as measured with TEM-EDS and EPMA (EPMA measurement are extracted from the 2D mappings of Figure V. 24).

It can be concluded that solute gradients in austenite play a major role on ferrite 's dissolution kinetics. They must therefore be considered in future calculations.

### III.2.c. Gradient description in austenite

In view of the previous results it is of great importance to properly chose solute gradients in austenite.

For the **dendritic arms**, given their elongated morphology, solute redistribution in austenite in the course of the transformation will be mainly radial. Therefore considering an initial radial composition profile in austenite is relevant. The EPMA mapping of Figure V. 36.a shows that several choices of solute gradient in austenite are possible. For example gradients can be chosen either near the dendrite intersection or far from it, as illustrated by the double arrows on the mapping. In the first case, the dendritic arm is surrounded only by secondary austenite resulting from solid-state transformation, while primary austenite (from solidification) is also present in the second case.

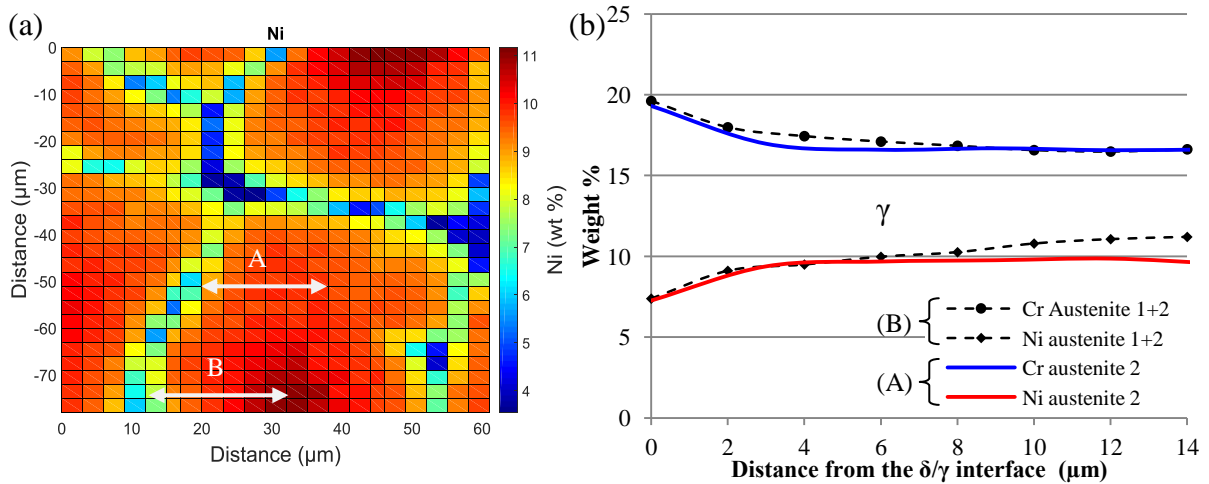


**Figure V. 36:** (a) Some possible choices of chromium and nickel gradients in austenite around a dendritic arm. (b) Comparison between the two gradients indicated by double arrows in (a).

The impact of the presence/absence of primary austenite ( $\gamma_1$ ) on the dissolution kinetics of a dendritic arm was tested with the two numerical experiments of Figure V. 37. Clearly, the dissolution kinetic curves show that  $\gamma_1$  has no noticeable effect on the course of the transformation. The explanation is that, given the relatively rapid dissolution of cylinders, diffusion lengths of Cr and Ni are not so spatially extended to interact with the primary austenite that is initially located far downstream the  $\delta/\gamma$  interface.

It can be concluded that for dendritic arms, it is not necessary to take into account primary austenite in the Cr and Ni initial gradients.

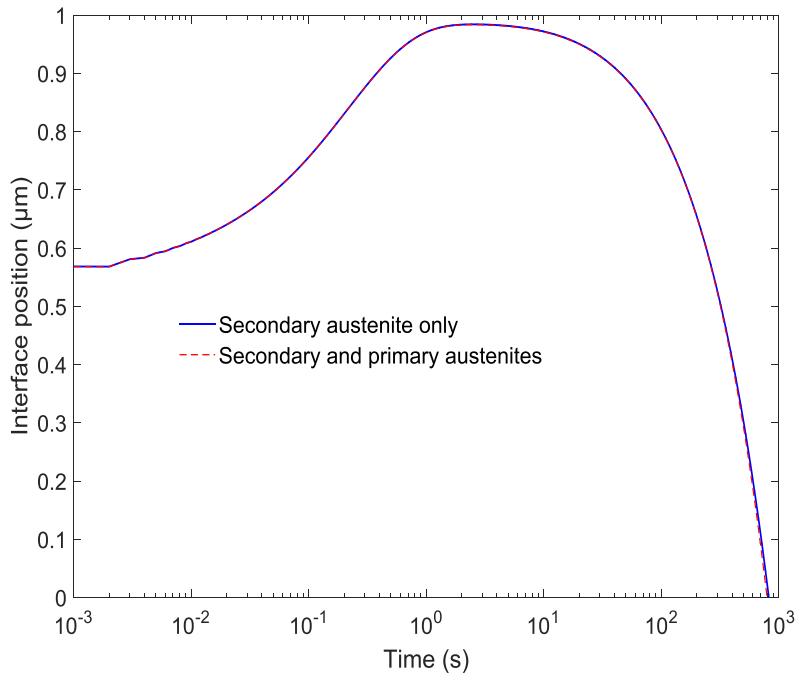


**Figure V. 37:** Effect of the primary austenite on the dissolution kinetics of a dendrite arm.

For **dendritic arm intersections (spherical particles)**, the choice of the composition gradient is more critical. As it is shown in the EPMA mapping of Figure V. 38, several ways are possible to describe gradients around an arm intersection: either by considering solute gradients only in austenite, which is accounted for by a linear profile crossing the particle. In such a case there are as many profiles as directions and each one of them can be considered as characteristic composition distribution in austenite (Figure V. 38.a). Or by considering the whole compositional environment around the ferrite particle: in this case, the composition distribution can be described with "iso-radius average" values around the ferrite particle (Figure V. 38.b). In this approach, at a given distance from the considered ferrite particle, the composition is averaged along a circular contour around the particle and even composition in neighboring ferrite arms are taken into consideration, as solute diffusion during the transformation will have to interact with the neighboring ferrite particles. Figure V. 39.a compares a linear profile to iso-radius average measurements. With the latter approach gradients are less steep and global content of Cr is higher and that of Ni is lower. This is partly due to the fact that compositions in neighboring ferrite particles are taken into account.

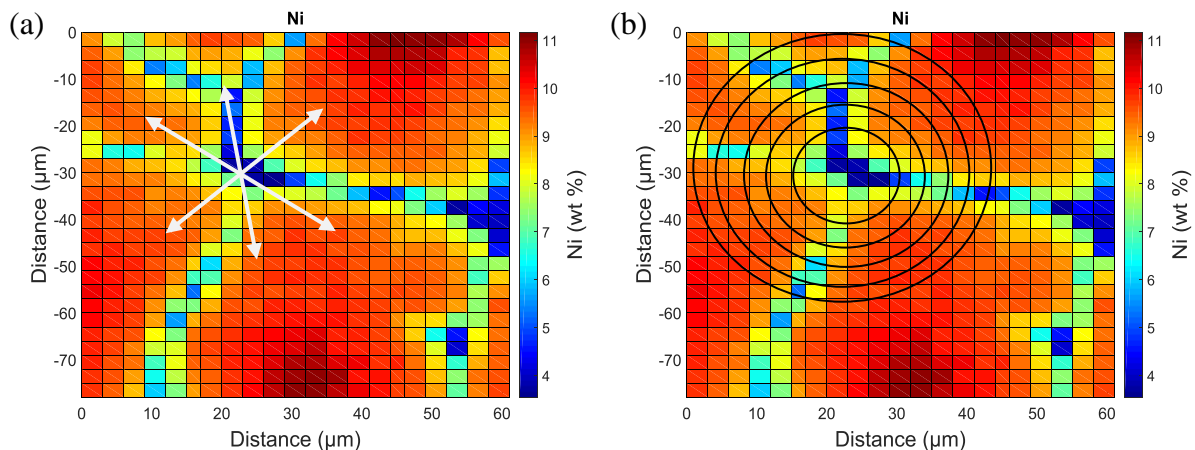


**Figure V. 38:** Two possible ways of considering chromium and nickel composition fields surrounding the an intersection of arms: (a) with a linear profile accounting only for gradients in austenite and (b) with the iso-radius average approach representing the whole chemical environment.

Comparative calculations are performed at 1240°C using both composition fields. In terms of dissolution kinetics, the use the isocontours approach considerably lengthens the dissolution time of a spherical ferrite particle from 30 to 55 min, *i.e.* by a factor near 2 as shown in Figure V. 39.b. This lengthening is far more consistent with experiments (see chapter III, §I.3. *Kinetics of ferrite dissolution*). That is why the iso-radius average approach will be adopted in future calculations.

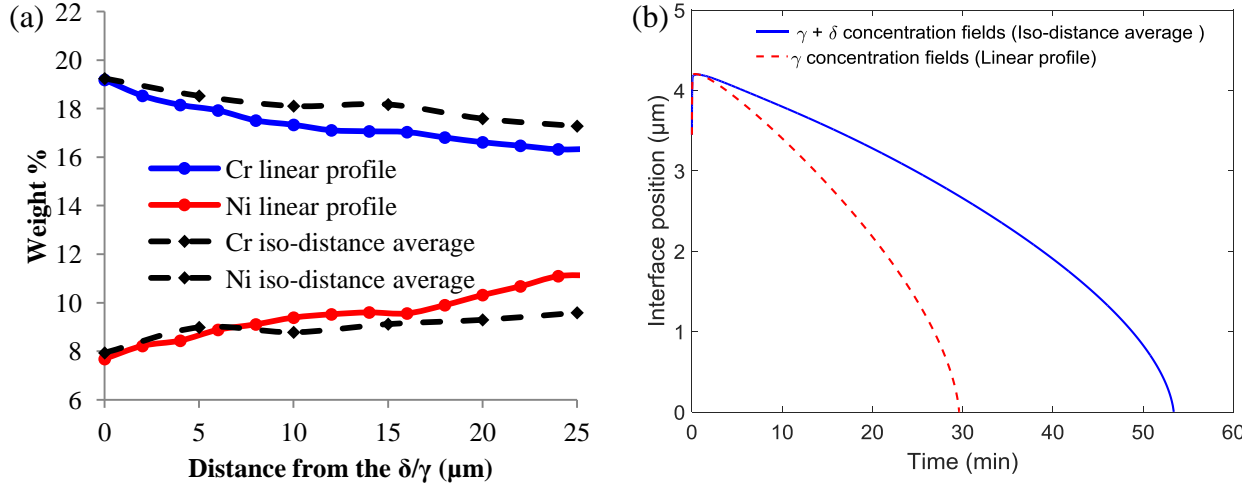
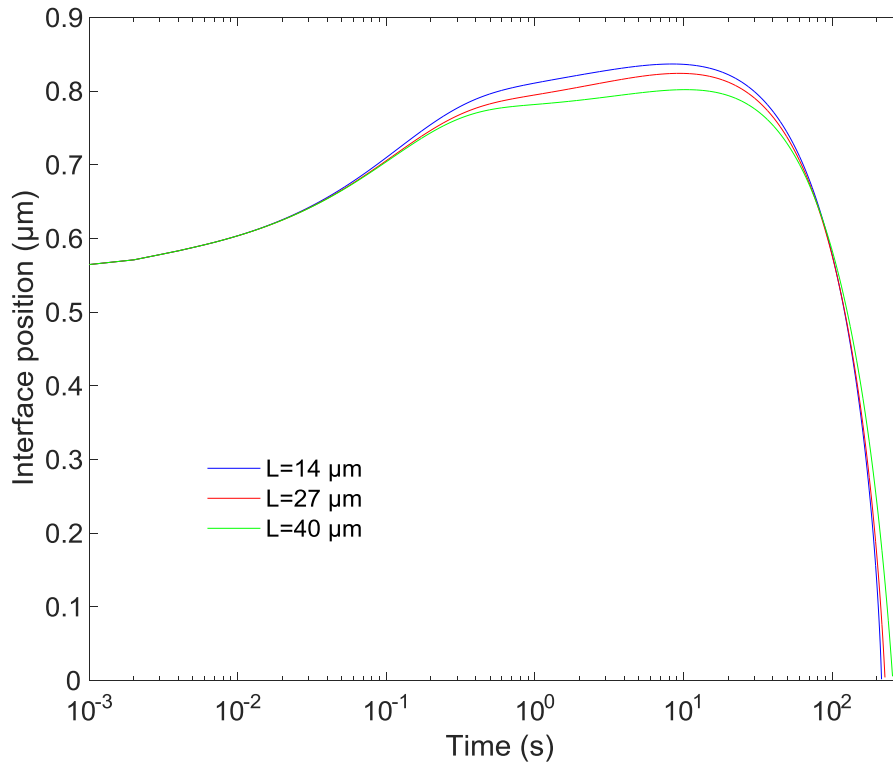


Figure V. 39: (a) Comparison between composition profiles obtained by a linear EPMA measurements and the iso-radius average approach. Gradients are more pronounced in linear profiles. (b) Effect of the two gradients on the dissolution kinetics of a spherical ferrite particle with initial radius of  $3.5\mu\text{m}$ .

### III.2.d. Characteristic diffusion length

In the as-cast microstructure, the dendritic network is described by two characteristic lengths : the secondary dendrite arm spacing ( $\lambda_2=27\mu\text{m}$ ) and the primary dendrite arm spacing ( $\lambda_1=80\mu\text{m}$ ). It is therefore difficult to choose the pertinent length in which diffusion will occur. Kobayashi *et al.* [82] and Thuinet [75] have considered  $\lambda_1$ ,  $\lambda_2$  and even  $(\lambda_2+\lambda_1)/2$  as characteristic lengths in their modeling of solute redistribution during solidification in a dendritic microstructure. In the present study, we will follow the same approach and the effect of the these 3 lengths on the dissolution of ferrite will be tested for each population. Note that, given the periodicity of the microstructure,  $\frac{1}{2}\lambda_2$ ,  $\frac{1}{2}\lambda_1$  and  $\frac{1}{2}[(\lambda_2+\lambda_1)/2]$  will be used instead of  $\lambda_1$ ,  $\lambda_2$  and  $(\lambda_2+\lambda_1)/2$ .

For **dendritic arms**, given their elongated morphology, we may strongly assume that solute redistribution during their dissolution will be mainly radial and taking place in the spacings between secondary dendritic arms. The choice of  $\lambda_2$  as the size of the calculation cell appears to be pertinent. For comparison, simulations with  $\frac{1}{2}\lambda_2$ ,  $\frac{1}{2}\lambda_1$  and  $\frac{1}{2}[(\lambda_2+\lambda_1)/2]$  as characteristic lengths have been performed. For simplicity, initial gradients are assumed flat. In Figure V. 40 it is shown that the dissolution kinetics is almost insensitive to the length of the calculation cell. This result is explained by the fact that, given the small size of dendritic ferrite arms, the dissolution is so rapid that solute diffusion in austenite does not reach the right end of the domain regardless of the extent of austenite.



**Figure V. 40:** Dissolution kinetics of cylindrical ferrite using three cell lengths:  $\frac{1}{2}\lambda_2=14\mu\text{m}$ ,  $\frac{1}{2}\lambda_1=40\mu\text{m}$ ,  $\frac{1}{2}(\lambda_2+\lambda_1)/2=27\mu\text{m}$ . Calculations are carried at  $1240^\circ\text{C}$  and with initial flat Cr and Ni profiles in austenite.

In the case of **dendritic intersections**, since the simulated particles have bigger sizes than elongated ones (up to  $5\mu\text{m}$ ), the dissolution takes much more time and hence the extent of Cr and Ni diffusion becomes more widespread. The sensitivity of the computational results to the cell size is therefore expected to become pronounced. A test with cell sizes of  $\frac{1}{2}\lambda_2$ ,  $\frac{1}{2}\lambda_1$  and  $\frac{1}{2}[(\lambda_2+\lambda_1)/2]$  is performed. The size of ferrite is set to  $5\mu\text{m}$  (4<sup>th</sup> class), which constitutes the most severe case for the testing (longer dissolution time). Initial compositions in austenite are derived from the iso-radius average method and are shown for each case in Figure V. 41.a. Ferrite composition is set to (26 wt.%Cr, 3.6 wt.%Ni) as extracted from the mappings of Figure V. 24. Calculations are carried at  $1240^\circ\text{C}$  and compared in Figure V. 41.b. The following observations can be drawn:

- With  $\frac{1}{2}\lambda_2$  as a characteristic diffusion length, the global compositions of spherical calculation cells lies within the  $\gamma+\delta$  region of the Fe-Cr-Ni phase diagram (according to Ptimec-Miettinen and TCFE6 descriptions) at certain temperatures, whereas the real alloy is fully austenitic as shown by experiments. Therefore, given this thermodynamic discrepancy, this size cannot be considered in future calculations.
- With  $\frac{1}{2}[(\lambda_2+\lambda_1)/2]$  as a characteristic diffusion length, composition of spherical calculation cells lie in the austenitic domain at the desired temperatures and the dissolution of ferrite ends after 110min which is very satisfying with experimental data at  $1240^\circ\text{C}$  (end =120min), as it will be shown in the next section. However, the global composition of the calculation cell does not match that of the real alloy (Fe-17.3%Cr-9.4%Ni), but is enriched

in Cr and depleted in Ni as shown in Table V. 11. This is not due to the presence of ferrite since the latter's volume fraction is very small (~0.1%) but to the composition profiles in austenite derived from the iso-radius average approach. Note that we consider the matching to the nominal composition of the alloy is important in order to have the same driving force for ferrite dissolution.

- With  $\frac{1}{2}\lambda_1$ , extra austenite is added to the cell in order to match the nominal composition of the alloy (Table V. 11). It should be remarked that Cr content in the added austenite (the right end of the cell, Figure V. 41) is 15 wt.%, which is below the minimum one encountered in the as-cast microstructure (16.5 wt.%), while Ni is quite representative of that encountered in primary austenite. In this configuration, the dissolution of ferrite ends after 90min at 1240°C, which is relatively close to the previous prediction.

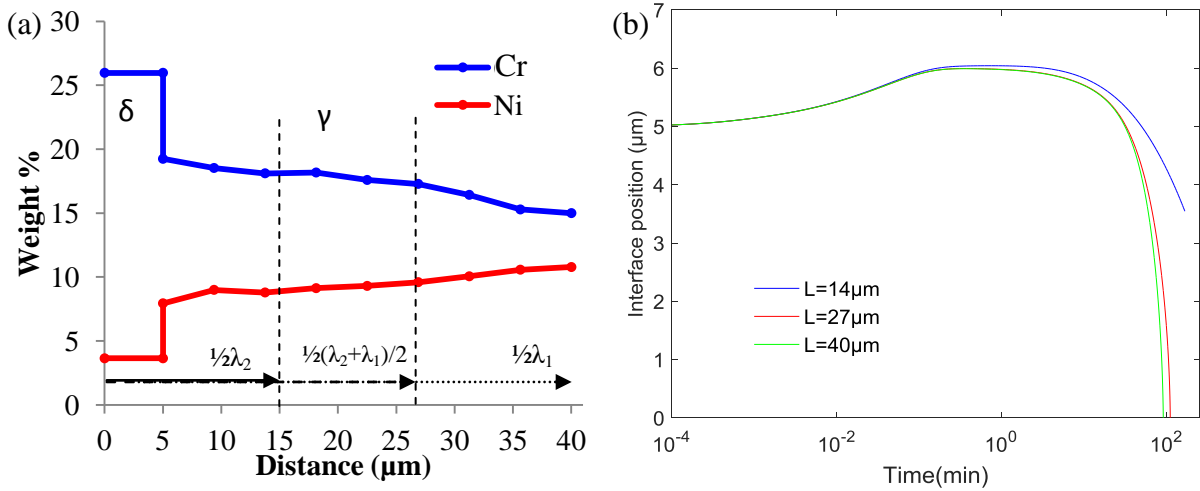


**Figure V. 41: Initial chromium and nickel compositions in a spherical calculation cell with initial ferrite radius of 5μm and three cell sizes:  $\frac{1}{2}\lambda_2=14\mu\text{m}$ ,  $\frac{1}{2}(\lambda_2+\lambda_1)/2=27\mu\text{m}$ ,  $\frac{1}{2}\lambda_1=40\mu\text{m}$ . (b) Correspondent dissolution kinetics of ferrite at 1240°C.**

From these observations, it can be concluded that  $\frac{1}{2}[(\lambda_2+\lambda_1)/2]$  or  $\frac{1}{2}\lambda_1$  as characteristic size leads to roughly the same dissolution results, with the later one leading to slightly slower kinetics but match the nominal composition of the ternary alloy.

**Table V. 11: Global composition in a spherical calculation cells with increasing size. Nominal composition of the ternary alloy is added for comparison.**

Size (μm)	Cr (wt. %)	Ni (wt. %)
$\frac{1}{2}\lambda_2=14$	18.8	8.6
$\frac{1}{2}[(\lambda_2+\lambda_1)/2]= 27$	18.1	9
$\frac{1}{2}\lambda_1=40$	17.3	9.5
Nominal composition	17.3	9.4

### III.2.e. Conclusions and summary

Parametric studies have been systematically performed in order to extract from the initial raw data describing the vermicular microstructure the most relevant parameters for the modeling. The relevant parameters concern:

- **The size of ferrite particles.** Consideration of radii distribution instead of average radius permits to be more consistent with experimental data by taking into account the role of the biggest particles on the dissolution kinetics.
- **Gradients in austenite** are of first order importance. For dendritic arms, they are chosen normal to their axes and for dendrite intersections they are derived by the iso-radius average method.
- **The size of the calculation cell.** For dendritic arms,  $\frac{1}{2}\lambda_2$  is a pertinent choice and for dendrite arms intersections  $\frac{1}{2}\lambda_1$  is the most pertinent one.

On the other hand, it was demonstrated that solute gradients in ferrite can be ignored, since they not have a noticeable effect on the transformation kinetics.

### III.3. Application of the model to the dissolution of vermicular ferrite

The dissolution of the vermicular ferrite will be simulated at 1140°C, 1200°C, 1240°C, 1260°C, 1280°C and 1300°C. The input parameters used in the calculations are summarized in Table V. 12.

**Table V. 12: Input data used in the simulation of the dissolution kinetics of vermicular ferrite in the Fe-17.3%Cr-9.4%Ni alloy.**

	Elongated particles	Coarse particles
Fraction in the as-cast microstructure	2.5%	3%
Weight of each geometry	45%	55 %
Equivalent geometry	Cylindrical	Spherical
Size of ferrite ( $\mu\text{m}$ ): 4 classes	0.26 - 0.42 - 0.75 - 1.1	1 - 2 - 3.5 - 5
Weight $w_i$ of each radius class (%)	19 - 66 - 10 - 5	17 - 41 - 34 - 8
Cell size L ( $\mu\text{m}$ )	$\frac{1}{2}\lambda_2=14$	$\frac{1}{2}\lambda_1=40$
Composition in ferrite (weight %)	Uniform: 26Cr-3.6Ni	Uniform: 26Cr-3.6Ni
Gradient in austenite	Linear	Iso-radius average
Type of meshing	Uniform 20 grid points	Double-uniform 100 grid points

Interdiffusion coefficients are computed with DICTRA<sup>®</sup> and the MOB2 database. Since future calculations will be carried at several temperatures, they are expressed in terms of frequency factor  $D_0$  and activation energy  $Q$ , as described in Table V. 13. The choice of the thermodynamic description (TCFE6, Ptimec-Miettinen) will be function of the temperature at which the dissolution is modeled.

**Table V. 13: Frequency factor and activation energy values used for the modeling of interdiffusion coefficients of chromium and nickel in ferrite and austenite (source MOB2).**

Phase	Element	Composition (wt. %)	$D_0$ (cm <sup>2</sup> /s)	Q (J)
Ferrite	Cr	25.3	4,11	221555
	Ni	2.9	8,53	255861
Austenite	Cr	17.4	1,91	287942
	Ni	11.6	1,23	292190

To obtain the global kinetics of ferrite dissolution, the mixing of spheres and cylinders will be performed in the following way: after average kinetics are obtained for each population (Eq.(V.1)), they are first normalized to their initial volume fraction  $F_\delta(0)$  and then the reduced kinetics  $F_\delta(t)/F_\delta(0)$  are mixed with respect to their respective fractions in the as-cast microstructure (Table V. 12).

### III.3.a. Dissolution at 1140°C

It has been demonstrated in §I. *Review of the Kajihara experiments* that, at 1100°C, the TCFE6 thermodynamic description is more convenient for the prediction of ferrite dissolution in  $\gamma/\delta/\gamma$  diffusion couples of the Fe-Cr-Ni system. With this in view, the use of TCFE6 seems also more appropriate at 1140°C. For the purpose of comparison, two calculations were performed: the first one with Ptimec-Miettinen and the second one with TCFE6.

Comparison between the two calculations and the experimental data are given in Figure V. 42. For each calculation, the cylindrical, spherical and the global dissolution kinetics are superimposed on the same graph. With the Ptimec-Miettinen description, the global dissolution of ferrite is very rapid compared to experimental results (4hrs against 8hrs) and initial growth of cylinders and spheres is extremely short (end of the growth 8s). On the contrary, with TCFE6, dissolution kinetics are much more consistent with experiments. The end of the transformation is very satisfactorily predicted and global dissolution curve fits very well the experiments.

In TCFE6 calculations, the rapid dissolution stage ends after 30min, after which time a net change in the slope of the dissolution curve is observed, in very good agreement with experiments. As shown in Figure V. 42.b, this stage is marked by the dissolution of cylinders that are representative of dendritic arms which were demonstrated to be the first to dissolve experimentally (Chapter III). At the subsequent stage, the transformation is uniquely driven by the dissolution of spheres.

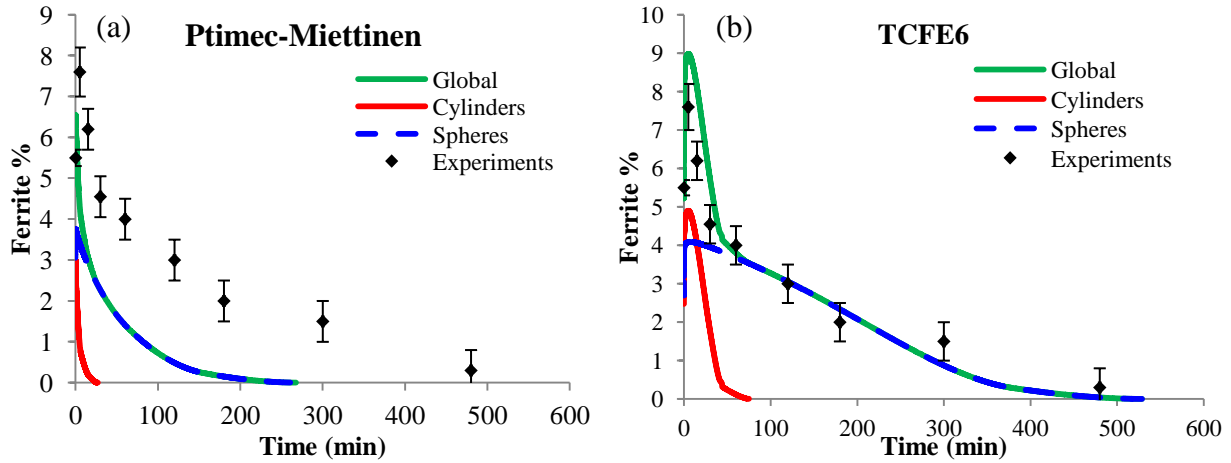


Figure V. 42: Computed and experimental dissolution of vermicular ferrite in the Fe-17.3%Cr-9.4%Ni alloy at 1140°C. Calculations are carried with (a) the Ptimec-Miettinen module and (b) the TCFE6 database.

### III.3.b. Dissolution at 1200°C

At this temperature, the choice of the thermodynamic description is not straightforward, as the relevance of the TCFE6 database and the Ptimec-Miettinen module was not yet assessed. Dissolution calculations are carried out with the two thermodynamic descriptions and compared to experimental results in Figure V. 43.

With the TCFE6 database, the extent of ferrite growth is largely overestimated both in the spherical and cylindrical geometries and the maximum ferrite fraction is 20% against 8% experimentally. Further, the end of the transformation occurs later than the experimental one: 4hrs against 3hrs. This makes the predictions not satisfactory even from a qualitative point of view and therefore it can be concluded that at this temperature, the TCFE6 database is clearly not suited for the dissolution calculations of the present system.

With the Ptimec-Miettinen description of the phase diagram, the kinetics of the transformation are more rapid, as the transformation ends after 2hrs (3hrs experimentally). In terms of ferrite fraction, calculations are qualitatively more consistent with the experimental data, though they slightly underestimate them. For the maximum growth, agreement is satisfactory with measured fraction, though predicted growth reached its maximum earlier.

It appears thus that, at this temperature, the Ptimec-Miettinen is more convenient for the thermodynamic description. Another support for this conclusion is provided by comparing both thermodynamic descriptions to interface compositions measured by EPMA at several holding times at 1200°C. As clearly shown in Figure V. 44, the Ptimec-Miettinen description is much more consistent with experimental interface compositions, especially at the austenite phase boundary.

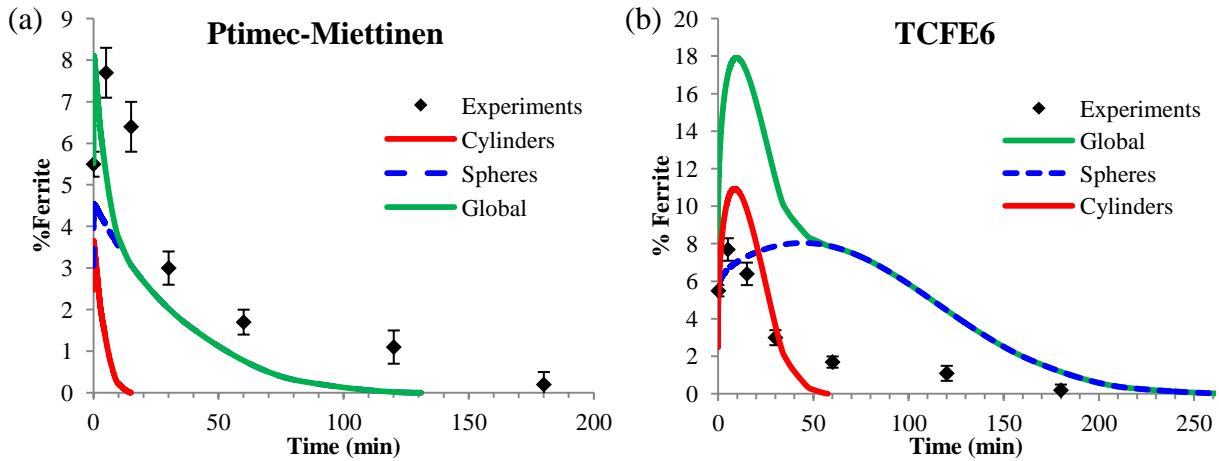


Figure V. 43: Computed and experimental dissolution of vermicular ferrite in the Fe-17.3%Cr-9.4%Ni alloy at 1200°C using (a) the Ptimec-Miettinen module and (b) the TCFE6 database.

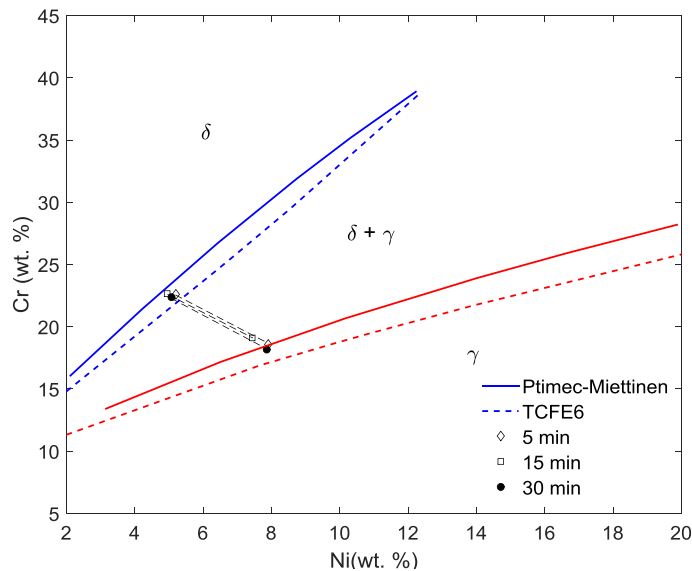


Figure V. 44: Comparison between the TCFE6 and the Ptimec-Miettinen thermodynamical descriptions of the Fe-Cr-Ni isothermal section at 1200°C with respect to EPMA measurements of interface compositions at different holding times.

### III.3.c. Dissolution at 1240°C, 1260°C, 1280°C, 1300°C and 1346°C

At 1240°C the Ptimec-Miettinen description will be used for calculations, as its pertinence at this temperature has been previously demonstrated (§II.1.a. Thermodynamic description). Regarding higher temperatures, the TCFE6 database is expected to be increasingly inaccurate, especially since the A4 temperature it predicts for the Fe-17.3%Cr-9.4%Ni alloy is 1270°C, while this alloy is known to remain fully austenitic at equilibrium even up to 1300°C. The Ptimec-Miettinen module predicts A4 at 1341°C, in good agreement with experiments (Chapter III). For these reasons, calculations will be carried using the Ptimec-Miettinen at 1240°C and higher temperatures.

Comparison between dissolution calculations and experimental results at 1240°C are presented in Figure V. 45.a. Global dissolution kinetics reproduces satisfactorily the experimental results. The initial growth at 5min is qualitatively well reproduced by calculations but is slightly underestimated. The maximum predicted growth reaches 10% after 20s annealing time, but no experiments are available to confirm this prediction. The disappearance of cylindrical particles at 12min marks an inflection in the global dissolution curve, which is rather consistent with the end of the first dissolution regime observed experimentally and occurring after 15min. The final dissolution regime is in a satisfactory agreement with the experiments but ferrite disappearance is predicted to occur after 90 min against 120 experimentally.

At 1260°C calculations are in better agreement with experiments, both qualitatively and quantitatively (Figure V. 45.b). The rapid dissolution rate of ferrite is well accounted for by the model. The dissolution of cylinders occurring after 12min marks a change in the dissolution regime that reproduces satisfactorily the experimental results. The late dissolution stage is also in good agreement with experiments, though the disappearance of ferrite is predicted to occur prematurely: 90min against 120 min experimentally.

With increasing temperature, the maximal reached fraction increases from 10% at 1240°C to 23% at 1300°C (Figure V. 45.d) and becomes temporally more extended as it can be clearly seen, for instance, for spheres whose growth ends after 10 and 15min at 1280°C and 1300°C respectively against 2min at 1140°C, 1200°C, 1240°C and 1260°C. These elevated fractions exceeds by far the experimental results and appears thus unrealistic. The extended growth of spheres results in the appearance of a plateau just after the dissolution of cylinders, which recalls the ones observed experimentally. But in quantitative terms, this plateau occurs at much higher ferrite fractions.

At 1280°C (Figure V. 45.d), dissolution calculations remain somewhat acceptable from a qualitative perspective, though the end of dissolution is largely underestimated (by a factor of 2). But at 1300°C, the global dissolution curve does not agree at all with the experiments.

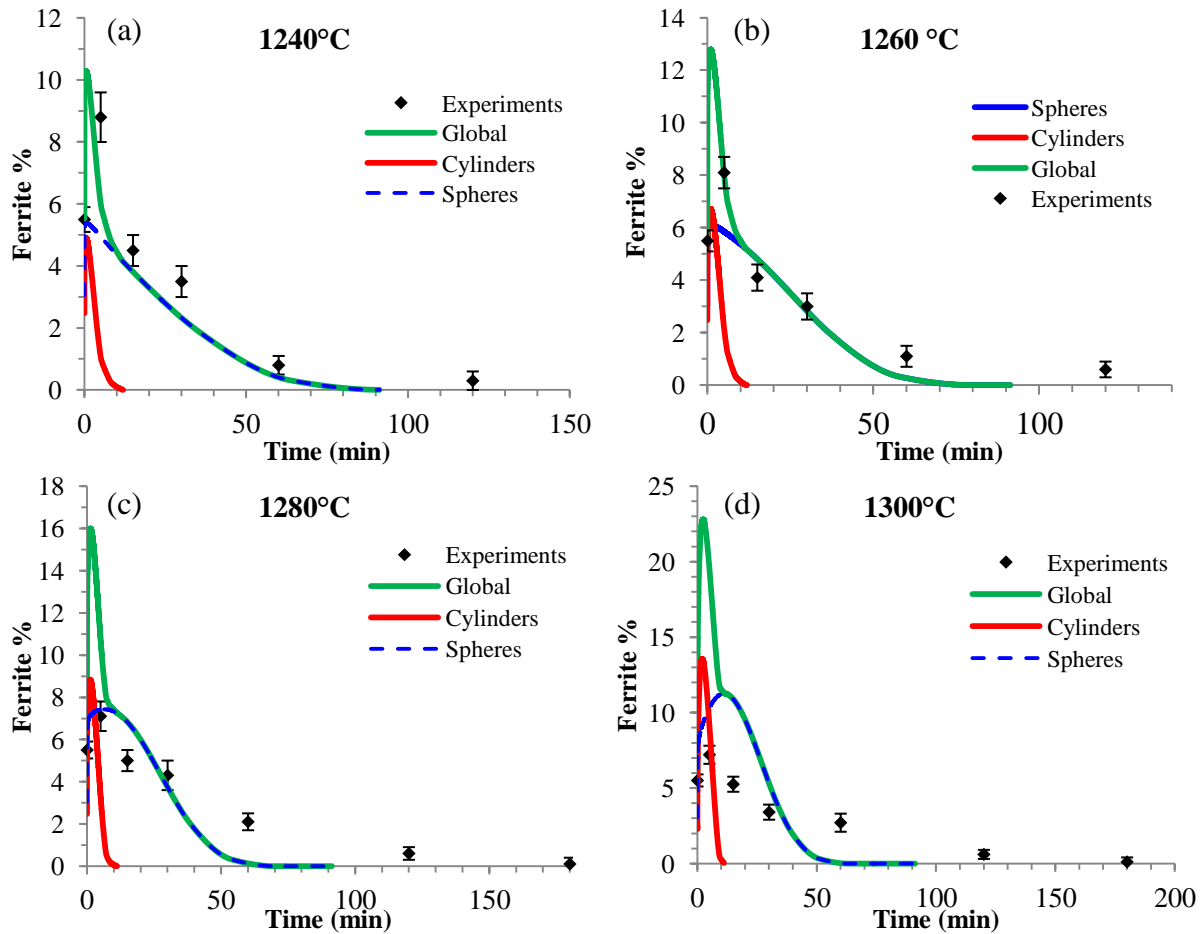


Figure V. 45: Computed and experimental dissolution of vermicular ferrite in the Fe-17.3%Cr-9.4%Ni alloy at (a) 1240°C, (b) 1260°C, (c) 1280°C and (d) 1300°C. Calculations are carried out with the Ptimec-Miettinen module.

A 1346°C, ferrite is expected to remain at equilibrium, as the A4 temperature of the Fe-17.3%Cr-9.4%Ni alloy is 1341°C according to the Ptimec-Miettinen module. Figure V. 46 shows a comparison between the predicted and experimental  $\delta \rightarrow \gamma$  transformation at 1346°C. Predicted ferrite fraction reaches 70% which is much higher than the experimentally determined one. This non realistic prediction stems surely from a wrong description of the Fe-Cr-Ni phase diagram.

On the other, calculations predicted complete ferrite dissolution, while experiments showed its stability at this temperature. This discrepancy is linked, as it will be shown in §III.4.e *Limitations of the modeling*, to an elevated deviation from mass conservation in the calculation cell that led to a change in the final equilibrium of system from  $\delta + \gamma$  to a purely  $\gamma$  one.

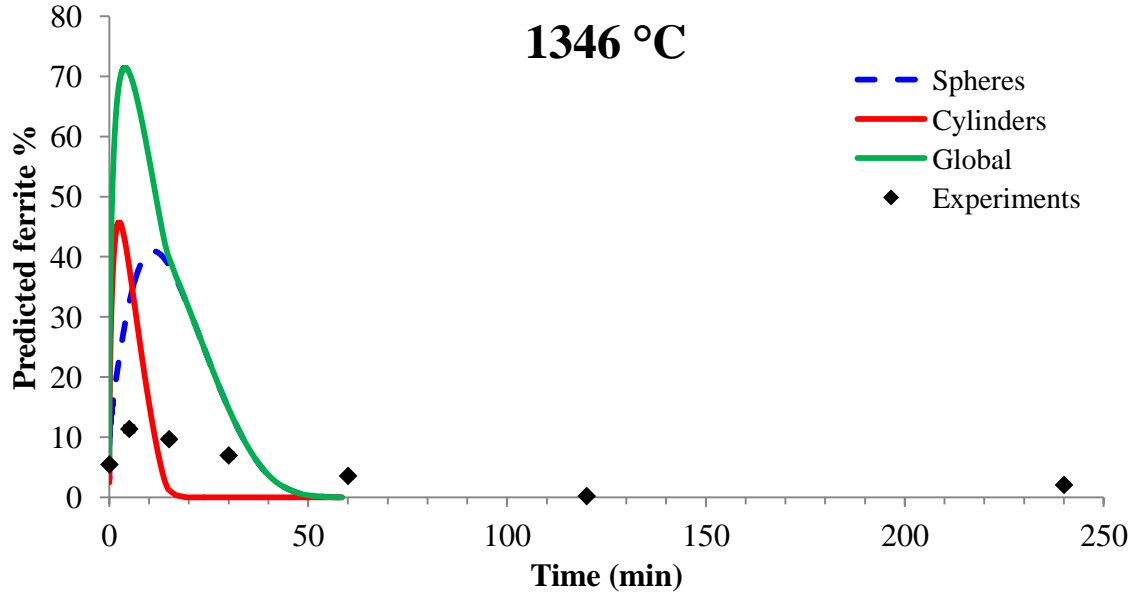


Figure V. 46: Computed and experimental  $\delta \rightarrow \gamma$  transformation of vermicular ferrite in the Fe-17.3%Cr-9.4%Ni alloy at 1346°C. According to Ptimec-Miettinen, ferrite is stable at this temperature, but calculations predicted complete dissolution due to the mass loss of solutes.

### III.4. Discussion

#### III.4.a. Difference in prediction between TCFE6 and Ptimec-Miettinen

Calculations with TCFE6 and Ptimec-Miettinen at 1140°C led to significant difference in the prediction of the kinetics of ferrite dissolution, either during the growth or the dissolution stages.

The growth stage can be driven by solute diffusion either in ferrite (Chapter I) or in austenite (§III.2.b.Effect of solute gradients) or both of them. In both calculations, conditions for the ferrite-driven growth are met and this stage is very short, due to the rapid homogenization of solute profiles in ferrite. Hence, it does not explain the discrepancy between both calculations. Note that growth ends after 8s and 6min when using the Ptimec-Miettinen and the TCFE6 descriptions respectively. The discrepancy is thus to be found in the austenite-driven growth. This can be qualitatively explained by examining the position of the initial compositions at the austenitic side of the interface  $(X_{Ni}^{\gamma/\delta}, X_{Cr}^{\gamma/\delta})_{t=0}$  with respect to the  $\gamma/(\delta+\gamma)$  phase boundary in the isothermal section at 1140°C of the Fe-Cr-Ni phase diagram. As shown in Figure V. 47, this composition lies in the  $\delta+\gamma$  region according to TCFE6 but in the  $\gamma$  region according to Ptimec-Miettinen. Therefore conditions required for the austenite-driven growth are matched only with TCFE6 and this is the reason for the extended ferrite growth with this thermodynamic description.

As for the dissolution, discrepancies between TCFE6 and Ptimec-Miettinen based calculations can be explained twofold. First, the volume fraction of ferrite at the end of the growth stage is more important with TCFE6 (9% against 6.5%). Thus it needs more time to be dissolved. Second, the average composition of austenite is closer to the  $\gamma/(\delta+\gamma)$  phase

boundary of TCFE6 than that of Ptimec-Miettinen (Figure V. 47). Accordingly, Cr and Ni gradients at the interface will be less important, leading to lower solute fluxes and thus lower a transformation rate.

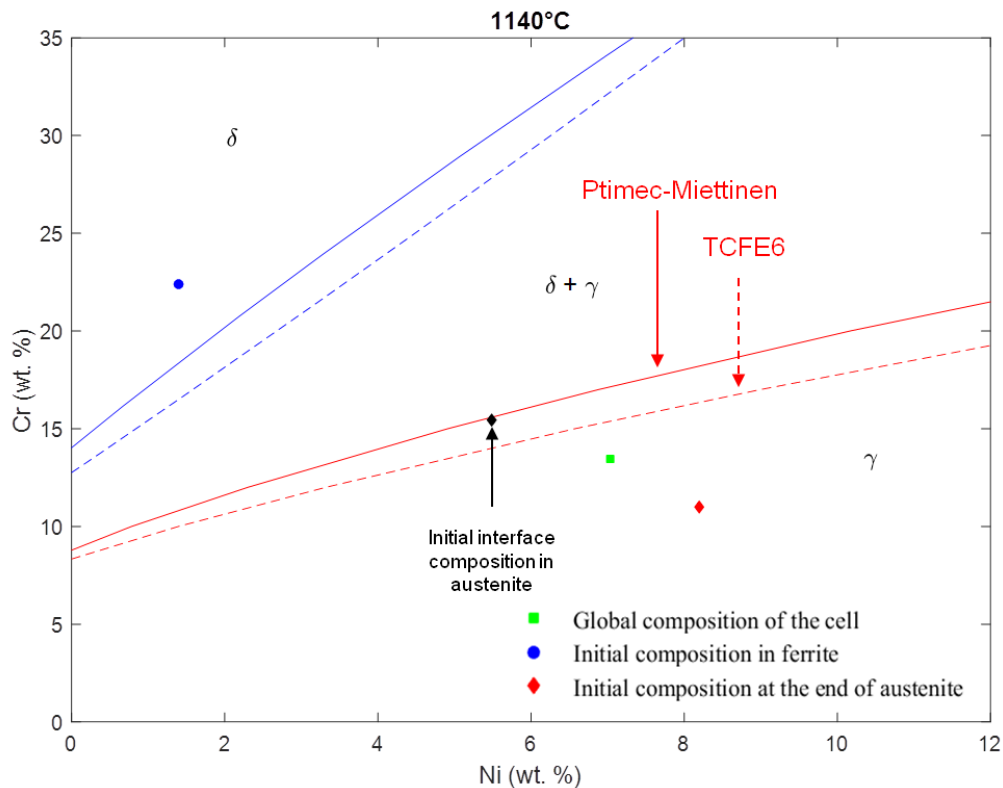


**Figure V. 47:** Initial compositions at the austenitic side of the interface superimposed on the Fe-Cr-Ni isothermal section at 1140°C as calculated using the TCFE6 database and the Ptimec-Miettinen module. The initial interface compositions lies in the  $\delta+\gamma$  region according to TCFE6 but in the  $\gamma$  region according to Ptimec-Miettinen.

### III.4.b. Growth of ferrite: increases with temperature

Predicted ferrite fraction at the end of the early growth stage increases with temperature: from 9% at 1140°C to 23% at 1300°C (Figure V. 45). Agreement with the experiments is satisfactory at temperatures up to 1240°C. However, at higher ones, the predicted growth largely overestimates those experimentally evidenced, the ratio between both of them being 2 at 1280°C and 3 at 1300°C. It should be remembered that experimentally determined growths (after 5min) are not necessarily the maximum reached ones. These latter may possibly be reached earlier. Nevertheless if it is the case, they are not expected to reach as high values as those calculated.

As explained in §III.2.B *Effect of solute gradients*, the growth of ferrite results from the establishment of a non monotonous solute profiles downstream the  $\delta/\gamma$  interface (see Figure V. 33), which are directly due to the position of initial interface compositions with respect to the  $\gamma/(\delta+\gamma)$  phase boundary in the Fe-Cr-Ni phase diagram (see Figure V. 34).

As temperature increases, the initial interface composition ( $X_{Cr}^{\gamma/\delta}, X_{Ni}^{\gamma/\delta}$ ) becomes increasingly remote to the  $\gamma/(\delta+\gamma)$  phase boundary. This is clearly shown in Figure V. 48.a where the gap between the initial  $X_{Cr}^{\gamma/\delta}$  (purple profile) and the operative one (after 2s transformation) increases from 1240°C to 1300°C. The resultant hump that develops in the Cr profile downstream the interface becomes thus more important and as a consequence solute flux  $J_{Cr}^{\gamma}$  that is oriented towards ferrite at this stage of the transformation becomes larger, leading to an increasingly extended ferrite growth.

The increase with temperature of  $D_{CrCr}^{\gamma}$  and  $D_{NiNi}^{\gamma}$  may be thought as playing the opposite effect, *i.e.* contributing to decreasing ferrite growth with temperature in a sense that it may be thought to lead to a more rapid disappearance of the hump. Figure V. 48.b shows that at an advanced stage of ferrite growth (30s), this is not the case as the hump at 1300°C is still well developed (meaning that ferrite growth is still occurring), while those at 1280°C and 1240°C are nearly flat, implying that the growth at these temperature will soon end.

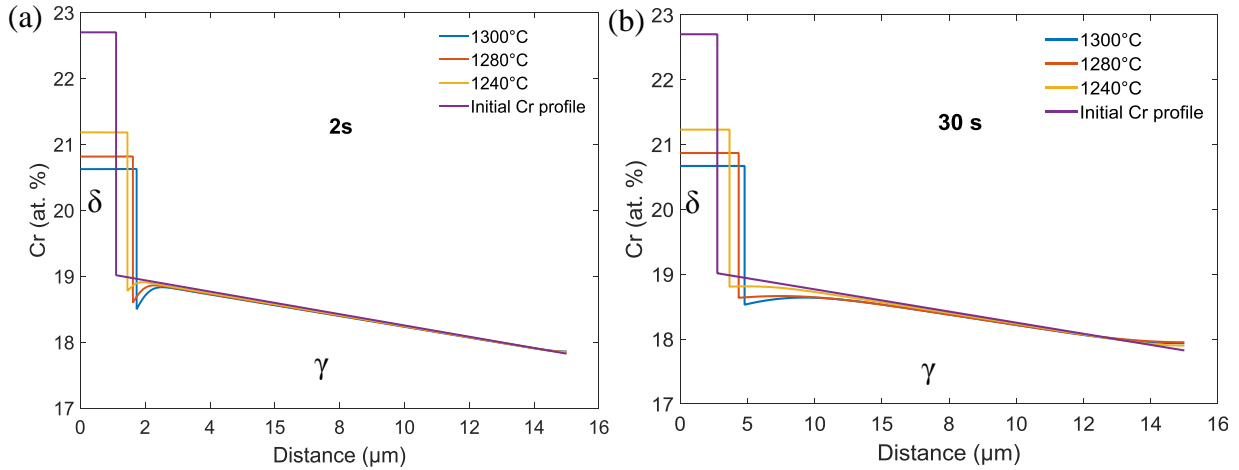


**Figure V. 48: Comparison between chromium profiles at 1240, 1280 and 1300°C after (a) 2s and (b) 30s. The hump downstream the interface becomes more pronounced as temperature increases. Initial profile is superimposed for comparison.**

Consequently, the increase with temperature of the maximum ferrite fraction, reached at the end of the growth stage, can be explained on a thermodynamic basis. Regarding the exaggerated growth observed at 1280°C and 1300°C, several questions arise:

- **Is the Ptimec-Miettinen description inaccurate at 1280°C and 1300°C?** No experimental data are available in the present study to answer this question, but according to Raghavan [83], the Miettinen thermodynamic interpolation fits very satisfactorily the experimental data collected at 1300°C (Figure V. 49.a). This tends to invalidate the hypothesis of the inaccuracy if the Miettinen interpolation. Nonetheless, it should be noted that the range of experimental data is not representative of the Fe-17.3%Cr-9.4%Ni alloy, but is located at higher Cr and Ni levels. It is therefore mandatory to assess the Miettinen interpolation on measurements of interface compositions of the cast alloy at this temperature, before deciding on its accuracy.

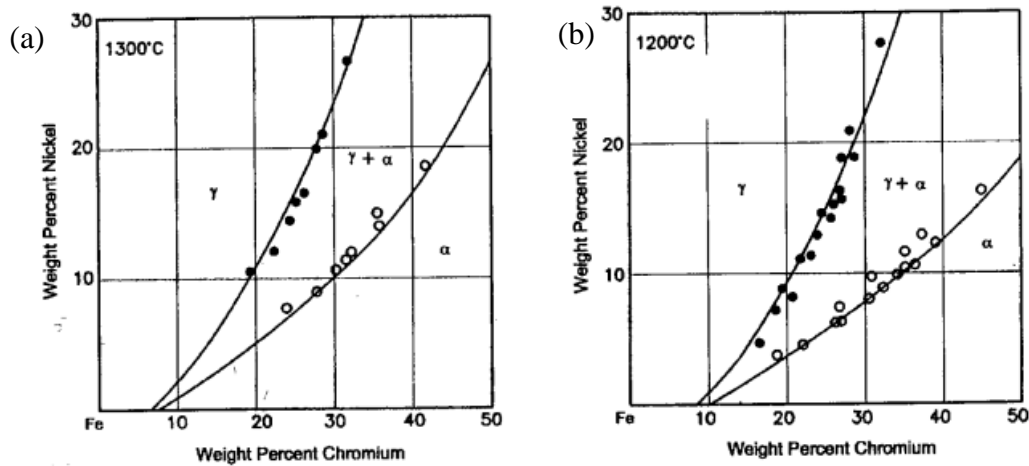


Figure V. 49: Fe-Cr-Ni isothermal sections at (a) 1300°C and (b) 1200°C according to the Miettinen interpolation [83].

- Does the heating of samples play a role in reducing ferrite growth?** In the present calculations, the heating ramp prior to the isothermal transformation is neglected. This stage lasts 90s, *i.e.* the same duration of ferrite growth. It was initially thought that it may have a non negligible impact on the evolution of solute profiles in austenite, as it may progressively change the operative tie-line as temperature increases, instead of an abrupt jump in interface compositions. Calculations including the a heating ramp of 5°C/s from 1000°C to 1300°C were performed (Figure V. 50) and outcome results show that the heating goes not contribute to reduce ferrite growth but increases it, as maximum fraction reaches 26% against 23% without heating.

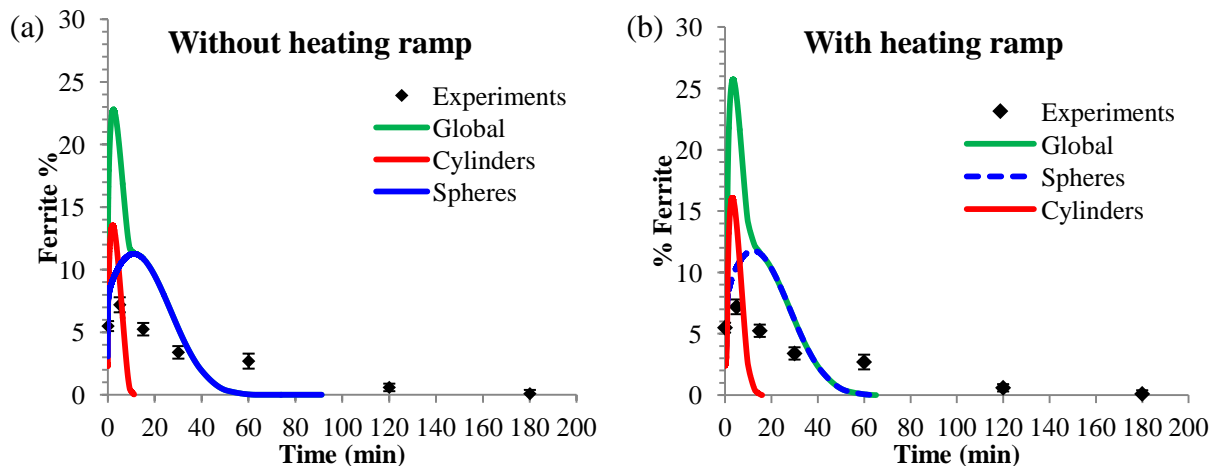


Figure V. 50: Simulated dissolution of vermicular ferrite in the Fe-17.3%Cr-9.4%Ni alloy at 1300°C (a) without a heating ramp prior to isothermal holding and (b) with a heating ramp of 5°C/s starting from 1000°C.

- Does the initial solute gradients affect the growth of ferrite ?** The way solute gradients are accounted for plays an important role on the extent of ferrite growth. The case of the cylindrical cells is quite illustrative: Cr and Ni gradients are assumed to vary linearly in the austenite region (Figure V. 31.b). This approximation underestimates the slope of

EPMA-measured gradients in the as-cast microstructure (Figure V. 35.b). Calculations have shown that such gradients lead to a more lengthened and extended ferrite growth.

As a conclusion, we consider the definition of solute gradients as the most contributing factor to the exaggerated growth of ferrite at 1280°C and 1300°C. Regarding the thermodynamic description, its impact is to be considered with less importance as suggested by [83], but further experimental results are necessary to decide on this issue.

#### **III.4.c. Dissolution of ferrite: from high to slow rate regimes**

In all calculations, the global dissolution curves encompass two regimes: a high rate regime marked by the dissolution of cylinders at and a low rate regime corresponding to spheres dissolution. The decrease in the dissolution rate stems from purely geometrical considerations: the interfacial area-to-volume ratio  $S_V$  measures  $\frac{2}{r}$  in cylinders and  $\frac{3}{r}$  in spheres,  $r$  being the radius of the ferrite particle. With the considered radius classes in both cylindrical and spherical populations (Table V. 9 and 10),  $S_V$  is larger in the case of cylinders (smaller radii), which means that solute exchange at the interface is more important and as a consequence the transformation rate is higher.

The transition from the high to the slow rate dissolution is well marked at 1140°C, 1280°C and 1300°C, whereas it is smooth at the other temperatures. This marked/smooth character depends on how advanced is the transformation of spheres where cylinders disappear. At 1140°C transition occurs at the beginning of spheres dissolution (Figure V. 41) and at the end of spheres growth at 1280°C and 1300°C (Figure V. 51). These situations give rise to a marked change in the slope of the dissolution curves which resemble those of the experimental dissolution kinetics of ferrite at the same temperatures (see Chapter III, Figure III. 12). On the contrary, at 1200°C, 1240°C and 1260°C, the disappearance of cylinders takes place when a non negligible amount of spheres (1% absolute) is consumed.

#### **III.4.d. Too fast a predicted ferrite dissolution**

From the previous results, it can be seen that, except at 1140°C, dissolution calculations underestimate the total time required for ferrite to dissolve. In view of the approximations made in describing the vermicular microstructure, this deviation is to be considered as small at 1240°C and 1260°C, since predicted dissolutions are roughly 30% faster than experiments. However, at 1280°C and 1300°C, the discrepancy is of 100%.

It was previously demonstrated how important the impact of the thermodynamic description on ferrite dissolution kinetics is. Comparisons between TCFE6 and Ptimec-Miettinen at 1140°C and 1200°C (Figure V. 39 and 42) are quite illustrative of this point as the discrepancy between both predictions is large. From 1200°C to 1300°C, the Ptimec-Miettinen description is rather accurate as shown by the calculations and in literature (Figure V. 49). Nevertheless, we expect that even small inaccuracies may have a considerable impact on the quality of the calculations.

Regarding the accuracy of Cr and Ni diffusivities, comparison between experimentally assessed interdiffusion coefficients and those extracted from the MOB2 database at temperatures from 1100°C to 1280°C is shown in Table V. 14. MOB2 values are in satisfactory agreement with experimentally determined ones. Therefore the hypothesis of the enhancement of the transformation being partly due to an overestimated diffusion coefficients is not appropriate in this case.

**Table V. 14: Interdiffusion coefficients of chromium and nickel in austenite at 1100, 1240 and 1280°C extracted from the MOB2 database [72] and compared to experimental values obtained from Duh *et al.* [55], the Smithells Metals Reference Book [73] and the experiments of Chapter III.**

T(°C)	Cr (wt. %)	Ni (wt. %)	$D_{CrCr}^Y$ (m <sup>2</sup> /s)	$D_{NiNi}^Y$ (m <sup>2</sup> /s)	Source
1100°C	17.4	11.6	<b>2.1</b> 10 <sup>-15</sup>	<b>9.4</b> 10 <sup>-16</sup>	MOB2
	17.5	9.3	3.7 10 <sup>-15</sup>	9.0 10 <sup>-16</sup>	Duh <i>et al.</i>
	16	23	2.4 10 <sup>-15</sup>	9.0 10 <sup>-16</sup>	
1240°C	17.4	11.6	<b>2.2</b> 10 <sup>-14</sup>	<b>1.0</b> 10 <sup>-14</sup>	MOB2
	17.4	11.6	2.7 10 <sup>-14</sup>	5.0 10 <sup>-15</sup>	Experiments (Chapter III)
1280°C	17.4	11.6	3.9 10 <sup>-14</sup>	<b>1.8</b> 10 <sup>-14</sup>	MOB2
	--	9.2	--	2.2 10 <sup>-14</sup>	Smithells
	--	14.9	--	1.1 10 <sup>-14</sup>	
	--	15.5	--	4.5 10 <sup>-14</sup>	

### III.4.e. Limitations of the modeling

The current dissolution modeling was performed using a schematic representation of a microstructure that is far more complex, either from a morphological or a physical point of view. Moreover, the numerical treatment of phase transformation is based on simplifying physical hypotheses and, by construction, leads to some limitation whose impact on the predictions may not be negligible. We present and discuss them:

- **Deviation from complete mass conservation.** In the modeling of ferrite dissolution in the multilayered microstructures, deviation from mass conservation was always kept under 0.1% relative. Such a reduced mass loss was encountered only in the planar geometry of the calculation cell and is achieved through the use of the artificial diffusion coefficient  $\bar{D}$  (see Chapter IV, §V.5.C Artificial diffusion).

On the contrary, in the cylindrical and spherical geometries this deviation reached non negligible levels (up to 5% relative). At 1346°C, this change in global composition has a dramatic effect on the prediction. In fact, the amount of the mass loss was high enough to change the equilibrium of the system (calculation cell) from  $\delta+\gamma$  domain at the beginning of the simulation to the  $\gamma$  domain at the end of it (Figure V. 51.a). This explains the predicted dissolution of ferrite at this temperature (Figure V. 46). However, at 1140 to 1300°C, global mass change did not change the stability of phases as initial and final compositions of the calculation cell remain in the  $\gamma$  domain (Figure V. 51.b). In these cases, it was initially

thought that this deviation in the cell composition would result in an increase in the driving force for ferrite dissolution, leading to enhanced dissolution of ferrite. However, calculations (with ThermoCalc<sup>®</sup> and CEQCSI) of the total Gibbs energy of the initial and final compositions have shown that the change in the driving force is negligible in these conditions (0.05%). Nevertheless, this change in composition could impact other thermodynamic quantities (operative tie-lines) which may lead to a different kinetics of ferrite dissolution.

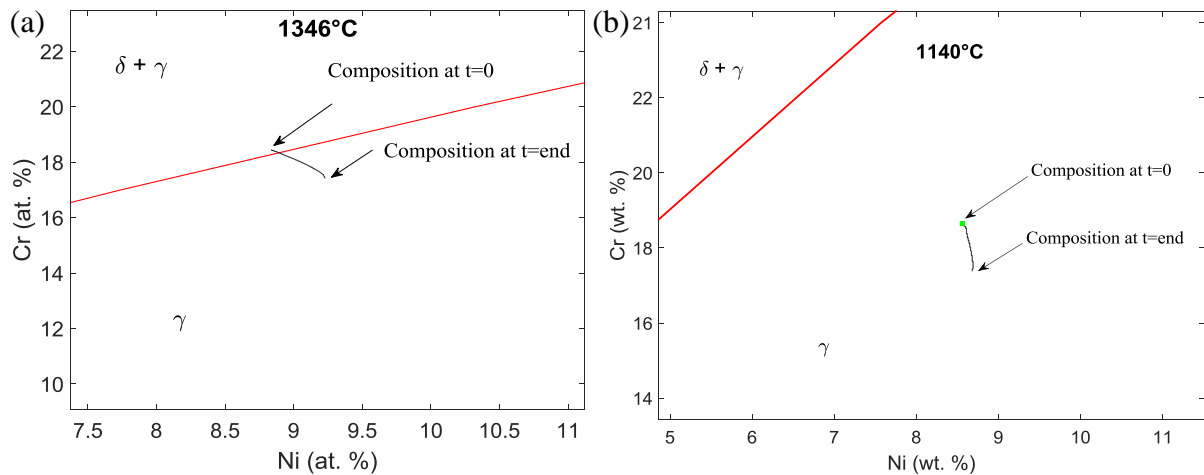


**Figure V. 51: Change in the global composition of the calculation cell from the beginning to the end of the transformation. (a) At 1346°C the initial composition of the calculation cell goes from the  $\delta + \gamma$  to the  $\gamma$  domain resulting in a complete dissolution of ferrite, although the latter is stable at this temperature. (b) At 1140°C the global composition of the calculation cell remains in the  $\gamma$  austenitic.**

Therefore, for cylindrical and spherical geometries in the actual formulation of our model, a systematic checking of the evolution of the global composition should be done in order to verify the reliability of the calculations.

In the case of non-isothermal transformations (Figure V. 22), a significant mass loss was also evidenced (even in the planar geometry). Its amplitude was not quantified yet, as it is expected to depend on the heating and cooling cycles.

- **The independence of interdiffusion coefficients of solute composition:** in the present model, and at a given temperature, interdiffusion coefficients are assumed independent of composition. This can result in the enhancement of the dissolution kinetics, as it was demonstrated in Appendix D. The amount of this enhancement is not known yet (its upper limit is 20%). It needs thus to be quantified in a further study, when composition dependency of interdiffusion coefficients will be taken into account in the model.

- **Chemical coupling** between neighboring particles is neglected, as dissolution of cylinders and spheres are carried out in separate calculation cells without exchange of solutes between them. The impact of such a limitation should however be relativised, since chemical coupling from dendritic arms to intersections is virtually assumed, as the contribution of dendritic arms to the composition fields around intersections is initially incorporated by the iso-radius average approach in the spherical calculation cells (§III.2.b.Effect of solute gradients).

- **Spheroidization of ferrite** that was observed at the intermediate stage of the transformation (see *Figure III. 15* in *Chapter III*) could not be taken into account in the present 1D model. Given the satisfactory predictions provided by the model, neglecting this phenomenon seems not to significantly alter the description of the dissolution of vermicular ferrite. This may be due to the fact that spheroidization of ferrite particles in the cast-alloy did not lead to an important increase in the size of ferrite particles.

- **Virtual interfaces** are created when separating dendrite arms from intersections. These interfaces do not exist in the as-cast microstructure. For dendrite arms these new interfaces correspond to the upper and lower bases of the equivalent cylinder. In the calculation cell, given that cylinders are assumed as infinitely long, these interfaces are not accounted for in calculations and do not contribute to any transformation process. On contrary, they are effectively considered in spheres. If each dendrite intersection is to be considered surrounded by 6 dendritic arms with average radius ( $r=0.4\mu\text{m}$ ), the total amount of the extra virtual interface is  $3\mu\text{m}^2$ , which represents 25% of the interface of a sphere of radius  $1\mu\text{m}$ , 6% of a sphere of  $2\mu\text{m}$ , 2% of a sphere of  $3.5\mu\text{m}$  and only 1% of a sphere of  $5\mu\text{m}$ . This simple calculation shows that this effect, though important for lower radius-spheres, is negligible for bigger sizes and consequently for the average kinetics of spheres dissolution.

- The **representativeness of 1D simulations** with regard to the real microstructure needs to be evaluated. In the calculation cells, we consider phases of perfect geometries in which the transformation is assumed isotropic, *i.e.* depending only on the radial distance to the interface. In reality dissolution is not isotropic but is influenced by neighboring particles. Let's take the example of the dendritic arms. The model assumes that dissolution is homogeneous along the whole length of the equivalent cylinder and no interaction with the neighboring spheres exists. However, as it can be observed on the micrograph of *Figure V. 52*, the dissolution sequence is not as simple. Given their non homogeneous thicknesses, dendritic arms first dissolve at their thinnest parts. Then the remaining fragments linked to a dendritic intersection may contribute to increase the size of the latter and its representative "equivalent sphere". This sequence is not taken into account in the present model. This phenomenon can only be taken into consideration in a 3D space.

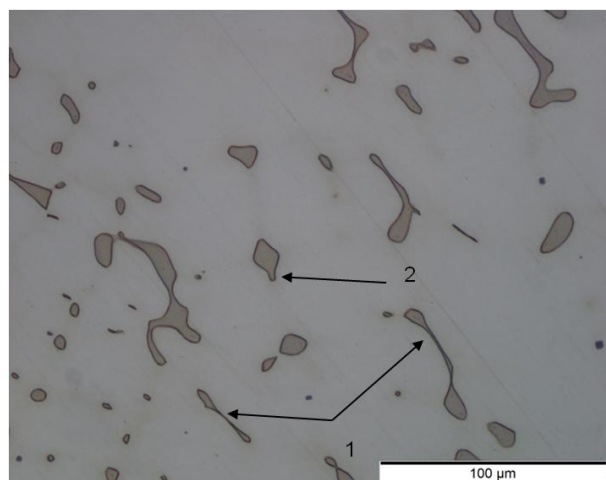


**Figure V. 52:** Vermicular microstructure after 15min at 1240°C showing initial dendrite arms dissolving at their thinnest parts (arrows n°1) and remaining fragments becoming part of the dendritic intersections (arrow n°2).

- **Dispersion of Cr and Ni gradients around ferrite particles:** small variation of Cr and Ni gradients near the interface is of a first order importance on the dissolution kinetics. The issue of the choice of initial solute fields in austenite (see §III.2.c. *Gradient description in austenite*) illustrates very well this point: preliminary calculations have shown that with a linear EPMA measurements of solute profiles, the dissolution kinetics do not agree at all with experimental results. On the contrary, when a 2D mapping of Cr and Ni composition fields was used, it has been possible to derive initial solute fields that provided results far more consistent with experiments. In a future work, there is a need to statistically assess the so-defined gradients in austenite. Supplementary EPMA mappings should thus be performed. Furthermore, the iso-radius average approach of defining solute fields have shown that the use of a 2D EPMA mapping is compulsory since it gives a more accurate description than a 1D one. This reasoning may be extended to the 3D space and we may expect that a 3D solute field mapping will permit to derive a more realistic picture of solute fields.

#### IV. Conclusion

In this chapter, the phase transformation model developed in Chapter IV has been applied to analyze the dissolution of ferrite in the multilayered microstructures and the ingot-cast alloy.

In the case of the multilayered microstructures, numerical results are highly encouraging. Predictions of dissolution kinetics were quantitatively very satisfactory for all investigated microstructural states. The model satisfactorily accounted for the initial ferrite growth. Regarding the composition profiles, there was also a very satisfying agreement with experimental data, which validates the used interdiffusion coefficients. In addition, reference to the measured interface compositions shows a satisfactory accuracy of the Ptimec-Miettinen description of the phase diagram at 1240°C.

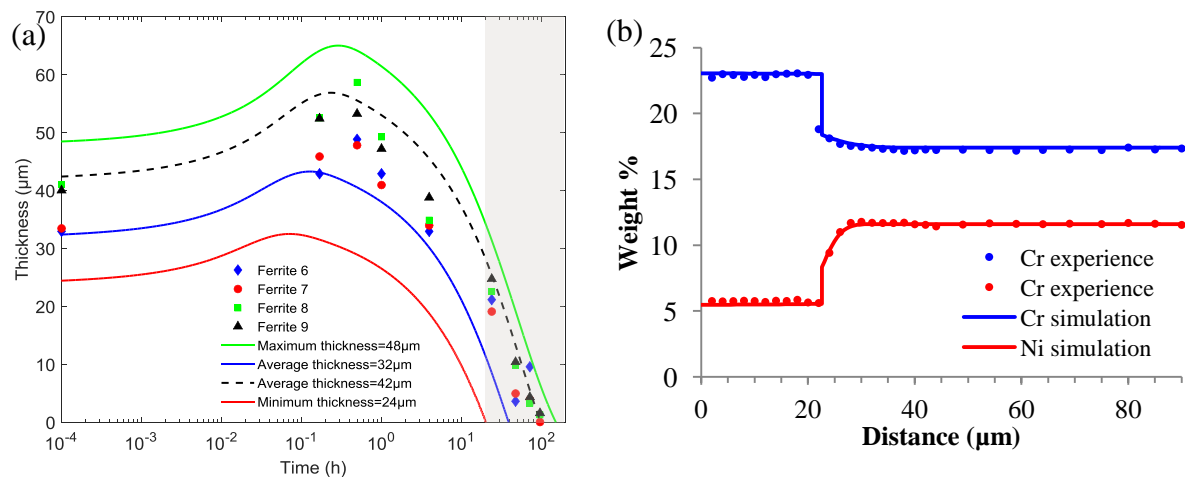


**Figure V. 53: Example of the model performances. Case of the multilayered microstructure in the CR1 state : (a) Experimental and predicted ferrite dissolution kinetics. (b) Experimental and predicted chromium and nickel profiles after 10min at 1240°C.**

Together with the numerical analysis of ferrite dissolution in  $\gamma/\alpha/\gamma$  diffusion couples at 1100°C, it was possible to check the relevance of the available thermodynamic descriptions as a function of temperature: the TCFE6 database was found to yield a more accurate description of the Fe-Cr-Ni phase diagram at 'lower' temperatures (around 1100°C), while the Ptimec-Miettinen module is preferred at 'higher temperatures' (around 1240°C). This constitutes a valuable outcome in a sense that it permits to select the proper thermodynamic description as function of temperature.

In the as-cast microstructure, dissolution of vermicular ferrite has been analyzed using a novel approach combining spherical and cylindrical calculation cells as an equivalent geometry for residual ferritic dendrites. Prior to dissolution simulations, preliminary analyses permitted to select the most pertinent parameters to be considered in calculations. As an outcome of this study, it appears that:

- ferrite radii distribution should be considered instead of the average radius for both morphologies.
- initial austenite composition in the spherical cells should be accounted for by the iso-radius average approach. For cylinders, a linear gradient provides a good description and there is no need to consider primary austenite.
- the most suited characteristic diffusion length is  $\frac{1}{2}\lambda_2$  for dendritic arms and  $\frac{1}{2}\lambda_1$  for arms intersections.

Although based on simplifying assumptions of the numerical model, dissolution calculations at the temperatures experimentally investigated were in satisfactory agreement except at 1280°C and 1300°C, where the origin of discrepancies needs to be investigated (solute gradients, thermodynamic description, etc.) with further experimentations. The modeling allowed to account for the initial growth of ferrite and reproduce the transition from high to low rate dissolution regimes, after complete dissolution of cylinders. Unlike the multilayered microstructures, the initial growth of vermicular ferrite cannot be explained on the basis of solute diffusion in ferrite, but relies on a new mechanism of growth that has been evidenced in this work: solute diffusion in austenite.

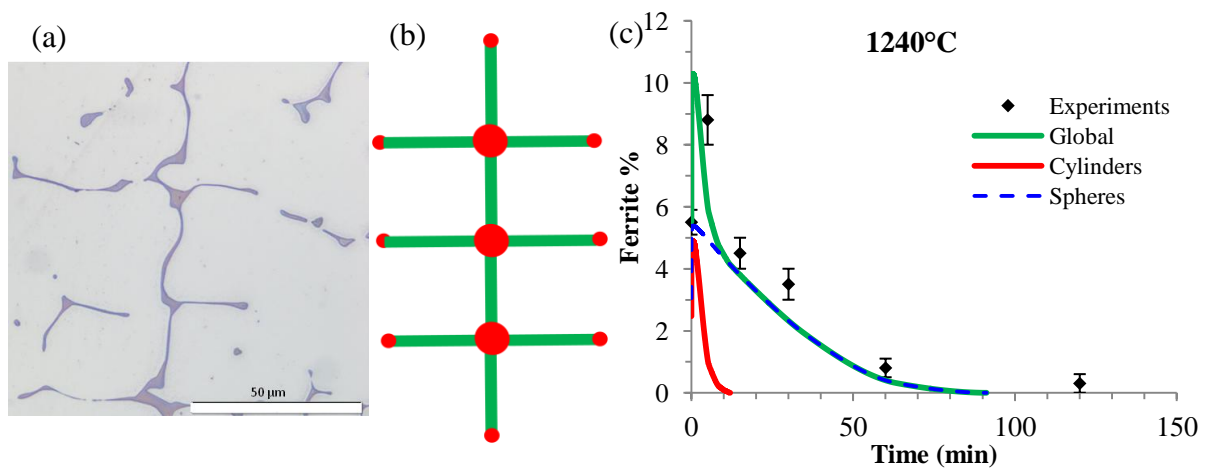


Figure V. 54: (a) Typical vermicular ferrite. (b) Equivalent morphology. (c) Comparison between experimental and predicted dissolution kinetics of vermicular ferrite at 1240°C.

Numerically, the success of the model relies on the use of the double-uniform meshing in austenite that renders results mesh-insensitive with a relatively small number of grid points. The issue of deviation from solute mass conservation has been resolved for the planar geometry (case of the multilayered microstructures), as mass loss was always kept under 0.1% relative. However in the cylindrical and spherical geometries mass loss is not negligible, as it reached up to 5% relative. This issue was shown to considerably impact the predictions as it may lead in some cases to a change in the final thermodynamic equilibrium of the system.

To sum up this chapter, one now has a numerical model that demonstrated its capabilities in predicting ferrite dissolution in two microstructures of the Fe-Cr-Ni system, in complex metallurgical conditions, despite the simplified description and the physical restrictions imposed by the model.



# Chapter VI

## Conclusions and perspectives

Residual  $\delta$ -ferrite is widely encountered in the as-cast microstructures of austenitic stainless steels. It stems from the incomplete high temperature solid-state  $\delta \rightarrow \gamma$  transformation occurring upon the solidification stage. Its presence in the austenitic matrix has high consequences on the hot workability of stainless steels and leads to the formation of edge cracks during hot rolling. The formation of ferrite in such alloys is widely studied in literature, especially in stainless steel welds. However, its dissolution by further heat treatments did not receive as much attention.

This PhD work, realized in partnership with APERAM Stainless, was intended to bring more insight into the mechanisms of the  $\delta \rightarrow \gamma$  transformation occurring during the heat treatments prior to the hot rolling of austenitic stainless steels. To achieve this goal, the guidelines fixed in this PhD work were as follows:

- Experimentally, study the influence of various metallurgical parameters (temperature, composition, microstructure, etc.) on the kinetics of ferrite dissolution. To facilitate this task, the transformation was studied in two simplified configurations: first, in a ternary Fe-Cr-Ni cast alloy with an equivalent composition close to the one encountered in industrial stainless steels and second in the multilayered microstructures with initially flat  $\delta/\gamma$  interfaces. This was the object of Chapter III.
- Numerically, develop a one-dimensional finite difference model to predict the  $\delta \rightarrow \gamma$  transformation under a given operative and metallurgical conditions. The model was described in Chapter IV. In a preliminary step, the model was validated on experimental results of ferrite dissolution in the multilayered microstructures that were designed for this purpose. Then, the numerical analysis was extended to study the dissolution in the ternary cast alloy, as presented in Chapter V.

### I. Overview of the work and scientific contribution

The salient features of this work are summarized as follows:

In the ternary alloy three ferrite morphologies were identified in the as-cast states across the ingot. Dissolution kinetics for each ferrite type was established at several temperatures typical of the hot rolling process of austenitic stainless steels. For vermicular ferrite, which was at the center of this study, the dissolution kinetics was found to follow an initial growth of ferrite followed by rapid then slow rate dissolution regimes.

With the HIP technique it was possible to elaborate multilayered microstructures with planar  $\delta/\gamma$  interfaces. Using successive hot and cold rollings, four thickness scales have been

obtained. A thorough experimental work permitted to characterize these microstructures after each reduction step and then study dissolution of ferrite bands at 1240°C.

A one-dimensional finite difference numerical model was developed in order to predict ferrite dissolution. It treats the movement of the  $\delta/\gamma$  interface driven by solute diffusion in the ternary Fe-Cr-Ni system. Based on simplifying assumptions, it permits to treat diffusion equations under various metallurgical conditions including non-isothermal heating cycles. In the course of the modeling, several challenges have been addressed, in particular the deviation from perfect mass conservation and the sensitivity of the calculations to the number of grid points. These issues have been largely resolved but further improvements remain necessary.

Through preliminary application to  $\alpha \rightarrow \gamma$  transformation in diffusion couples and in the multilayered microstructures, the model was found to quantitatively predict the kinetics of ferrite dissolution and the change in composition across the interface, in good agreement with experimentally reported data. The flexibility of the model with regard to the input thermodynamic and kinetics parameters allowed to outline the major importance of selecting the proper thermodynamic description at a given temperature. In addition, with the numerical analysis of ferrite dissolution in the cast alloy, it was shown that accurate and unique description of the Fe-Cr-Ni phase diagram in the 1100-1346°C temperature range is not yet reached.

The prediction of ferrite dissolution in the ingot-cast alloy was conducted with a novel approach in which the complex morphology of vermicular ferrite was approximated by an equivalent combination of spheres and cylinders. Though schematic, and in view of the approximations made in describing the vermicular microstructure, this approach yielded very satisfying predictions with regard to the experimental data at temperatures up to 1260°C. Further, the various stages of the  $\delta \rightarrow \gamma$  transformation kinetics were well accounted for and their underlying mechanisms outlined.

Through extensive preliminary calculations, the most relevant metallurgical parameters for the prediction of ferrite dissolution in such a complex morphology were outlined and their impact on the quantitative prediction was addressed and quantified. They are:

- **Ferrite size:** distribution of ferrite radii should be considered instead of the average radius.
- **Solutes fields:** the description of the initial gradients in austenite should be performed with the iso-radius average approach in case of dendritic arms intersections.
- **The characteristic lengths:** in the vermicular microstructure are  $\frac{1}{2}\lambda_2$  for dendritic arms and  $\frac{1}{2}\lambda_1$  for dendrite arms intersections.

## II. Recommendations for easy prediction of ferrite dissolution

Two recommendations can be drawn from previous simulations, for easy prediction of the dissolution of vermicular ferrite in industrial 304L stainless steel slabs. First, there is no need to consider secondary dendrite arms in the initial simulation inputs, as transformation at

advanced stages is only driven by the dissolution of dendrite arms intersections (Figure VI. 1). Second, since dissolution ends by the disappearance of the biggest dendrite arms intersections (4<sup>th</sup> spherical class in Figure VI. 1), we suggest to predict the end of the dissolution as follows: instead of proceeding to a thorough characterization of the as-cast state (including measurement of ferrite fraction and sizes) which can rapidly be time-consuming, it would be preferred to carry out the following procedure:

1. Measure the radius  $R$  of the biggest dendrite arms intersections.
2. Measure the solute fields around these particles by EPMA and derive characteristic gradients  $G$  by the iso-radius average approach.
3. Measure the characteristic length around these particles:  $\frac{1}{2}\lambda_1$  in the case of vermicular-type ferrite.
4. Run the dissolution calculations with one spherical ferrite particle. The input parameters are :  $R$ ,  $G$  and  $\frac{1}{2}\lambda_1$ .
5. The adequate isothermal heat-treatment will be chosen either for full ferrite dissolution or for a given value under which the presence of ferrite is not detrimental for the hot workability of the austenitic stainless steel slab.

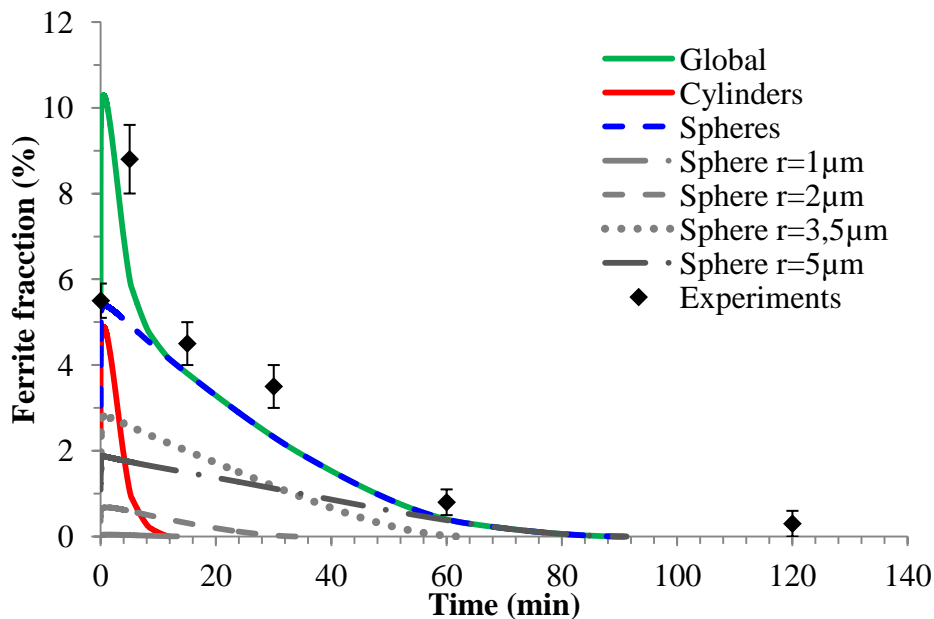


**Figure VI. 1:** Computed and experimental dissolution kinetics of vermicular ferrite at 1240°C. Note that cylinders disappear very early and that the final stage of the dissolution is driven by biggest spherical particles.

### III. Perspectives

Several issues and development paths have been raised but could not be addressed in this PhD work due to time constraints. Of great interest is to consider them in a future research work. Accordingly, some perspectives are suggested below in order to complement the topics investigated in this PhD thesis. They are formulated threefold:

**Experimentally**, the lack of experimentally assessed thermodynamic data of the Fe-Cr-Ni phase diagram at high temperatures (tie-lines at 1260, 1280 and 1300°C) prevented to check the pertinence of the Ptimec-Miettinen description. Measurement of the interface compositions in the multilayered or the cast microstructures can thus be used to fulfill this requirement.

On the other side, the study of ferrite dissolution can be extended to industrial 304L stainless steels. This work has already been started in the framework of this thesis but put in standby due to time constraints. Two 304L grades presenting different Ni levels were considered: 18Cr-8Ni and the 18Cr-10Ni. Characterization of the as-cast microstructure in terms of ferrite fraction, secondary dendrite arms spacing ( $\lambda_2$ ), inter-lath spacing (d) and solute microsegregation in ferrite and austenite has already been performed. In a future work, since both grades possess a non negligible amount of nitrogen, dissolution heat treatments should be carried under controlled atmosphere of Ar+N<sub>2</sub> mixtures in order to avoid nitrogen escape, which was demonstrated to be very rapid at high temperatures (see Appendix D).

**Numerically**, several development paths are raised. First, the issue of deviation from mass conservation for spherical and cylindrical geometries should be resolved. Some ideas are set out in [66] [67], including a better numerical treatment of the interface mass balance equation. Second, some of the simplifying assumptions under which the model is build can be lifted in a future work in order to render the model applicable to more complex situations, such as those where chemical interaction between solutes is strong, or where interdiffusion coefficients strongly depend on composition. Finally, to optimize the algorithm, it is of great interest to rewrite the whole set of equations into a matrix form and to apply an acceleration algorithm (like the multidimensional Newton-Raphson one) in order to reduce the number of iterations necessary for system convergence.

Regarding **modeling**, this work can be pursued to analyze the dissolution of lathy ferrite. From an industrial point of view, it is interesting to focus on lathy ferrite in the skin, since edge-cracks initiate in this zone. The morphology of lathy ferrite needs first to be evidenced by selective etching and then equivalent geometries can thus be derived for the calculations. In this microstructure, another characteristic length is to be considered in addition: the inter-lath spacing (d).

On the other hand, it is of interest to extend this model in the 3D space in order to allow chemical interactions between neighboring particles and to study the dissolution in a more realistic morphology of ferrite. For this purpose the three-dimensional morphology of ferrite should be evidenced by advanced imagery techniques, such as the holotomography (phase contrast can be enhanced if heavy elements like Mo are present in the alloy).

Finally, the present numerical model together with the multilayered microstructures designed by Hot Isostatic Pressing turn out to be interesting tools in the studying of phase transformation in simplified systems. They offer several perspectives. A short overview of these perspectives is given below:

- If the numerical model is to be extended to a quaternary system, (the Fe-Cr-Ni-Mo for example), simple microstructures with the right compositions can be elaborated by HIP in order to provide the necessary thermodynamic and kinetic data for model validation.
- The multilayered microstructure can be used to assess high temperature phase diagrams of multicomponent systems approaching the austenite stainless steel compositions. To study a wide range of compositions, one could pile up several sheet alloys with various compositions in the same stack.
- The multilayered microstructures provide also a tool to study the  $\delta \rightarrow \gamma$  transformation in Duplex stainless steels whose  $\delta + \gamma$  microstructure after hot rolling exhibit an elongated austenite and ferrite shapes (Figure VI. 2). On the other hand, the model can be used in order to predict phase proportions during the successive industrial annealings of Duplex stainless steels.

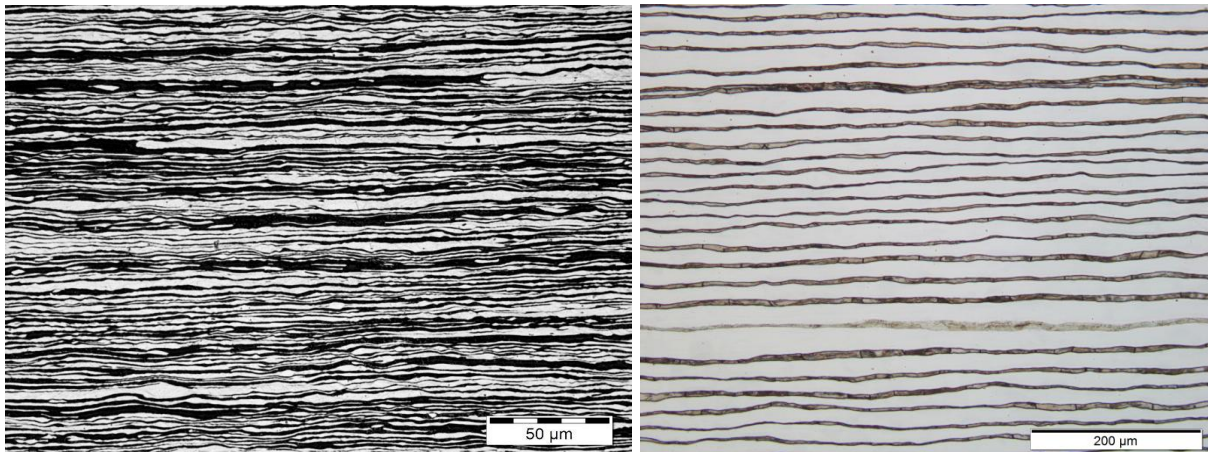


**Figure VI. 2:** (a) Microstructure of a superduplex stainless steel after hot and cold rolling exhibiting elongated ferrite (dark) and austenite (white) morphologies (thickness 1.5mm). (b) The multilayered microstructure in the CR2 state. Note the resemblance between both microstructures.



## Bibliography

- [1] “International Stainless Steel Forum.” [Online]. Available: [www.worldstainless.org](http://www.worldstainless.org).
- [2] “[www.aperam.com](http://www.aperam.com).”
- [3] T. Ogawa and E. Tsunetomi, “Hot Cracking Susceptibility of Austenitic Stainless Steels,” *Welding journal*, 1982.
- [4] C. Gonnet, “Caractérisation fine de brames brutes de solidification de la nuance 304L,” Master thesis, Phelma Engineering school, INPG, Grenoble, France, 2011.
- [5] S. K. Kim, Y. K. Shin, and N. J. Kim, “Distribution of  $\delta$  ferrite content in continuously cast type 304 stainless steel slabs,” *Ironmak. Steelmak.*, vol. 22, no. 4, pp. 316–325, 1995.
- [6] F. Czerwinski, J. Y. Cho, A. Brodtka, A. Zielinska-Lipiec, J. H. Sunwoo, and J. A. Szpunar, “The edge-cracking of AISI 304 stainless steel during hot-rolling,” *J. Mater. Sci.*, vol. 34, no. 19, pp. 4727–4735, Oct. 1999.
- [7] J.-Y. Cho, “Effect of delta ferrite on edge-crack formation during hot rolling of austenitic stainless steel,” Master thesis, McGill, Montreal, Canada, 1999.
- [8] P. Lacombe and B. Baroux, *Les Aciers inoxydables*, EDP Sciences. 1991.
- [9] C. R. Speich, “Chromium-iron nickel system,” *ASM Met. Handb.*, pp. 424–426, 1973.
- [10] E. Schurmann, J. Brauckmann, “Etude des équilibres de fusion dans le coin de fer du système ternaire Fer-Chrome-Nickel,” *Arch. Eisenhüttenwes.*, pp. 3–7, 1977.
- [11] H. Fredriksson, “Solidification and casting of metals,” *Met. Soc. Lond.*, pp. 131–138, 1979.
- [12] S. Schaeffler, “Constitution Diagram for Stainless-steel Weld Metal. 2. Schaeffler Diagram,” *Met. Prog.*, vol. 106, no. 1, pp. 227–227, 1974.
- [13] D. J. Kotecki and T. A. Siewert, “WRC-1992 constitution diagram for stainless steel weld metals: a modification of the WRC-1988 diagram,” *Weld. J.*, vol. 71, no. 5, pp. 171–178, 1992.
- [14] O. Hammer and U. Svensson, “Solidification and casting of metals,” *Met. Soc. Lond.*, vol. 401, 1979.
- [15] P. L. Ferrandini and C. T. Rios, “Solute segregation and microstructure of directionally solidified austenitic stainless steel,” *Mater. Sci. Eng. A*, vol. 435, pp. 139–144, 2006.
- [16] J. A. Brooks, A. . Thompson, and J. . Williams, “A Fundamental Study of the Beneficial Effects of Delta Ferrite in Reducing Weld Cracking,” *Weld. J.*, vol. 63, pp. 71–83, 1984.
- [17] J. W. Elmer, S. M. Allen, and T. W. Eagar, “Microstructural development during solidification of stainless steel alloys,” *Metall. Trans. A*, vol. 20, no. 10, pp. 2117–2131, 1989.

- [18] M. Bobadilla, J. Lacaze, and G. Lesoult, "Influence des conditions de solidification sur le déroulement de la solidification des aciers inoxydables austénitiques," *J. Cryst. Growth*, vol. 89, no. 4, pp. 531–544, 1988.
- [19] J. W. Elmer, S. M. Allen, and T. W. Eagar, "The influence of cooling rate on the ferrite content of stainless steel alloys," in *Proceedings of the 2nd International Conference on Trends in Welding Research*, 1989, pp. 14–18.
- [20] J. A. Brooks and A. W. Thompson, "Microstructural development and solidification cracking susceptibility of austenitic stainless steel welds," *Int. Mater. Rev.*, vol. 36, no. 1, pp. 16–44, 1991.
- [21] H. Fredriksson, "The solidification sequence in an 18-8 stainless steel, investigated by directional solidification," *Metall. Trans.*, vol. 3, no. 11, pp. 2989–2997, 1972.
- [22] Y. S. Y. J. W. Fu, "Formation of a two-phase microstructure in Fe-Cr-Ni alloy during directional solidification," *J. Cryst. Growth*, vol. 311, no. 1, pp. 132–136, 2008.
- [23] S. A. David, G. M. Goodwin, and D. N. Braski, "Solidification behavior of austenitic stainless steel filler metals," vol. 58, no. 11, p. 330s–336s, 1979.
- [24] J. C. Lippold and W. F. Savage, "Solidification of austenitic stainless steel weldments: Part 2—The effect of alloy composition on ferrite morphology," *Weld. J.*, vol. 59, no. 2, p. 48s–58s, 1980.
- [25] Y. ARATA, F. MATSUDA, and S. KATAYAMA, "Solidification crack susceptibility in weld metals of fully austenitic stainless steels (Report II): Effect of ferrite, P, S, C, Si and Mn on ductility properties of solidification brittleness," *Trans. JWRI*, vol. 6, no. 1, pp. 105–116, 1977.
- [26] Ö. Hammer and U. Svensson, "Influence of steel composition on segregation and microstructure during solidification of stainless steels," *Solidification and Casting of Metals*, 1977.
- [27] V. Shankar, T. P. S. Gill, S. L. Mannan, and S. Sundaresan, "Solidification cracking in austenitic stainless steel welds," *Sadhana*, vol. 28, no. 3–4, pp. 359–382, Jun. 2003.
- [28] J. A. Brooks, J. C. Williams, and A. W. Thompson, "Microstructural origin of the skeletal ferrite morphology of austenitic stainless steel welds," *Metall. Trans. A*, vol. 14, no. 7, pp. 1271–1281, 1983.
- [29] N. Suutala, T. Takalo, and T. Moio, "Ferritic-austenitic solidification mode in austenitic stainless steel welds," *Metall. Trans. A*, vol. 11, no. 5, pp. 717–725, 1980.
- [30] T. Takalo, N. Suutala, and T. Moio, "Influence of ferrite content on its morphology in some austenitic weld metals," *Metall. Trans. A*, vol. 7, no. 10, pp. 1591–1592, 1976.
- [31] W. W. Mullins and R. F. Sekerka, "Stability of a planar interface during solidification of a dilute binary alloy," *J. Appl. Phys.*, vol. 35, no. 2, pp. 444–451, 1964.
- [32] S. A. David, "Ferrite morphology and variations in ferrite content in austenitic stainless steel welds," Oak Ridge National Lab., TN, 1981.
- [33] O. J. Pereira and J. Beech, "Factors Influencing the Delta-Ferrite Content of Cast Austenitic Stainless Steels," *Solidif. Technol. Foundry Cast House*, pp. 315–321, 1980.

- [34] P. R. Scheller, R. Flesch, and W. Bleck, "Solidification Morphology and Microstructure Properties at Increased Cooling Rates for 18-8 Cr-Ni Stainless Steel," *Adv. Eng. Mater.*, vol. 1, no. 3-4, pp. 209-214, 1999.
- [35] T. Z. Kattamis and M. C. Flemings, "Dendrite Morphology Microsegregation and homogenization of low-alloy steel," *Trans. Metall. Soc. AIME*, vol. 233, no. 5, p. 992, 1965.
- [36] M. Kajihara, C.-B. Lim, and M. Kikuchi, "Experimental study on dissolution of  $\alpha$  phase in  $\gamma/\alpha/\gamma$  diffusion couples of the Fe-Cr-Ni system," *ISIJ Int.*, vol. 33, no. 4, pp. 498-507, 1993.
- [37] S. H. Kim, H. K. Moon, T. Kang, and C. S. Lee, "Dissolution kinetics of delta ferrite in AISI 304 stainless steel produced by strip casting process," *Mater. Sci. Eng. A*, vol. 356, no. 1-2, pp. 390-398, 2003.
- [38] V. S. Raghunathan, V. Seetharaman, S. Venkadesan, and P. Rodriguez, "The influence of post weld heat treatments on the structure, composition and the amount of ferrite in type 316 stainless steel welds," *Metall. Trans. A*, vol. 10, no. 11, pp. 1683-1689, 1979.
- [39] M. McLean, "Microstructural instabilities in metallurgical systems—a review," *Met. Sci.*, vol. 12, no. 3, pp. 113-122, 1978.
- [40] D. E. Coates, "Diffusion controlled precipitate growth in ternary systems: II," *Metall. Trans.*, vol. 4, no. 4, pp. 1077-1086, 1973.
- [41] J. S. Kirkaldy, "Diffusion in Multicomponent Metallic Systems: II. Solutions for Two-Phase Systems with Applications to Transformations in Steel," *Can. J. Phys.*, vol. 36, no. 7, pp. 907-916, 1958.
- [42] L. S. Darken, "Diffusion of carbon in austenite with a discontinuity in composition," *Trans AIME*, vol. 180, pp. 430-438, 1948.
- [43] L. Onsager, "Reciprocal Relations in Irreversible Processes. I.," *Phys. Rev.*, vol. 37, no. 4, pp. 405-426, 1931.
- [44] L. Onsager and R. M. Fuoss, "Irreversible Processes in Electrolytes. Diffusion, Conductance and Viscous Flow in Arbitrary Mixtures of Strong Electrolytes," *J. Phys. Chem.*, vol. 36, no. 11, pp. 2689-2778, 1931.
- [45] A. Schneider and G. Inden, "Computer simulation of diffusion controlled phase transformations," *Contin. Scale Simul. Eng. Mater. Fundam.-Microstruct.-Process Appl.*, pp. 1-36, 2004.
- [46] A. Borgenstam, L. Höglund, J. Ågren, and A. Engström, "DICTRA, a tool for simulation of diffusional transformations in alloys," *J. Phase Equilibria*, vol. 21, no. 3, pp. 269-280, 2000.
- [47] H. Lukas and B. Sundman, "Computational thermodynamics: the Calphad method," *Cambridge University Press*, 2007.
- [48] N. Saunders and A. P. Miodownik, *CALPHAD (Calculation of Phase Diagrams): A Comprehensive Guide*. Elsevier, 1998.
- [49] M. Kajihara and M. Kikuchi, "Analysis of dissolution of  $\alpha$  phase in  $\gamma/\alpha/\gamma$  diffusion couples of the Fe-Cr-Ni system using analytical solutions for semi-infinite diffusion couples," *Acta Metall. Mater.*, vol. 43, no. 2, pp. 807-820, 1995.

- [50] R. W. Heckel, A. J. Hickl, R. J. Zaehring, and R. A. Tanzilli, "Transient growth of second phases during solution treatment," *Metall. Trans.*, vol. 3, no. 10, pp. 2565–2569, 1972.
- [51] R. A. Tanzilli and R. W. Heckel, "Numerical solutions to finite diffusion-controlled 2-phase moving-interface problem," *Trans. Metall. Soc. AIME*, vol. 242, pp. 2313–2321, 1968.
- [52] E. Randich and J. I. Goldstein, "Non-isothermal finite diffusion-controlled growth in ternary systems," *Metall. Trans. A*, vol. 6, no. 8, pp. 1553–1560, 1975.
- [53] W. D. Murray and F. Landis, "Numerical and machine solutions of transient heat-conduction problems involving melting or freezing," *J. Heat Transf.*, vol. 81, pp. 106–112, 1959.
- [54] M. Hasebe and T. Nishizawa, "Analysis and Synthesis of Phase Diagrams of the Fe-Cr-Ni, Fe-Cu-Mn and Fe-Cu-Ni Systems," in *Applications of Phase Diagrams in Metallurgy and ceramics*, 1978, vol. 2, pp. 911–939.
- [55] J. G. Duh and M. A. Dayananda, "Interdiffusion in Fe-Ni-Cr Alloys at 1100°C," *Defect Diffus. Forum*, vol. 39, pp. 1–50, 1985.
- [56] M. Kajihara and M. Kikuchi, "Numerical analysis of dissolution of  $\alpha$  phase in  $\gamma/\alpha/\gamma$  diffusion couples of the Fe-Cr-Ni system," *Acta Metall. Mater.*, vol. 41, no. 7, pp. 2045–2059, 1993.
- [57] J. Andersson, L. Höglund, B. Jönsson, and J. Ågren, "Computer simulation of multicomponent diffusional transformations in steel," in *International symposium on fundamentals and applications of ternary diffusion*, New York, 1990.
- [58] J.-O. Andersson, T. Helander, L. Höglund, P. Shi, and B. Sundman, "Thermo-Calc & DICTRA, computational tools for materials science," *Calphad*, vol. 26, no. 2, pp. 273–312, 2002.
- [59] M. Hillert and C. Qiu, "A thermodynamic assessment of the Fe-Cr-Ni-C system," *Metall. Trans. A*, vol. 22, no. 10, pp. 2187–2198, 1991.
- [60] J. Fridberg, L.-E. Torndahl, and M. Hillert, "Diffusion in iron," *Jernkontorets Ann*, vol. 153, no. 6, pp. 263–276, 1969.
- [61] J. M. Vitek, S. A. Vitek, and S. A. David, "Numerical modeling of diffusion-controlled phase transformations in ternary systems and application to the ferrite/austenite transformation in the Fe-Cr-Ni system," *Metall. Mater. Trans. A*, vol. 26, no. 8, pp. 2007–2025, 1995.
- [62] Z. Liu and G. Wang, "Numerical modeling of  $\delta$ -ferrite dissolution kinetics in austenitic stainless steels," *Steel Res. Int.*, vol. 77, no. 7, pp. 507–511, 2006.
- [63] J. M. Vitek and S. A. Vitek, "Modeling Phase Transformations in Ternary Systems: Ferrite Dissolution During Continuous Cooling," in *Thermal/Mechanical Processing of Steel Symposium*, Vancouver, 1995.
- [64] S. Crusius, G. Inden, U. Knoop, L. Höglund, and J. Ågren, "On the numerical treatment of moving boundary problems," *Z. Für Met.*, vol. 83, no. 9, pp. 673–678, 1992.
- [65] B.-J. Lee, "Numerical simulation of diffusional reactions between multiphase alloys with different matrix phases," *Scr. Mater.*, vol. 40, no. 5, pp. 573–579, 1999.

- [66] B.-J. Lee, “Numerical procedure for simulation of multicomponent and multi-layered phase diffusion,” *Met. Mater.*, vol. 5, no. 1, pp. 1–15, 1999.
- [67] B.-J. Lee and K. H. Oh, “Numerical treatment of the moving interface in diffusional reactions,” *Z Met.*, vol. 87, no. 3, pp. 195–204, 1996.
- [68] *ASM Handbook Volume 9: Metallography and Microstructures - ASM International*, 9th edition. 1985.
- [69] “Thermo-Calc software TCFE6 Steels/Fe-alloys database version 6 (www.thermocalc.com).”
- [70] “www.arcelormittal.com.”
- [71] M. Bobadilla, “Mode de solidification des aciers inoxydables du type AK21 et AS70: influence qualitative de la vitesse de refroidissement sur le déplacement des équilibres l/s et s/s,” IRSID report, PC95NT57, 1995.
- [72] “MOB2, Mobility database.” Foundation of Computational Thermodynamics. Stockholm/Sweden: Royal Institute of Technology (www.thermocalc.com).
- [73] W. F. Gale and T. C. Totemeier, *Smithells Metals Reference Book*. Butterworth-Heinemann, 2003.
- [74] L. Thuinet and H. Combeau, “A new model of microsegregation for macrosegregation computation in multicomponent steels. Part I: theoretical formulation and algorithm,” *Comput. Mater. Sci.*, vol. 45, no. 2, pp. 294–304, 2009.
- [75] L. Thuinet, “Solidification des aciers ternaires : modélisation de la microségrégation en croissance dendritique colonnaire, prise en compte de la réaction péritectique,” INPL, 2005.
- [76] A. E. P. Veldman and K. Rinzema, “Playing with nonuniform grids,” *J. Eng. Math.*, vol. 26, no. 1, pp. 119–130, Feb. 1992.
- [77] J. Crank, *The Mathematics of Diffusion*. Clarendon Press, 1979.
- [78] P. J. Roache, *Computational fluid dynamics*. Hermosa Publishers, 1972.
- [79] M. Rappaz, M. Bellet, and M. Deville, *Modélisation numérique en science et génie des matériaux*. PPUR presses polytechniques, 1998.
- [80] A. N. Brooks and T. J. Hughes, “Streamline upwind/Petrov-Galerkin formulations for convection dominated flows with particular emphasis on the incompressible Navier-Stokes equations,” *Comput. Methods Appl. Mech. Eng.*, vol. 32, no. 1, pp. 199–259, 1982.
- [81] “TCFE Steel and Fe-alloys database,” *www.thermocalc.com*.
- [82] S. Kobayashi, “A Mathematical model for solute redistribution during dendritic solidification,” *Trans. Iron Steel Inst. Jpn.*, vol. 28, no. 7, pp. 535–542, 1988.
- [83] V. Raghavan, “Cr-Fe-Ni (chromium-iron-nickel),” *J. Phase Equilibria*, vol. 24, no. 3, pp. 261–264, May 2003.
- [84] S. Patankar, *Numerical Heat Transfer and Fluid Flow*. CRC Press, 1980.



# Appendix A

## Morphological evolutions of vermicular ferrite during its dissolution

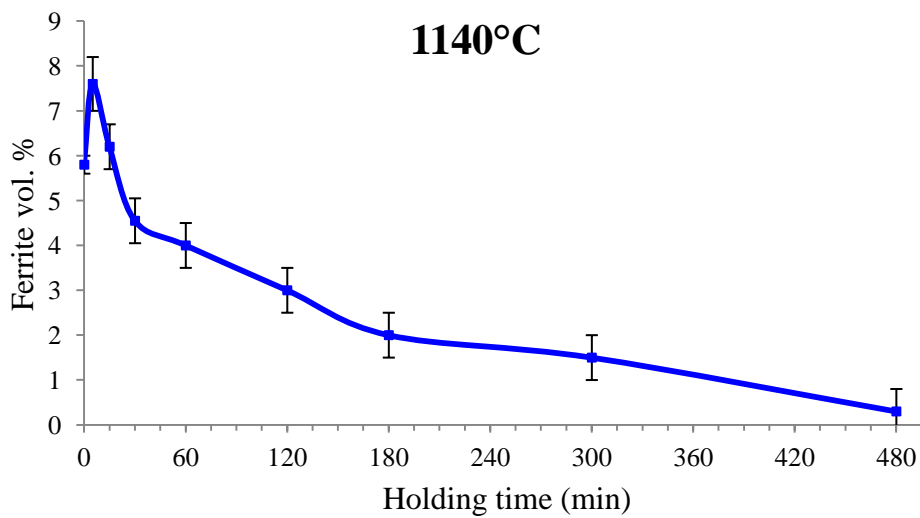
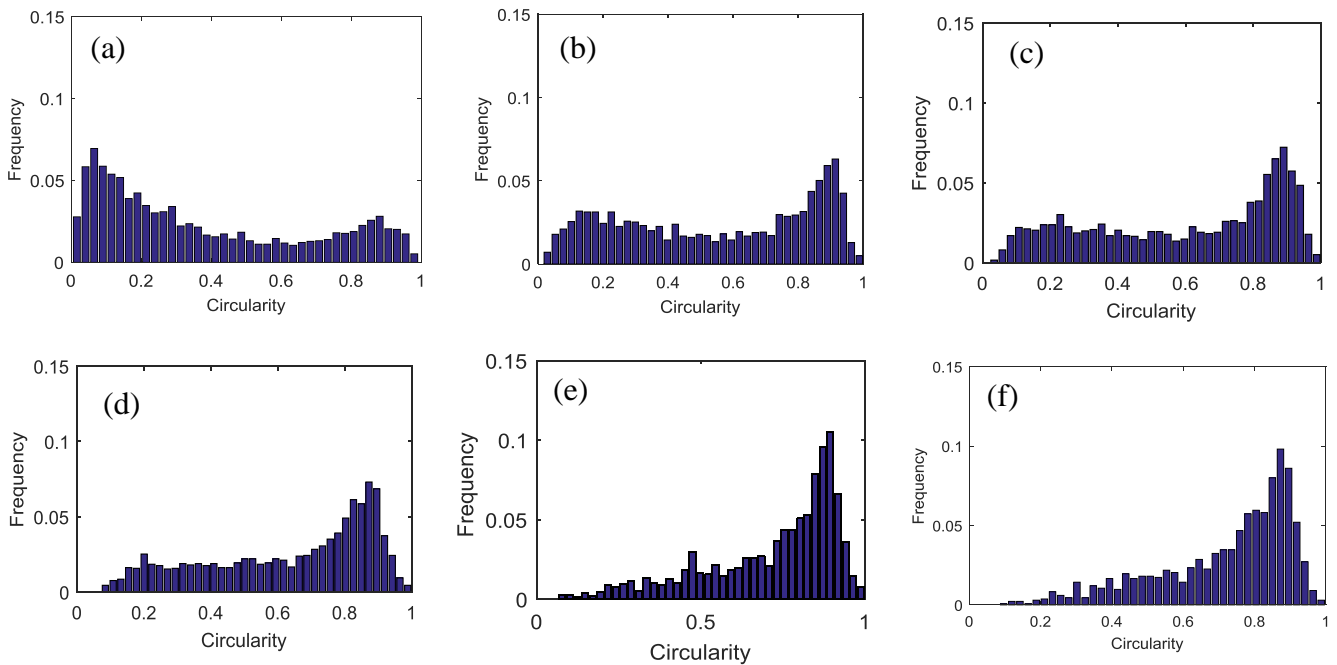


Figure A. 1: Evolution of the fraction of vermicular ferrite with the annealing time at 1140°C.



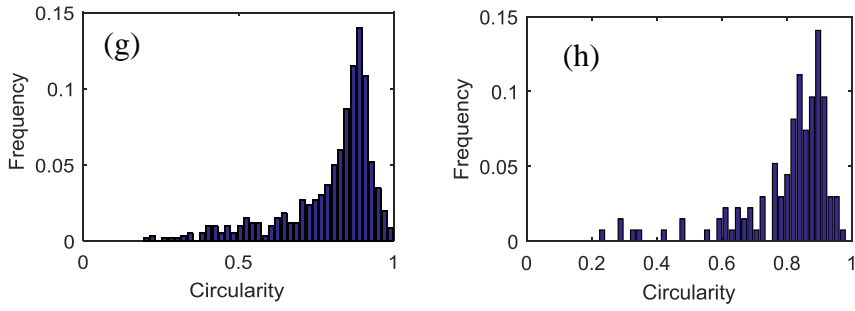


Figure A. 2: Distribution of the circularity of ferrite particles in (a) the as-cast state and during their dissolution at 1140°C after (b) 5min (c) 15min, (d) 30min, (e) 1hr, (f) 2hrs, (g) 5hrs and (h) 8hrs.

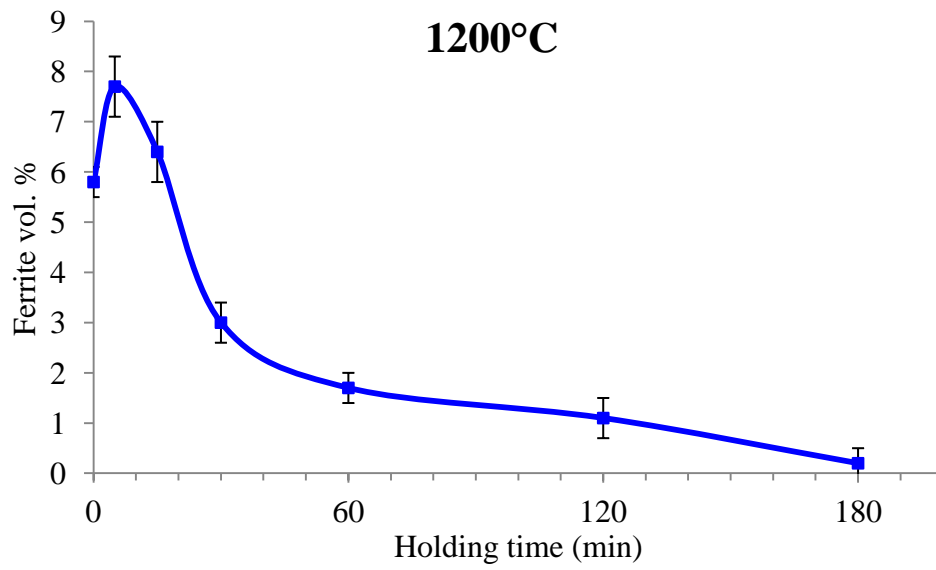


Figure A. 3: Evolution of the fraction of vermicular ferrite with the annealing time at 1200°C.

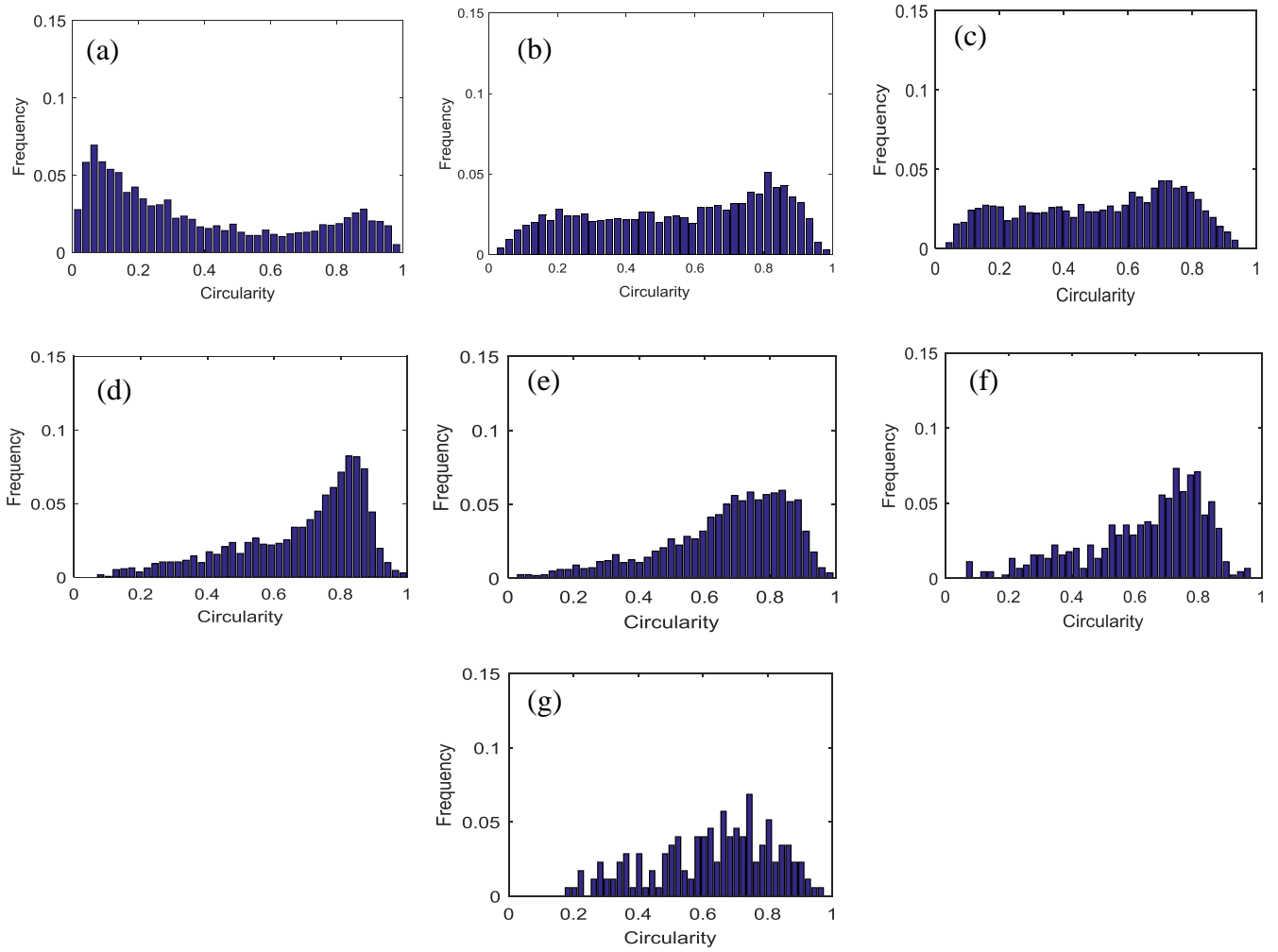


Figure A. 4 : Distribution of the circularity of ferrite particles in (a) the as-cast state and during their dissolution at 1200°C after (b) 5min, (c) 15min, (d) 30min, (e) 1hr, (f) 2hrs and (g) 3hrs.

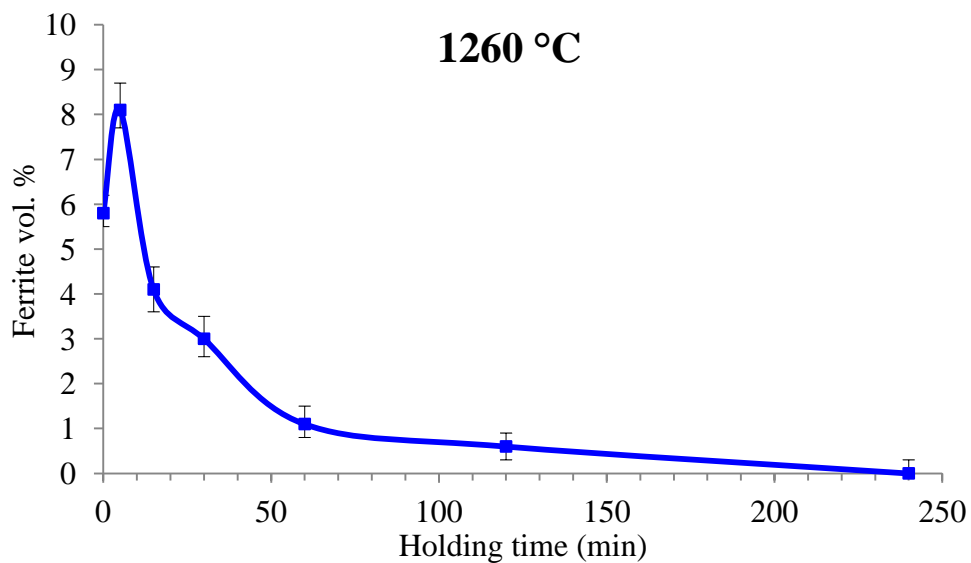


Figure A. 5: Evolution of the fraction of vermicular ferrite with the annealing time at 1260°C.

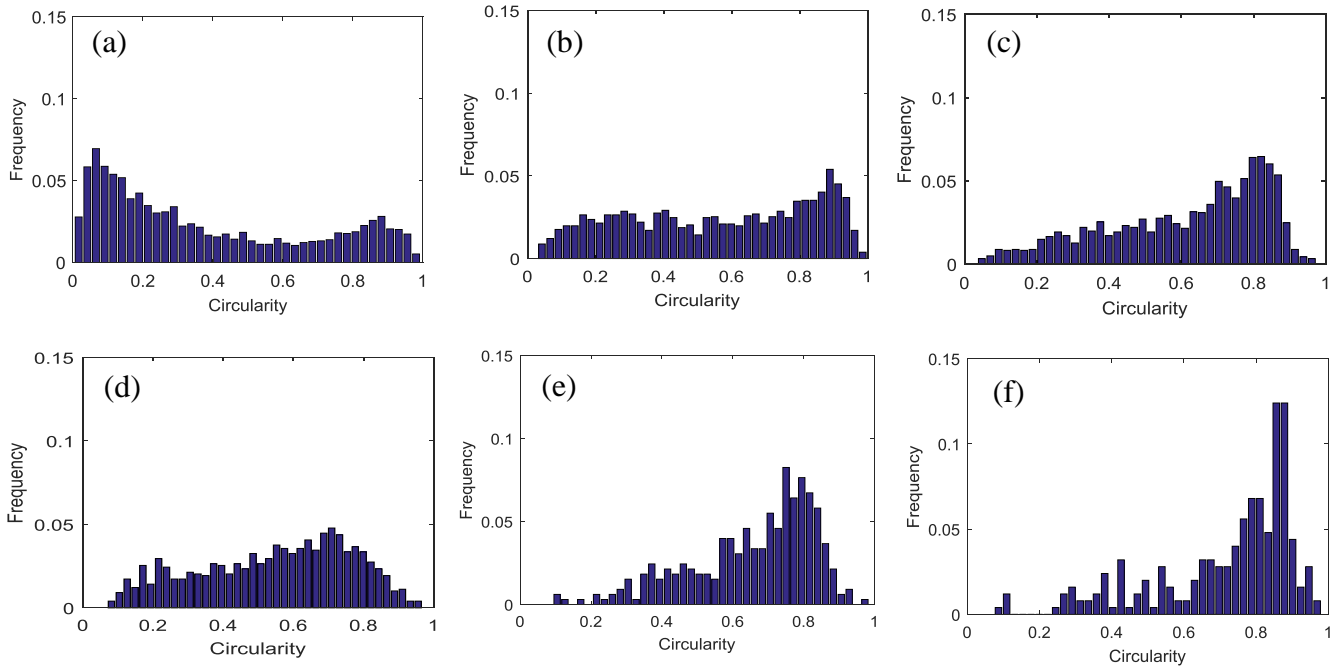


Figure A. 6: Distribution of the circularity of ferrite particles in (a) the as-cast state and during their dissolution at 1260°C after (b) 5min, (c) 15 min, (d) 30 min, (e) 1hr and (f) 2hrs.

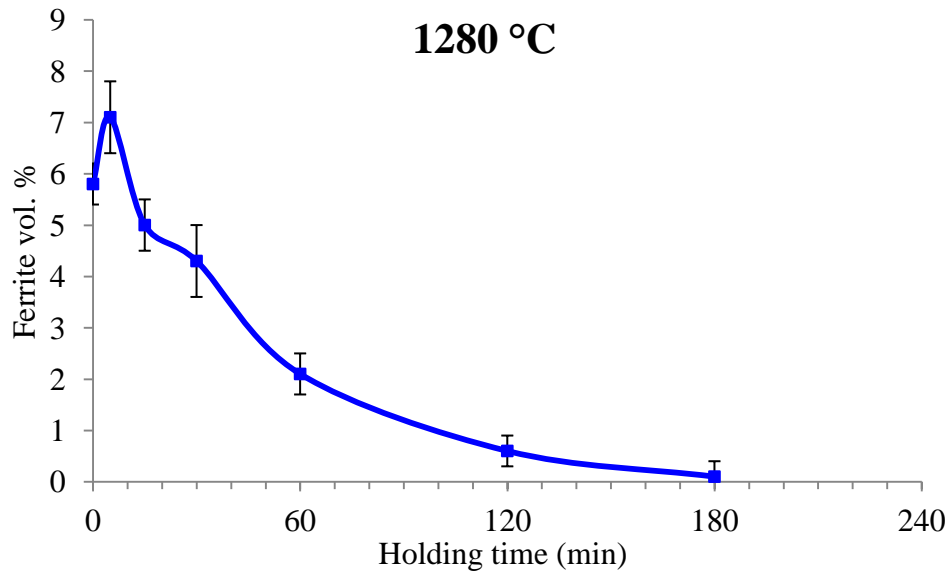


Figure A. 7: Evolution of the fraction of vermicular ferrite with the annealing time at 1280°C.

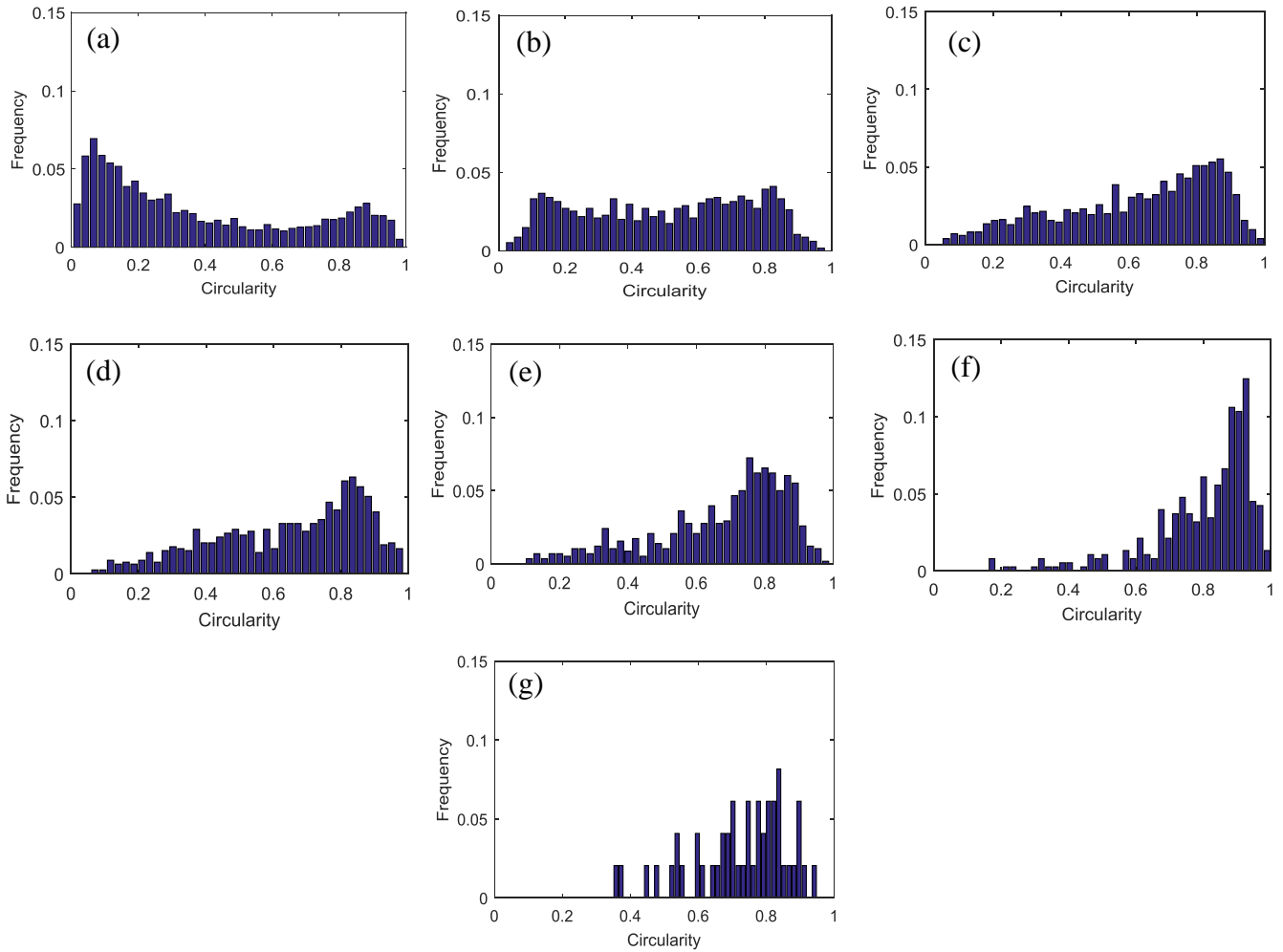


Figure A. 8: Distribution of the circularity of ferrite particles in (a) the as-cast state and during their dissolution at 1280°C after (b) 5min, (c) 15min, (d) 30min, (e) 1h, (f) 2hrs and (g) 3hrs.

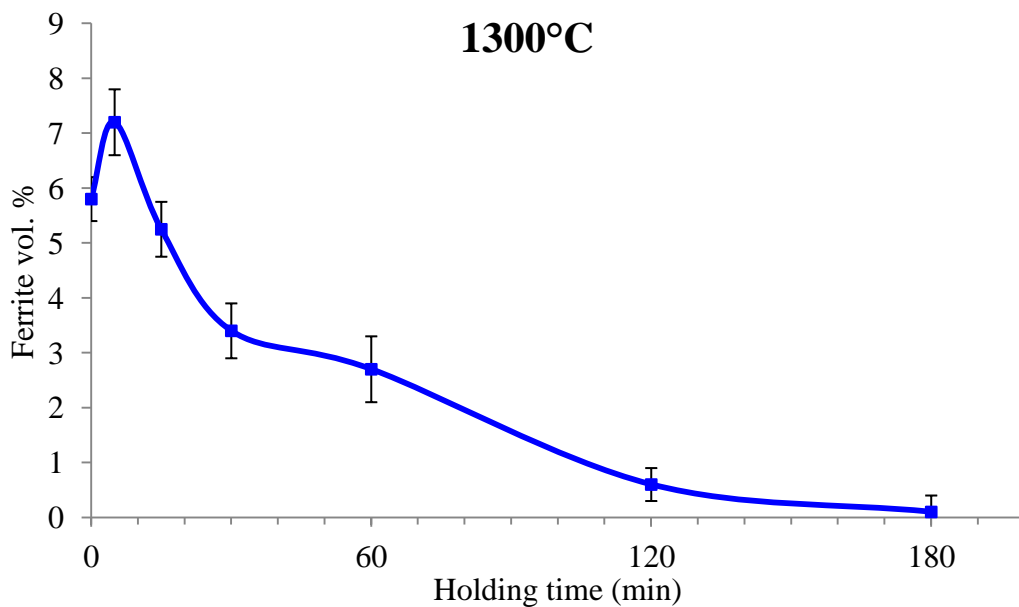


Figure A. 9: Evolution of the fraction of vermicular ferrite with the annealing time at 1300°C.

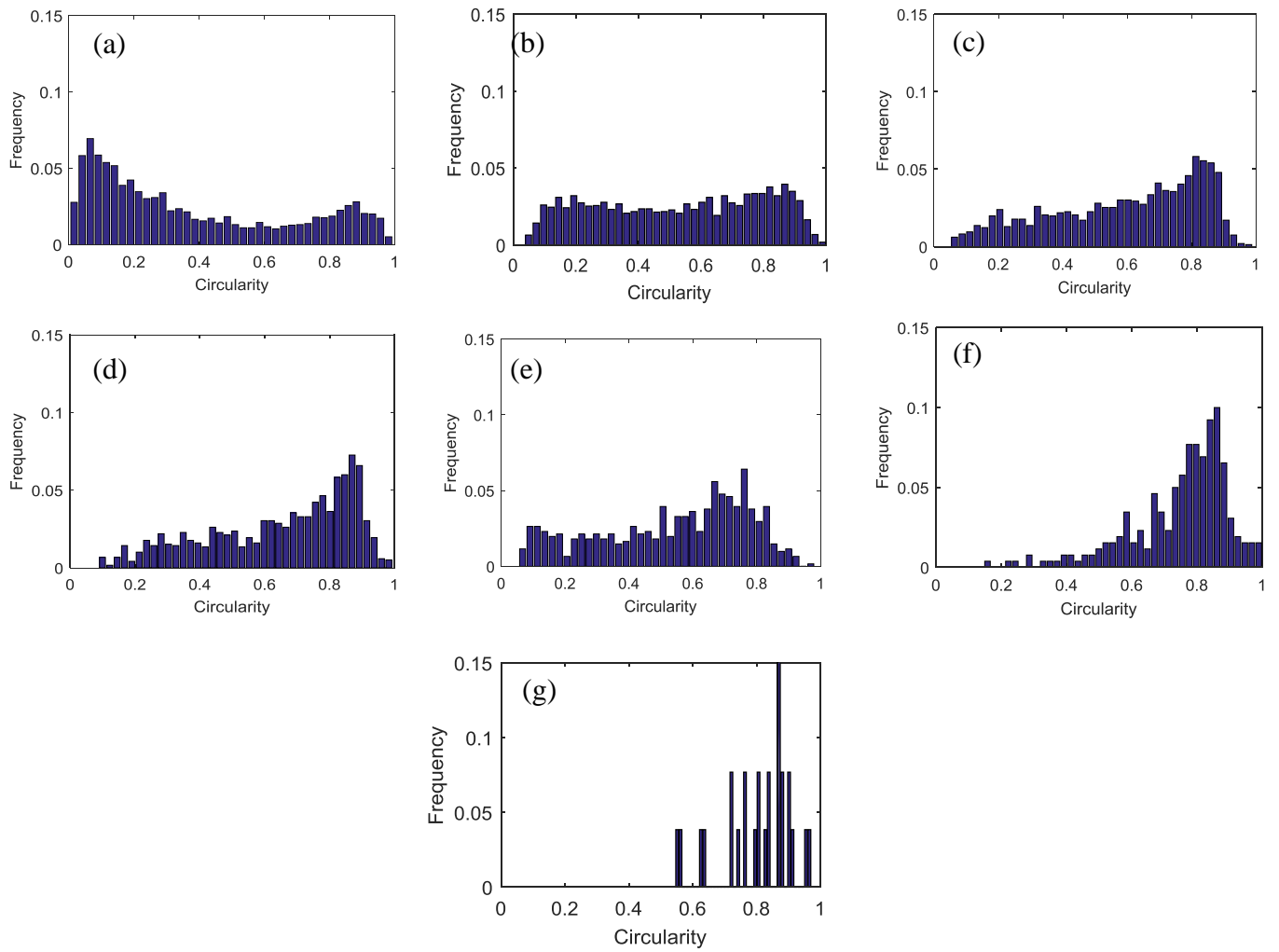


Figure A. 10: Distribution of the circularity of ferrite particles in (a) the as-cast state and during their dissolution at 1300°C after (b) 5min, (c) 15min, (d) 30min, (e) 1h, (f) 2hrs and (g) 3hrs.

## Appendix B

### The multilayered microstructure at different states

In this appendix, the micrographs and composition profiles of the multilayered microstructure at different states (HR1, CR1, HR2 and CR2) and annealing times are presented. Cases already shown in Chapter III will not be presented in this appendix.

#### I. In the first hot rolling state (HR1)

##### I.1. Microstructures

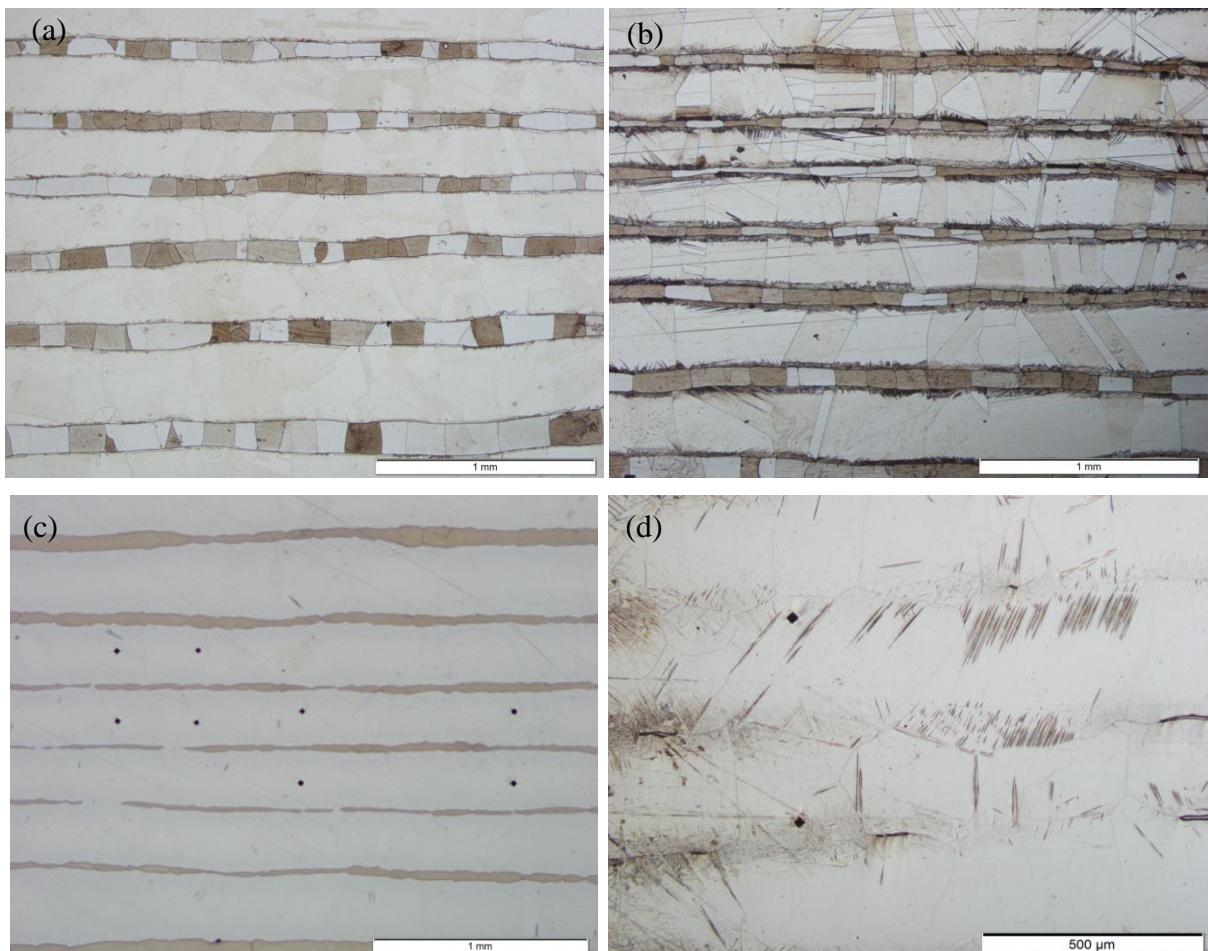


Figure B. 1: Multilayered microstructure in the HR1 state after (a) 4h, (b) 24h, (c) 72h and (d) 164h annealing at 1240°C (Electronitric etching).

## I.2. Composition profiles

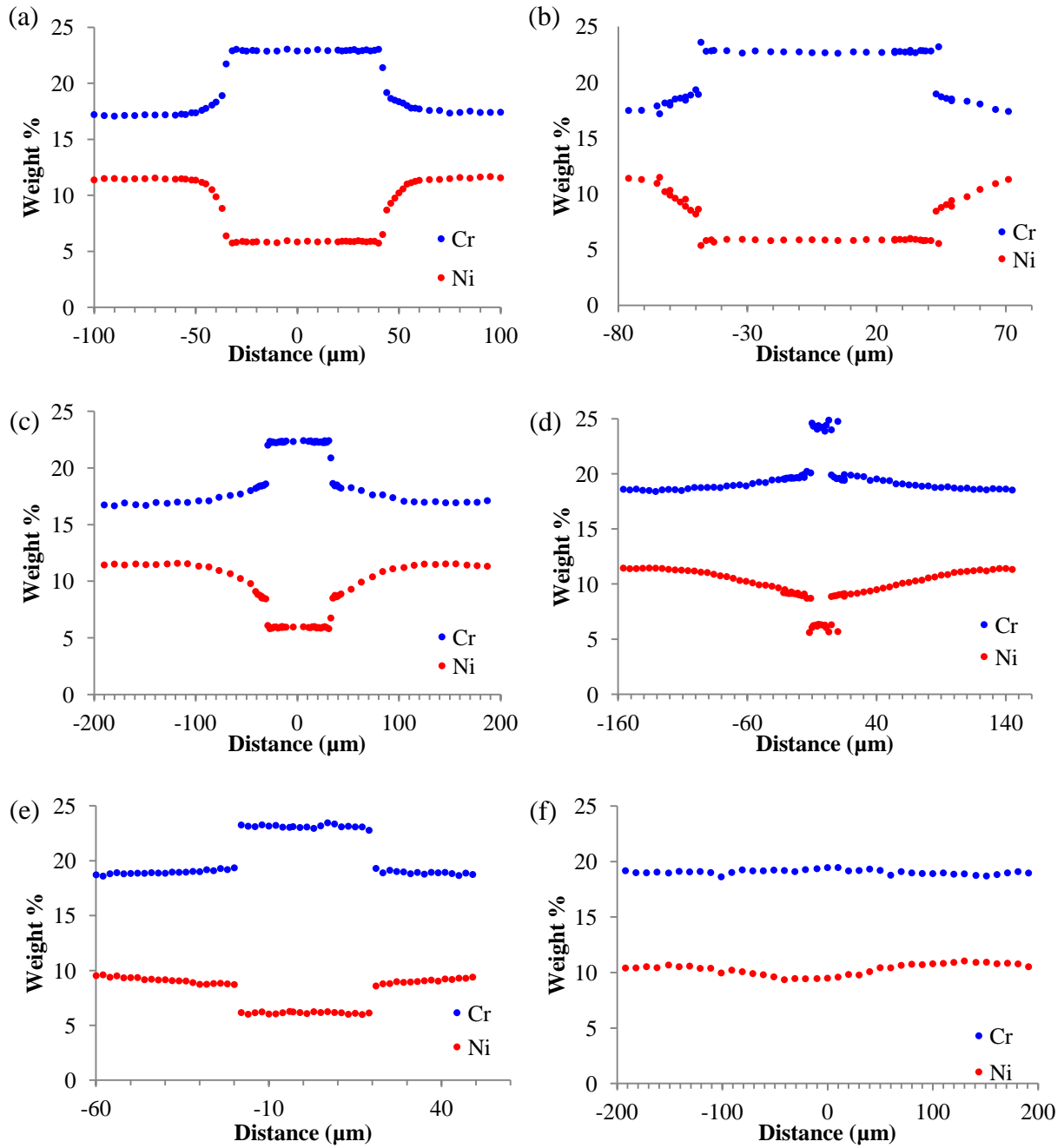


Figure B. 2: Composition profiles in ferrite and austenite bands in the multilayered microstructure in the HR1 state after (a) 1hr, (b) 4hrs, (c) 24hrs (d) 72hrs, (e) 96hrs and (f) 164hrs annealing at 1240°C.

## II. In the first cold rolling state (CR1)

### II.1. Microstructures

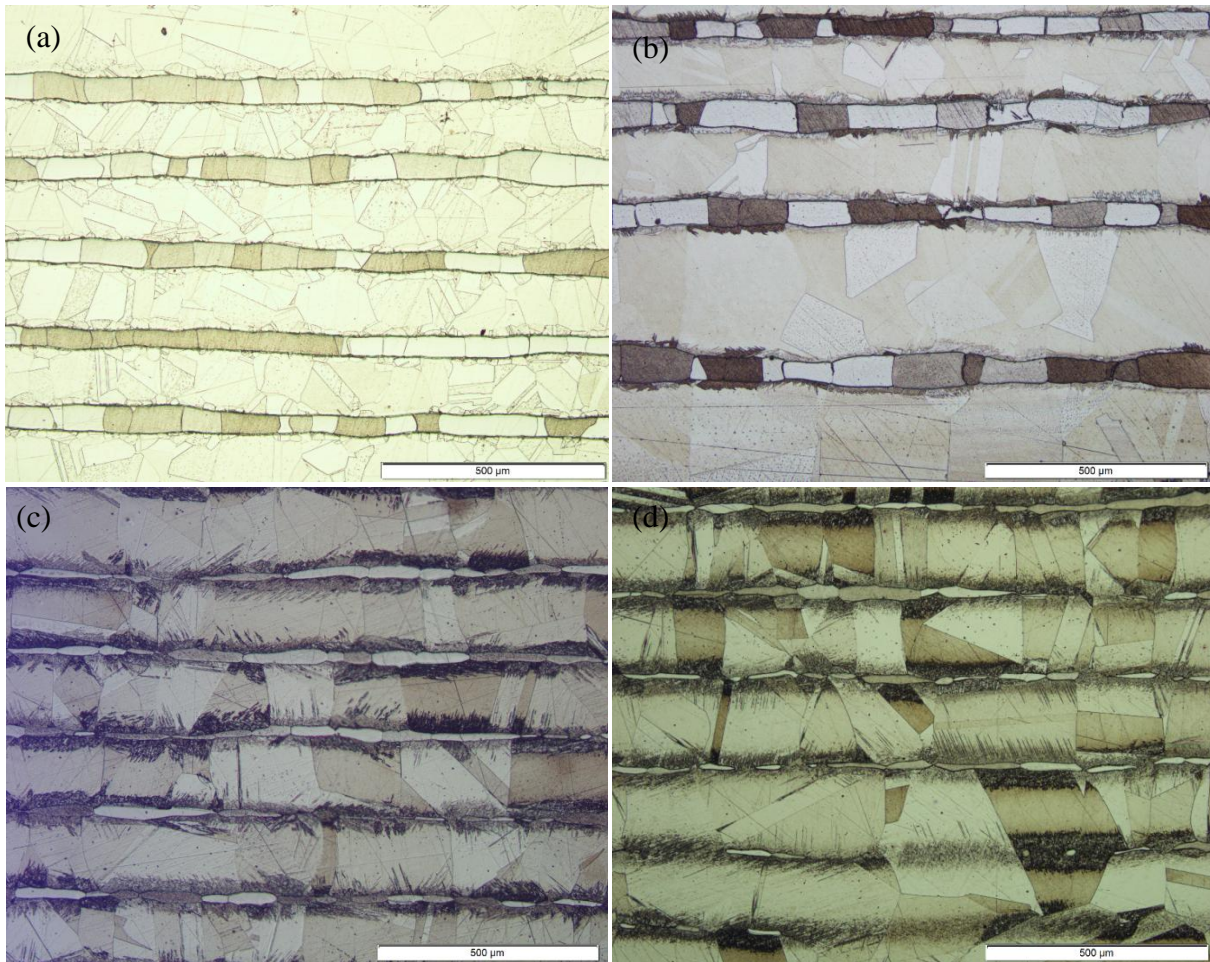
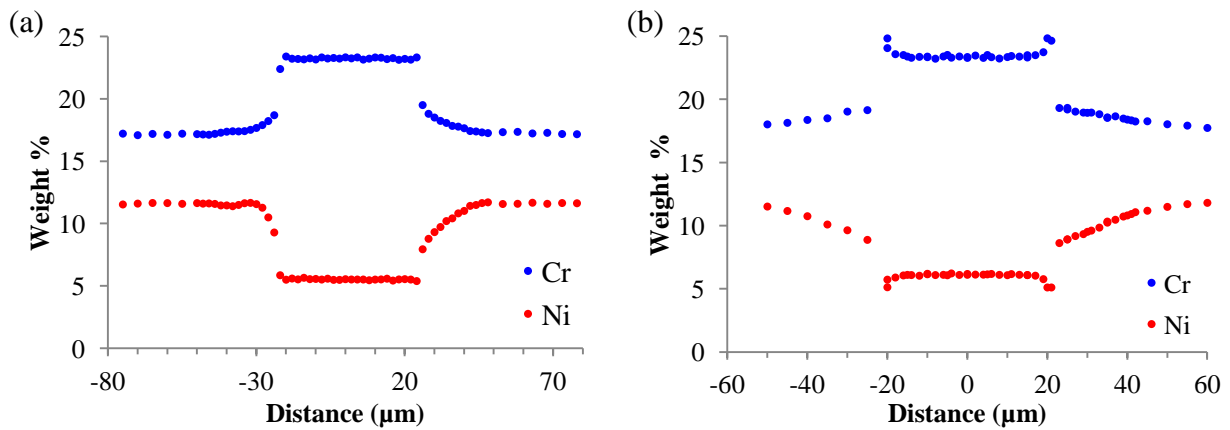


Figure B. 3: Multilayered microstructure in the CR1 state after (a) 30 min, (b) 4hrs, (c) 24hrs and (d) 48hrs annealing at 1240°C (Electronitric etching).

### II.2. Composition profiles



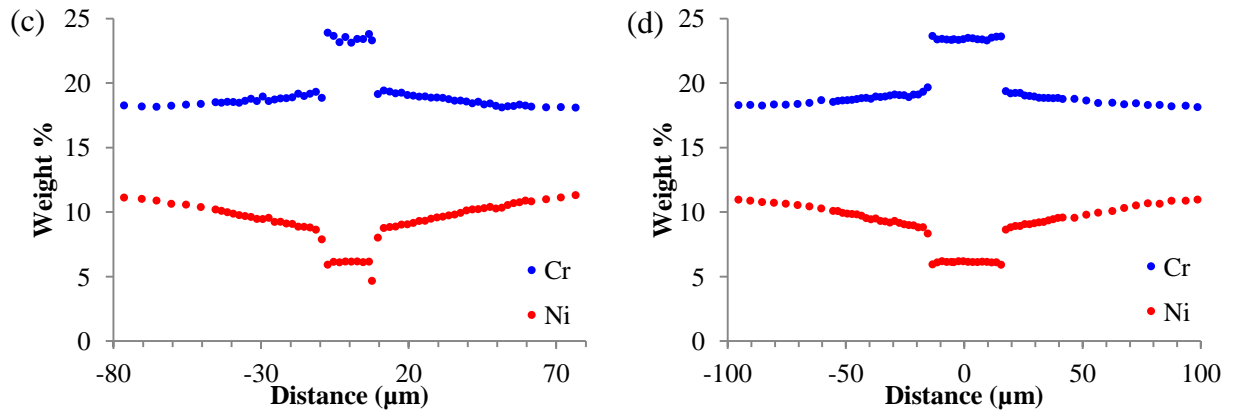
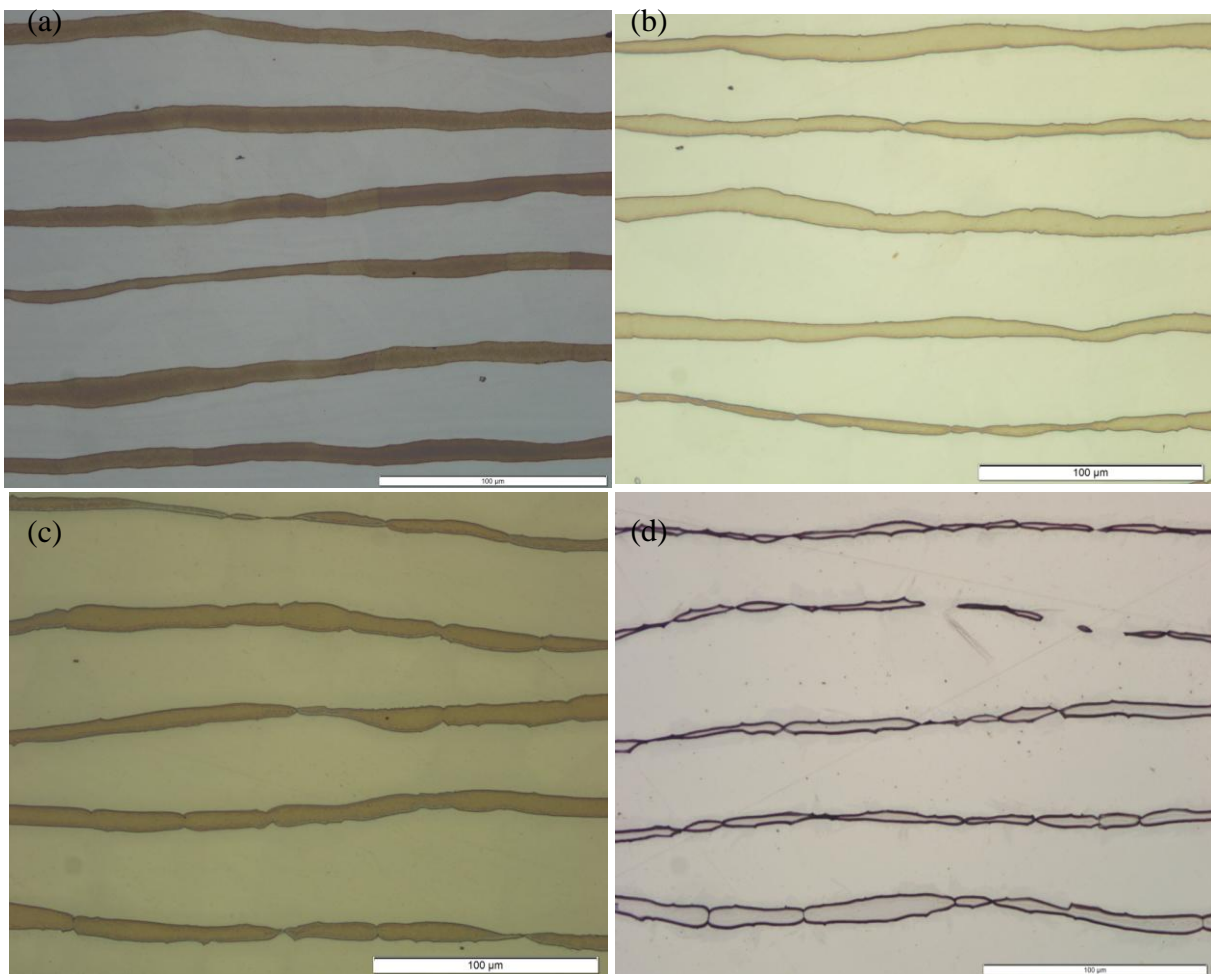


Figure B. 4: Composition profiles in ferrite and austenite bands in the multilayered microstructure in the CR1 state after (a) 30min, (b) 4hrs, (c) 24hrs and (d) 48hrs annealing at 1240°C.

### III. In the second hot rolling state (HR2)

#### III.1. Microstructures



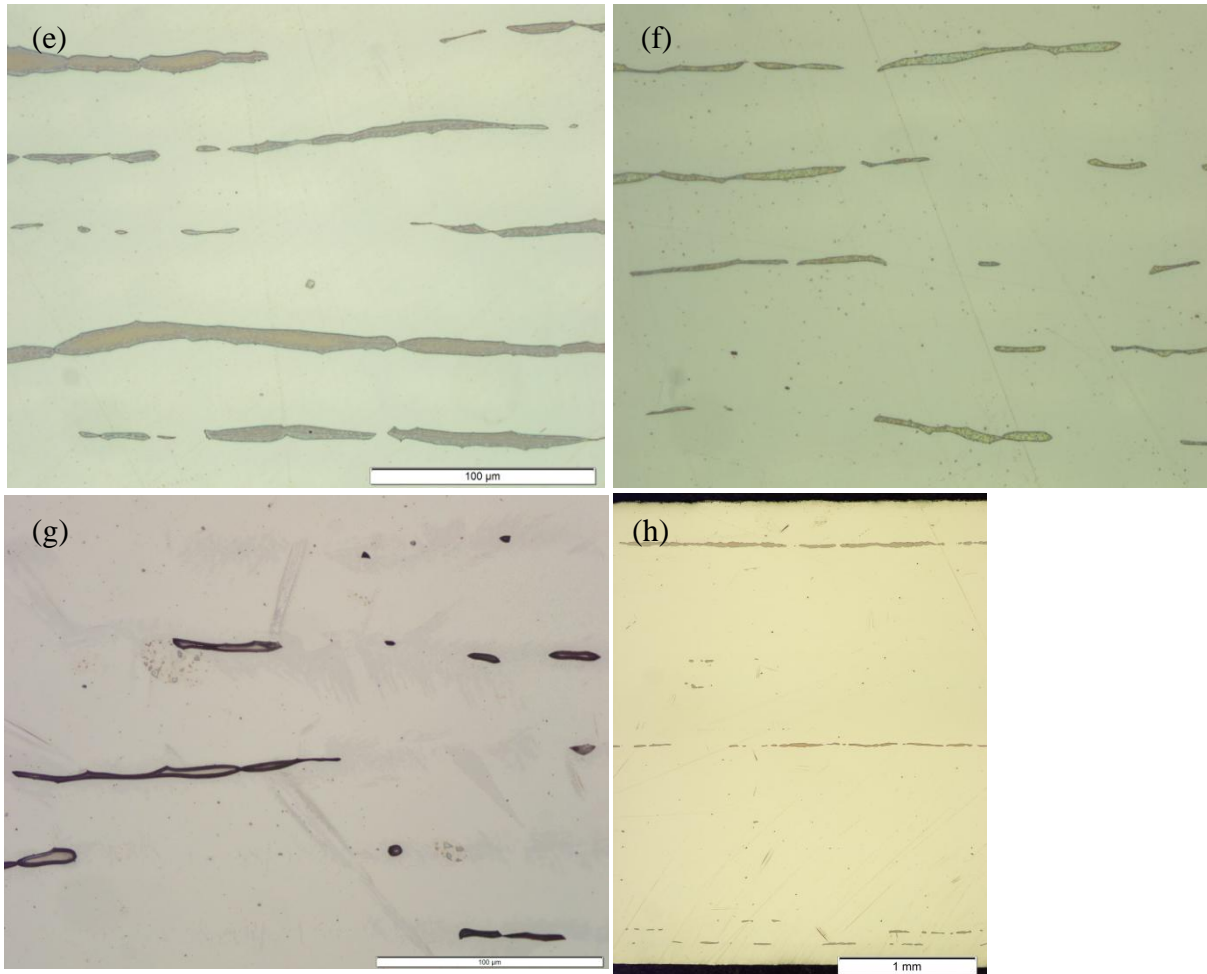
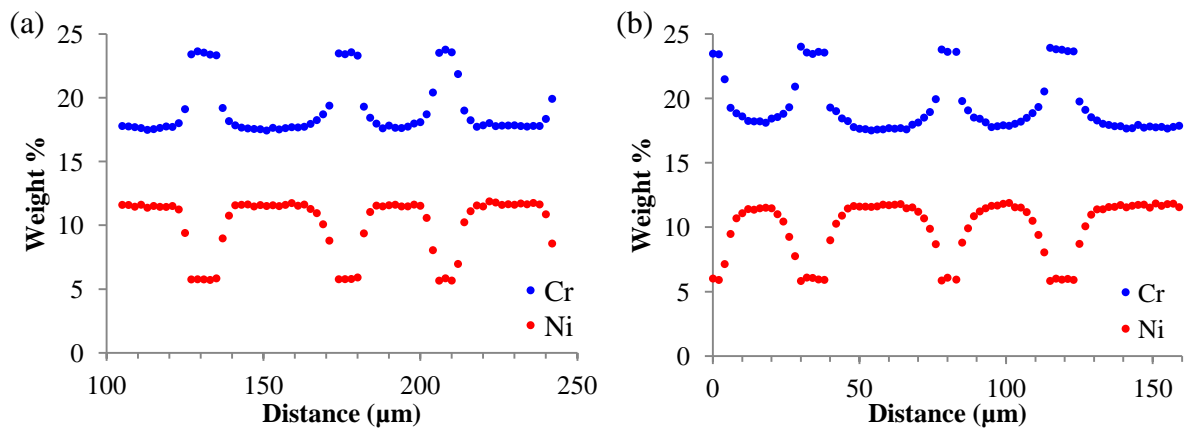


Figure B. 5: Multilayered microstructure in the HR2 state (a) in the as-received state and after (b) 5min, (c) 15min, (d) 30min, (e) 1hr, (f) 2hrs, (g) 3hrs and (h) 24hrs annealing at 1240°C (NaOH etching).

### III.2. Composition profiles



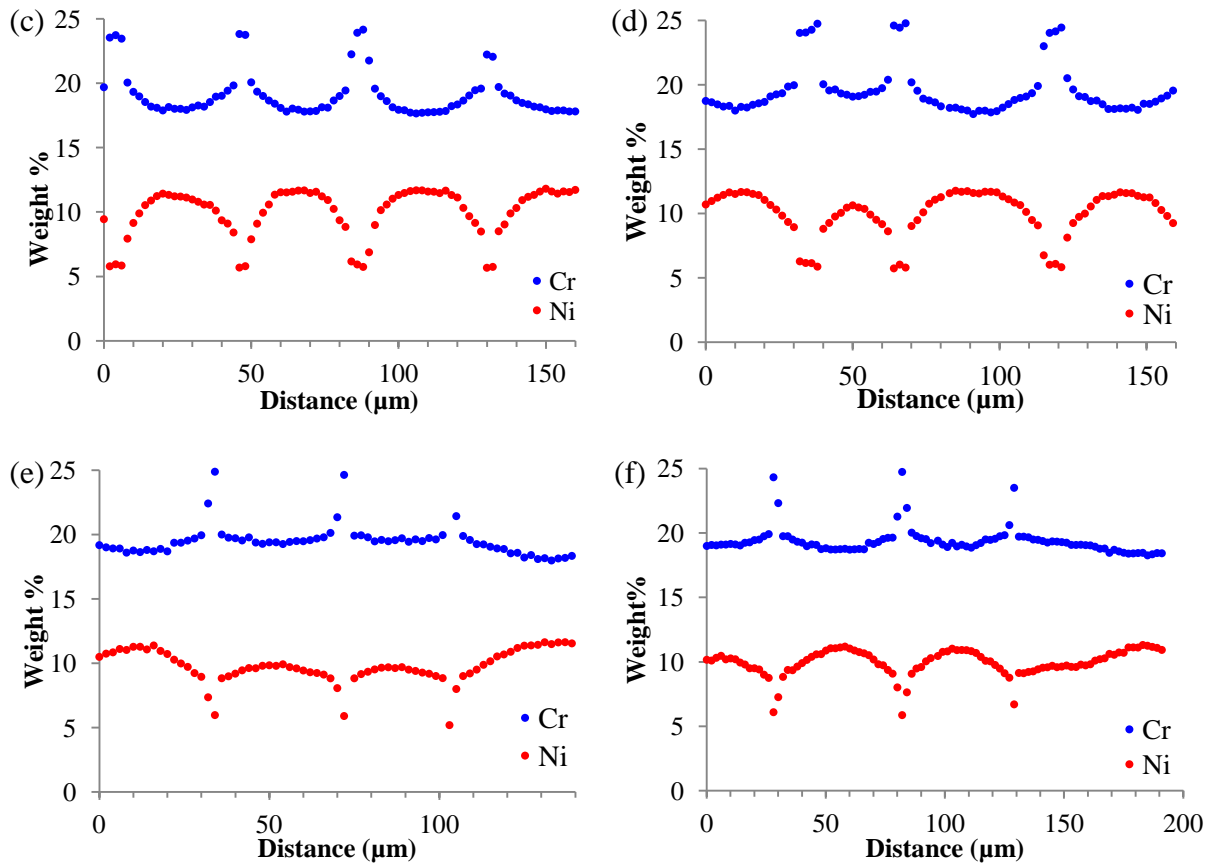
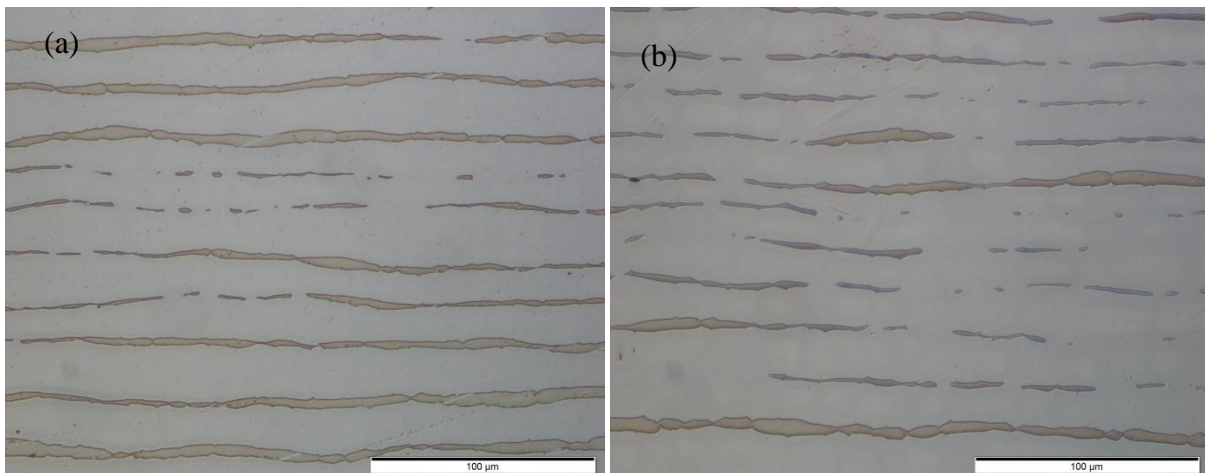
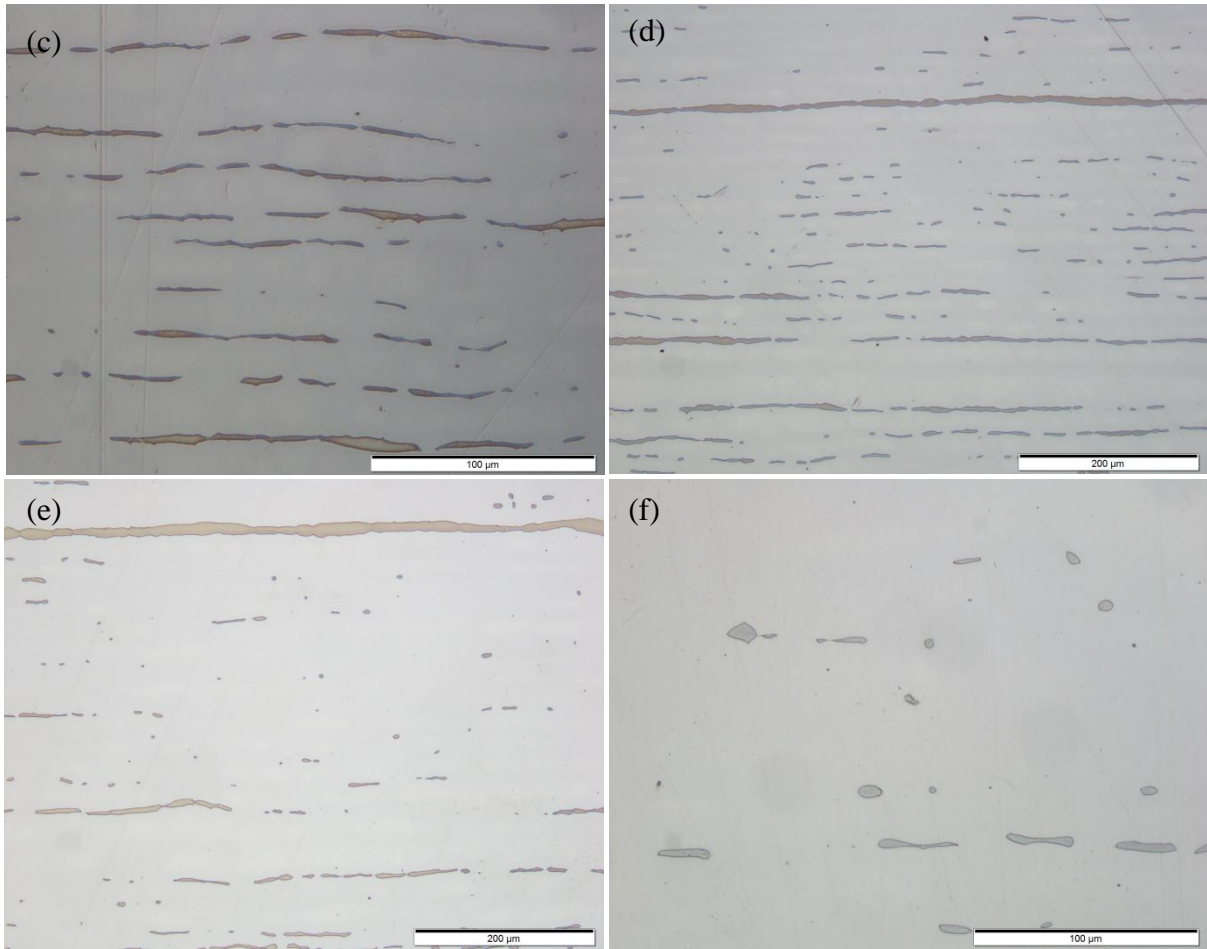


Figure B. 6: Composition profiles in ferrite and austenite bands in the multilayered microstructure in the HR2 state after (a) 5min, (b) 15min, (c) 30min, (d) 1hr, (e) 2hrs and (f) 3hrs annealing at 1240°C.

#### IV. In the second cold rolling state (CR2)

Only microstructures will be presented in this paragraph, composition profiles having not been measured.





**Figure B. 7: Multilayered microstructure in the CR2 state after (a) 5 min, (b) 10 min, (c) 15min, (d) 30min, (e) 60min and (g) 90min annealing at 1240°C (NaOH etching).**



# Appendix C

## Thermodynamic descriptions

This appendix aims at providing the interpolation data used in the parameterizations of the iron rich corner of Fe-Cr-Ni phase diagram. Thermodynamic equilibria are tabulated using:

- the Ptimec-Miettinen module with CEQCSI® software [70].
- the TCFE6 database [69] with Thermo-Calc® software [58].

Several isothermal sections at temperatures ranging from 1000°C to 1360°C were computed. Ferrite and austenite phase boundaries were then parameterized by interpolating the equilibrium data. The interpolation equations with  $X_{Cr}^{\gamma}$  as independent variable is of the form:

$$X_i^{\varphi} = K_1^{\varphi} + K_2^{\varphi} X_{Cr}^{\gamma} + K_3^{\varphi} (X_{Cr}^{\gamma})^2 \quad (C.1)$$

where  $X_i^{\varphi}$  is the interface composition of solute  $i = Cr, Ni$  in phase  $\varphi = \delta, \gamma$  and the coefficients  $K_1$ ,  $K_2$  and  $K_3$  are temperature-dependant and expressed using third order polynomial interpolation :

$$K_i^{\varphi} = a + bT + cT^2 + dT^3 \quad (C.2)$$

### I. The Ptimec-Miettinen module

Table C. 1 shows the interpolation coefficients used to parameterize the equilibrium data extracted from the Ptimec-Miettinen module. The resultant parameterizations of ferrite and austenite phase boundaries are compared to equilibrium data in Figure C. 1.

**Table C. 1: Interpolation constants for coefficients  $K_1$ ,  $K_2$  and  $K_3$  in Eq.(C.2), from 1000°C to 1360°C, Ptimec-Miettinen module.**

		a	b	c	d
$Cr^{\delta}$	K1	-0.0000172977954222858	0.000117506397784084	-1.04932276410074E-07	1.45756412885678E-11
	K2	0.000157165151856439	-0.00170086048801434	2.82058205178445E-06	-7.79604558389756E-10
	K3	-0.000325425049657521	0.0237907351984233	-0.0000262639392608012	7.14919859783711E-09
$Ni^{\delta}$	K1	-4.54249533113208E-06	-0.000635937834869115	7.82685604408326E-07	-2.45640594634707E-10
	K2	0.000044419855732333	0.00873136960128985	-0.0000117229439751675	3.98563004167261E-09
	K3	-0.000102924015680928	-0.0229789615474259	0.0000319898660049435	-1.08154729590233E-08
$Ni^{\gamma}$	K1	-0.0000142655941370114	0.000293857137572946	-4.25578444441643E-07	1.43951957080755E-10
	K2	0.000144164853849895	-0.00282912881700906	2.78402217124855E-06	-5.40325870213822E-10
	K3	-0.000341293422453695	0.0127503913591461	-0.0000111220750583877	2.283949765021E-09

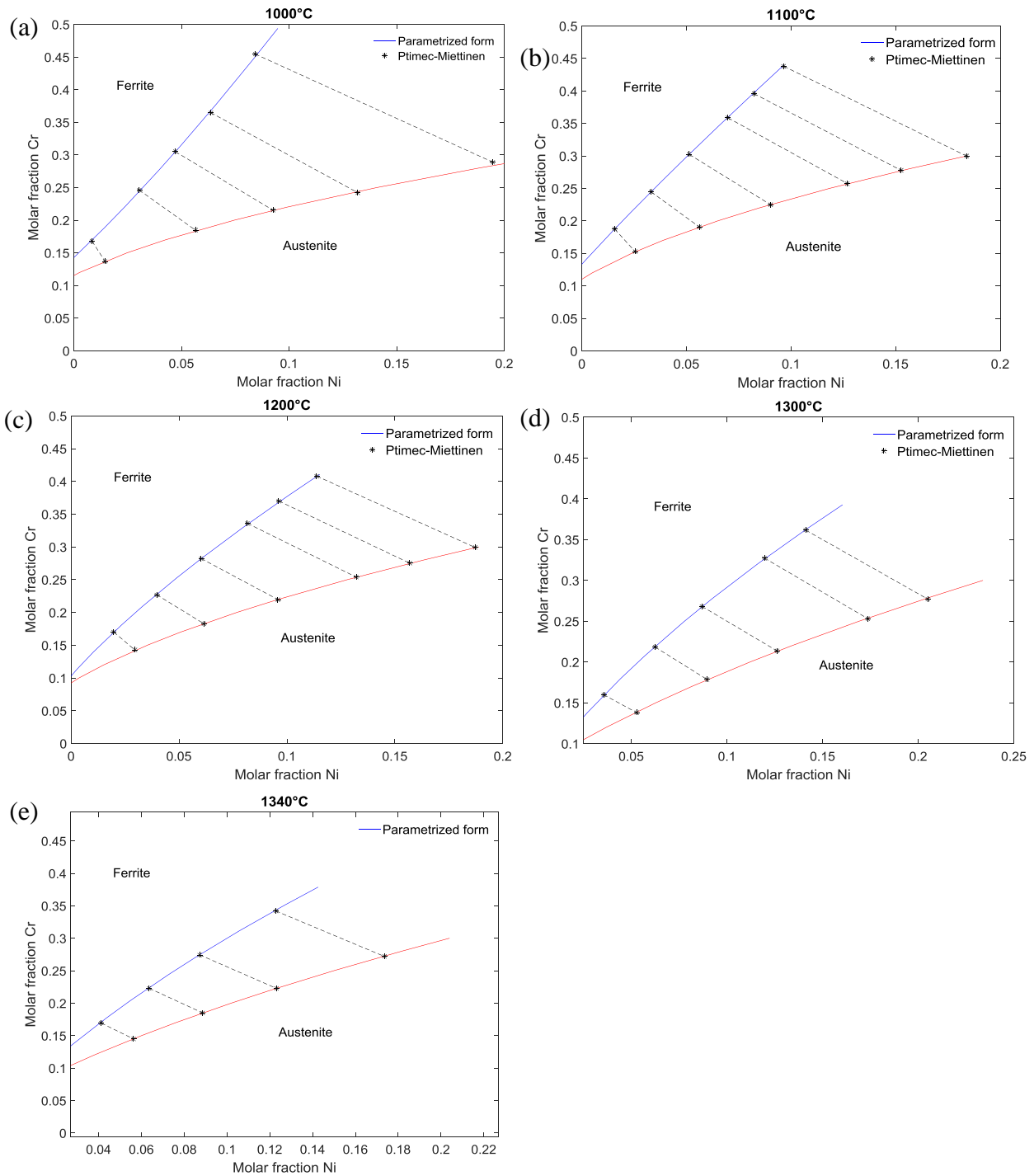


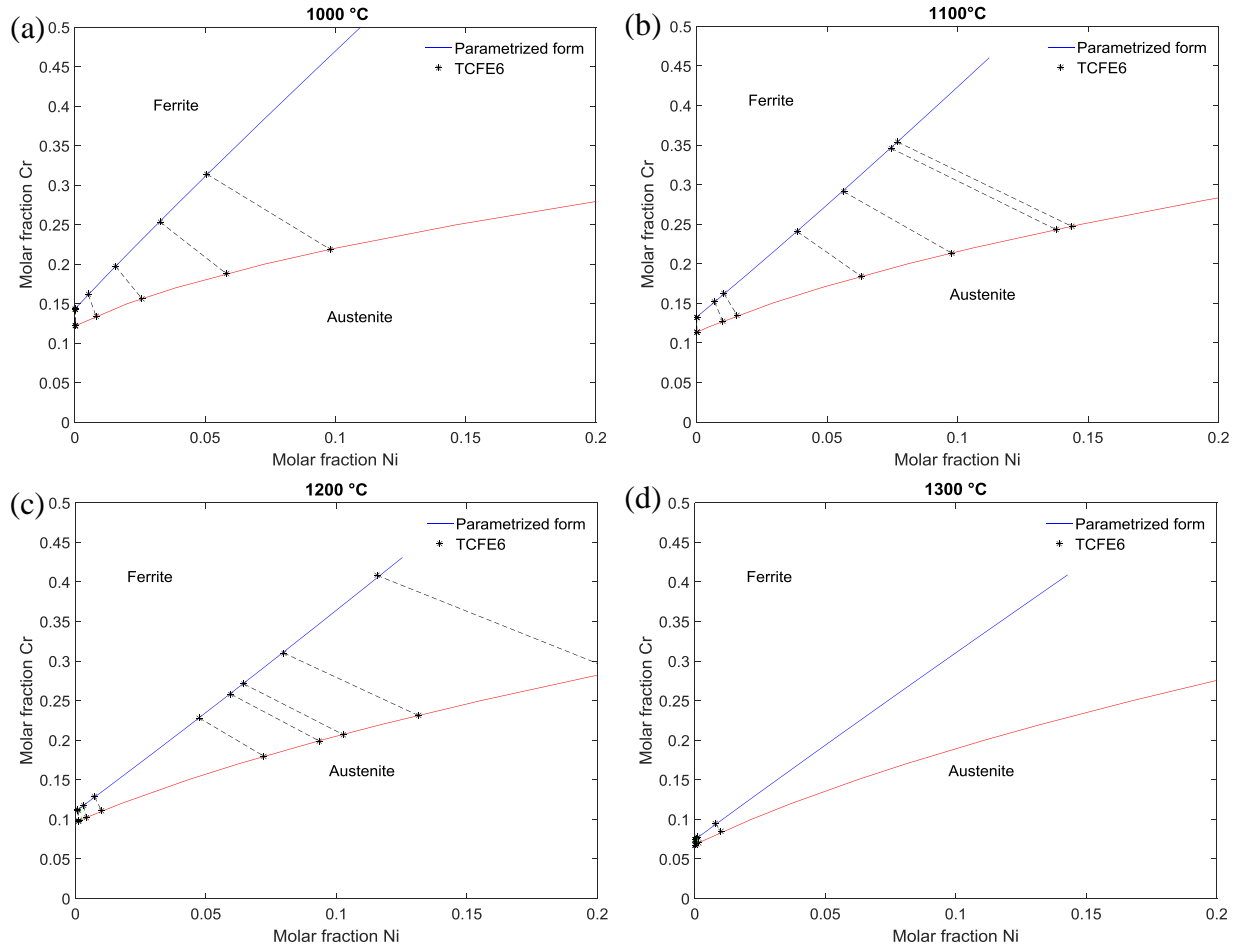
**Figure C. 1:** Isothermal sections of the iron rich corner of the Fe-Cr-Ni phase diagram at (a) 1000°C, (b) 1100°C, (c) 1200°C, (d) 1300°C and (e) 1340°C. The solid lines represent the interpolated phase boundaries and starred points correspond the calculated equilibria using the CEQCSI<sup>®</sup> software and the Ptimec-Miettinen module.

## II. The TCFE6 thermodynamic database

Table C. 2 shows the interpolation coefficients used to parameterize the equilibrium data extracted from the TCFE6 database. The resultant parameterizations of ferrite and austenite phase boundaries are compared to equilibrium data in Figure C. 2.

**Table C. 2: Interpolation constants for coefficients  $K_1$ ,  $K_2$  and  $K_3$  in Eq.(C.2), from 1000°C to 1360°C, TCFE6 database.**

		a	b	c	d
$\text{Cr}^\delta$	K1	1.55915016337109	-0.00285162393958995	1.71392308038994E-06	-3.38866202696522E-10
	K2	-26.1072271936742	0.0483284693799719	-2.84576238919661E-05	5.54937305818498E-09
	K3	107.794955812034	-0.185518731092856	0.000107836772803980	-2.10342696815643E-08
$\text{Ni}^\delta$	K1	5.46697094447846	-0.0105072284757735	6.56355654707180E-06	-1.33903072047522E-09
	K2	-63.6790586599279	0.124062525729097	-7.97772123205529E-05	1.70511065906161E-08
	K3	194.286440052370	-0.381118577952056	0.000249037439091555	-5.40873279053612E-08
$\text{Ni}^\gamma$	K1	4.62125346994694	-0.00811877996172076	4.54081970467211E-06	-8.01943207897747E-10
	K2	-46.7436092396069	0.0803923870520026	-4.53061925763375E-05	8.42663127096224E-09
	K3	141.146173606895	-0.241865029132085	0.000140153669354601	-2.71998179839420E-08



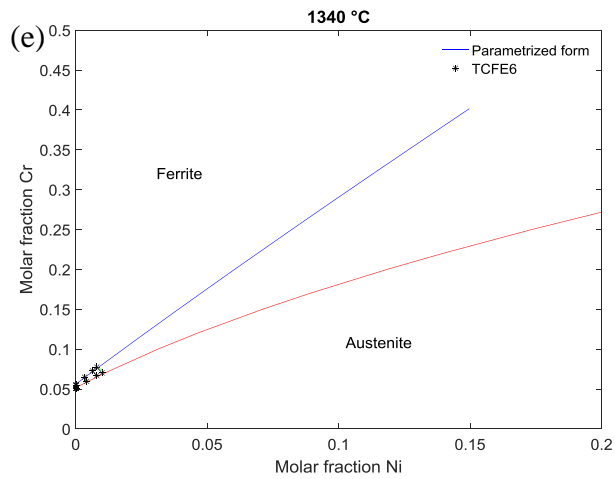


Figure C. 2: Isothermal sections of the iron rich corner of the Fe-Cr-Ni phase diagram at (a) 1000°C, (b) 1100°C, (c) 1200°C, (d) 1300°C and (e) 1340°C. Solid lines represent the interpolated phase boundaries and starred points correspond to the calculated tie-lines with the TCFE6 database and the Thermo-Calc<sup>®</sup> software.

# Appendix D

## Interdiffusion coefficients in ferrite and austenite

In Chapter IV, the numerical model is based, among others, on the following assumptions regarding interdiffusion coefficients of Cr and Ni in ferrite and austenite:

- Coupled interdiffusion coefficients are negligible compared to main ones.
- Interdiffusion coefficients are independent on composition.

In this appendix, we present preliminary calculations of Cr and Ni interdiffusion coefficients that are at the basis of these hypotheses.

### I. Main vs. coupled interdiffusion coefficients

Diffusivity matrices are calculated at Cr and Ni compositions in ferrite and austenite in the as-received state of the multilayered microstructures (Table D. 1).

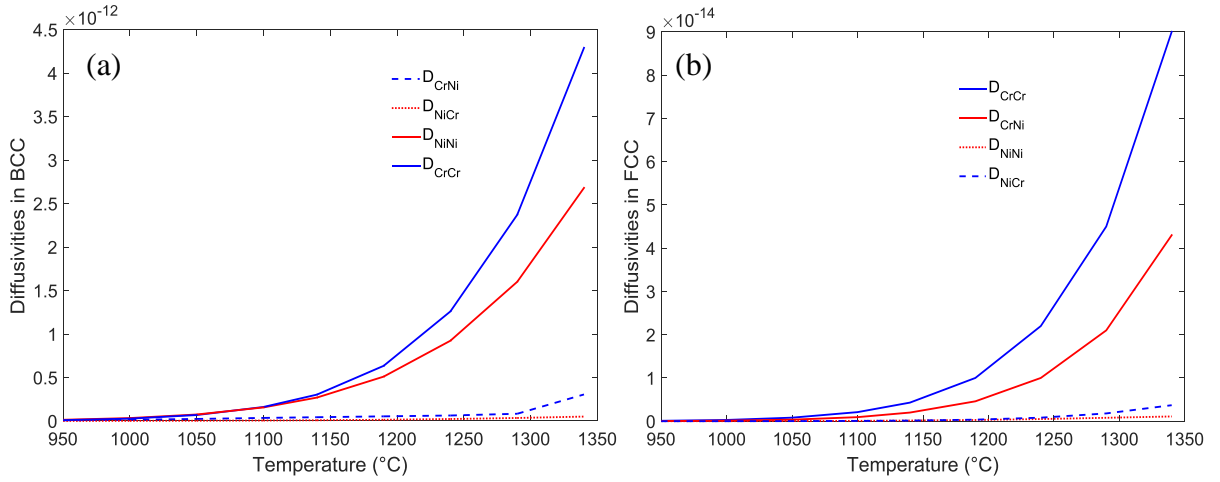
**Table D. 1: Chromium and nickel compositions at which diffusivity matrices are calculated.**

Phase	Composition (wt. %)	
	Cr	Ni
Ferrite	25.3	2.9
Austenite	17.4	11.6

Calculations are performed at temperatures ranging from 1000°C to 1340°C using the DICTRA<sup>®</sup> software and the MOB2 mobility database [72]. From Table D. 2 (and Figure D. 1 for an easier reading) it can be noticed that, except for the ratio  $D_{CrCr}^{\delta}/D_{CrNi}^{\delta}$  at 1000 and 1100°C, the ratio between main and coupled interdiffusion coefficients is higher than 10. This means that when coupled interdiffusion terms are not taken into account in the expression of solute fluxes, the relative error committed in is of 10% at most, which is negligible, in view of the uncertainty on the experimentally determined interdiffusion coefficients. Therefore the assumption of the coupled interdiffusion coefficients being negligible compared to main ones can be regarded as appropriate for  $T > 1100^{\circ}\text{C}$ .

**Table D. 2: Main and coupled interdiffusion coefficients of chromium and nickel in ferrite and austenite of the ternary Fe-Cr-Ni system at temperatures from 1000°C to 1340°C (source: MOB2).**

T (°C)	Ferrite				Austenite			
	$D_{CrCr}^{\delta}$	$D_{CrNi}^{\delta}$	$D_{NiCr}^{\delta}$	$D_{NiNi}^{\delta}$	$D_{CrCr}^{\gamma}$	$D_{CrNi}^{\gamma}$	$D_{NiCr}^{\gamma}$	$D_{NiNi}^{\gamma}$
1000	3,2 E-14	1,0 E-14	5.8 E-16	2,4 E-14	2,8 E-16	1,7 E-17	7,1 E-18	1,3 E-16
1100	1,5 E-13	2,5 E-14	2,1 E-15	1,4 E-13	2,1 E-15	9,4 E-17	6,1 E-17	9,6 E-16
1140	2,7 E-13	2,8 E-14	3,3 E-15	2,7 E-13	4,2 E-15	1,6 E-16	1,3 E-16	2.0 E-15
1190	5,1 E-13	2,1 E-14	5,6 E-15	5.8 E-13	9.9 E-15	3,2 E-16	3,2 E-16	4,6 E-15
1240	9,3 E-13	1,7 E-14	8,7 E-15	1,1 E-12	2,2 E-14	5,7 E-16	7,5 E-16	1,0 E-14
1340	2,7 E-12	3,5 E-13	1,7 E-14	4.0 E-12	8.9 E-14	1,4 E-15	3,4 E-15	4,3 E-14


**Figure D. 1: Main and coupled interdiffusion coefficients of chromium and nickel in ferrite and austenite of the ternary Fe-Cr-Ni system at temperatures from 1000°C to 1340°C (values of Table D. 2)**

## II. Sensitivity of interdiffusion coefficients to composition

From EPMA measurements of Cr and Ni profiles in the multilayered microstructures (Chapter III), the range of Cr and Ni variations in ferrite and austenite are already known. In Chapter I, interdiffusion coefficients have been defined as depending on solute concentration via the chemical potential  $\mu = \mu(c_1, c_2, \dots, c_n)$ ,  $c_k$  being solute concentration of specie k:

$$D_{ki} = \sum_{j=1}^n L'_{kj} \frac{\partial \mu_j}{\partial c_i} \quad (D.1)$$

In this part, we propose to study the impact of variations in Cr and Ni compositions on the values of interdiffusion coefficients  $D_{CrCr}^{\delta}$ ,  $D_{NiNi}^{\delta}$ ,  $D_{CrCr}^{\gamma}$  and  $D_{NiNi}^{\gamma}$ .

In austenite,  $D_{CrCr}^{\gamma}$  and  $D_{NiNi}^{\gamma}$  are calculated for three compositions pairs extracted from Cr and Ni profiles of Figure D. 2.a. The first pair (at the interface) corresponds to the maximum Cr and minimum Ni compositions that can be found in austenite, while the third pair is representative of the minimum Cr and maximum Ni ones (in the as-received state). Correspondent interdiffusion coefficients are listed in Table D. 3. It can be seen that, as austenite becomes enriched in Cr and depleted in Ni,  $D_{CrCr}^{\gamma}$  and  $D_{NiNi}^{\gamma}$  decrease by 15% and 25% respectively.

In ferrite,  $D_{CrCr}^{\delta}$  and  $D_{NiNi}^{\delta}$  are also calculated at three composition pairs extracted from Cr and Ni profiles at different holding times (Figure D. 2.b). Values listed in Table D. 3 show that  $D_{CrCr}^{\delta}$  and  $D_{NiNi}^{\delta}$  diminish with decreasing Cr and increasing Ni contents in ferrite by 7% and 33% respectively.

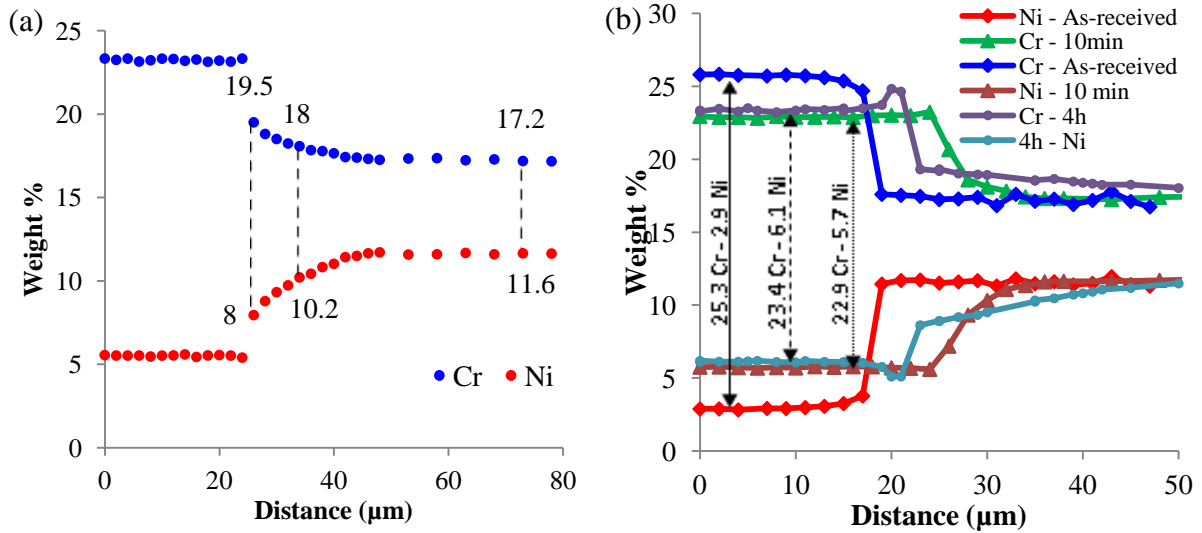


Figure D. 2: (a) Chromium and nickel composition pairs (a) in austenite and (b) in ferrite used for the estimation of the sensitivity of interdiffusion coefficients to composition.

Table D. 3: Interdiffusion coefficients of chromium and nickel in ferrite and austenite of the ternary Fe-Cr-Ni system at 1240°C calculated by DICTRA® and the MOB2 database at the composition pairs of Figure D. 3.

Phase	Composition pairs		$D_{CrCr}$ (m <sup>2</sup> /s)	$D_{NiNi}$ (m <sup>2</sup> /s)
	Cr (wt. %)	Ni (wt. %)		
Austenite	19.5	8	1,9 E-14	8,1 E-15
	18	10.2	2,0 E-14	9,3 E-15
	17.2	11.6	2,2 E-14	1,0 E-14
Ferrite	25.3	2.9	9,3 E-13	1,2 E-12
	22.9	5.7	1,0 E-12	1,6 E-12
	23.4	6.1	1,0 E-12	1,6 E-12

It appears thus that interdiffusion coefficients of Cr and Ni in ferrite and austenite decrease during the transformation and that those of the as-received state (Table D. 1) can be seen as their upper values. The impact of the decrease in interdiffusion coefficients is studied in the following cases:

- **Case 1.** Reference case: interdiffusion coefficients are calculated for the Cr and Ni compositions in the as-received state (Table D. 2).
- **Case 2.** Sensitivity to composition in ferrite:  $D_{CrCr}^{\delta}$  and  $D_{NiNi}^{\delta}$  are taken at their lowest values: -7% and -33% with respect to the reference case .
- **Case 3.** Sensitivity to composition in austenite:  $D_{CrCr}^{\gamma}$  and  $D_{NiNi}^{\gamma}$  are taken at their lowest values: -15% and -25% with respect to the reference case.

Simulations are carried for the CR1 state at 1240°C. A comparison between the three cases is shown in Figure D. 4. Composition dependency in ferrite has a negligible effect on the dissolution kinetics. However, in austenite, results are quite sensitive as the dissolution of ferrite is 20% longer with the lowest diffusion coefficients (at the interface).

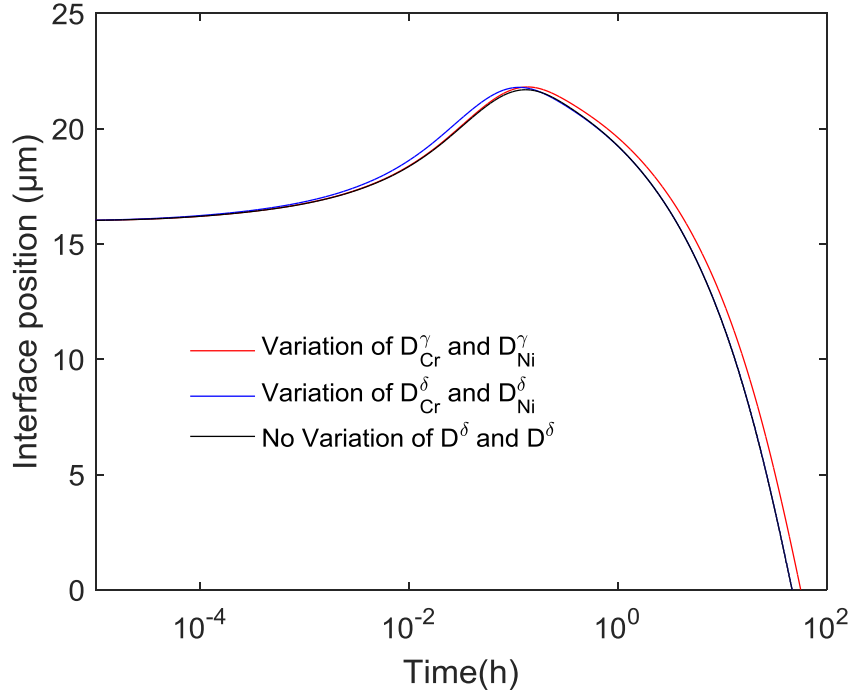


**Figure D. 4: Sensibility of the calculation results on the dependence of diffusion coefficients on concentration.**

From these numerical experiments, the assumption that the main interdiffusion coefficients being composition-independent has no impact in ferrite, while it is not the case for austenite. Since the model does not treat the composition-dependency of interdiffusion coefficients, the discrepancy ensuing from the use of constant coefficients cannot be quantified straightforwardly, though it was proven to exist. In addition, given the difficulty to numerically handle this composition-dependency, it was chosen, for the sake simplicity, to assume constant interdiffusion coefficients.

## Appendix E

### Discretization schemes

The transport-diffusion equation is approximated using the  $\theta$ -scheme in which first and second spatial derivatives operators are weighted over two times  $t + 1$  and  $t$ , using Taylor expansions. For  $\theta = 0, 0.5$  and  $1$  we obtain respectively Euler explicit, Crank-Nicolson and Euler implicit schemes [77][85]. The stability and accuracy of each scheme is given in Table E. 1. The Crank-Nicolson appears as the most appropriate scheme since it possesses a higher time precision and an unconditional stability.

**Table E. 1: Stability and truncation accuracy of the Euler implicit, Euler explicit and Crank-Nicolson schemes.**

	Euler explicit	Euler implicit	Crank-Nicolson
Stability	Conditionally stable	Unconditionally stable	Unconditionally stable
Precision	$\mathcal{O}(\Delta x^2 + \Delta t)$	$\mathcal{O}(\Delta x^2 + \Delta t)$	$\mathcal{O}(\Delta x^2 + \Delta t^2)$

For simplicity we will consider the case of uniform meshing. The transport-diffusion equation becomes for each internal node  $i$ :

$$\begin{aligned}
 \frac{X_i^{t+1} - X_i^t}{\Delta t} - D^\delta \left\{ \theta \frac{X_{i+1}^{t+1} - 2X_i^{t+1} + X_{i-1}^{t+1}}{(\Delta x_\delta^2)^{t+1}} + (1 - \theta) \frac{X_{i+1}^t - 2X_i^t + X_{i-1}^t}{(\Delta x_\delta^2)^t} \right\} \\
 - \left\{ \theta \frac{x_i^{t+1}}{z^{t+1}} \left( \frac{dz}{dt} \right)^{t+1} \frac{X_{i+1}^{t+1} - X_{i-1}^{t+1}}{(2\Delta x_\delta)^{t+1}} + (1 - \theta) \frac{x_i^t}{z^t} \left( \frac{dz}{dt} \right)^t \frac{X_{i+1}^t - X_{i-1}^t}{(2\Delta x_\delta)^t} \right\} \\
 - nD^\delta \left\{ \frac{\theta}{x_i^{t+1}} \frac{X_{i+1}^{t+1} - X_{i-1}^{t+1}}{(2\Delta x_\delta)^{t+1}} + \frac{(1 - \theta) X_{i+1}^t - X_{i-1}^t}{x_i^t (2\Delta x_\delta)^t} \right\} = 0
 \end{aligned} \tag{E.1}$$

in ferrite, and

$$\begin{aligned}
 \frac{X_i^{t+1} - X_i^t}{\Delta t} - D^\gamma \left\{ \theta \frac{X_{i+1}^{t+1} - 2X_i^{t+1} + X_{i-1}^{t+1}}{(\Delta x_\gamma^2)^{t+1}} + (1 - \theta) \frac{X_{i+1}^t - 2X_i^t + X_{i-1}^t}{(\Delta x_\gamma^2)^t} \right\} \\
 - \left\{ \theta \left( \frac{L - x_i^{t+1}}{L - z^{t+1}} \right) \left( \frac{dz}{dt} \right)^{t+1} \frac{X_{i+1}^{t+1} - X_{i-1}^{t+1}}{(2\Delta x_\gamma)^{t+1}} + (1 - \theta) \left( \frac{L - x_i^t}{L - z^t} \right) \left( \frac{dz}{dt} \right)^t \frac{X_{i+1}^t - X_{i-1}^t}{(2\Delta x_\gamma)^t} \right\} \\
 - nD^\gamma \left\{ \frac{\theta}{x_i^{t+1}} \frac{X_{i+1}^{t+1} - X_{i-1}^{t+1}}{(2\Delta x_\gamma)^{t+1}} + \frac{(1 - \theta) X_{i+1}^t - X_{i-1}^t}{x_i^t (2\Delta x_\gamma)^t} \right\} = 0
 \end{aligned} \tag{E.2}$$

in austenite.  $\Delta t$  represents the time step interval,  $\Delta x_\delta^{t+1}$ ,  $\Delta x_\delta^t$ ,  $\Delta x_\gamma^{t+1}$  and  $\Delta x_\gamma^t$  the grid spacings in ferrite and austenite at times  $t + 1$  and  $t$  respectively,  $\left( \frac{dz}{dt} \right)^{t+1}$  and  $\left( \frac{dz}{dt} \right)^t$  the interface velocity at times  $t + 1$  and  $t$  respectively and  $n$  the geometry of the calculation cell. Here the central approximation of the first derivative is used and  $D^\delta$  and  $D^\gamma$  stand for the diffusion coefficients in ferrite and austenite respectively. These equations can be arranged into the following general form:

$$A_i c_{i-1}^{t+1} + B_i c_i^{t+1} + C_i c_{i+1}^{t+1} = D_i c_{i-1}^t + E_i c_i^t + F_i c_{i+1}^t \quad (\text{E.3})$$

where the coefficients  $A_i, B_i, C_i$  and  $D_i, E_i, F_i$  are functions of the time-step and the grid spacings at times  $t + 1$  and  $t$  respectively. At time  $t + 1$  the right hand side of the Eq.(E.3) is known since it depends on the compositions inherited from time  $t$ . This set of linear equations are arranged in the following matrix form:

$$M^{t+1} c^{t+1} = M^t c^t \quad (\text{E.4})$$

where  $M^{t+1}$  and  $M^t$  are tri-diagonal matrixes composed of  $A_i, B_i, C_i$  and  $D_i, E_i, F_i$  terms respectively. This equation is solved by the TriDiagonal Matrix Algorithm (TDMA), which is a variant of the Gauss pivot elimination for tri-diagonal matrixes [77]. Table E. 2 and Table E. 3 summarize the expressions of  $A_i, B_i, C_i, D_i, E_i$  and  $F_i$  in the case of centered difference approximation of the first derivative of composition.

**Table E. 2: Analytical expressions of the  $A_i, B_i, C_i, D_i, E_i$  and  $F_i$  coefficients for the internal nodes in the ferrite region.**

Ferrite	
$A_i = -\frac{D^\delta \Delta t \theta}{(\Delta x_\delta^2)^{t+1}} + \left(\frac{x_i^{t+1}}{z^{t+1}}\right) \left(\frac{dz}{dt}\right)^{t+1} \frac{\theta \Delta t}{2(\Delta x_\delta)^{t+1}} + \frac{nD^\delta \Delta t \theta}{2x_i^{t+1}(\Delta x_\delta)^{t+1}}$	
$B_i = 1 + \frac{2\theta D \Delta t}{(\Delta x_\delta^2)^{t+1}}$	
$C_i = -\frac{D^\delta \Delta t \theta}{(\Delta x_\delta^2)^{t+1}} - \left(\frac{x_i^{t+1}}{z^{t+1}}\right) \left(\frac{dz}{dt}\right)^{t+1} \frac{\theta \Delta t}{2(\Delta x_\delta)^{t+1}} - \frac{nD^\delta \theta \Delta t}{2x_i^{t+1}(\Delta x_\delta)^{t+1}}$	
$D_i = \frac{D^\delta \Delta t (1 - \theta)}{(\Delta x_\delta^2)^t} - \left(\frac{x_i^t}{z^t}\right) \left(\frac{dz}{dt}\right)^t \frac{(1 - \theta) \Delta t}{2(\Delta x_\delta)^t} - \frac{nD^\delta \Delta t (1 - \theta)}{2x_i^t (\Delta x_\delta)^t}$	
$E_i = 1 - \frac{2D^\delta \Delta t (1 - \theta)}{(\Delta x_\delta^2)^t}$	
$F_i = \frac{D^\delta \Delta t (1 - \theta)}{(\Delta x_\delta^2)^t} + \left(\frac{x_i^t}{z^t}\right) \left(\frac{dz}{dt}\right)^t \frac{\Delta t (1 - \theta)}{2(\Delta x_\delta)^t} + \frac{nD^\delta \Delta t (1 - \theta)}{2x_i^t (\Delta x_\delta)^t}$	

**Table E. 3: Analytical expressions of the  $A_i, B_i, C_i, D_i, E_i$  and  $F_i$  coefficients for the internal nodes in the austenite region.**

Austenite	
$A_i = -\frac{D^\gamma \Delta t \theta}{(\Delta x_\gamma^2)^{t+1}} + \left(\frac{L - x_i^{t+1}}{L - z^{t+1}}\right) \left(\frac{dz}{dt}\right)^{t+1} \frac{\Delta t \theta}{2(\Delta x_\gamma)^{t+1}} - \frac{nD^\gamma \Delta t \theta}{2x_i^{t+1}(\Delta x_\gamma)^{t+1}}$	
$B_i = 1 + \frac{2D^\gamma \Delta t \theta}{(\Delta x_\gamma^2)^{t+1}}$	
$C_i = -\frac{D^\gamma \Delta t \theta}{(\Delta x_\gamma^2)^{t+1}} - \left(\frac{L - x_i^{t+1}}{L - z^{t+1}}\right) \left(\frac{dz}{dt}\right)^{t+1} \frac{\Delta t \theta}{2(\Delta x_\gamma)^{t+1}} - \frac{nD^\gamma \Delta t \theta}{2x_i^{t+1}(\Delta x_\gamma)^{t+1}}$	
$D_i = \frac{D^\gamma \Delta t (1 - \theta)}{(\Delta x_\gamma^2)^t} - \left(\frac{L - x_i^t}{L - z^t}\right) \left(\frac{dz}{dt}\right)^t \frac{(1 - \theta) \Delta t}{2(\Delta x_\gamma)^t} - \frac{nD^\gamma \Delta t (1 - \theta)}{2x_i^t (\Delta x_\gamma)^t}$	
$E_i = 1 - \frac{2D^\gamma \Delta t (1 - \theta)}{(\Delta x_\gamma^2)^t}$	
$F_i = \frac{D^\gamma \Delta t (1 - \theta)}{(\Delta x_\gamma^2)^t} + \left(\frac{L - x_i^t}{L - z^t}\right) \left(\frac{dz}{dt}\right)^t \frac{(1 - \theta) \Delta t}{2(\Delta x_\gamma)^t} + \frac{nD^\gamma \Delta t (1 - \theta)}{2x_i^t (\Delta x_\gamma)^t}$	

For the boundary nodes, the equations to resolve in ferrite and austenite are respectively:

$$\begin{cases} B_1 c_1^{t+1} + C_1 c_2^{t+1} = E_1 c_1^t + F_1 c_2^t \\ A_{N^\gamma} c_{N^\gamma-1}^{t+1} + B_{N^\gamma} c_{N^\gamma}^{t+1} = D_{N^\gamma} c_{N^\gamma-1}^t + E_{N^\gamma} c_{N^\gamma}^t \end{cases}$$

The expression of the coefficients  $A_N$ ,  $B_1$ ,  $B_N$ ,  $C_1$ ,  $D_N$ ,  $E_N$  and  $F_1$  are given in Table E. 4.

**Table E. 4: Analytical expressions of the  $A_N$ ,  $B_1$ ,  $B_N$ ,  $C_1$ ,  $D_N$ ,  $E_1$ ,  $E_N$  and  $F_1$  coefficients for boundary nodes in ferrite and austenite phase region.**

Ferrite	Austenite
$B_1 = 1 + \frac{D^\delta \Delta t \theta}{(\Delta x_\delta^2)^{t+1}}$	$A_{N^\gamma} = -\frac{D^\gamma \Delta t \theta}{(\Delta x_\gamma^2)^{t+1}}$
$C_1 = -\frac{D^\delta \Delta t \theta}{(\Delta x_\delta^2)^{t+1}}$	$B_{N^\gamma} = 1 + \frac{D^\gamma \Delta t \theta}{(\Delta x_\gamma^2)^{t+1}}$
$E_1 = 1 - \frac{D^\delta \Delta t (1 - \theta)}{(\Delta x_\delta^2)^t}$	$D_{N^\gamma} = \frac{D^\gamma \Delta t (1 - \theta)}{(\Delta x_\gamma^2)^t}$
$F_1 = \frac{D^\delta \Delta t (1 - \theta)}{(\Delta x_\delta^2)^t}$	$E_{N^\gamma} = 1 - \frac{D^\gamma \Delta t (1 - \theta)}{(\Delta x_\gamma^2)^t}$



## Appendix F

### Comparison of several meshings: sensitivity of the calculation results to the number of grid points

In this Appendix, various meshings will be tested and their efficiency outlined. Calculations will be carried on the reference case of ferrite dissolution in the CR1 state of the multilayered microstructure.

#### I. Uniform meshing

##### I.1. Effect of the meshing size in the austenitic phase region

Figure F. 1 shows the movement and the velocity of the interface as function of annealing time for three grid numbers in austenite: 100, 500 and 1000, the number of grids in ferrite being fixed to 20. The kinetics of ferrite dissolution are significantly affected by the number of grid points in austenite and its dissolution decreases from 52hrs to 46hrs for an increasing grid number.

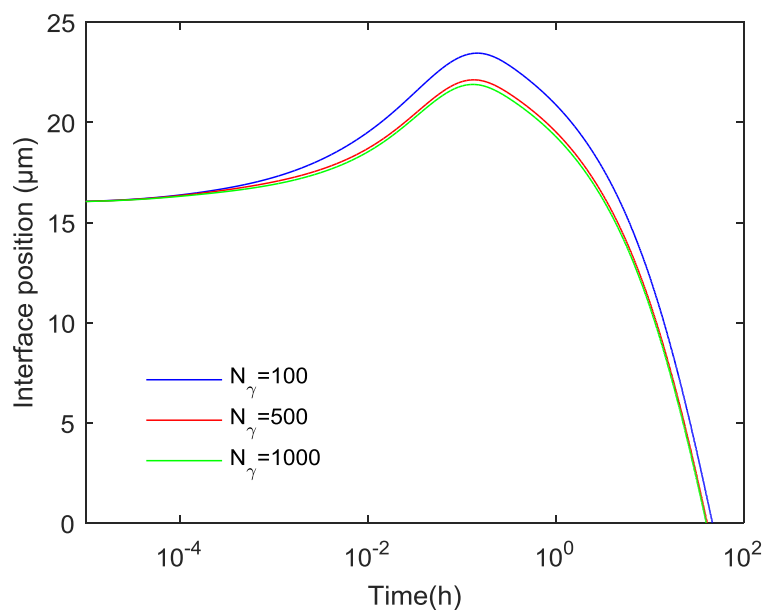
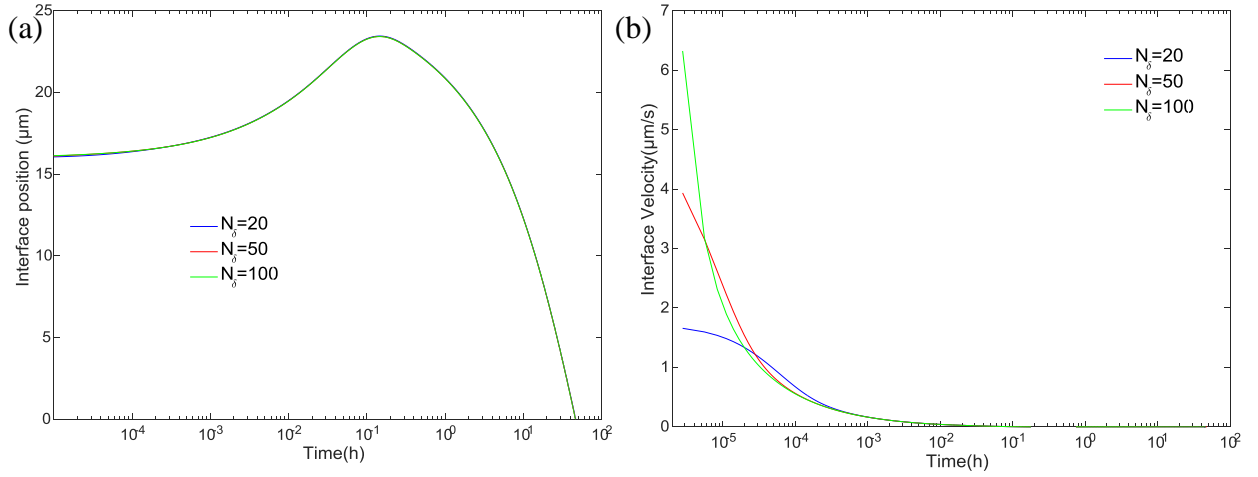


Figure F. 1: Kinetics of ferrite dissolution in the CR1 multilayered microstructure for 100, 500 and 1000 grid points in the austenite region.

## I.2. Effect of the meshing size in the ferritic phase region

The same numerical experiment was conducted with a number of grids in the ferrite region equal to 20, 50 and 100, while that in the austenite region is fixed to 100. Figure F. 2 shows the evolution of the interface position and velocity as function of time for the three grid numbers. In contrast with what has been observed in the previous paragraph, the grid number in ferrite affects the interface position only at the very beginning of the transformation ( $t < 1s$ ), whereas it has a negligible effect at the later stage of the transformation dissolution of ferrite.



**Figure F. 2: (a) Kinetics of ferrite dissolution in the multilayered microstructure in the CR1 state at 1240°C using 20, 50 and 100 grid points in the ferritic region. (b) Corresponding velocity of the interface showing the effect of the meshing in ferrite on the very beginning of the transformations.**

## I.3. Discussion

To understand the dependence of the calculation results on the number of grid points, one has to consider the mass balance equation:

$$(X^{\delta/\gamma} - X^{\gamma/\delta}) \frac{dz}{dt} = D^{\gamma} \left. \frac{\partial X}{\partial x} \right|^{\gamma} - D^{\delta} \left. \frac{\partial X}{\partial x} \right|^{\delta}$$

At the beginning, given that  $D^{\delta} \gg D^{\gamma}$  (see Appendix D) and assuming that initial solute gradients in austenite and ferrite are of the same order of magnitude:

$$D^{\delta} \left. \frac{\partial X}{\partial x} \right|^{\delta} \gg D^{\gamma} \left. \frac{\partial X}{\partial x} \right|^{\gamma}$$

Thus the migration rate of the interface may be approximated by the following equation

$$\frac{dz}{dt} \approx - \frac{1}{X^{\delta/\gamma} - X^{\gamma/\delta}} D^{\delta} \left. \frac{\partial X}{\partial x} \right|^{\delta}$$

Knowing that solute gradient in ferrite is inversely proportional to the meshing size in ferrite  $\Delta x_{\delta}$  by the relation

$$\left. \frac{\partial X}{\partial x} \right|^\delta = \frac{(X_{N-2} + 3X_{\delta/\gamma} - 4X_{N-1})}{2\Delta x_\delta}$$

It can be understood that, initially, when solute gradients are well established in ferrite, the velocity of the interface is mainly affected by  $\Delta x_\delta$  and this phenomenon can be seen in Figure F. 2.b. As the transformation proceeds, solute gradients in ferrite become rapidly flat so that:

$$D^\delta \left. \frac{\partial X}{\partial x} \right|^\delta \ll D^\gamma \left. \frac{\partial X}{\partial x} \right|^\gamma$$

and the transformation becomes driven by diffusion in austenite. Therefore the velocity of the interface will be affected mainly by  $\Delta x_\gamma$  and this is the reason why the calculation results are strongly dependant of  $\Delta x_\gamma$  (and not of  $\Delta x_\delta$ ) at later stages of the transformation.

From these observation, one can conclude that when phase transformation is studied between two materials in which solutes diffusivities are much different, the calculation results will depend essentially on the meshing size of the phase region having the lowest diffusivity.

## II. Geometrical meshing: accuracy and mass loss

With the geometrical meshing, grid spacings are fine near the interface and become gradually coarse when approaching the boundaries of the calculation cell. The progressive change in grid spacing is made possible using the following equation relating each grid spacing to its previous neighbor:

$$\Delta x_i = k. \Delta x_{i-1}$$

where  $k$  is the geometrical factor and  $i = 2, \dots, N$ . In ferrite grid spacing decreases towards the interface, *i.e.*  $k^\delta < 1$ , while in austenite  $k^\gamma > 1$  since grid spacing increases towards the cell boundary (Figure F. 3).

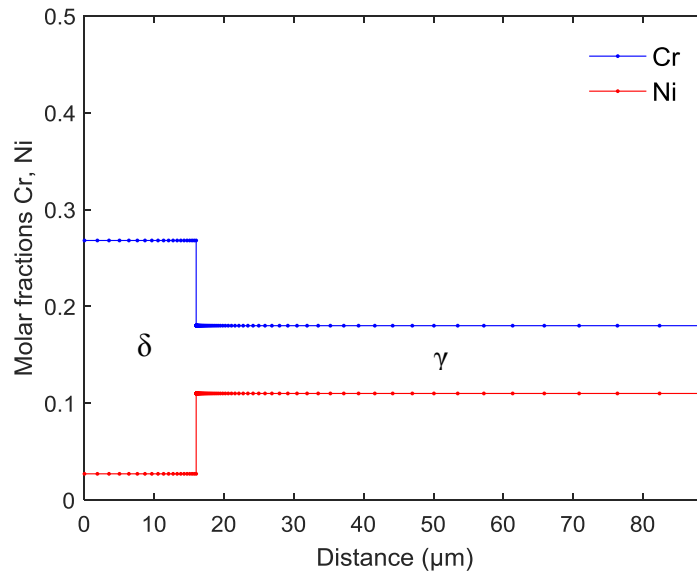


**Figure F. 3: Geometrical meshing in the calculation cell for the simulation of ferrite dissolution in the CR1 state of the multilayered microstructure.**

With the geometrical meshing, the expressions of the first and second derivatives of composition become:

$$\frac{\partial X_i^t}{\partial x} = \frac{X_{i+1}^t + (k^2 - 1)c_i^t - k^2 X_{i-1}^t}{k(1+k)\Delta x_{i-1}} + \mathcal{O}(\Delta x_{i-1}^2)$$

$$\frac{\partial^2 X_i^t}{\partial x^2} = \frac{2 X_{i+1}^t - 2(1+k) X_i^t + 2k X_{i-1}^t}{k(1+k)\Delta x_{i-1}^2} + \mathcal{O}(\Delta x_{i-1})$$

It is important to note that truncation errors are of second order for the first derivative and only of first order for the second derivative.

Calculations of ferrite dissolution in the CR1 state were reiterated with the geometrical meshing (20 grid points in  $\delta$ ,  $k^\delta = 0.9$ , 100 grid points in  $\gamma$ ,  $k^\gamma = 1.1$ ). Resultant dissolution kinetics are shown in Figure F. 4. Calculations with the uniform meshing having 1000 grid points in austenite are superimposed as well. The use of geometrical meshing predicts the same dissolution time as with the uniform meshing with a high number of grid points. From that perspective the geometrical meshing succeeds in predicting accurately the dissolution time. However, from a mass conservation perspective, it leads to major mass loss as it can be seen in Table F. 1, which renders the results less reliable. We suspect that this mass loss is mainly due to the loss of truncation accuracy in the expression of the second derivative. It should be noted that the mass loss was found to depend on the values of the geometrical factors.

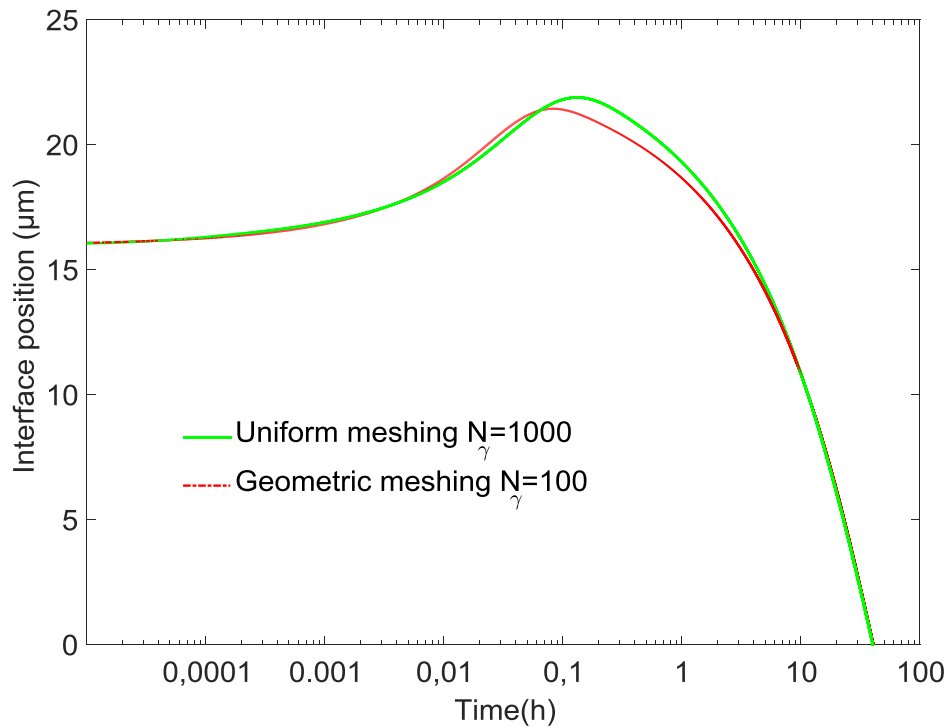


**Figure F. 4: Kinetics of ferrite dissolution in the CR1 state at 1240°C using the geometrical meshing and the uniform meshing with 1000 grid points in austenite.**

**Table F. 1: Chromium and nickel mass loss when a geometrical meshing is used.**

Average Cr	Average Ni
5 %	8%

### III. Double-uniform meshing

Figure F. 5 shows the kinetics of ferrite dissolution in the multilayered microstructure in the CR1 state at 1240°C using the double-uniform, the geometric and the uniform meshings. Clearly, with a small number of grid points the double-uniform meshing allows to obtain results consistent with previous calculations. Of great importance is to note that, unlike the geometric meshing, very little deviation from mass conservation is observed ( $\sim 0.01\%$ ). Furthermore, calculations with this meshing have proven to be insensitive to the number of grid points in austenite.

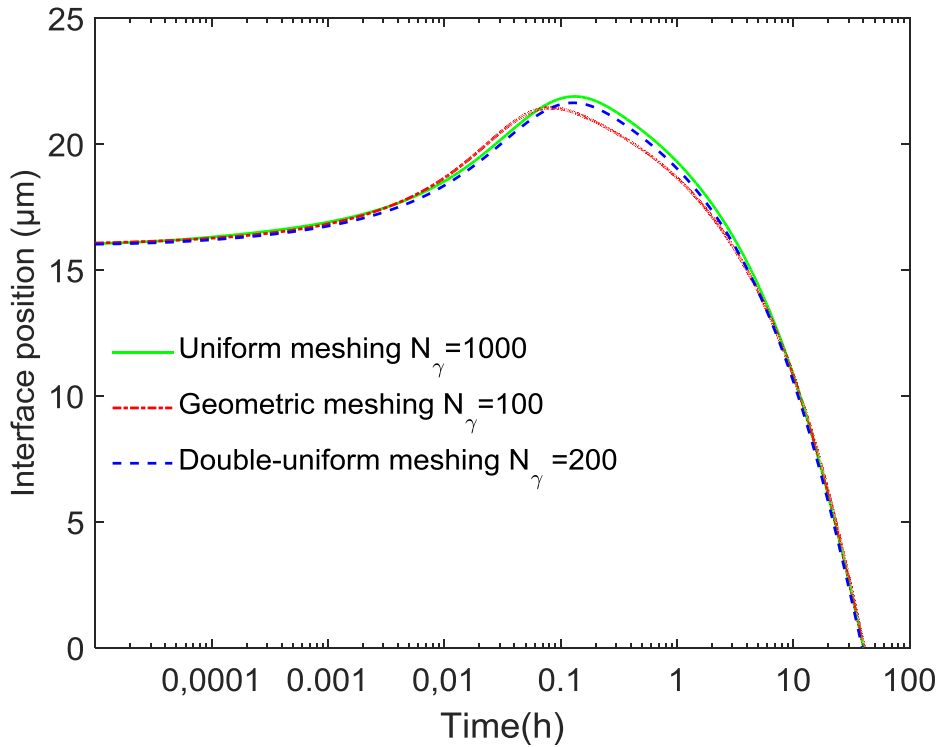


**Figure F. 5: Kinetics of ferrite dissolution in the CR1 state at 1240°C using the double-uniform, the geometric and the uniform meshing with 1000 grid points in austenite.**

### IV. Conclusion

With the three types of meshing, it is possible to obtain the same mesh-insensitive result, but at certain cost when uniform and geometrical meshings are used. The double-uniform meshing has proven to be the most efficient one, as it permits to capture the gradient at the interface without using an elevated number of grid points.

In terms of deviation from mass conservation, the uniform and the double-uniform meshings permit to keep it at a very low extent (between 0.01% and 0.1% relative) for calculations made in the planar geometry (we will show that with cylindrical and spherical geometries this is not true). However, with the geometrical meshing deviation from mass conservation is of several percent relative, which makes ensuing results less reliable.

## Appendix G

### Stability analysis for the of the diffusion-transport equation

The aim of this section is to provide details of the mathematical analysis of spatial stability of the diffusion-transport equation:

$$\frac{\partial X_i}{\partial t} - D \frac{\partial^2 X_i}{\partial x^2} - V \frac{\partial X_i}{\partial x} = 0$$

where  $D$  is the interdiffusion coefficient and  $V = \frac{dx_i}{dt}$ . Let's consider the stationary part of the diffusion-transport equation, with centered first derivative:

$$-D \frac{(X_{i+1} - 2X_i + X_{i-1}))}{\Delta x^2} - V \frac{X_{i+1} - X_{i-1}}{2\Delta x} = 0$$

This expression can be arranged into the following way

$$(2 - Pe)X_{i-1} - 4X_i + (2 + Pe)(X_i - X_{i+1}) = 0$$

where  $Pe$  is the Péclet grid number, defined by

$$Pe = \frac{V\Delta x}{D}$$

It can be shown that in order to prevent oscillation from occurring, the ratio

$$\frac{(X_{i+1}^{t+1} - X_i^{t+1})}{(X_i^{t+1} - X_{i-1}^{t+1})} = \frac{(2 - Pe)}{(2 + Pe)}$$

must be strictly positive, which is only possible when  $Pe > 2$  or  $Pe < -2$ . This condition is required to ensure the stability of the centered scheme used in the approximation of the diffusion-transport equation. In order to match this stability criterion, one should use the upwind scheme that is stable regardless of the value of  $Pe$  or add a corrective artificial diffusion coefficient to physical one. The reader can refer to Chapter IV for further details.



## Appendix H

### where does numerical diffusion come from?

Numerical diffusion refers to the diffusion artificially created by the discretization schemes. It can be negative, as in the centered schemes where physical diffusion is underestimated. But it can be positive and thus physical diffusion is exaggerated as it is the case with the upwind schemes. In this section demonstration of both phenomena are mathematically explained.

#### I. Why do centered schemes underestimate diffusion ?

Let's consider the centered approximation of the diffusion-transport equation:

$$\frac{X_i^{t+1} - X_i^t}{\Delta t} - V \frac{X_{i+1}^{t+1} - X_{i-1}^{t+1}}{\Delta x} - D \frac{(X_{i+1}^{t+1} - 2X_i^{t+1} + X_{i-1}^{t+1})}{\Delta x^2} \quad (\text{H.1})$$

where  $D$  and  $V = \frac{dx_i}{dt}$  are assumed constant for simplicity. Each term of the Eq.(H.1) is evaluated using the following Taylor expansions around  $(x_i, t)$ :

$$X_{i+1}^{t+1} = X_i^{t+1} + \Delta x \left. \frac{\partial X}{\partial x} \right|_i^{t+1} + \frac{\Delta x^2}{2} \left. \frac{\partial^2 X}{\partial x^2} \right|_i^{t+1} + \mathcal{O}(\Delta x^3)$$

$$X_{i-1}^{t+1} = X_i^{t+1} - \Delta x \left. \frac{\partial X}{\partial x} \right|_i^{t+1} + \frac{\Delta x^2}{2} \left. \frac{\partial^2 X}{\partial x^2} \right|_i^{t+1} + \mathcal{O}(\Delta x^3)$$

$$X_i^{t+1} = X_i^t + \Delta t \left. \frac{\partial X}{\partial t} \right|_i^t + \frac{\Delta t^2}{2} \left. \frac{\partial^2 X}{\partial t^2} \right|_i^t + \mathcal{O}(\Delta t^3)$$

Substituting these equations into Eq.(H.1) gives

$$\left[ \left. \frac{\partial X}{\partial t} \right|_i^t + \frac{\Delta t}{2} \left. \frac{\partial^2 X}{\partial t^2} \right|_i^t + \mathcal{O}(\Delta t^2) \right] - D \left[ \left. \frac{\partial^2 X}{\partial x^2} \right|_i^{t+1} + \mathcal{O}(\Delta x^2) \right] - V \left[ \left. \frac{\partial X}{\partial x} \right|_i^{t+1} + \mathcal{O}(\Delta x^2) \right] = 0 \quad (\text{H.2})$$

or, by dropping the indexes  $t$  and  $i$ ,

$$\left[ \frac{\partial X}{\partial t} - D \frac{\partial^2 X}{\partial x^2} - V \frac{\partial X}{\partial x} \right] - \frac{\Delta t}{2} \frac{\partial^2 X}{\partial t^2} + \mathcal{O}(\Delta x^2, \Delta t^2) = 0 \quad (\text{H.3})$$

For  $\Delta x, \Delta t \rightarrow 0$ , this equation tends to the original diffusion-transport equation. But for  $\Delta t > 0$  and by dropping the higher order terms, Eq.(H.3) becomes:

$$\left[ \frac{\partial X}{\partial t} - D \frac{\partial^2 X}{\partial x^2} - V \frac{\partial X}{\partial x} \right] - \frac{\Delta t}{2} \frac{\partial^2 X}{\partial t^2} = 0 \quad (\text{H.4})$$

Let's evaluate the term  $\frac{\partial^2 X}{\partial t^2}$  and replace it by space derivatives. Recalling that :

$$\frac{\partial X}{\partial t} - D \frac{\partial^2 X}{\partial x^2} - V \frac{\partial X}{\partial x} = 0 \quad (\text{H.5})$$

we obtain

$$\begin{aligned} \frac{\partial^2 X}{\partial t^2} &= \frac{\partial}{\partial t} \left( D \frac{\partial^2 X}{\partial x^2} + V \frac{\partial X}{\partial x} \right) \\ \frac{\partial^2 X}{\partial t^2} &= D \frac{\partial^3 X}{\partial t \partial x^2} + V \frac{\partial^2 X}{\partial t \partial x} \end{aligned} \quad (\text{H.6})$$

Changing the order of chain differentiation and substituting for  $\frac{\partial X}{\partial t}$  from Eq.(H.5) gives

$$\begin{aligned} \frac{\partial^2 X}{\partial t^2} &= D \frac{\partial^2}{\partial x^2} \left( D \frac{\partial^2 X}{\partial x^2} + V \frac{\partial X}{\partial x} \right) + V \frac{\partial}{\partial x} \left( D \frac{\partial^2 X}{\partial x^2} + V \frac{\partial X}{\partial x} \right) \\ \frac{\partial^2 X}{\partial t^2} &= V^2 \frac{\partial^2 X}{\partial x^2} - 2VD \frac{\partial^3 X}{\partial x^3} + D^2 \frac{\partial^4 X}{\partial x^4} \end{aligned} \quad (\text{H.7})$$

Injecting Eq.(H.7) into Eq.(H.4) gives

$$\frac{\partial X}{\partial t} - \left( D - \frac{V^2 \Delta t}{2} \right) \frac{\partial^2 X}{\partial x^2} - V \frac{\partial X}{\partial x} + \left( DV \Delta t \frac{\partial^3 X}{\partial x^3} + \frac{D \Delta t}{2} \frac{\partial^4 X}{\partial x^4} \right) = 0 \quad (\text{H.8})$$

Generally the higher order terms are much smaller than the second derivative, so they can be dropped. Thus Eq.(H.8) becomes

$$\frac{\partial X}{\partial t} - D_{eff} \frac{\partial^2 X}{\partial x^2} - V \frac{\partial X}{\partial x} = 0 \quad (\text{H.9})$$

where

$$D_{eff} = D - \frac{V^2 \Delta t}{2} \quad (\text{H.10})$$

It is clear that Eq.(H.1), which initially results from the discretization of Eq.(H.5), resolves in fact Eq.(H.9). Because the form of Eq.(H.9) is equivalent to the original diffusion-transport equation, we refer to  $D_{eff}$  as "effective diffusion coefficient". This coefficient comprises, in addition to the physical diffusion  $D$ , an artificial diffusion term  $-\frac{V^2 \Delta t}{2}$  which is purely numeric. Since  $\Delta t > 0$ ,

$$D_{eff} < D.$$

and for this reason centered schemes underestimate the physical diffusion. In case of convection dominated cases, which usually occur at the beginning of the transformation,  $\frac{V^2 \Delta t}{2}$  is comparable to  $D$  so that the underestimation is non negligible.

## II. Why do upwind schemes overestimate diffusion ?

Following the same approach as for centered schemes and considering only the stationary part of the diffusion-transport equation, upwind schemes are equivalent to the following diffusion-transport equation, after dropping of the higher order term:

$$-\left(D + \frac{V\Delta x}{D}\right)\frac{\partial^2 X}{\partial x^2} - V\frac{\partial X}{\partial x} = 0 \quad (\text{H.11})$$

Clearly, the diffusion coefficient comprises an extra numerical diffusion  $\frac{V\Delta x}{D}$  in addition to the physical diffusion coefficient  $D$ . That is why this scheme overestimates diffusion. It is to be noted that, in Eq.(H.11), the temporal term is dropped as mathematical explanations in literature are only provided for steady state equations.



## Résumé :

La ferrite résiduelle  $\delta$ , présente dans les microstructures de coulée des aciers inoxydables austénitiques, résulte de la transformation incomplète  $\delta \rightarrow \gamma$  ayant lieu l'étape de solidification. Sa présence peut nuire à la forgeabilité à chaud des aciers inoxydables en conduisant à la formation de criques de rives et de pailles en J lors du laminage à chaud des brames. Ce travail de thèse a pour but de comprendre les mécanismes de la transformation  $\delta \rightarrow \gamma$  à haute température dans les aciers inoxydables austénitiques via une modélisation expérimentale et numérique. La transformation a été étudiée dans un alliage ternaire Fe-Cr-Ni coulé par lingot et de composition proche de celle des alliages industriels. Trois morphologies de ferrite ont été mises en évidence à l'état brut de solidification: lattes au bord du lingot, vermiculaire et lattes au centre. Leur cinétique de dissolution est étudiée à des températures allant de 1140°C à 1340°C et caractérisée en termes de fraction de ferrite et profils de composition du Cr et du Ni. La dissolution de la ferrite vermiculaire comprend trois étapes : une croissance initiale transitoire suivie par un régime de dissolution rapide puis un régime de dissolution lente. Par ailleurs, la dissolution de la ferrite a aussi été étudiée dans des microstructures multicouches élaborées par l'empilement de plaques de ferrite et d'austénite du système Fe-Cr-Ni et soudées à l'état solide par Compression Isostatique à Chaud puis réduits en épaisseur par laminages successifs. L'étude et la caractérisation de la cinétique de dissolution de la ferrite est plus facile dans ces microstructures étant donnée la planéité initiale des interfaces  $\delta/\gamma$ . L'analyse des résultats expérimentaux a été menée via le développement d'un modèle de transformation de phase à interface mobile. La diffusion peut être traitée dans les géométries plane, cylindrique et sphérique. En guise de validation, le modèle a été utilisé pour analyser la dissolution de la ferrite dans les microstructures multicouches. Par la suite il a été appliqué au cas de la ferrite vermiculaire en usant d'une approche novatrice où la morphologie des dendrites est approximée par une combinaison de cylindres et de sphères. Malgré la simplicité des hypothèses sous-jacentes, le modèle a reproduit de façon satisfaisante les cinétiques de dissolution expérimentales. Il a aussi permis d'expliquer les mécanismes de croissance initiale et de changement de régime de dissolution de la ferrite vermiculaire. D'autre part, via une étude paramétrique, l'effet des données d'entrée a été étudié et les plus pertinentes d'entre eux en termes de prédiction quantitative ont été mises en avant, en particulier la description thermodynamique du diagramme Fe-Cr-Ni, le gradient initial et la distribution des rayons des particules de ferrite.

## Abstract:

Residual  $\delta$ -ferrite is widely encountered in the as-cast microstructure of austenitic stainless steels. It stems from the incomplete high temperature solid-state  $\delta \rightarrow \gamma$  transformation occurring upon the solidification stage. Its presence has a detrimental effect the hot workability of stainless steels, leading to the formation of edge cracks and sliver defects during slabs hot rolling. This PhD work aims at bringing more understanding of the kinetics of high temperature  $\delta \rightarrow \gamma$  transformation in austenitic stainless steels via experimental and numerical modeling. The transformation was studied in a ternary Fe-Cr-Ni ingot-cast alloy with composition close to the industrial alloys. Three ferrite morphologies were identified: lathy at the edge of the ingot, vermicular and lathy at the center. Their dissolution kinetics were established at temperatures ranging from 1140°C to 1340°C and characterized in terms of ferrite fraction and Cr and Ni diffusion. The vermicular ferrite undergoes a transient growth followed by a high then a low rate dissolution regimes. On the other hand, ferrite dissolution was also studied in the multilayered microstructures. such microstructures were elaborated by alternating ferrite and austenite sheets of the Fe-Cr-Ni system, diffusion-bonded by Hot isostatic Pressing and reduced in thickness by successive rollings. Dissolution is easier to handle in such microstructures thanks to the initial planar  $\delta/\gamma$  interfaces. Analysis of the experimental results were carried out with a numerical moving-boundary model of diffusion-controlled  $\delta \rightarrow \gamma$  transformation. Diffusion can be treated in the planar, cylindrical and spherical geometries. As a preliminary validation, the model was used to analyze kinetics of ferrite dissolution in the multilayered microstructures. It was then applied to the cast alloy using an original descriptive approach combining spheres and cylinders as equivalent morphology of dendritic ferrite. Although based on simplifying assumptions, the model was able to reproduce experimental results with satisfactory agreement. Mechanisms underlying the initial growth of vermicular ferrite and the transition in dissolution regimes were outlined. The effect of a wide range of input parameters has been considered and relevant parameters for quantitative calculations were brought to light, such as thermodynamical descriptions of the Fe-Cr-Ni system, composition gradients and distribution of ferrite's radii.